

2000 SUMMER RESEARCH PROGRAM FOR HIGH SCHOOL JUNIORS
AT THE
UNIVERSITY OF ROCHESTER'S
LABORATORY FOR LASER ENERGETICS

STUDENT RESEARCH REPORTS

PROGRAM COORDINATOR

Dr. R. Stephen Craxton

March 2000

Lab Report 319

2000 SUMMER RESEARCH PROGRAM FOR HIGH SCHOOL JUNIORS

AT THE

UNIVERSITY OF ROCHESTER'S

LABORATORY FOR LASER ENERGETICS

STUDENT RESEARCH REPORTS

PROGRAM COORDINATOR

Dr. R. Stephen Craxton

LABORATORY FOR LASER ENERGETICS

University of Rochester

250 East River Road

Rochester, NY 14623-1299

During the summer of 2000, 14 students from Rochester-area high schools participated in the Laboratory for Laser Energetics' Summer High School Research Program. The goal of this program is to excite a group of high school students about careers in the areas of science and technology by exposing them to research in a state-of-the-art environment. Too often, students are exposed to "research" only through classroom laboratories, which have prescribed procedures and predictable results. In LLE's summer program, the students experience many of the trials, tribulations, and

rewards of scientific research. By participating in research in a real environment, the students often become more excited about careers in science and technology. In addition, LLE gains from the contributions of the many highly talented students who are attracted to the program.

The students spent most of their time working on their individual research projects with members of LLE's technical staff. The projects were related to current research activities at LLE and covered a broad range of areas of interest including laser modeling and characterization, diagnostic development, hydrodynamics modeling, liquid crystal chemistry, superconductors, optical coatings, laser damage, and the development of a novel laser glass. The students, their high schools, their LLE supervisors, and their project titles are listed in the table. Their written reports are collected in this volume.

The students attended weekly seminars on technical topics associated with LLE's research. Topics this year included lasers, fusion, holography, optical materials, nonlinear optics, the OMEGA Cryogenic Target System, and scientific ethics. The students also received safety training, learned how to give scientific presentations, and were introduced to LLE's resources, especially the computational facilities.

The program culminated with the High School Student Summer Research Symposium on 23 August at which the students presented the results of their research to an audience including parents, teachers, and LLE staff. Each student spoke for approximately ten minutes and answered questions. At the symposium the William D. Ryan Inspirational Teacher award was presented to Mr. James Shannon, a chemistry teacher at Pittsford-Mendon High School. This annual award honors a teacher, nominated

by alumni of the LLE program, who has inspired outstanding students in the areas of science, mathematics, and technology.

A total of 117 high school students have participated in the program since it began in 1989. The students this year were selected from approximately 70 applicants. Each applicant submitted an essay describing their interests in science and technology, a copy of their transcript, and a letter of recommendation from a science or math teacher.

LLE plans to continue this program in future years. The program is strictly for students from Rochester-area high schools who have just completed their junior year. Applications are generally mailed out in early February with an application deadline near the end of March. For more information about the program or an application form, please contact Dr. R. Stephen Craxton at LLE.

This program was supported by the U.S. Department of Energy Office of Inertial Confinement Fusion under Cooperative Agreement No. DE-FC03-92SF19460.

High School Students and Their Projects (2000)			
Student	High School	Supervisor	Project
Andrew Campanella	Webster	P. Jaanimagi	Large Area, Low Voltage X-Ray Source
Jill Daum	Rushville	D. Smith/J. Taniguchi	Experimental Simulation of Damage in Spatial Filter Lenses
Abraham Fetterman	Pittsford Mendon	M. Skeldon	Modeling Pulse Shape Distortions in the OMEGA Laser
Ming-fai Fong	Pittsford Sutherland	S. Regan	Experimental Investigation of Smoothing by Spectral Dispersion with Apertured Near Fields
Robert Forties	Irondequoit	F. Marshall	X-ray Sensitivity Measurements of Charge Injection Devices (CID's)
Binghai Ling	Brighton	R. Epstein	Simulation of Plasma Spectra and Images of Foil Targets Using the Prism SPECT3D Radiation-Transport Post-Processor
Anne Marino	Hilton	S. Jacobs	Durable Phosphate Glasses with Low Glass Transition Temperatures
Elizabeth McDonald	Harley	J. Zuegel	Adapting ASBO/VISAR for Foam Targets
Ronen Mukamel	Brighton	S. Craxton	Frequency Conversion of Phase-Aberrated Laser Beams for the National Ignition Facility
Gloria Olivier	Honeoye Falls-Lima	K. Marshall	Improvements in the Strength of Visible Selective Reflection in Lyotropic Liquid Crystals Made from Cellulose Urethanes
Colin Parker	Brighton	J. Marozas	Dynamic Focal Spot Size Using a Static Phase Plate
Priya Rajasethupathy	Brockport	J. Delettrez	Improving Equation of State Tables
John Savidis	Gates-Chili	R. Sobolewski	Characterization of Ultrafast Superconducting Optoelectronic Devices
Stephanie Wolfe	Spencerport	D. Smith/J. Oliver	Coatings for Ultraviolet Lithography

Large Area, Low Voltage X-Ray Source

Andrew Campanella
Webster High School

Advised by Dr. Paul Jaanimagi

University of Rochester
Laboratory for Laser Energetics
2000 Summer High School Academic Research Program

1. Abstract

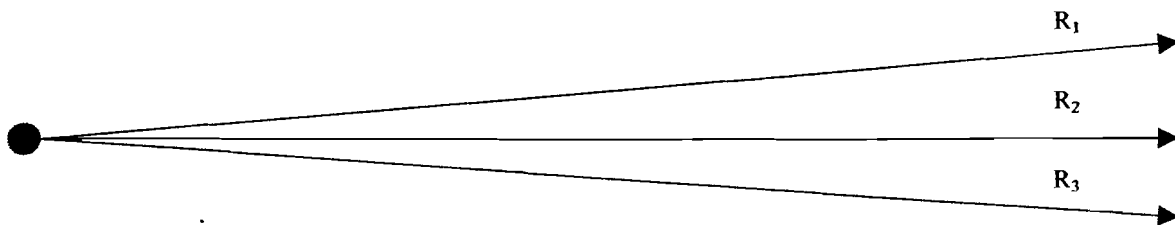
The calibration of various x-ray diagnostics at the Laboratory for Laser Energetics requires a spatially uniform x-ray source, the flat-fielding of an x-ray streak camera providing an example. Uniformity may be achieved with a point source far away or with a large area source nearby. Our source is based on the bombardment of a 1cm by 10cm gold anode with a 3-5 keV electron beam of uniform flux. The beam originates as thermionic emission from a long tungsten filament, and is amplified by secondary electron emission in a discrete dynode chain to the mA level. The spatial non-uniformity of the x-ray source was measured to be +/- 5%. The source may also be gated at 100Hz, useful for measuring geometric distortions in x-ray streak cameras.

2. Introduction

One of the primary diagnostics used in the Laboratory for Laser Energetics inertial confinement fusion (ICF) program is the streak camera. Streak cameras help the ICF program by measuring the detailed pulse shape used in a particular shot, but two key errors limit the accuracy of the recorded images. The first error is a flat field error that exists in any optical system. Flat field errors affect the intensity of a given pixel but not its location. The second error is a geometric distortion that affects pixel location but not its intensity. Both of these imperfections can be corrected by calibrating the cameras with a high spatial uniformity source. Uniformity can be achieved using a point source held at a distance from the detector screen because the large distance reduces non-

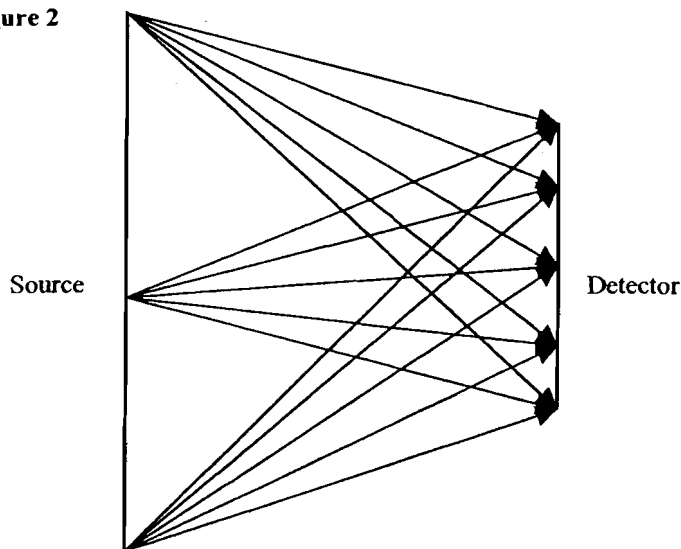
uniformities caused by the $1/R^2$ decrease in irradiance. The problem with this method is that there is low flux reaching the detector plane. Another method of achieving high detector uniformity is to use a high (80-90%) uniformity large area source held at a relatively close distance to the detector. With this type of source the same degree of detector uniformity is achieved, but flux is not sacrificed. This project centered on building such a large area x-ray source for the calibration of x-ray sensitive streak cameras.

Figure 1



From a point source, non-uniformities are introduced because $R_1 \neq R_2 \neq R_3$. There is only a slight gradient in intensity caused by the differences in $1/R_n^2$, for large R .

Figure 2



With a large area source each point on the detector sees the sum of intensities from each point along the source. The detector also sees high flux. Slight non-uniformities in the source are acceptable because of the large number of emitting points along the source surface.

3. Overview

Our source is based on the bombardment of a thin gold anode with a 3-5 keV electron beam of uniform flux. The beam originates as thermionic emission from a Tungsten filament and is amplified to the mA level through a discrete dynode chain. The

dynode chain consists of six amplification stages and ends with the acceleration of the electron beam onto the anode. The anode is a piece of Beryllium foil coated with a thin (500 Å) layer of Gold.

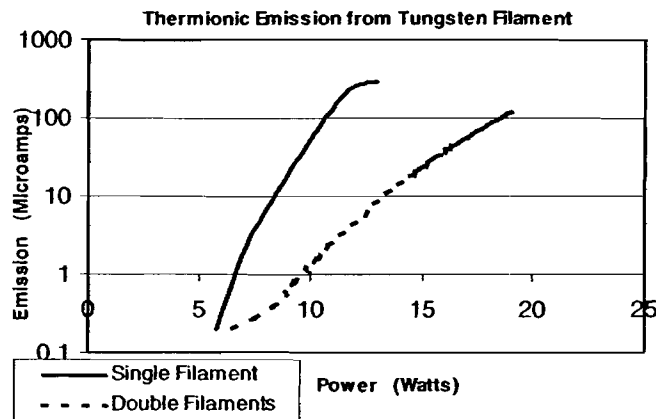
4. Electron beam production

The thermionic emission from the filament as a function of temperature is governed by the Richardson equation¹, shown as equation 1

$$J (\text{A/cm}^2) = 4 \pi m k^2 e / h^3 (1 - r) T^2 \exp [-e\phi / k T], \quad (1)$$

where e is the absolute value of the electronic charge, k is Boltzmann's constant and h is Planck's constant, m is the mass of an electron, $e\phi$ is the work function of Tungsten (4.5eV) and r is a reflection coefficient (0.5 for most metals). As current passes through the filament it heats up and emits the original electron beam. When testing the source a picture was taken of the output x-rays with the current flowing from left to right down the filament, then the direction of current flow was reversed and another picture taken. We observed a noticeable difference between the two pictures, suggesting that there is a thermal gradient along the length of the filament or that the thermionic emission is experiencing ExB drift in the direction of current flow along the filament. To correct this source of non-uniformity we proposed running two filaments, with currents running in opposite directions to average out any thermal gradient or ExB affects seen at the anode. Another advantage of a dual filament system was that the dynode chain has a two-channel design, so each filament could feed one half of the dynode chain. As figure 3 shows, however, in order to get the necessary $10\mu\text{A}$ of

Figure 3



thermionic emission there must be approximately 13 Watts of electrical power into the dual filaments, compared with 8 Watts for a single filament. Almost all of the power is radiated out according to the Stefan-Boltzmann lawⁱⁱ, shown in equation 2

$$W = \sigma T^4, \tag{2}$$

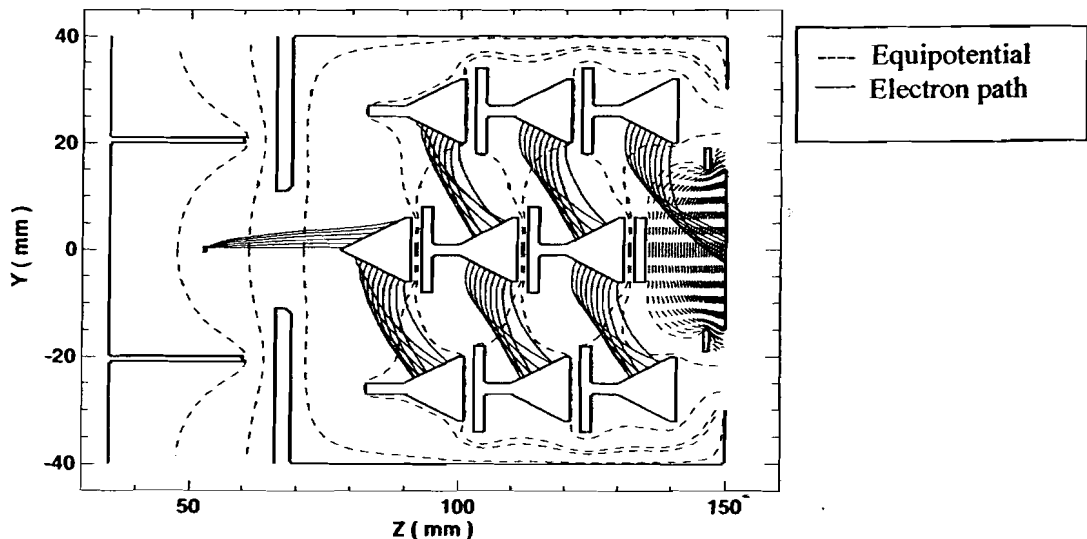
where $\sigma = 5.67 \times 10^{-12} \text{ W/cm}^2$ and T is expressed in Kelvin. Thermal loading is currently the main problem with the system, so having the ability to run the filament at a low power is essential.

5. Electron beam amplification

5.1 Dynode geometry

Adequate x-ray flux is produced when the current bombarding the anode is 0.4-3mA, so our original beam current must be amplified. We could run higher power in the filament to achieve our final electron beam current, but as figure 3 shows this would dissipate 15-20 Watts of power into the system, leading to excessive thermal loading. With our discrete dynode chain, we can achieve these current levels with as little as 0.5W of additional power dissipated into the vacuum. Electron multiplication occurs by secondary emission in the dynode chain. The original electron beam is accelerated towards the first dynode, where electrons deposit their energy in the surface layers, knocking out more electrons and producing an amplification of the original beam current. Figure 4 shows the modeled behavior of the dynode geometry used in our sourceⁱⁱⁱ.

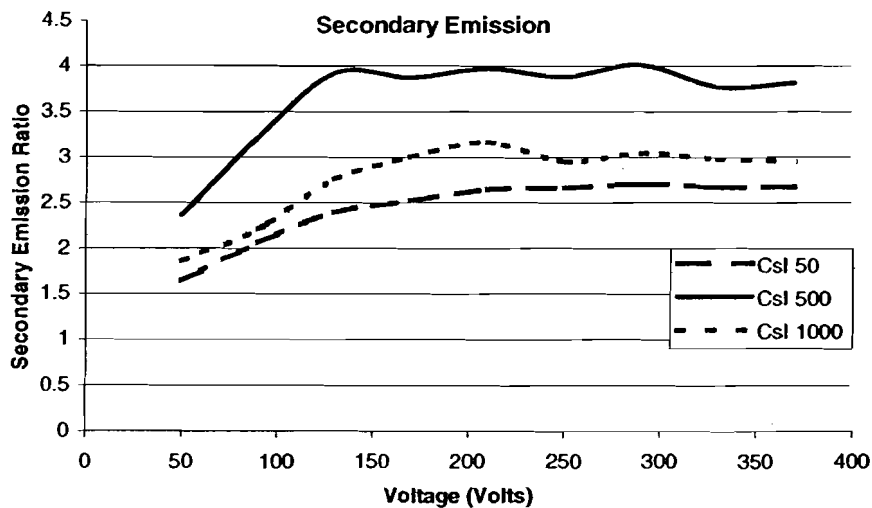
Figure 4



5.2 Coatings

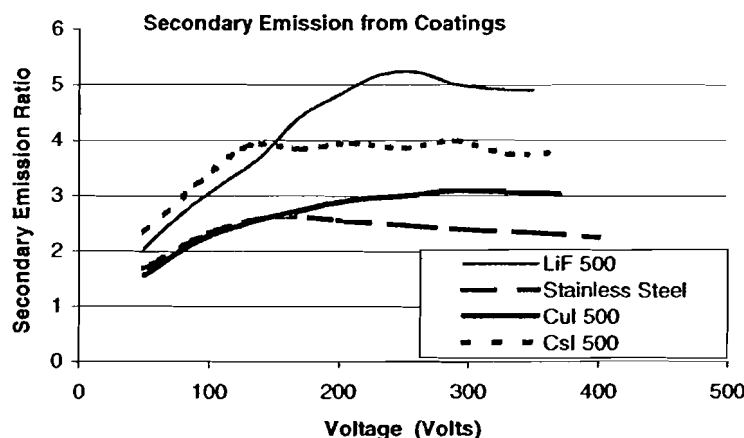
The secondary emission ratio is the average number of secondary electrons emitted for every incident primary electron, and it gives an idea of the total amplification expected for a certain material given a known number of dynode stages. In order to greatly reduce the thermal loading in the system we looked for a material with a large secondary emission ratio to coat the stainless steel dynode structures, thus increasing the amount of amplification throughout the dynode chain and allowing the filament to be run at a lower power. Special consideration was taken with regard to the thickness of each coating. When the electron beam hits each dynode stage it deposits its energy in the first 10-40 Å, so a coating that is too thin will not receive all of the input electrons from the original beam. Figure 5 shows the secondary emission ratio of CsI as a function of the voltage between the filament and dynode 1, for 3 different thickness coatings. The 50 Å coating was too thin to be completely uniform, which may have affected its performance. The 1000 Å coating does not perform well, most likely because of surface charging of the dynode stages, which may affect the extraction efficiency between stages. Optimal coating thickness appears to be 500 Å for all materials tested; at 500 Å thickness uniform coatings can be assured but surface charging is not an observable problem.

Figure 5



The secondary emission ratio of the stainless steel used to build the dynode structure only provides an amplification of 2x per stage, which is not adequate given the number of stages in our source. The ideal coating would have a high (4-6) secondary emission ratio, would be easy to deposit and not be hygroscopic or susceptible to other erosion. The main materials considered were those used for x-ray photocathodes, which operate on the detection of their secondary electron emission, and thus were natural for consideration in our source. Figure 6 shows the secondary emission ratios of four of the materials tested, LiF, CsI, CuI, and stainless steel. LiF was considered because it became apparent during testing that low Z materials were more effective secondary emitters in this system.

Figure 6



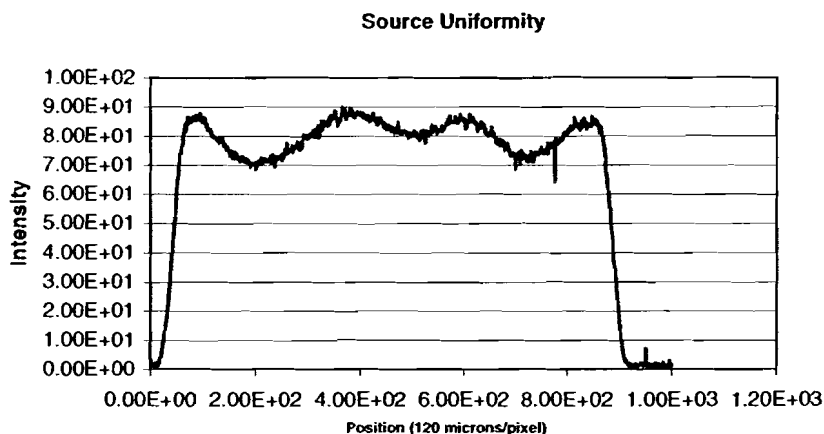
LiF demonstrated emission ratios of over 5, which yields a theoretical amplification of 15,625x, but when implemented the system produced amplification in the 1000-2000x range. This discrepancy can be attributed to slight surface charging, incomplete extraction at each dynode stage, and degradation of coatings over time. There are also some questions regarding the coupling of emission between the first two dynodes, which may be responsible for a reduction of the number of effective stages to 5.

6. Results

After the dynode stages the amplified current is accelerated across 2-5kV onto the anode where it is converted into x-ray emission. A lineout of the x-ray emission along the 10cm dimension is shown in figure 7. It shows the uniformity of the source after

being run for several minutes straight; most of the non-uniformities seen can be attributed to degradation of the thin gold layer.

Figure 7



The imaging system used to take this picture consisted of a pinhole camera that displayed on a phosphor screen deposited on a fiber optic faceplate. A CCD camera was used to record the images from the fiber optic faceplate. All of the pictures taken with the dynode system in place, both with coatings and without, showed sufficient uniformity.

7. Recommendations

The main factor responsible for non-uniformity that we have recognized is the relatively severe deterioration of the gold anode over extended periods of time. One way to reduce this problem is a slight revision in the design, by changing to a thick anode that operates in reflection mode we may be able to correct this problem. Other ways to improve the system include running the source in gated mode and adding more dynode stages to reduce thermal loading. Running in gated mode was observed to increase the secondary emission ratio of coatings because any surface charging would be significantly reduced. Insertion of additional mesh layers to selectively attenuate the electron beam before and after the dynode chain could be used to shape the electron beam and therefore improve x-ray uniformity.

8. References

-
- i *Handbook of Physics*. McGraw-Hill Book Company, Inc., 1958.
 - ii *The Photonics Handbook*. Laurin Publishing Co., Inc., 1997.
 - iii Dynode geometry designed and modeled by Dr. Paul Jaanimagi

9. Acknowledgements

I would like to thank Dr. Paul Jaanimagi for his numerous patient and enlightening explanations. Next I would like to thank Dr. R.S. Craxton for allowing me to participate in this excellent program. I would also like to recognize and thank Steve Noyes for taking his time to coat the seemingly endless supply of materials tested and the other students in the program, I will miss you all very much.

Experimental Simulation of Damage in Spatial Filter Lenses

Jill Daum, Jason Taniguchi, Linda Pazral

Laboratory for Laser Energetics, University of Rochester

250 East River Road, Rochester, New York 14623-1299

ABSTRACT

Experiments were performed simulating the conditions of the stage E-input spatial filter lenses on the OMEGA laser system to determine whether vacuum pump oil, which has been shown to contaminate the lenses is a possible damage mechanism. Care was taken to grind 2" diameter Damage Testing Optics (DTO's) of crystalline fused quartz silica (CFQ) to a 4 mm thickness, rather than the normal 6 mm thickness, for bending stress simulation. E-input lenses were not used, due to their size and scarcity. Damage was inflicted prior to sol-gel coating, by both ball bearings and a diamond scribe. The DTO's were placed in vacuum cells that were either clean or contaminated with used vacuum pump oil. Finally, they were then raster scanned under stress by a Q-switched Nd:YAG laser emitting 1064-nm light with 10-ns pulse lengths. Results determined vacuum pump oil is a damage mechanism.

INTRODUCTION

The spatial filter lenses of the OMEGA laser system have required replacement due to large damage sites that form on the vacuum surface of the lenses, apparently aided by back streaming of oil from the mechanical vacuum pump. If left on the system, these defects can penetrate the optic deep enough to break it. This hazard not only

affects the safety of the personnel, but of the rest of the system as well. The E-ins specifically must be removed from the system before reaching a point where they become weak enough to implode and strike the inside of the spatial filter as well as the lens at the other end of the vacuum, possibly continuing breakage. These damages are considered to generally form into the surface of the lens in a semi-circular, or halfpenny, shape. At OMEGA, the lenses are removed when a defect reaches one half of the calculated critical depth, which is the depth at which the lens will be in danger of breaking. This is calculated using the following formula, assuming a halfpenny defect where Y (the geometric factor of the flaw) = 1, and the depth = the radius of the flaw, where a_c = the critical flaw depth, K_c = the fracture toughness of the glass, and P = the bending stress [1].

$$a_c = \frac{(K_c)^2}{(\pi) (Y P)^2}$$

Replacement of the lenses is very expensive, and preferably avoided. When removed, heavily damaged optics smell of vacuum pump oil, leading to the speculation that the contamination assisted in the development of damage sites. Supporting this speculation is the effect of oil contamination on the index of refraction of sol-gel coating, causing the crystalline fused silica (CFQ) to behave as though not coated. The purpose of the performed experiments was to simulate all conditions existing on the OMEGA system, the control being optics tested under clean vacuum, and the experimental group being those tested under vacuum containing used vacuum pump oil vapor, to investigate oil vapor as a possible damage mechanism.

EXPERIMENTS

E-ins removed from OMEGA exhibit clamshell defects (see fig. 1a and fig. 1b) on their vacuum surface sides. Past experience has shown that these defects seem to grow into larger damage sites. These defects have not previously been duplicated off the system. The defects form in a 2-dimensional plane extending from the vacuum surface into the substrate, growing deeper in the shape of a clamshell. When tested, these dark-colored defects were found to contain carbon, which is a product of the laser light vaporizing the oil. One aim of this experiment was to create conditions under which clamshell defects could be replicated.

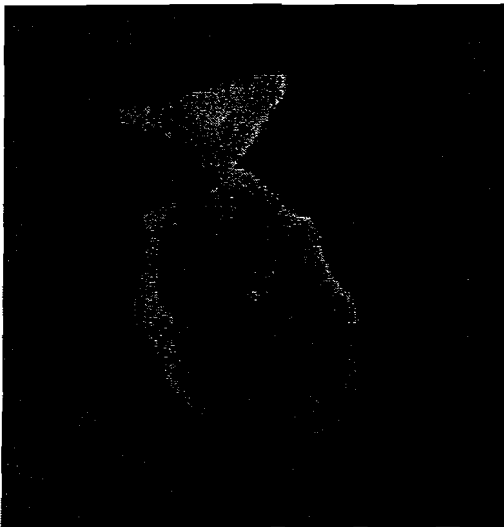


Figure 1a: A side view of a clamshell defect extending into the silica from the vacuum surface.

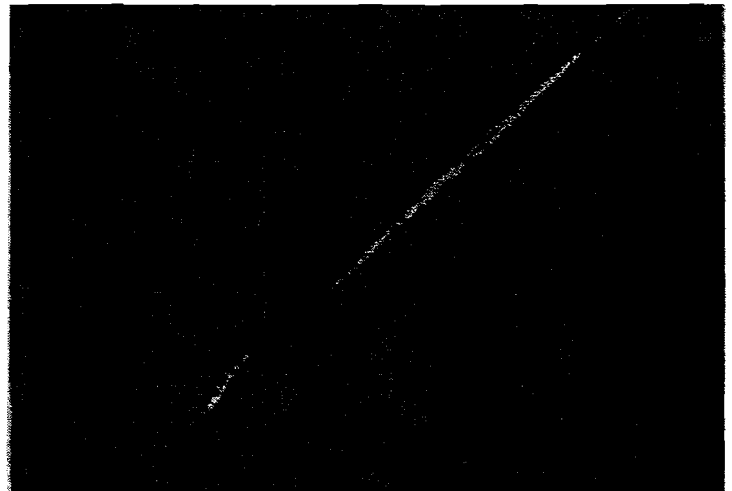


Figure 1b: A vacuum surface view of the clamshell defect that extends from this crack into the silica.

To simulate all conditions existing on OMEGA, bending stresses had to be similar. The bending stress is the tension that the substrate experiences due to the

vacuum pressure. This tension on the vacuum surface may be a necessary factor in the formation of the defects, as it may assist in causing minor tension fractures, which allow the oil to condense. In the lab, we were able to obtain a vacuum pressure of ~20mTorr. Using the standard 6mm thick, 2" diameter Damage Testing Optic (DTO), this allowed for bending stresses of ~25 psi. The stage E-input lenses of OMEGA, which were used as a model, have bending stresses of ~232 psi, under a vacuum of ~10mTorr. It was calculated that if a 4mm thick DTO was used, then the bending stresses at the optic's clear aperture would average ~227 psi, under a vacuum of ~20mTorr. This was an acceptable value for the experiment.

Figure 2: The apparatus for dropping ball bearings onto DTO's

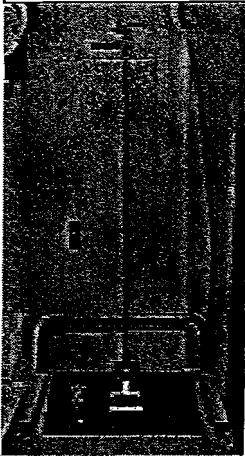
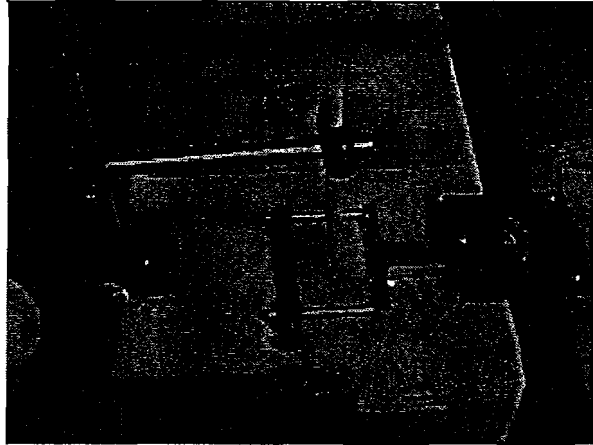


Figure 3: The diamond scribe on tip-tilt base used to damage DTO's. (Shown here with witness substrate.)



After being thinned, the optics were damaged in two different ways (see fig. 2 and 3). Some test sites were touched with a diamond scribe on a tip-tilt base to initiate a very small damage site. Other damage sites were created by dropping ball bearings from a calculated height to damage the optic, without breaking it. This was done to create a surface crack that might deepen into a clamshell defect. Some test sites were left undamaged prior to coating. The optics were damaged prior to coating due to

RESULTS



Figure 4: A vacuum surface picture of a clamshell defect from a removed OMEGA lens.

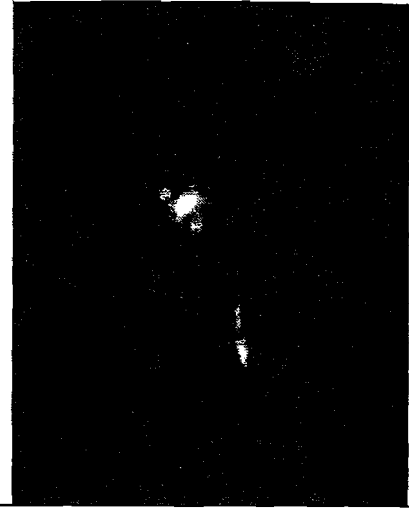
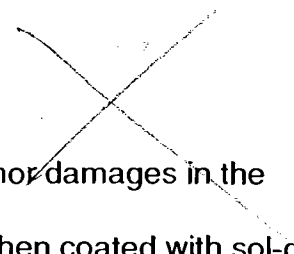


Figure 5: A vacuum surface picture of a defect created in an oil-contaminated DTO.

In vacuums not contaminated with vacuum pump oil, large, shallow, shatter-morphology damage sites were observed on the vacuum surface, which is typical of CFQ substrates coated with an AR (antireflective) coating such as sol-gel. Meanwhile, in vacuums contaminated with used vacuum pump oil, deep, thin damage sites propagated from the vacuum surface into DTO. In uncontaminated samples, the average fluence at which growth starts is 35 J/cm^2 . That is significantly higher than the average starting fluence of 29 J/cm^2 which was observed under vacuums contaminated with oil, showing that the oil is a damage mechanism.

CONCLUSION

Samples contaminated with vacuum pump oil vapor showed damage initiation at lower fluences than clean samples, and damage morphology on Damage Testing Optics under vacuum differed between those with and without oil vapor. These results



speculation that damage growth on OMEGA might form from minor damages in the grinding process before the optics are coated. The DTO's were then coated with sol-gel, an anti-reflective coating. This is the coating on OMEGA lenses whose refractive index changes when contaminated by vacuum pump oil vapor.

Once coated, the optics were put at either end of a vacuum cell and pumped down to a pressure of ~20mTorr. The thinned, damaged, and coated DTO's were put at the side of the cell which would receive incident laser light, while a standard thickness, sol-gel coated DTO was put on the side of the cell where the laser light would exit. The front DTO's were the heavily observed, and each one was divided into four testing sites. These testing sites were either ball bearing damaged, scribe-damaged, or not intentionally damaged. For each above described damage condition, there were DTO's tested in an uncontaminated vacuum, and others tested under vacuum containing vacuum pump oil vapor.

To assure contamination, used vacuum oil was put into the vacuum cell before it was sealed off with the DTO's. The cell was then pumped down to pressure with the DTO's in place, so that the oil would reach vapor pressure. Once vapor pressure was reached, the liquid oil would decrease in visible volume, but enough liquid was added in every case that saturation at pressure was obtained with extra liquid pump oil remaining. Thus, the oil vapor saturation level was reached for ~20mTorr prior to each contaminated sample testing. When the proper pressure had been reached, the optics were raster scanned.

suggest that vacuum pump oil contamination is at least one factor in causing the OMEGA spatial filter lenses to damage. Experiments will be continuing to further determine the oil's behavior as a damage mechanism.

ACKNOWLEDGEMENTS

This work was supported by the U.S Department of Energy Office of Inertial Confinement Fusion under Cooperative Agreement No. DE-FC03-92SF19460, the University of Rochester, and the New York State Energy Research and Development Authority. The support of DOE does not constitute an endorsement by DOE of the views expressed in this article.

REFERENCES

1. Amy L. Rigatti, Douglas J. Smith, Ansgar W. Schmid, Seymon Papernov, John H. Kelly, "Damage in fused-silica spatial-filter lenses on the OMEGA laser system," 1996.

**Experimental Investigation of Smoothing by Spectral Dispersion
with Apertured Near Fields**

Ming-fai Fong

Summer High School Student Program 2000
LABORATORY FOR LASER ENERGETICS
University of Rochester
250 East River Road
Roschester, NY 14623-1299

Abstract

Far field intensity distributions of an OMEGA laser beam were measured with apertured near fields. A rectangular slit of width one sixth the near field diameter was placed in the near field and the orientation of the slit was aligned along each of the two SSD axes. Power spectra of measured far fields were computed for the two slit orientations. One nanosecond square laser pulses smoothed with 1 THz SSD and distributed polarization rotators were studied. Simulations show good agreement with the experimental data. This investigation can be extrapolated to SSD smoothing of beams that irradiate only a portion of the phase plate, such as the ultrafast picket fence pulse.

INTRODUCTION

Laser beam smoothing is essential for direct-drive inertial confinement fusion.[1] Nonuniformities in laser-irradiation imprint target mass perturbations, which seed the ablative Rayleigh-Taylor hydrodynamic instability and degrade target performance. Laser-irradiation nonuniformities are reduced using the following smoothing techniques: (1) smoothing by spectral dispersion (SSD), (2) distributed phase plates (DPPs), and (3) distributed polarization rotators (DPRs). In this research far field intensity distributions of an OMEGA laser beam were measured with apertured near fields. A rectangular slit of width one-sixth the near field diameter was placed in the near field and the orientation of the slit was aligned along each of the two SSD axes. Power spectra of measured far fields were computed for the two slit orientations. One-nanosecond square laser pulses smoothed with 1 THz SSD and distributed polarization rotators were studied.

The following sections discuss (1) a brief background of Fourier analysis, (2) the experimental set up of the investigation, (3) the technique used to align the rectangular slit along either of the two SSD bandwidth axes, (4) the analysis of far field measurements of pulses with 1 THz SSD and DPRs, and (5) the calculated power spectral densities of these pulses in comparison with theoretical predictions. This investigation shows that the simulations for SSD smoothing of beams with apertured near fields are in good agreement with the experimental results. It can also be extrapolated to SSD smoothing of beams that irradiate only a portion of the phase plate, such as the ultrafast picket fence pulse.[2]

FOURIER ANALYSIS

Fourier analysis was essential in this research. Initially the far field intensity of a near field with a rectangular aperture and no laser beam smoothing was modeled. Fig. 1a shows the near field intensity (the square of the electric field). The apertured beam cross-section has -

constant intensity. The far field image, shown in Fig. 1b, is created by taking a 2-D Fourier transform of the near field electric field. The speckle structure of the far field intensity shows the interference pattern resulting from the apertured near field. The speckles are elongated in the direction perpendicular to the angular orientation of the slit. Power spectra of the far field intensity distribution were studied by taking the 2-D Fourier transform of the far field. The result is shown in Fig. 1c. Because it has the same shape as the near field aperture, the 2-D Fourier transform is a useful tool for determining the slit orientation and aligning the aperture in the near field. More importantly, however, the 2-D Fourier transform is used to evaluate the power spectra. The power spectral density, plotted as a function of wave number in μm^{-1} in Fig. 1d, is the azimuthal sum of the square of the Fourier amplitudes. This graph indicates the smoothness of the laser beam intensity profile.

EXPERIMENTAL SETUP

The investigation was carried out on the OMEGA Wavefront Sensor (OWS), shown in Fig. 2, and the far field images were recorded on a CCD camera.[1] The alignment was performed with a CW ultraviolet laser. A small fraction of the energy from a pulsed OMEGA laser beam was directed to the OWS and passed through a DPP and an OMEGA lens. It was then down-collimated from a diameter of ~ 27.5 cm to a diameter of 63 mm. A rectangular aperture, shown in Fig. 2, was placed in the near field of the beam with a slit width of 10.5 mm (one-sixth the diameter of the down-collimated beam). The aperture shown in Fig. 3 was mounted on a horizontal translator, and could be rotated to any orientation. Finally, after passing through the aperture the beam was brought to focus on a CCD camera (not shown), where the ultraviolet equivalent-target-plane (UVETP) image was recorded.

APERTURE ALIGNMENT

This investigation required the near field slit to be aligned with each of the two SSD

smoothing axes for separate analysis. In order to measure the angular orientation of the smoothing axes, the measured far field of a laser pulse with 1 THz SSD and no near field aperture was used. The 2-D Fourier transform of a measured far field was calculated for a laser beam smoothed with 1 THz SSD and no near field aperture. This image is shown in Fig. 4. The perpendicular SSD smoothing axes coincide with the 'x' structure seen in Fig. 4. In order to determine the angular orientation of the SSD axes, a computer program was used to rotate the image to a position where one axis appeared horizontal. At this position, a vertical lineout method was used to determine the accuracy of the rotation. The vertical lineout method involved analyzing five vertical columns across the image. These lineouts are plotted in Fig. 5. The image was rotated until the peak values of the five lineouts coincided with the vertical line shown in Fig. 5. Using the vertical lineout method, the orientations of the SSD smoothing axes were determined to be at 53.5° and 149° from the horizontal position of the CCD camera.

Once the angular orientations of the SSD smoothing axes were determined (see Fig. 6a), the aperture on OWS was rotated to these positions. The 2-D Fourier transforms of measured far fields for apertured beams without smoothing were analyzed to check the alignment. Again, the lineout method was used to detect rotation errors, and the slit was adjusted accordingly. Positions of exact angles were noted on the near field aperture, as shown in Fig. 3. 2-D Fourier transforms of far field images produced by this analysis are shown in Fig. 6b and 6c for the two slit orientations.

FAR FIELD ANALYSIS

The near field aperture was accurately aligned along either the smaller or larger SSD bandwidth axes and the far field images for each were recorded. From the measured far fields, 2-D Fourier transforms and power spectra were calculated. Images produced for the smaller SSD bandwidth axis are shown in Fig. 7a and 7b. Images produced for the larger SSD

bandwidth are shown in Fig. 7c and 7d. More smoothing was observed when the slit was aligned with the larger of the SSD bandwidth axis. The normalized power spectra for the two near field slit orientations shown in Fig. 7b (the smaller smoothing axis) and 7d (the larger smoothing axis) are similar for low wave numbers ($k < 0.4$). However, in the higher wave numbers, the power spectral density of the larger SSD bandwidth dropped more sharply. This difference can be seen in Fig. 8c.

SIMULATIONS

The power spectral densities produced by the simulations show good agreement with experimental data, as indicated in Fig. 8a and Fig. 8b. More smoothing was predicted and measured for the slit orientation along the larger SSD bandwidths. However, the amount of smoothing for the larger SSD bandwidth orientation is less than the case with no near field aperture, which is shown in Fig. 9. The σ_{rms} values indicate slight differences between the theoretical and experimental work. These discrepancies will be the subject of further studies.

CONCLUSION

In this study, smoothing by spectral dispersion with apertured near fields was studied. Far field images were recorded and the power spectra of the intensity distributions were analyzed. This investigation shows that the simulations for SSD smoothing of beams with apertured near fields are in good agreement with the experimental results. These results can also be extrapolated to SSD smoothing of beams that irradiate only a portion of the phase plate, such as the ultrafast picket fence pulse.[2]

REFERENCES

- [1] S.P. Regan et al., "Experimental Investigation of Smoothing by Spectral Dispersion", J. Opt. Soc. Am. B **17**, 1483–1489 (2000).
- [2] J.A. Marozas, private communication.

FIGURE CAPTIONS

Figure 1

Simulated UVETP images are shown. Near field intensity (the square of the electric field) is shown at (a), indicating constant intensity of an apertured beam. Far field is 2-D Fourier transform of electric field, shown at (b). 2-D Fourier transform of far field at (c) is used to check near field aperture alignment and evaluate power spectra. Power spectral density at (d) is the azimuthal sum of square of the Fourier amplitudes. Normalized power spectral density is plotted as a function of wave number in μm^{-1} on a logarithmic scale.

Figure 2

I am adjusting near field aperture on OWS in target bay. Small amount of energy from a pulsed OMEGA laser beam is passed through a DPP and OMEGA lens, and then down-collimated to one-sixth its diameter. Next, it is passed through a rectangular aperture and brought to focus on a CCD camera (not shown), where far fields are measured.

Figure 3

Near field aperture shown centered on beam on OWS. Aperture placed on horizontal translators and rotated to appropriate position. Marks along outer frame indicate various slit orientations used during experiment.

Figure 4

2-D Fourier transform of measured far field (shot number 19930) with 1 THz SSD smoothing and no near field aperture. Aperture is aligned with the two SSD axes traced by the concentrated red speckles ('x' pattern).

Figure 5

Vertical lineouts of 2-D Fourier transform of far field image with 1 THz SSD and no near field aperture shown. Computer program calculates 2-D Fourier transform of far field and rotates

calculated image to angle of 53.5° . Lineouts are taken at five evenly-spaced vertical locations, normalized to peak value, and plotted together. The peaks are offset slightly for viewing ease. The vertical line at 352 on the plot indicates the middle pixel of the image where peaks are expected to fall.

Figure 6

SSD axes deduced from lineout method drawn over 2-D Fourier transforms of far field images. Image (a) shows Fig. 4 with SSD axes calculated using lineout shown in Fig. 5. Images (b) and (c) show 2-D Fourier transforms of far fields where near field aperture was aligned along the larger and smaller SSD bandwidths, respectively. The larger SSD bandwidth axis is plotted in (b) and the smaller one is plotted in (c).

Figure 7

2-D Fourier transforms and normalized power spectra of far field images of apertured beams smoothed with 1 THz SSD and DPRs are shown. Results with slit aligned along smaller SSD bandwidth axis are shown in (a) and (b) and results with the slit aligned along the larger SSD bandwidth axis are shown in (c) and (d). The power spectra for the slit aligned along the smaller SSD bandwidth axis (b) shows less smoothing than the case with the slit aligned along the larger SSD bandwidth axis (d).

Figure 8

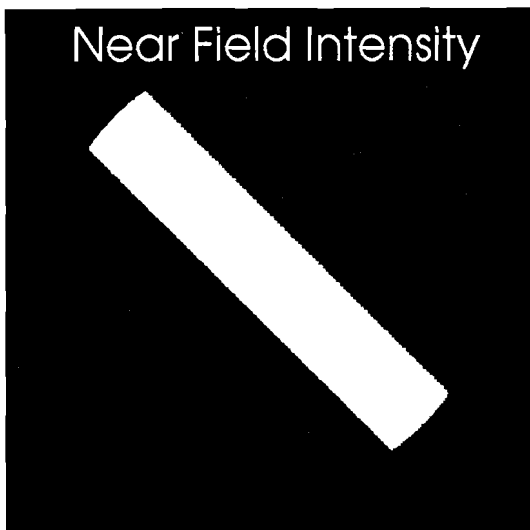
Normalized power spectral density plots indicate that simulations show good agreement with experimental values. In (a), simulation (dotted line) is plotted over experimental results for the slit aligned along the larger SSD bandwidth axis (solid red line). In (b), simulation is plotted over experimental results for the slit aligned along the smaller SSD bandwidth axis (solid green line).

Figure 9

A comparison of measured power spectra with a near field aperture (solid curve) and without a near field aperture (dotted curve). The near field aperture is aligned along the larger SSD bandwidth axis. In both cases the laser beams are smoothed with 1 THz SSD and distributed polarization rotators. More smoothing is observed without the near field aperture.

Fig. 1

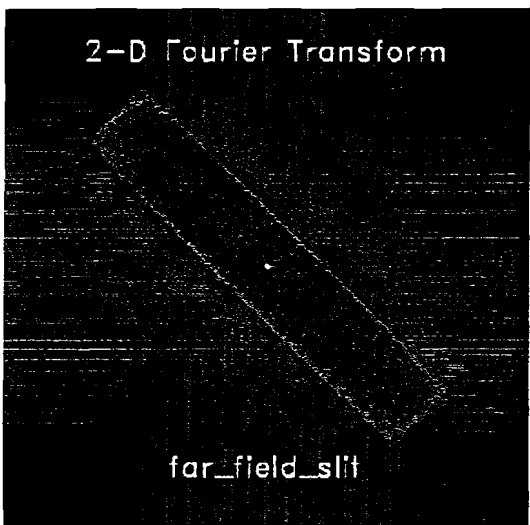
(a)



(b)



(c)



(d)

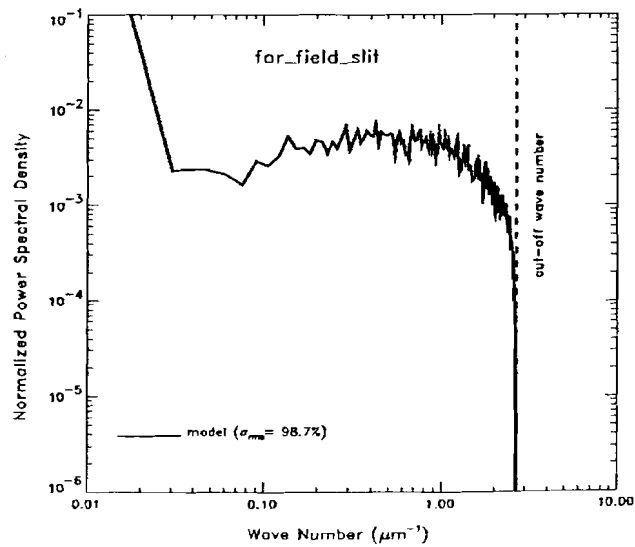


Fig. 2

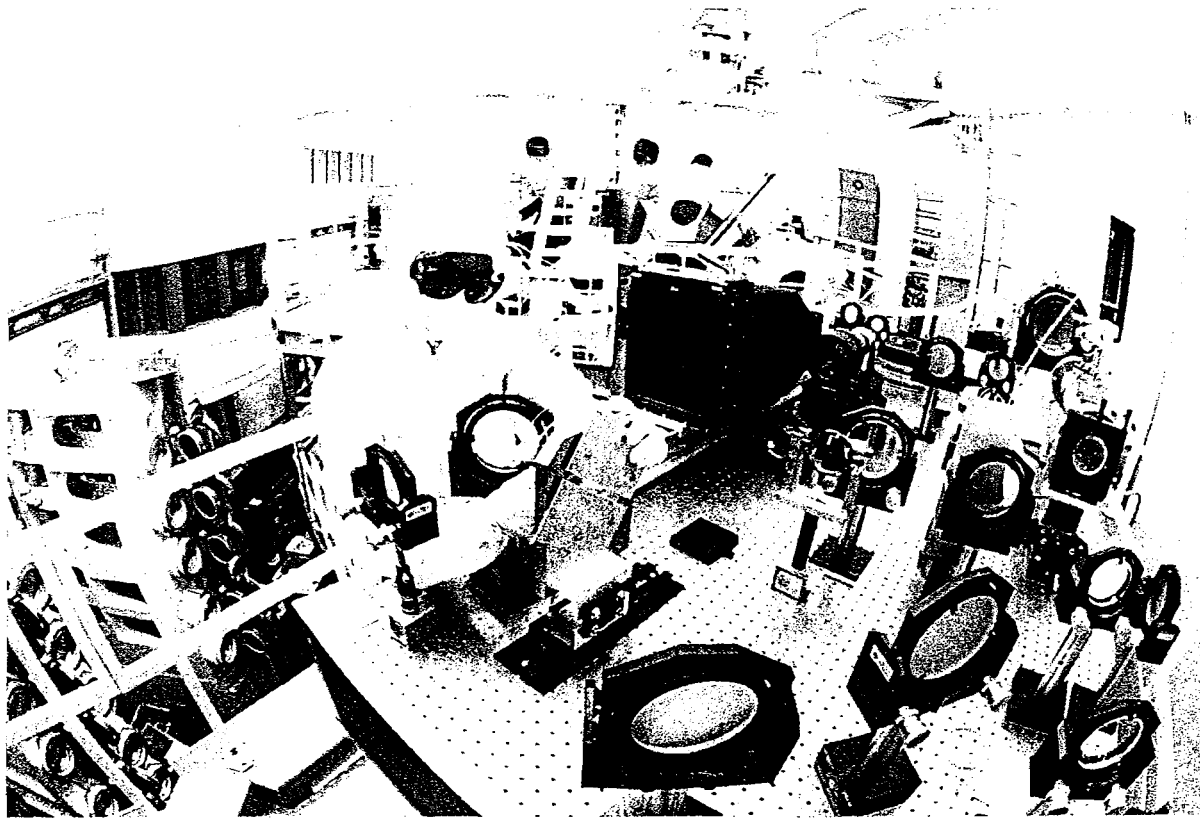


Fig. 3

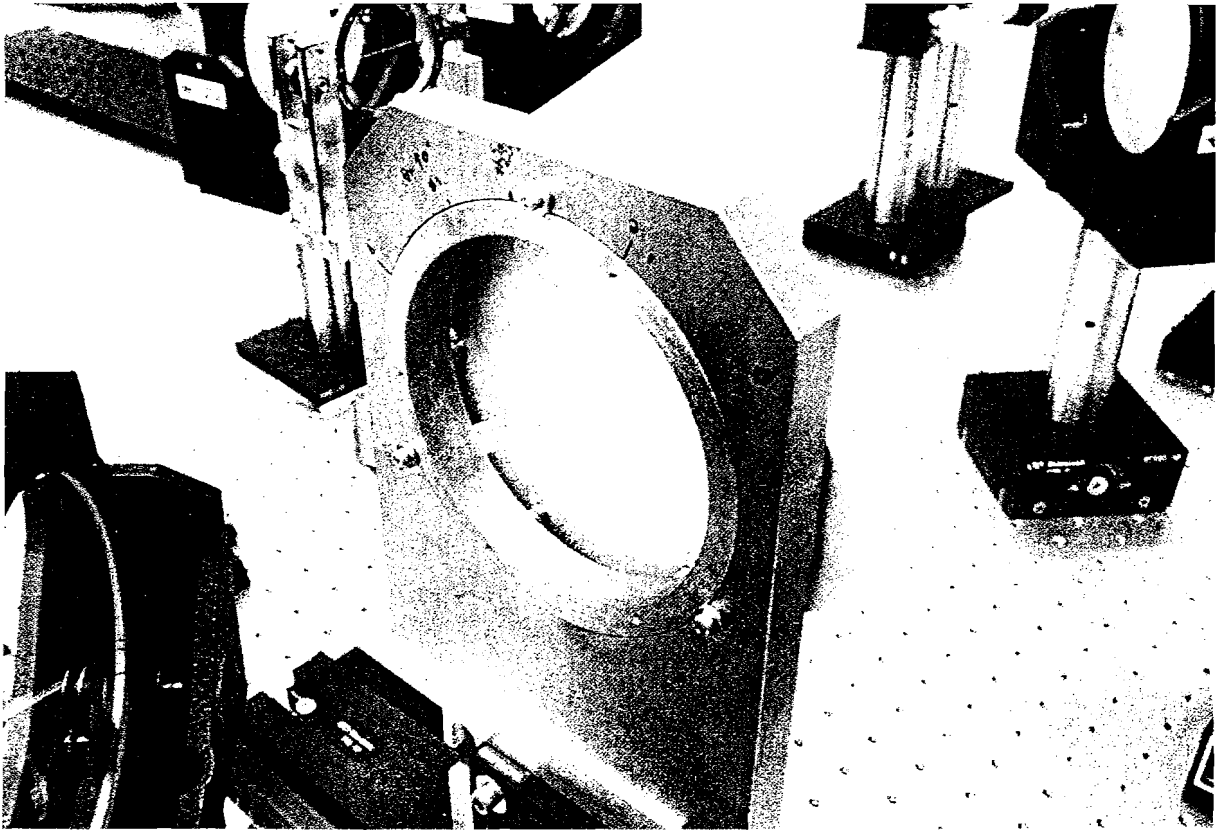


Fig. 4



Fig. 5

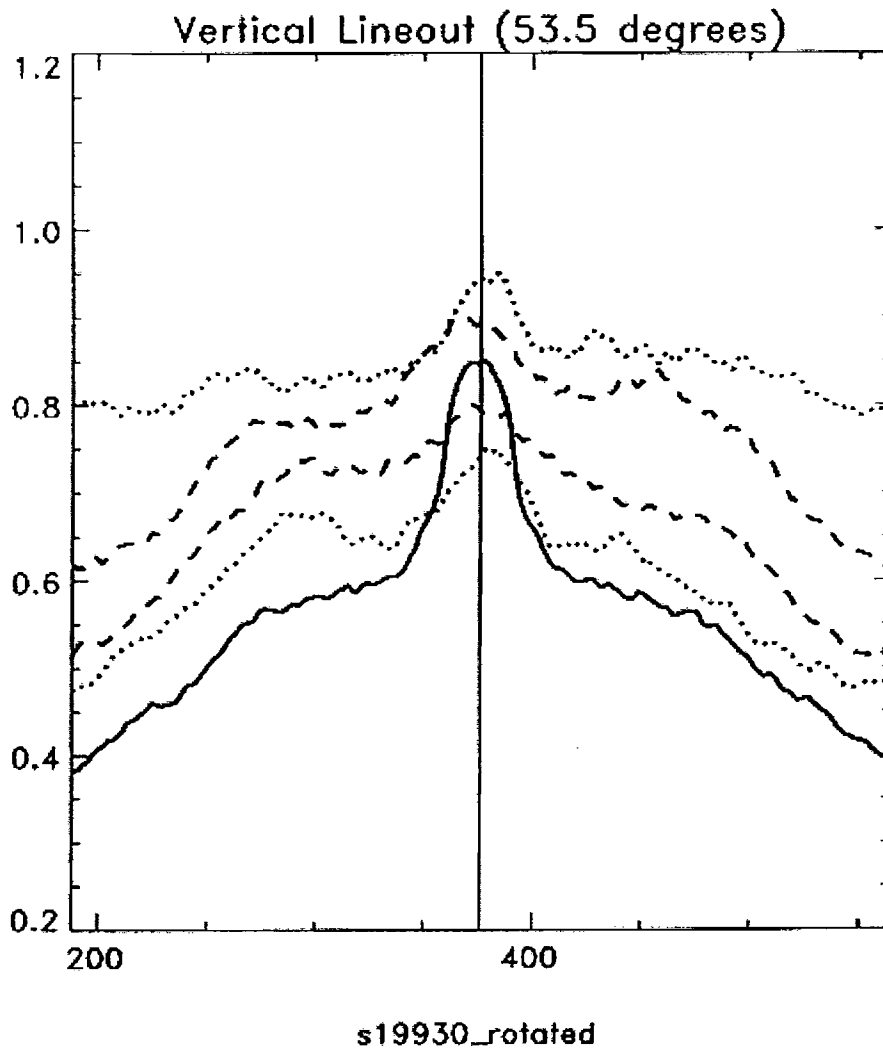
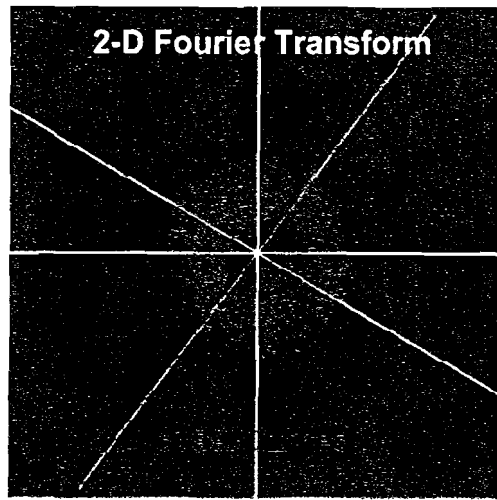
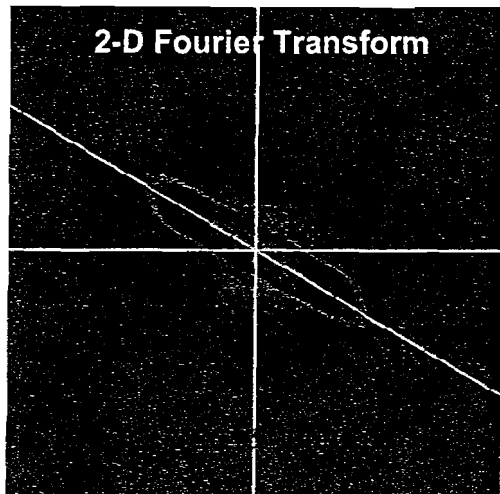


Fig. 6

1 THz SSD
(a) (no NF aperture)



NF slit aligned to larger
SSD bandwidth axis
(b) (no SSD)



NF slit aligned to smaller
SSD bandwidth axis
(c) (no SSD)

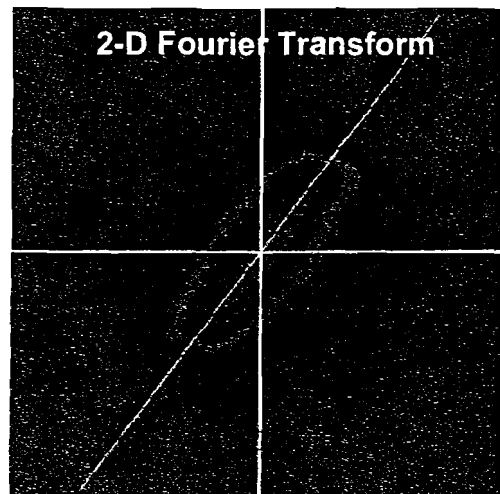


Fig. 7

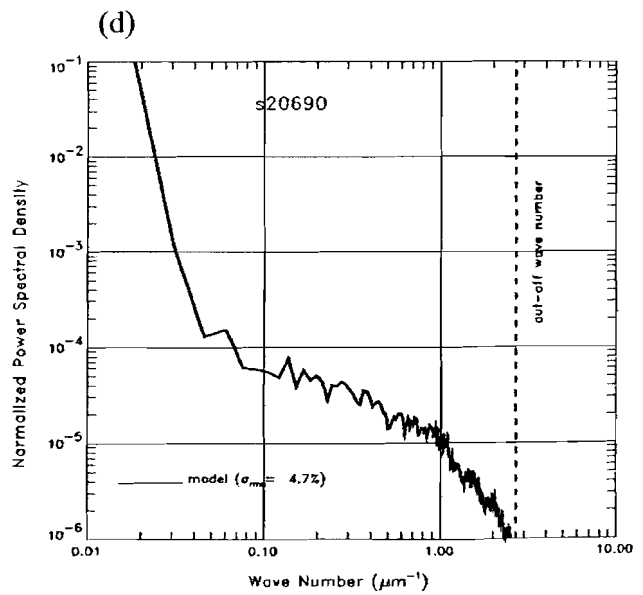
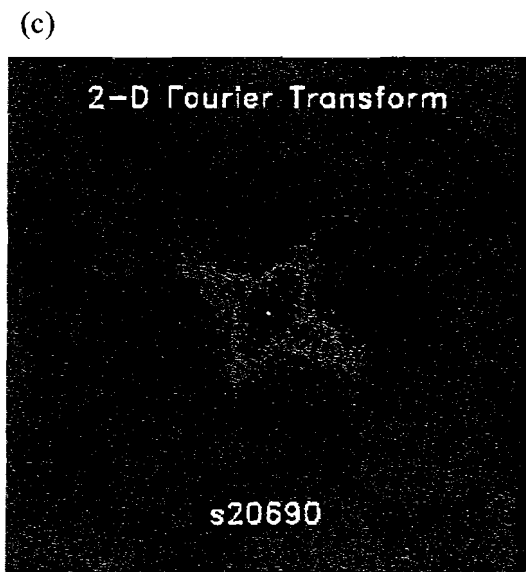
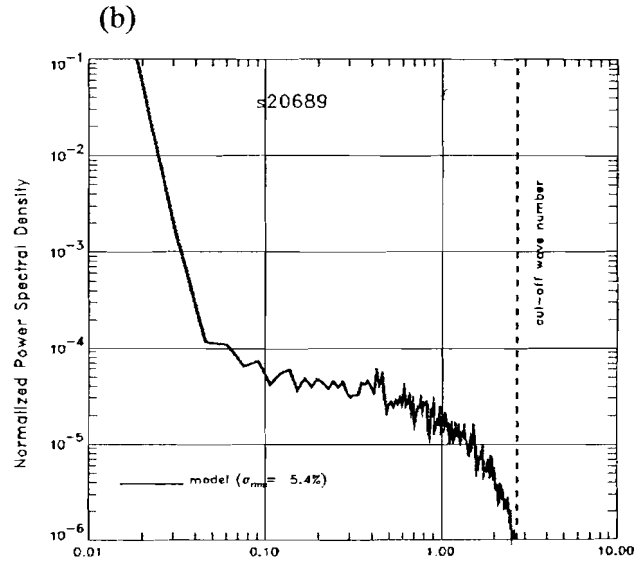
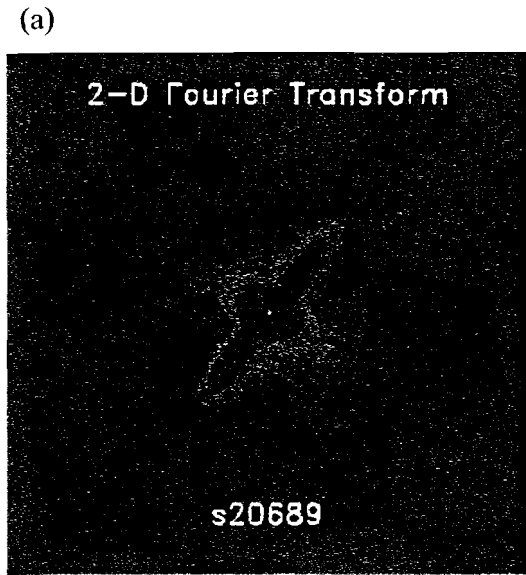


Fig. 8

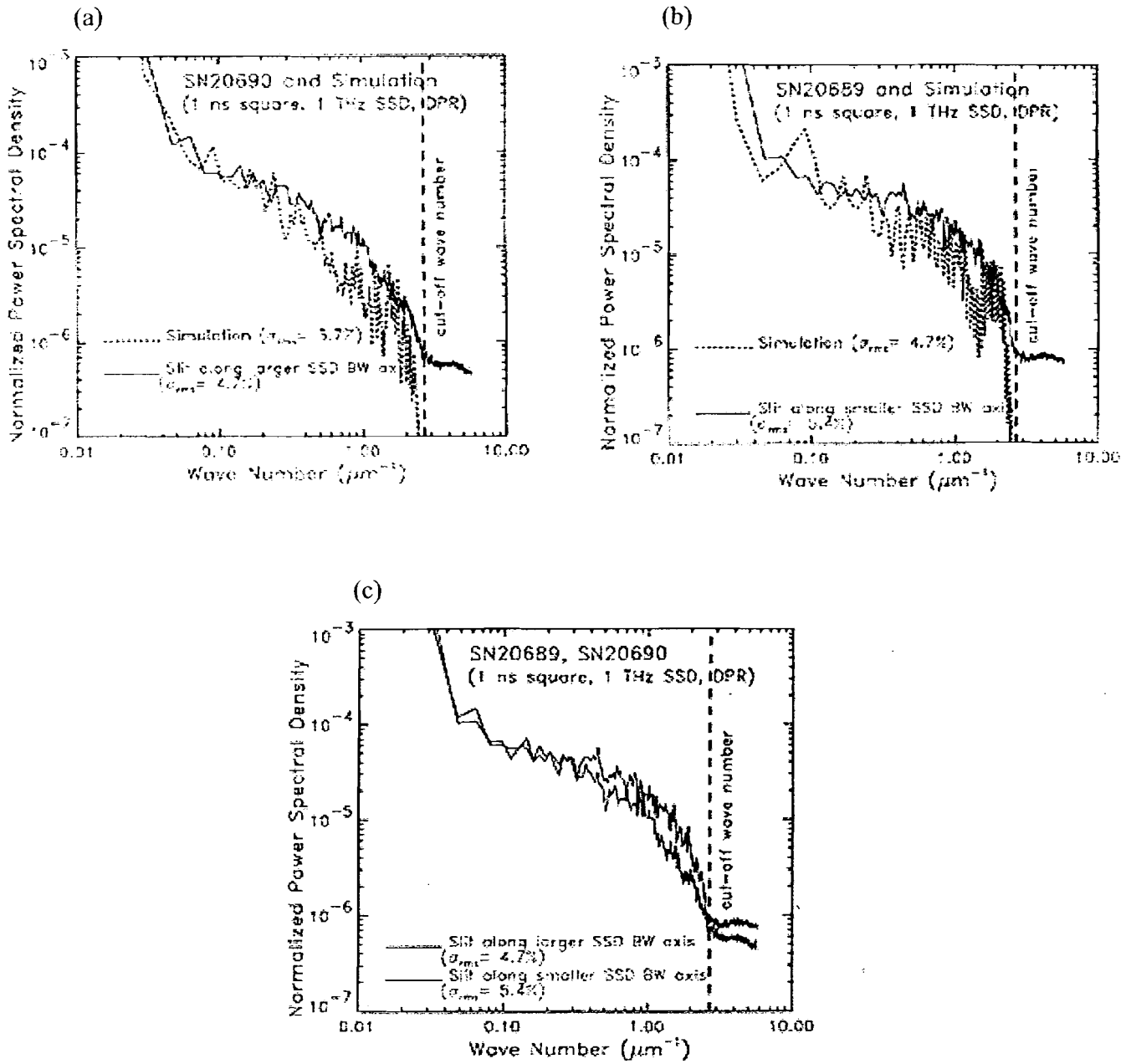
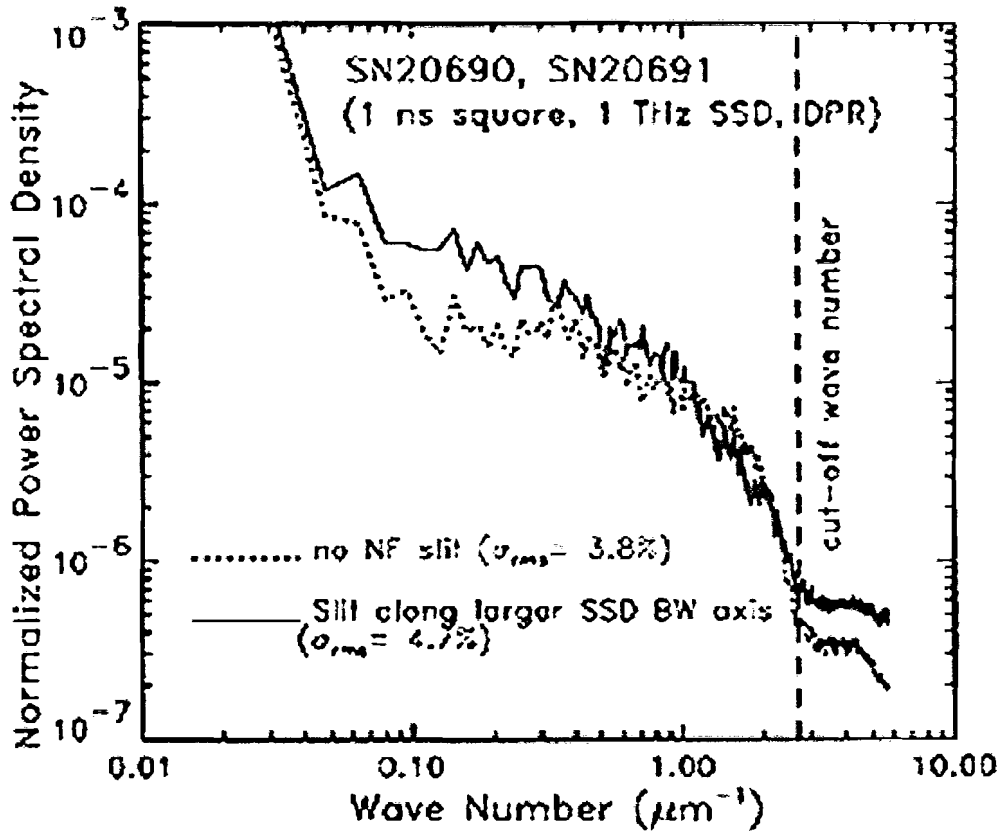


Fig. 9



Modeling Pulse Shape Distortions in the OMEGA Laser

Abraham J. Fetterman

Advisor: Dr. Mark Skeldon

University of Rochester

Laboratory for Laser Energetics

Summer High School Research Program 2000

We present a study of two potential sources of pulse shape distortion: Stimulated Brillouin Scattering (SBS) in optical fibers and a gain grating in the active medium of the regenerative amplifier. SBS, the major contributor to nonlinearities in optical fibers, is shown to be insignificant in OMEGA. Scattering from the gain grating formed in the laser crystal was included into a model of regenerative amplification. The developed model demonstrates good agreement with experiment. The model is not yet complete, but may have the potential to identify and explain other pulse shape distortions in the OMEGA front end.

The mission of the OMEGA laser is threefold: to conduct implosion experiments and basic physics experiments in support of the National Inertial Confinement Fusion (ICF) program, to develop new laser and materials technologies, and to conduct research and development in advanced technology related to high-energy-density phenomena. The laser begins with a monomode laser, which emits a 200-nanosecond Gaussian optical pulse. A 20 ns square pulse is cut from its peak and is focused into a fiber, where it reaches high intensities. The pulse enters a pulse shaping system, which shapes the pulse according to its settings. The pulse is then sent to the pulse generation room (PGR) where it is injected into a regenerative amplifier (regen). In the regen, the pulse is amplified. A pulse is sliced out of the regen pulse train, and sent through

various OMEGA amplifiers, frequency tripled, and sent into the target chamber. The two nonlinear processes that I concentrated on were stimulated Brillouin scattering (SBS) in optical fibers, which occurs when high laser intensities enter the optical fiber, and pulse shape distortions which occur in the regen if the pulse overlaps with itself in the gain medium.

I. SBS in Optical Fibers

When the laser beam first enters an optical fiber, directly after the monomode laser, it reaches high intensities which can cause various nonlinear effects, one of which is stimulated Brillouin scattering (SBS). The SBS process begins when a high intensity pulse propagates in a medium, such as the optical fiber. The wave may scatter in the backward direction off density fluctuations. The backward-scattered wave will then form a “beat” with the original waveform, and drive an acoustic wave through the process of electrostriction. More incident light will then scatter off the acoustic wave with the result that the scattered wave experiences exponential gain. The scattered wave has a frequency of $\nu - \Omega$, where the incident light has a frequency of ν and the acoustic wave has a frequency of Ω . There are several reasons for SBS to be of concern to OMEGA. One of them, the most obvious, is that the backward scattered light causes a reduction

and temporal distortion of the input pulse energy. The SBS light may damage the monomode laser, but a Faraday isolator is used to prevent such. Also, the distortion of the original pulse by even a few percent is significant at the intensities seen in the OMEGA laser, and lower original

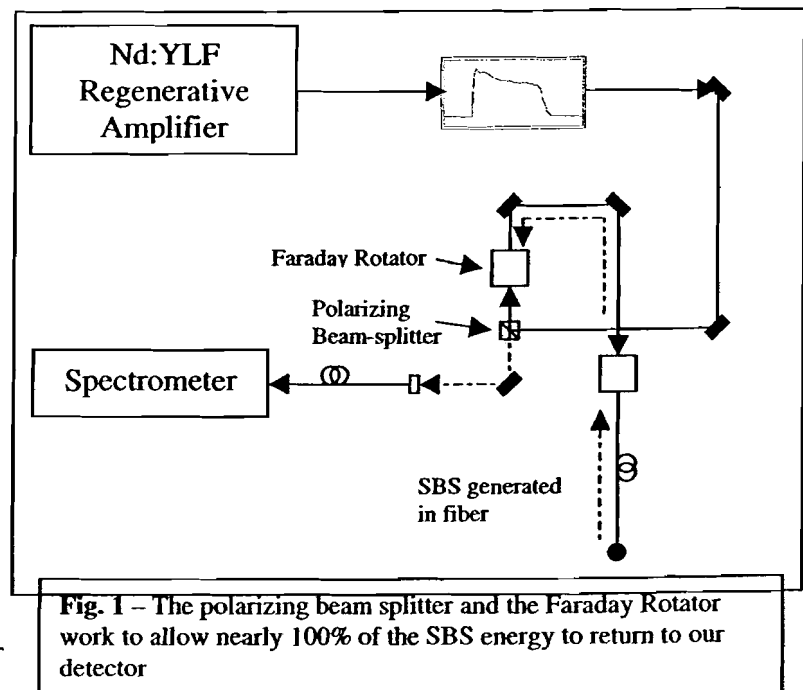


Fig. 1 – The polarizing beam splitter and the Faraday Rotator work to allow nearly 100% of the SBS energy to return to our detector

pulse energy means less overall amplification. Finally, the pulse shape is distorted by the SBS, leading to a faster rise time which may, depending on the project, distort the results.

The intensity of the backward-scattered SBS depends on many factors, and is given by¹

$$I_s(z,t) = I_s(l,t) \exp \left\{ 2 \sqrt{\frac{g_B^e(\max) E_L c t}{n A \tau_B}} - \frac{t}{\tau_B} \right\} \quad (1)$$

where $I_s(z, t)$ is the intensity of the output SBS signal, $I_s(l, t)$ is the intensity of the noise or Stokes signal, g_B is the gain coefficient particular to SBS in a given medium, E_L is the energy of the input laser, c is the speed of light in a vacuum, t is the interaction time, n is the refractive index of the medium, A is the cross-sectional area of the interaction region, and τ_B is the phonon lifetime. Typical values given for τ_B and g_B in the literature² are $\tau_B = 10\text{-}100$ ns, and $g_B = 5 \times 10^{-9}$ cm/W. Our goal was to verify these values and to determine whether SBS would be a threat to future projects on the OMEGA laser and, if so, to what degree.

Our setup was designed to be able to produce high intensities into the fiber, as well as to

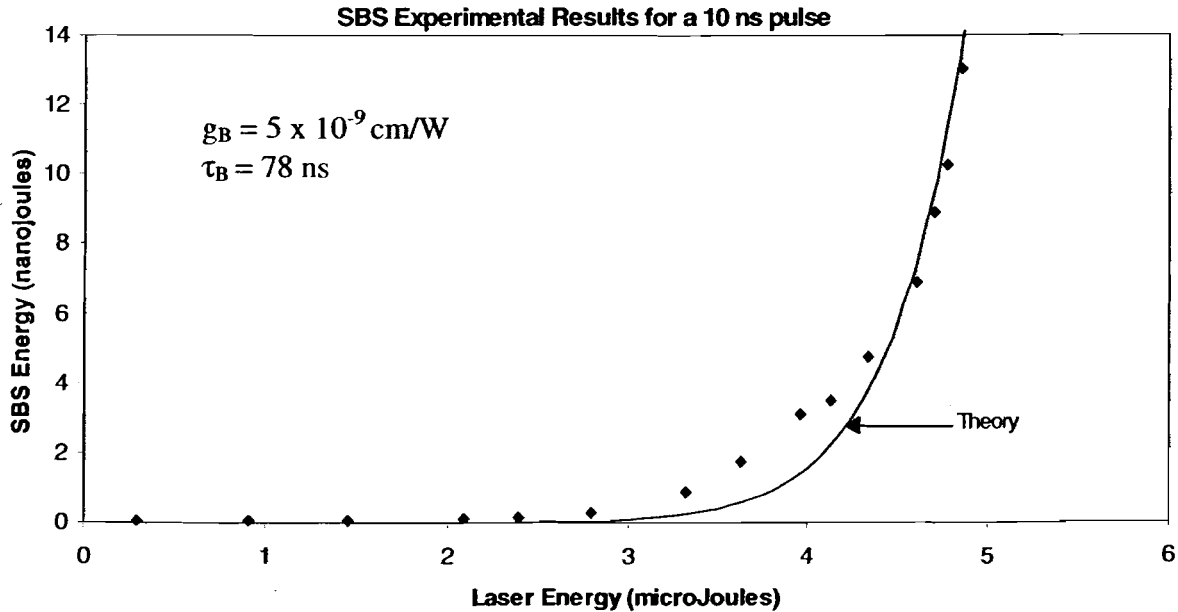


Fig. 2 – The theory shows good agreement with experimental results.

be able to analyze the SBS coming back out. This was achieved by using polarizers, a polarizing beam splitter, and a 45° Faraday Rotator as shown in Fig. 1. The polarizing beam-splitter directed the input pulse through the Faraday Rotator and into the fiber. The SBS was linearly polarized coming back so that it would not be reflected, but would instead pass through the beam splitter into the spectrometer, where it could be analyzed to ensure that it was at the correct frequency for SBS. The fiber under test was a single mode polarization-maintaining fiber from 3M (FS-PM-5121), with a mode field diameter of 7.2 μm .

We took a series of measurements, and fitted Eq. 1 to the experimental results by choosing an appropriate phonon lifetime. The results are shown in Fig. 2. The variables g_B and τ_B that gave the best fit could then be plugged back into Eq. 1 for varying pulse widths. These results are shown in Fig. 3.

Our results stayed well within the bounds of previous experiments, and showed that SBS

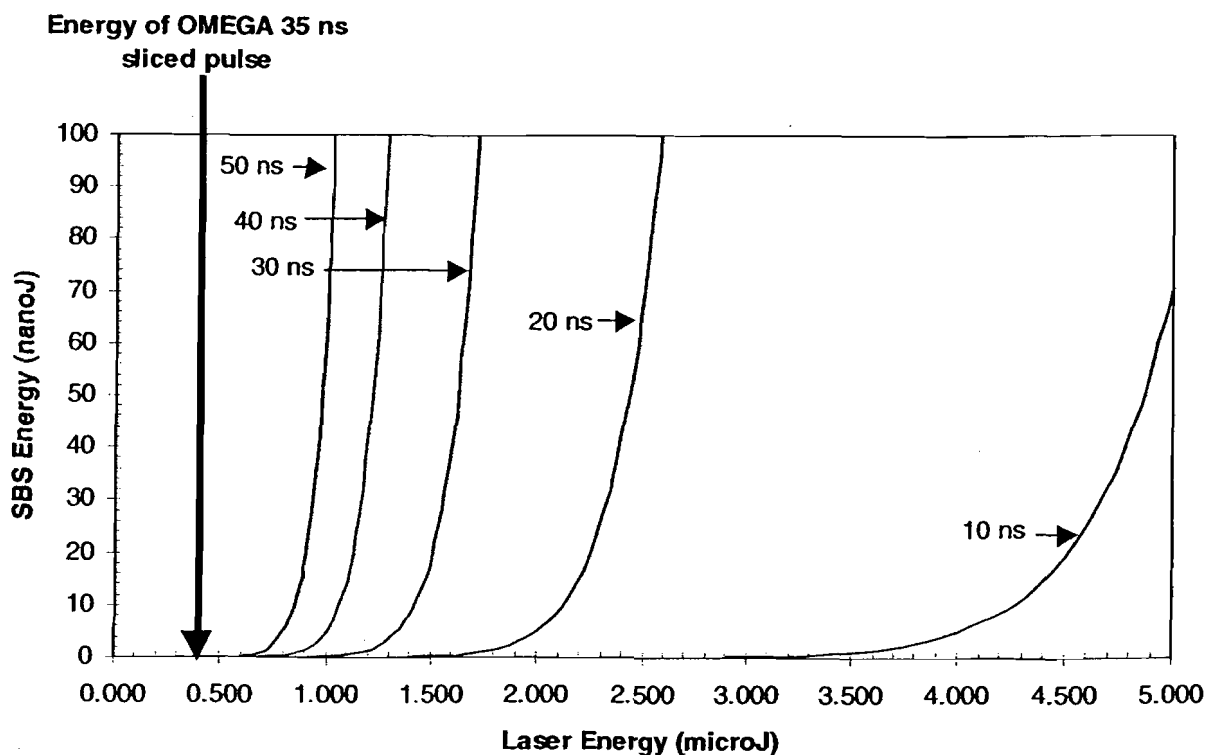
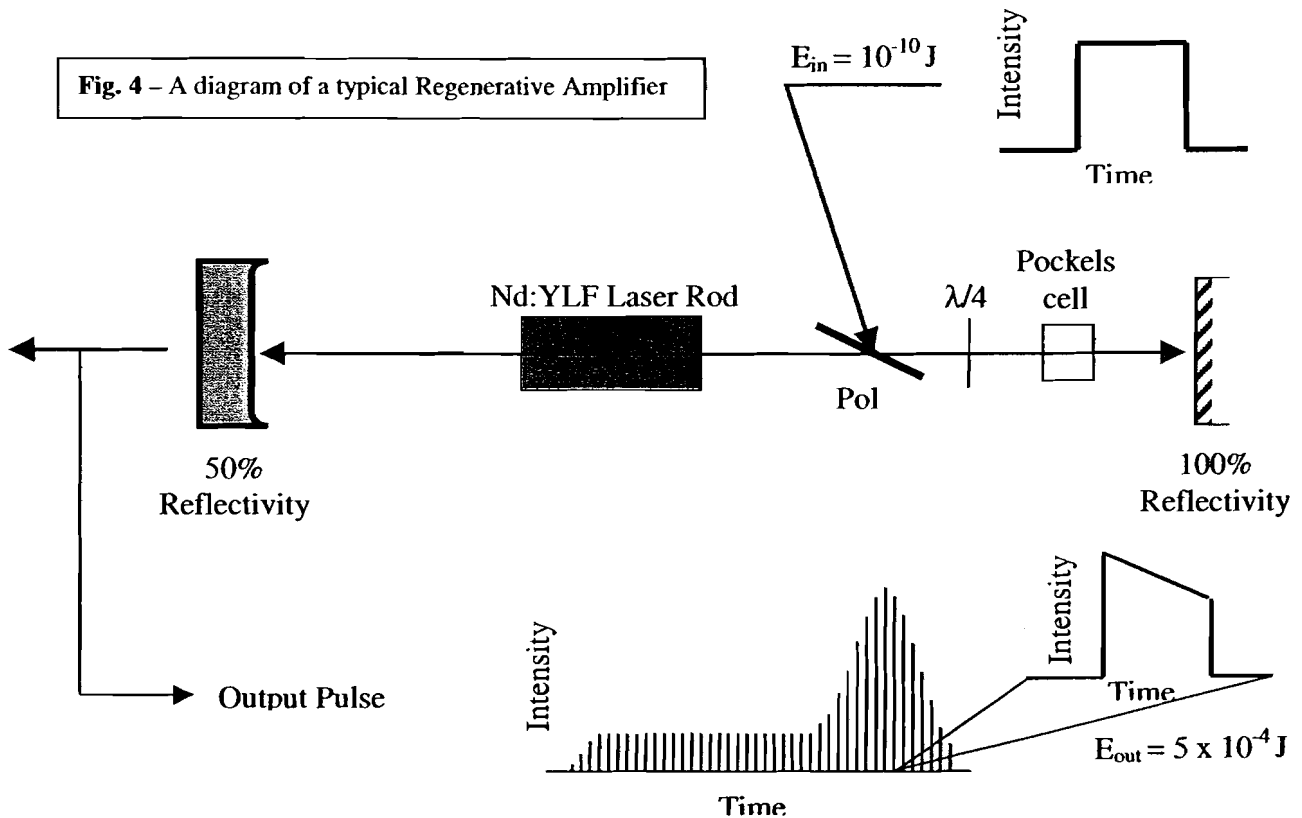


Fig. 3 – With current OMEGA energies, no pulse widths approach the SBS threshold.

was unlikely to become a problem with the short pulses (1-4 ns) generally used in the OMEGA system. Also, the current monomode laser energy (400 nJ) at which OMEGA is operating does not show significant amounts of SBS for greater pulse widths, such as the 40 or 50 ns pulse widths shown in Fig. 3.

II. Gain Gratings in a Regenerative Amplifier



A regenerative amplifier begins with the injection of a shaped pulse, with energy approximately 0.1 nJ. That pulse travels through the cavity, receiving gain each time it goes through the laser rod. Also, each time it hits the output coupler (50% reflectivity mirror), a pulse is released from the amplifier. The other 50% of the pulse is reflected and receives more gain from the laser rod. The Pockels cell is used for feedback purposes and produces the shape of the output pulse train seen in Fig. 4. After many round trips through the cavity, the pulse reaches its

peak, and is “switched out” of the pulse train to be used in the experiment. The output pulse is expected to have some square pulse distortion due to gain saturation, and experiences a gain of approximately five million. When the pulse width is longer than the round-trip-time between the end of the gain medium and the end mirror (6 ns), there are some unusual effects that are observed which have not been analyzed before. This pulse shape distortion can be seen in Fig. 5.

A theory is developed whereby gain gratings are set up in the gain medium for pulse widths greater than 6 ns, the beginning and the end of the pulse interfere with each other in the

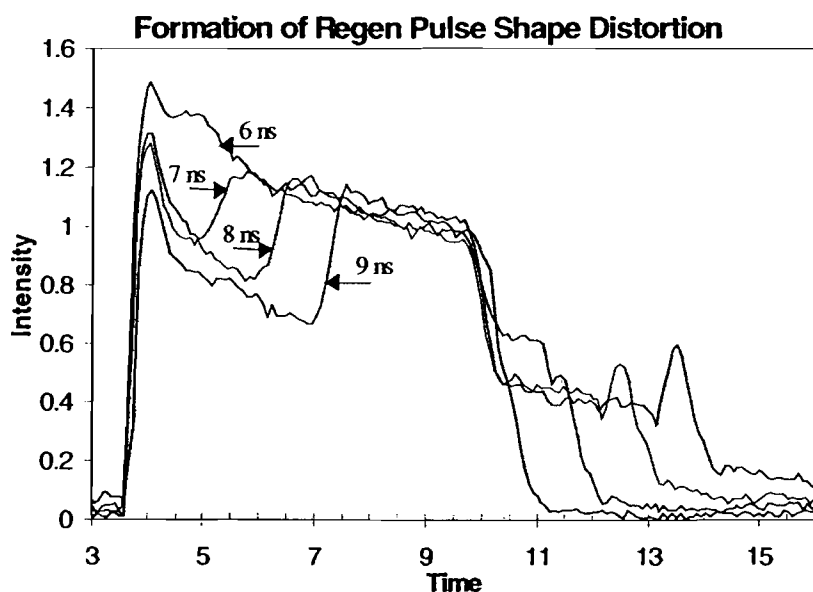


Fig. 5 – As the pulse shape grows longer than 6 ns, the regen pulse shape distortion becomes prominent

gain medium to form a standing wave. The standing wave forms a gain grating through the process of spatial hole burning, from which the light may then scatter. The greater the width of the pulse, the more time the standing wave is formed, and consequentially the stronger the effect. When the pulse

reflects from the gain grating, it undergoes a π -phase shift³, and so is subtracted from the electric field of the original pulse. Therefore, we see two reflections that are π phase shifted, displaced from the original pulse on either side by the round trip time from the gain medium to the nearest end mirror (which, in our case, is six nanoseconds).

Let us consider the total electric field in the medium. The process is modeled as four waves in the classical four wave mixing setup shown in Fig. 6. The total electric field is the sum of the electric fields of all of the interacting waves as follows:

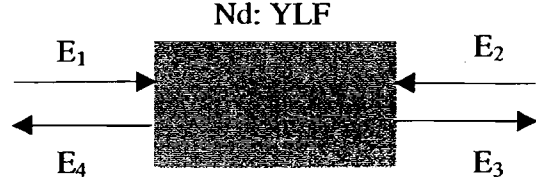


Fig. 6 – The gain grating resembles the traditional four-wave mixing effect.

$$E^T = E_1 + E_2 + E_3 + E_4. \quad (2)$$

We can write the wave equation for the total electric field in the gain medium as:

$$\frac{\partial^2 E^T}{\partial z^2} - \frac{1}{c^2} \frac{\partial^2 E^T}{\partial t^2} = \frac{4\pi}{c^2} \frac{\partial^2 P}{\partial t^2} \quad (3)$$

where c is the speed of light, and P is the polarization of the material which is dependent on the susceptibility, χ , and the total electric field as follows:

$$P = \chi E^T \quad (4)$$

$$\chi = \frac{i2g}{k}. \quad (5)$$

In Eq. 5, i is $\sqrt{-1}$, k is the wave number, and g is the gain coefficient. Both k and g are defined as:

$$k = \frac{2\pi}{\lambda} \quad (6)$$

$$g = g_o \exp\left[-\frac{U^T}{U^S}\right] \quad (7)$$

where U^S is the saturation fluence, 0.7 J/cm^2 for the Nd:YLF laser rod we are using, λ is the wavelength of the laser (1053 nm), and U^T is defined as:

$$U^T = \int_0^t I'(z, t') dt'. \quad (8)$$

These equations cannot be solved analytically. They have been solved numerically³, however we developed a model that simply takes into account the π phase shifted reflections of the gain gratings. This model is far from complete, but has been shown to model the experimental data to a high degree of accuracy.

This simplified program was designed which would reflect a certain percentage of the pulse off the gain grating for every

round trip in the regen. There is also a transient effect as the very beginning of the pulse travels through the gain material. There is a transient reflection time on the very front of the pulse, for a period approximately equal to the time it

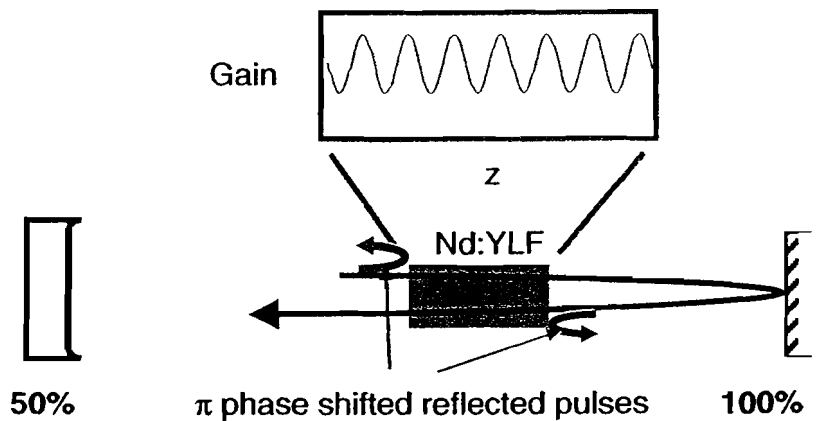


Fig. 7 – The front and back of the pulse both interfere in the gain medium to form a gain grating

takes light to pass through the gain material. This is due to scattering from a distributed gain grating as opposed to reflecting from a plane surface.

In order to detect this phenomenon, we used the same regen design as is found in OMEGA, but we use longer pulses. The laser rod is about one meter from the end 100% reflecting mirror. The pulse exits through the 50% reflecting end mirror, and is cut out of a train of pulses. It then enters an optical fiber coupled detector (New Focus 1414) where it can be read by the Tektronix SCD 5000 oscilloscope.

Theory was calculated by using the process described earlier. A square pulse was created with a specified width. The square pulse (Fig. 8A) was then decreased by the reflectivity of the

grating (taking into account a transient response time), amplified, combined with a later reflection (the later reflection is π out of phase, and therefore its electric field is subtracted from the electric field of the pulse). It is then reflected off of the mirror (some calculations involved a 50% rather than 100% reflecting mirror), reflected off of the gain grating (again with transient effects – this reflection has already been recombined with the pulse), amplified, and combined

with the original reflection (which is, again, π -phase shifted). The three pulses produced can be seen relative to each other in Fig. 8B, and the output after one round trip can be seen in Fig. 8C. This process is repeated many times, as the pulse goes through many round trips in the regen. The pulse is then modeled as a function of intensity (i.e. E^2), rather than one of electric field, since the intensity is what is actually measured. Square pulse distortion is simulated by dividing the pulse into temporal sections and amplifying each section by a decreasing amount of gain. Finally, the pulse is convolved with a Gaussian in order to simulate limited bandwidth.

The theory calculated by the process above seems to match the experimental results well. For example, using a nine-nanosecond pulse and a grating reflectivity of only 0.03% and 20 round trips, Fig. 9 was produced. The experimental data matches up very

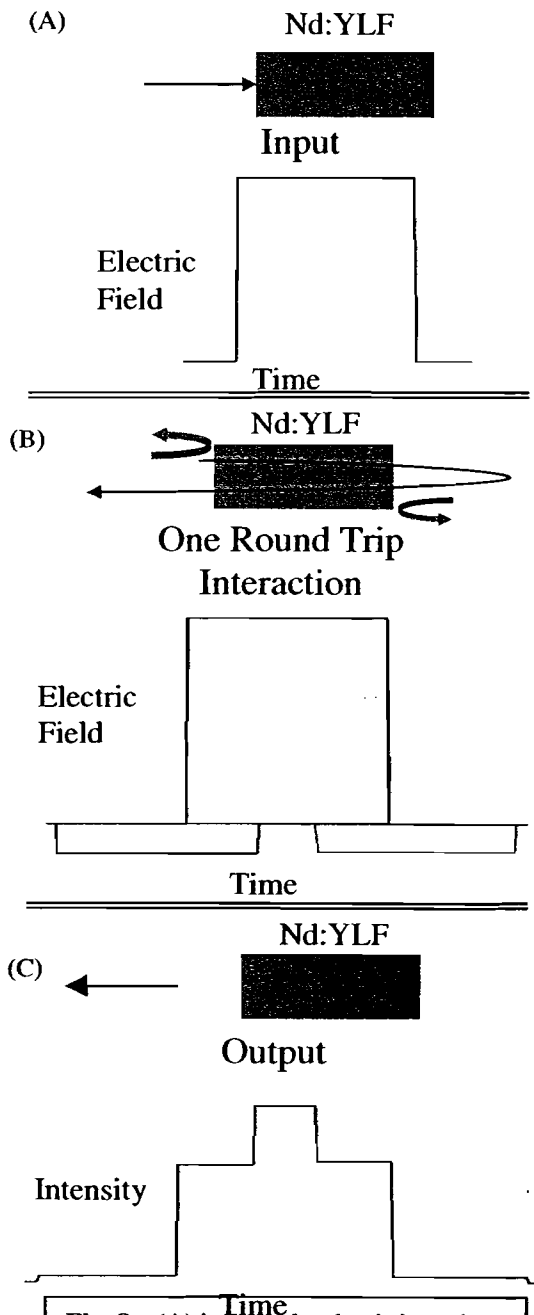


Fig. 8 – (A) is the pulse that is input into the regen; (B) shows the input pulse superimposed on the two reflected pulses; (C) shows the output intensity.

Regen pulse shape distortion in a 9 ns square pulse

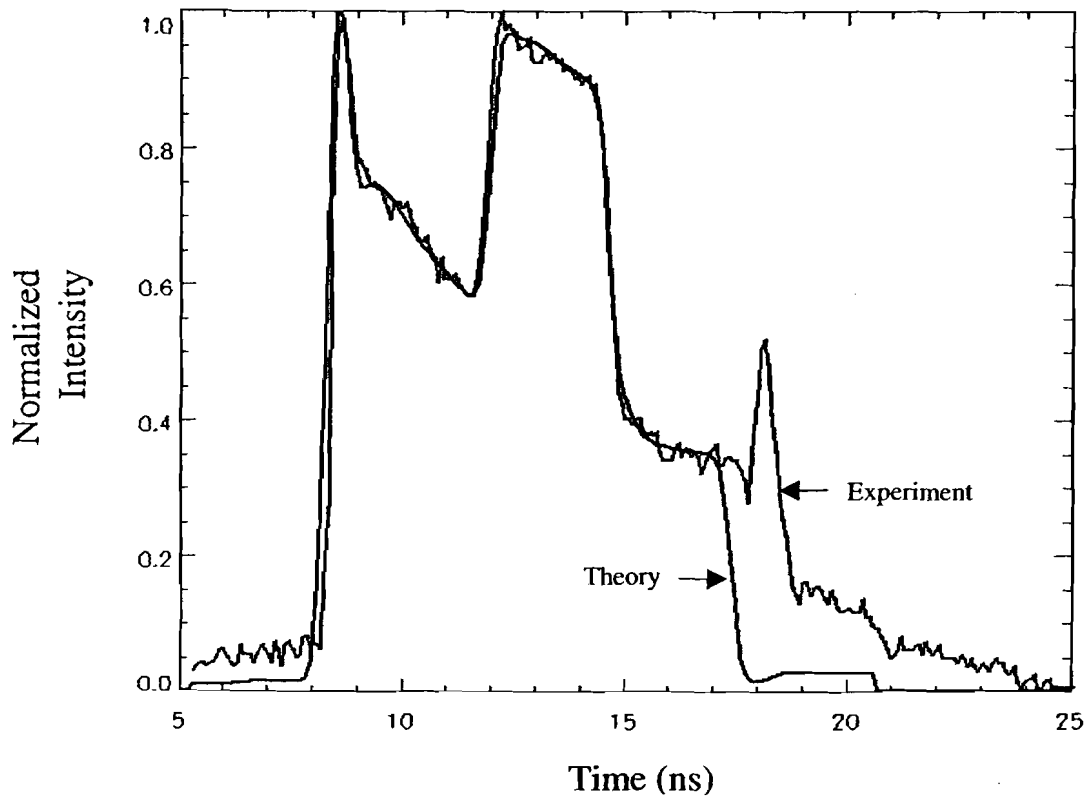


Fig. 9 – Theory based on the formation of a gain grating accurately models the regen pulse distortion, except for the peak on the trailing edge of the pulse

well with the theoretical curve, as you can see, with the exception of the nose seen at the end of the pulse. Seeing that this model is sufficient to describe the experimental data, we can put in some other data to determine the output under different conditions.

There are also many other effects that may be observed using this model, such as a dip or a stair step, simply by modifying some basic parameters, as you can see in Fig. 10. These models match other sorts of distortions which have been noted in the regenerative amplifier, and show that this model may have potential to explain them. However, since the model is still fairly inaccurate (there is a long list of properties which have not been taken into account), there are still some things which are not well understood, as well as some events which can not be accurately modeled.

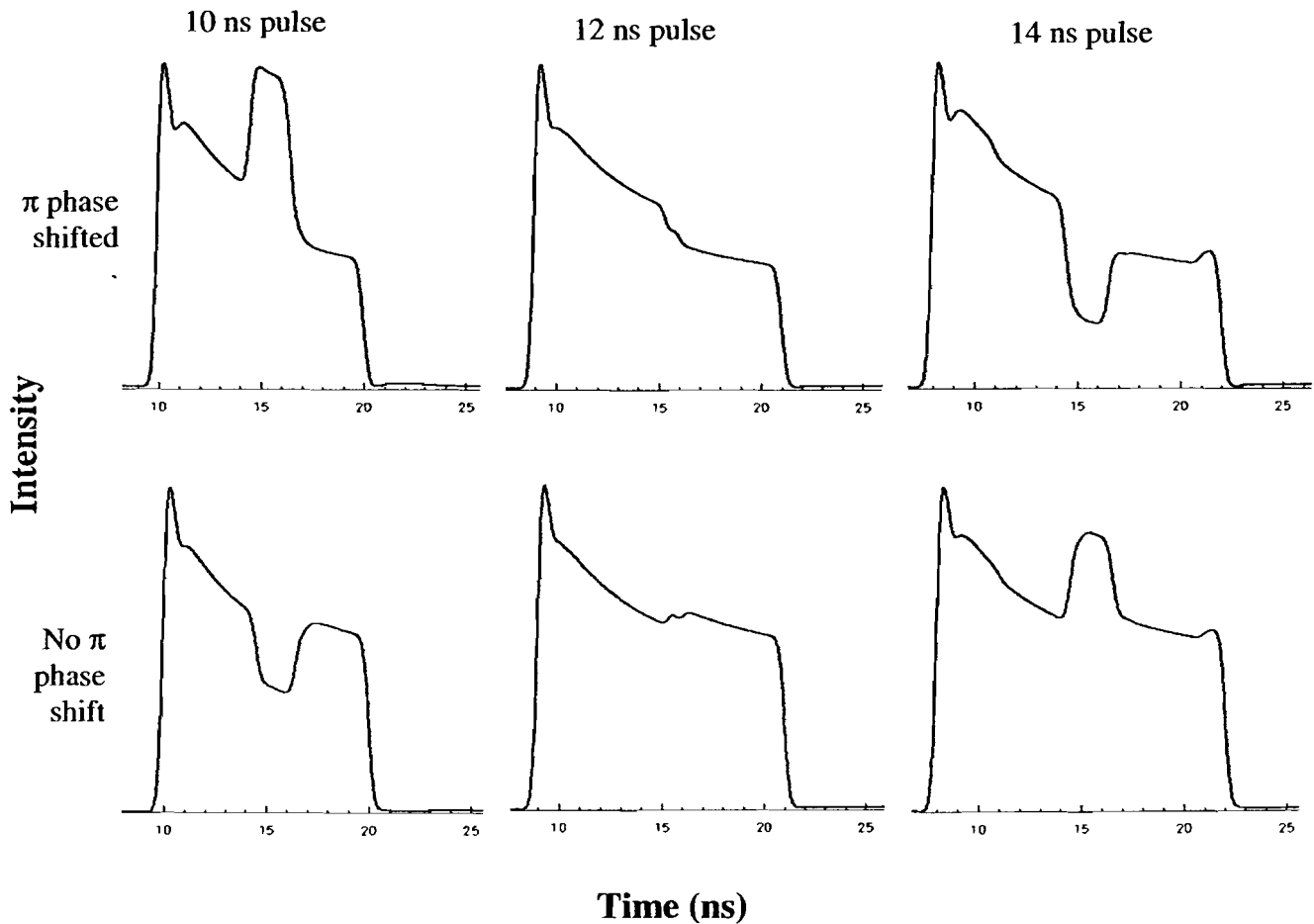


Fig. 10 – Different features are evident in each of these simulations of the regen pulse shape distortion. The round trip time of the simulated cavity is 6 ns

Clearly, the improved modeling of the OMEGA front end has led to identification and evaluation of the potential sources for pulse shape distortions. SBS is shown to be insignificant in OMEGA. More importantly, an accurate model for the pulse shape distortion in the regenerative amplifier based on a gain grating has been developed. This model may have the potential to explain other, more essential, sources of pulse shape distortion in the regenerative amplifier if improved on.

References:

1. Kaiser, W. and Maier, M. in *Laser Handbook*, vol. 2, ed. By F. T. Arecchi and E. O. Schultz-Dubois (North-Holland, Amsterdam, 1972) Chap. E2
2. Agrawal, Govind P. Nonlinear Fiber Optics. New York: Academic, 1989.
3. Minassian, Ara, Crofts, Graham J., and Damzen, Michael J. "Spectral Filtering of Gain Gratings and Spectral Evolution of Holographic Laser Oscillators." *IEEE Journal of Quantum Electronics*, vol 36 no 7. July, 2000.

X-ray Sensitivity Measurements of Charge Injection Devices (CID's)

Robert Forties
Laboratory for Laser Energetics
Summer High School Academic Program, August 2000

ABSTRACT

Charge injection devices (CID's) are digital cameras that can be used to directly image x-ray emission. The signal level from the CID can be related to the absolute x-ray flux provided an accurate calibration of the CID sensitivity as a function of photon energy is known. Measurements of the CID sensitivity at specific energies were made using energy dependent filters (Ross filters) and a laboratory x-ray source. These calibration values will be used in conjunction with values previously derived from comparison of CID and film images to obtain accurate measurements of image intensity and x-ray spectral intensity on the OMEGA laser.

INTRODUCTION

X rays are produced by illumination of targets by the OMEGA laser.¹ The laser beams compress and heat the targets creating short-lived ($\leq 1 \times 10^{-9}$ sec), high-temperature ($> 1 \times 10^6$ K) plasmas. Plasmas at these high temperatures emit x rays, which can be imaged. Regions of higher density and temperature emit more x rays, so an x-ray image of the target can reveal the symmetry of the implosion. Currently, film-based cameras are used to make images of target x-ray emission. The film has good resolution ($\leq 10 \mu\text{m}$), and it has been calibrated so that the incident photon flux density can be measured. However, developing film is a lengthy process (taking about 40 minutes). Digitizing film to the accuracy needed for scientific work requires expensive equipment and adds much additional time to the process. Using film also requires loading and unloading from cameras in the target bay, developing, and digitizing. It is preferable to use digital cameras, which produce results almost instantaneously. CID cameras^{2,3} are an example of a digital camera that has been used to make images of targets on OMEGA. Measurements of a CID camera's quantum efficiency have been made by comparison of CID and film recorded images, but further calibration is needed.⁴

The subject of this paper is the measurement of the response of the CID cameras to x-rays at several different energies. Since the camera sensitivity varies as a function of x-ray energy, energy dependent measurements are needed. To calibrate a camera, a nearly monochromatic beam of x rays is needed. Monochromatic radiation contains

photons that are all of the same energy. X rays can be produced by high-energy electrons striking a solid target. When subjected to electrons at a high enough voltage, the target will emit an x-ray spectrum that contains several emission lines. An associated continuous spectrum of radiation is produced by electrons that are deflected by the atoms of the target and give off part of their energy in the form of an x ray.^{5,6} Using pairs of filters (Ross filters)^{7,8} a narrow, nearly monochromatic x-ray flux was produced and used to calibrate a CID camera.

EXPERIMENTS

Measurements were conducted in air using an X-TECH model 1303 sealed Cu-tube x-ray source.⁹ X rays from the X-TECH source passed through a lead-lined collimator and filter box impinging on either a CID camera or a lithium drifted silicon detector (abbreviated Si(Li) detector), which is an accurate photon counter.¹⁰ Both detectors were mounted on a computer-controlled table to allow precise positioning. The total distance from the source aperture to the recording device was 16 cm. A diagram of the setup used for experiments is shown in Figure 1.

Filters were used to measure the response of the camera in a narrow energy band. The x-ray emission was filtered using two filters, one having a K-shell absorption edge just below the desired energy and the other having a K-shell absorption edge just above the desired energy. The thicknesses of the filters were calibrated so that the transmission of the filters was nearly equal except in the region between their K absorption edges. In this region, called the pass band, the first filter strongly absorbed the x-rays (including the $K\alpha$ emission) and the second strongly transmitted them. This technique is known as Ross

(4)

filtering.^{7, 8} Figure 2 shows the transmission for a sample set of filters. The response of the camera to x rays transmitted through both filters was measured, and then subtracted. The difference between the responses of the camera to the two filters is due almost entirely to the energies within the pass band. There is some error in this method because the transmission of the filters cannot be perfectly matched for the regions outside the pass band, so some of the difference in the responses is due to radiation outside the desired region. Also, the pass band includes radiation in a narrow region, not a single energy, and therefore is not strictly monochromatic. However, the result is much more monochromatic than that which can be achieved with a single filter.

To compute the quantum efficiency of the CID from the measurements the flux reaching the camera and the Si(Li) detector was assumed to be the same. Since the CID measures energy, the flux it measures in units of photons/($\mu\text{m}^2 \times \text{sec}$) can be expressed as

$$\phi_{\text{CID}} = \frac{\Delta N_{\text{ADU}} / E_{\text{photon}}}{A_{\text{pixel}} \Delta t_{\text{exposure}} T_{\text{Win}}(E) \text{QE}_{\text{CID}}} \times C, \quad (1)$$

where ΔN_{ADU} is the number of “analog-to-digital-units” (ADU’s) recorded by the CID, T_{Win} is the transmission of the Be window covering the camera at energy E, which is assumed to be nearly one, $\Delta t_{\text{exposure}}$ is the exposure time for the CID in seconds, A_{pixel} is the area of a CID pixel ($1482 \mu\text{m}^2$, assuming a $38.5 \mu\text{m}$ square pixel), QE_{CID} is the quantum efficiency of the CID, E_{photon} is the mean energy of the incident photons in keV/photon, and C is a constant that converts ADU’s to keV.

(5)

Since the Si(Li) detector is a photon counter, the flux it measures in photons/($\mu\text{m}^2 \times \text{sec}$) can be expressed by

$$\phi_{\text{Si(Li)}} = \frac{\Delta N_{\text{counts}}}{A_{\text{pin}} \Delta t_{\text{int}} \epsilon_{\text{Si(Li)}}(E)}, \quad (2)$$

Where ΔN_{counts} is the number of photons recorded by the Si(Li) detector, $\epsilon_{\text{Si(Li)}}(E)$ is the efficiency of the Si(Li) detector at energy E including the transmission of the Be window covering it (which are collectively assumed to be nearly 1), A_{pin} is the area of the pinhole in front of the Si(Li) detector in μm , and Δt_{int} is the exposure time for the Si(Li) detector in seconds. The equations for the flux on both detectors may then be set equal to each other and solved to find the quantum efficiency of the CID, resulting in

$$\text{QE}_{\text{CID}} = \frac{\frac{\Delta N_{\text{ADU}} / E_{\text{photon}}}{A_{\text{pixel}} \Delta t_{\text{exposure}} T_{\text{win}}(E)}}{\frac{\Delta N_{\text{counts}}}{A_{\text{pin}} \Delta t_{\text{int}} \epsilon_{\text{Si(Li)}}(E)}} \times C. \quad (3)$$

RESULTS

Lower energy measurements were taken using a 25- μm thick Sc filter and 100- μm thick Polyvinylidene chloride (PVDC) filter to create a difference spectrum with an average energy of 4.06 keV. Both measurements were made with the X-TECH source set

to 9 kV and 0.19 mA, and with a lead pinhole in front of the Si(Li) detector. Figure 3(a) shows the results of the Si(Li) from these measurements, and Figure 3(b) shows the difference spectrum resulting from Sc and PVDC filters. Average lineouts of the CID response at 4.06 keV are shown in Figure 4. For higher energy measurements a 10- μm thick Ni filter and a 15- μm thick Fe filter were used to isolate the copper $K\alpha$ emission, which has an energy of 8.04 keV. One measurement was taken with the X-TECH source set to 19 kV and 0.10 mA and a pinhole in a 10- μm thick Pt substrate over the Si(Li) detector and a 50.8 μm Al filter to reduce low-energy noise. The results of these measurements are shown in Figure 5 for the Si(Li) detector and Figure 6 for the CID. The other 8.04 keV measurement was taken at 19 kV and 0.19 mA with a pinhole in a Pb substrate over the Si(Li) detector and a 101.6 μm aluminum filter. A background was taken for each CID image and then subtracted from the corresponding image. After the remaining background was set to zero, the image was then corrected to compensate for continued exposure of the camera to radiation during the readout phase using the readout rate of 0.5 MHz and assuming that it is only sensitive during half of each phase of the readout cycle. The image produced by the difference between CID measurements with Fe and Ni filters is shown in Figure 7. A CID 4150² was used for all experiments, and was read out with a 12-bit GAGE digitizer card.¹¹ The Si(Li) detector measurement was made using an AMPTEK XR-100CR x-ray detector and a PX2T/CR amplifier¹² with the gain set to 3.0.

Table 1 shows all data obtained from experiments. The results are listed by filter pair used to obtain the desired x-ray energy, with the filter absorbing at that energy listed

first (Filter A) and the filter transmitting the desired energy listed second (Filter B).

QE_{CID} is the quantum efficiency of the CID calculated using equation 3.

If the proportionality constant (C) in equation 3 is set to 1.31, the data from this experiment can be normalized to the known absorption of a 7- μm thick Si depletion region covered by an electrically inactive layer with an absorption equivalent to 1 μm of Si.¹³ The known absorption curve is compared to normalized data in Figure 8(a). In addition, Figure 8(b) shows that, when calibrated with this same constant, the data follows a curve of CID quantum efficiency generated by comparison of CID and film images of grating-dispersed x-rays⁴ (although some uncertainty in the absolute quantum efficiency still remains due to uncertainty in the value of C).

CONCLUSIONS

Measurements of CID quantum efficiency as a function of energy have been made with Ross filters by comparing the response of a CID to x rays with that of a Si(Li) detector. These measurements follow the trend expected based on the known absorption of silicon and assumed dead layer and depletion layer thicknesses. These measurements also agree in trend with a previous CID calibration made by comparison of CID and film images. However the proportionality constant needed to calculate CID quantum efficiency is not well known, so it is only possible to verify that the ratios between the measurements at different energies are correct. Estimates of the absolute quantum

efficiency therefore have some remaining uncertainty which could be minimized by further measurements.

ACKNOWLEDGEMENTS

I would most of all like to thank my advisor Dr. Frederick J. Marshall for all of his help and support throughout this project. I would also like to thank Dr. R. Steven Craxton and the Laboratory for Laser Energetics for their support of the summer high school academic program and Tom Ohki for his help at the beginning of the summer.

REFERENCES

1. T. R. Boehly, D. L. Brown, R. S. Craxton, R. L. Keck, J. P. Knauer, J. H. Kelly, T. J. Kessler, S. A. Kumpan, S. J. Loucks, S. A. Letzring, F. J. Marshall, R. L. McCrory, S. F. B. Morse, W. Seka, J. M. Soures, and C. P. Verdon. *Opt. Commun.* **133**, 495 (1997).
2. CID technologies, Inc., 101 Commerce Blvd., Liverpool, NY 13088.
3. J. Carbone, Z. Alam, C. Borman, S. Czebiniak and H. Ziegler. *Proceedings of SPIE*, **3301**, 90 (1998).
4. F. J. Marshall and T. Ohki, accepted for publication *Rev. Sci. Instrum.*, to appear in **Special Issue, 13th Conference on High Temperature Plasma Diagnostics, Tucson, AZ (June 2000)**.
5. B. D. Cullity. Pages 7-12 and 21-27 of *Elements of X-ray Diffraction*, (Reading, Massachusetts: Addison-Wesley, 1978).
6. Harold P. Klug and Leroy E. Alexander. Pages 60-79 of *X-ray Diffraction Procedures* (New York: Wiley, 1974).
7. B. D. Cullity. Pages 19-21 and 227-229 of *Elements of X-ray Diffraction*, (Reading, Massachusetts: Addison-Wesley, 1978).
8. Harold P. Klug and Leroy E. Alexander. Pages 105-107 of *X-ray Diffraction Procedures* (New York: Wiley, 1974).
9. X-TECH Co., W. Hershyn Co.'s Inc., 1570 Soquel Dr., Santa Cruz, CA 95065.
10. B. D. Cullity. Pages 210-213 of *Elements of X-ray Diffraction*, (Reading, Massachusetts: Addison-Wesley, 1978)

11. Gage Applied Sciences, Inc., 2000, 32nd Ave., Lachine Montreal, QC Canada, H8T 3H7.

12. AMPTEK, Inc., 6 De Angelo Drive, Bedford, Mass. 01730.

13. B. L. Henke, E. M. Gullikson, and J. C. Davis, *At. Nucl. Data Tables*, **54**, 181 (1993)

FIGURE CAPTIONS

Figure 1. Diagram of the setup used for taking measurements. The collimator and filter holder were both lead lined to prevent x-ray leakage. All elements were mounted on an optical table.

Figure 2. Plot of the transmission of Fe and Ni filters. The filter transmission is almost identical except in the pass band. Thus, when the camera responses to the two filters are subtracted, the difference is due almost entirely to x rays with energies falling in the pass band. This filter pair was used to isolate the Cu $K\alpha$ line.

Figure 3. Si(Li) detector data from Sc and PVDC filtered x-ray spectra. (a) Sc and PVDC filtered spectra plotted with the unfiltered spectrum; (b) difference spectrum for Sc and PVDC filters.

Figure 4. CID response to PVDC and Sc filtered x-ray spectra averaged across columns 200 to 300, plotted with the difference spectrum.

Figure 5. Si(Li) detector data from Fe and Ni filtered x-ray spectra. (a) Fe and Ni filtered spectra plotted with the unfiltered spectrum; (b) difference spectrum from Fe and Ni filters.

Figure 6. CID response to Fe and Ni filtered x-ray spectra averaged across columns 200 to 300, plotted with the difference between the two responses.

Figure 7. Image produced by the difference between CID images of Fe and Ni filtered x-ray spectra.

Figure 8. Quantum efficiencies calculated from results: (a) shown normalized at 4.06 keV to the known absorption of 7- μm of Si with a 1- μm Si dead layer; (b) plotted with an efficiency curve obtained by comparison of CID and film images.⁴

Table 1

Filters (A/B)	Mean Energy (keV)	Si(Li) Δt_{int} (sec)	Si(Li) Detector			Si(Li) Flux $\left(\frac{\text{Photons}}{\mu\text{m}^2 \times \text{sec}}\right)$	ΔA_{pin} Si(Li) (μm^2)	CID Δt_{exp} (sec)	CID Camera			QE_{CID}
			N Filter A (Counts)	N Filter B (Counts)	ΔN (B-A) (Counts)				N Filter A (ADU's)	N Filter B (ADU's)	ΔN (B-A) (ADU's)	
PVDC/ Sc	4.06	200	12	3570	3558	0.0100	1770	2	30	75	45	0.49
PVDC/ Sc	4.06	200	14	3789	3775	0.0107	1770	2	23	64	41	0.42
Fe/Ni + 50.8 μm Al	8.04	100	498	2212	1714	0.2417	70.9	1	106	282	176	0.080
Fe/Ni + 101.6 μm Al	8.04	200	11008	57883	46875	0.1324	1770	2	64	263	199	0.083

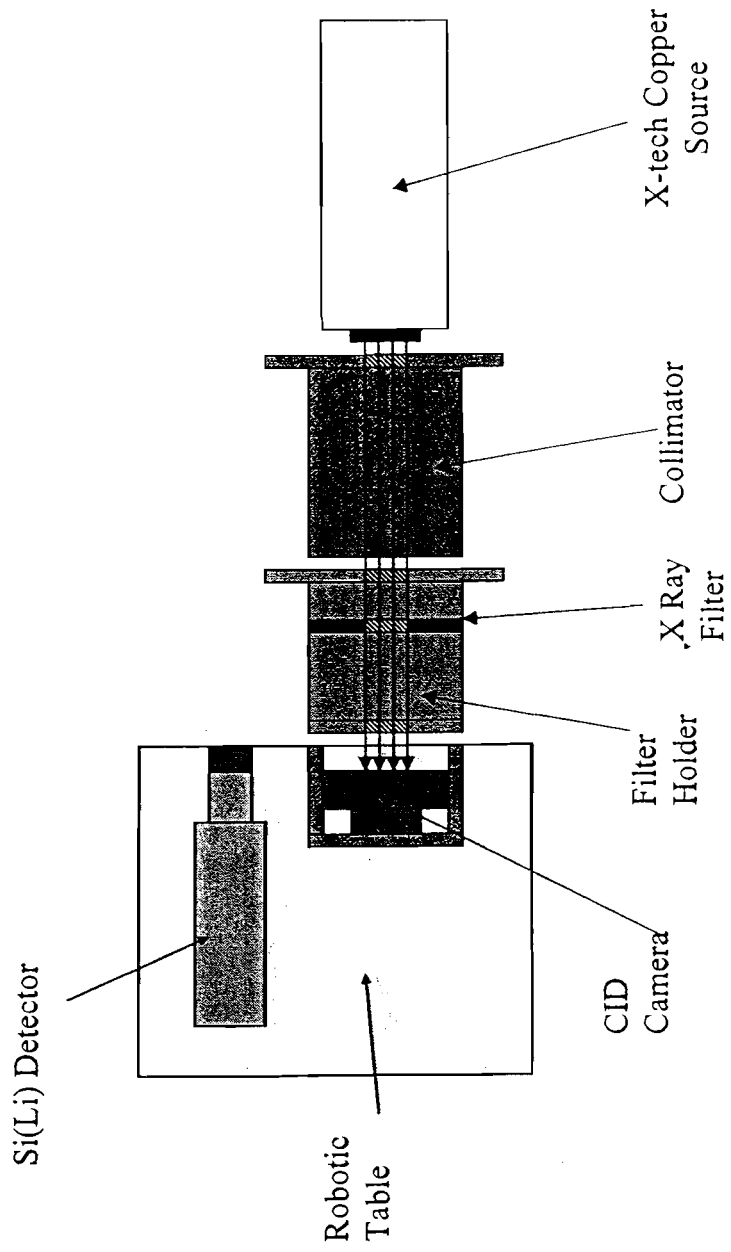


Figure 1

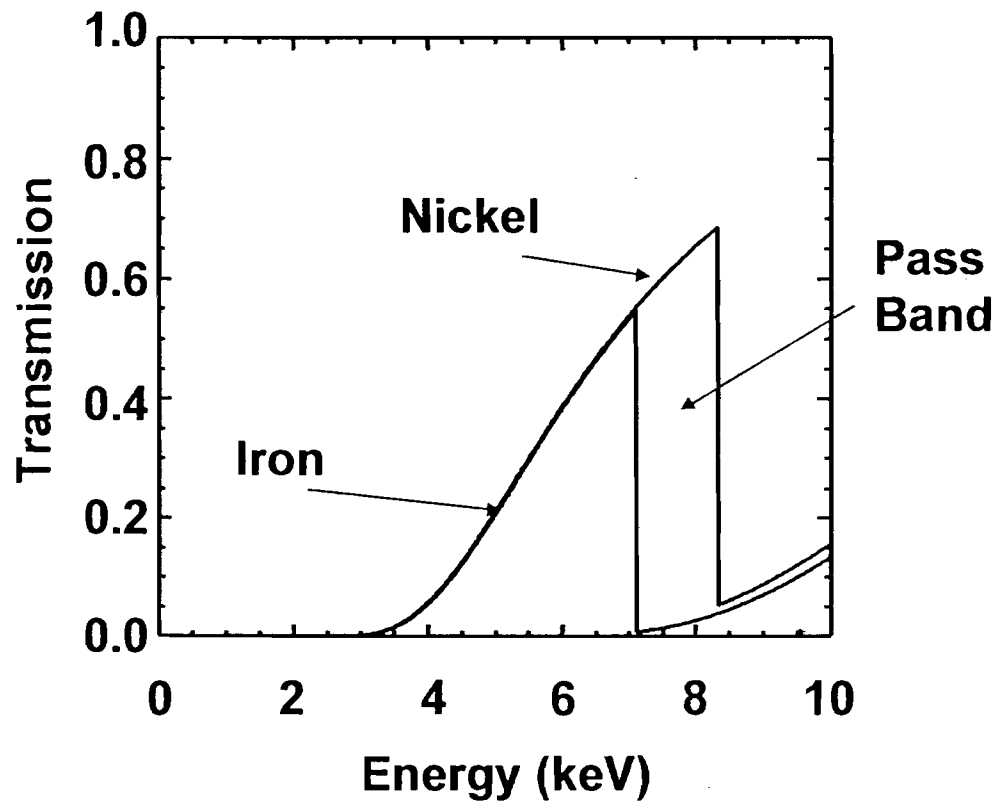


Figure 2

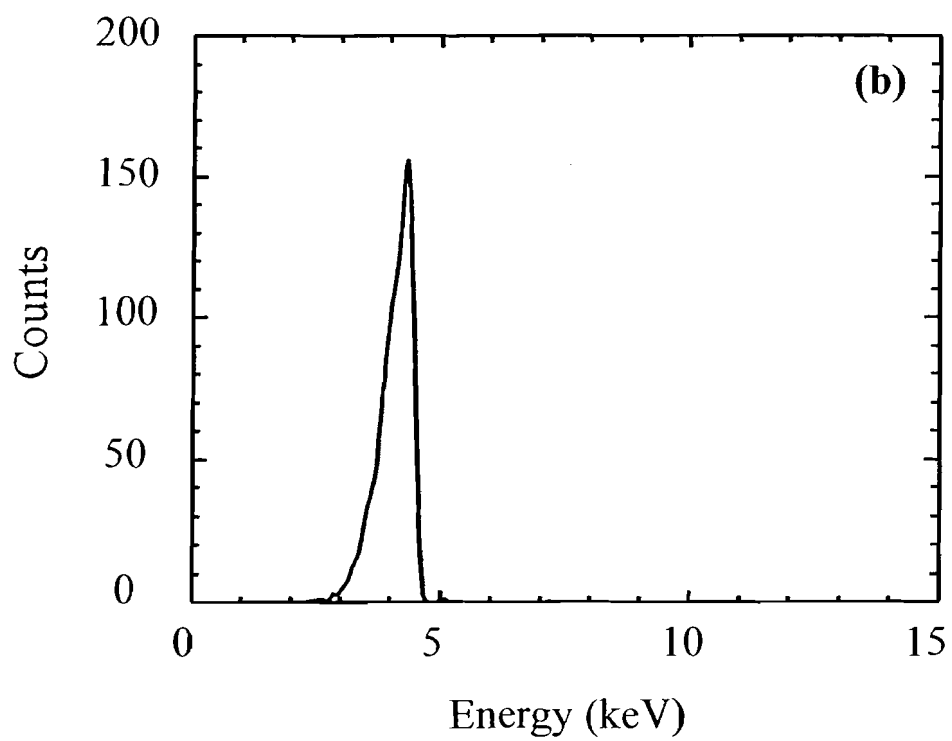
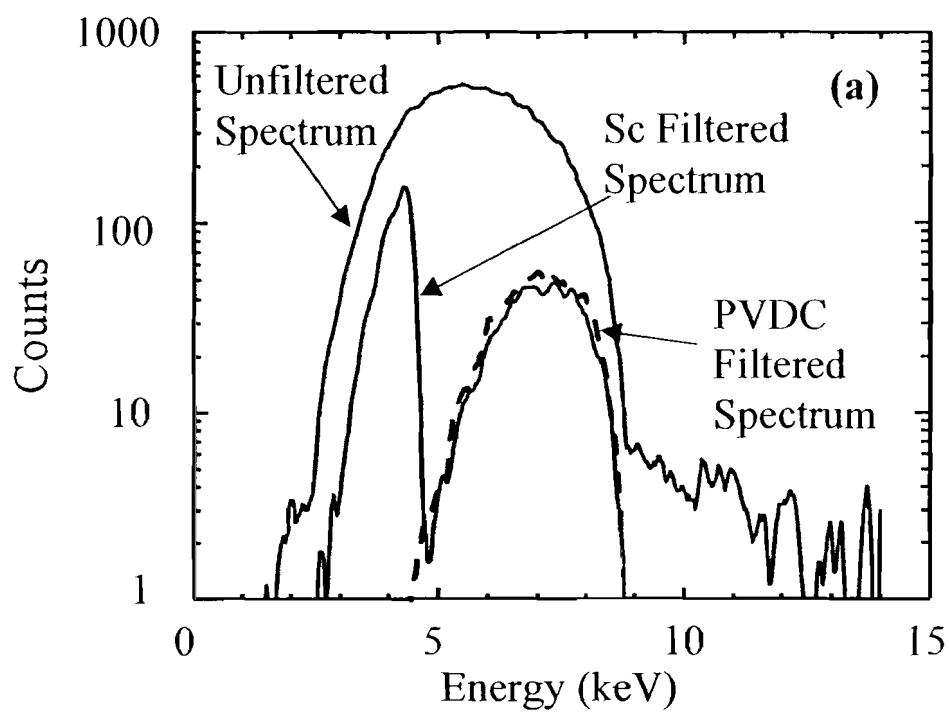


Figure 3

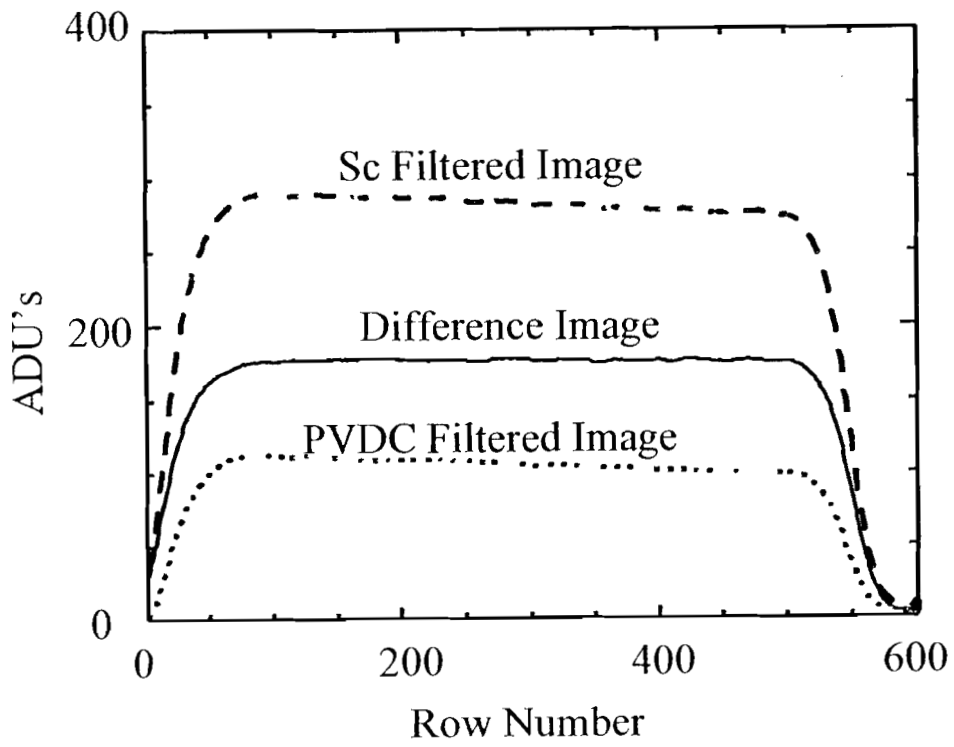


Figure 4

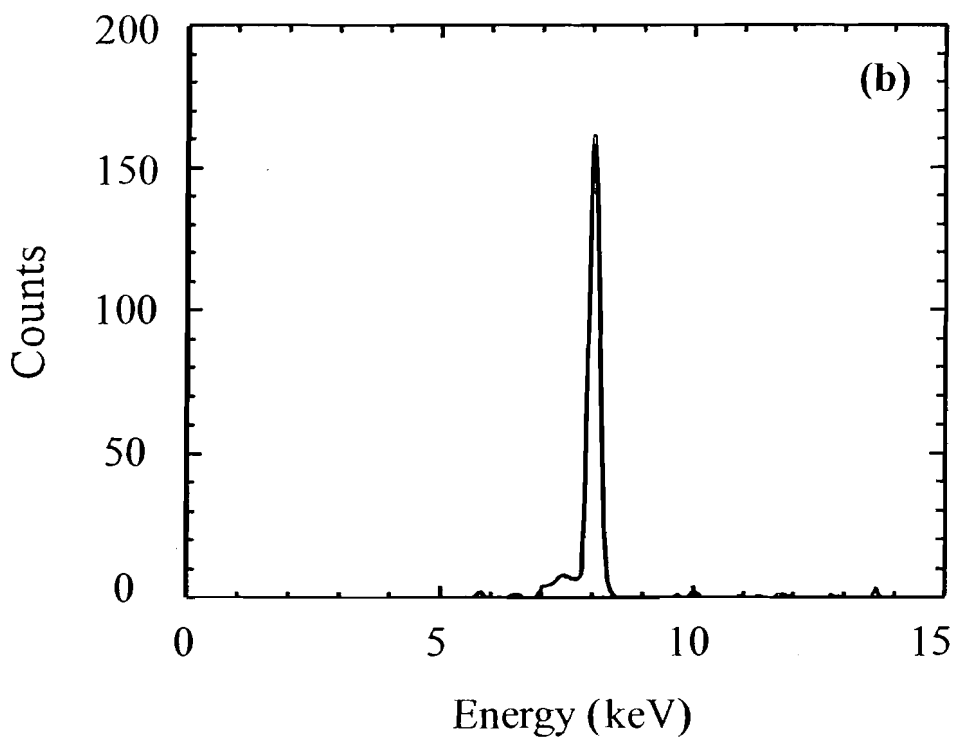
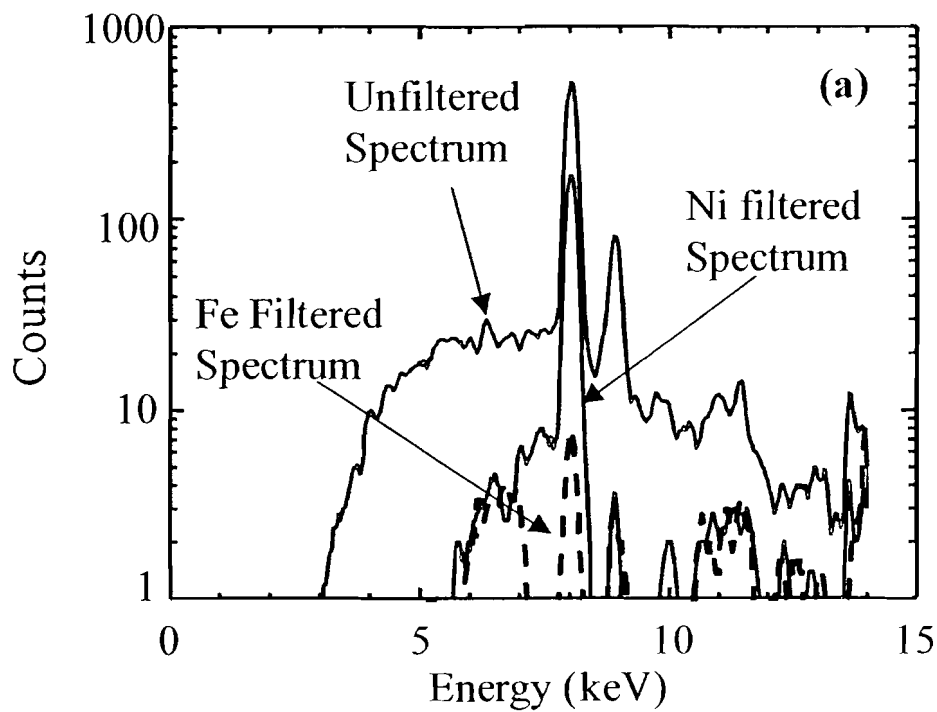


Figure 5

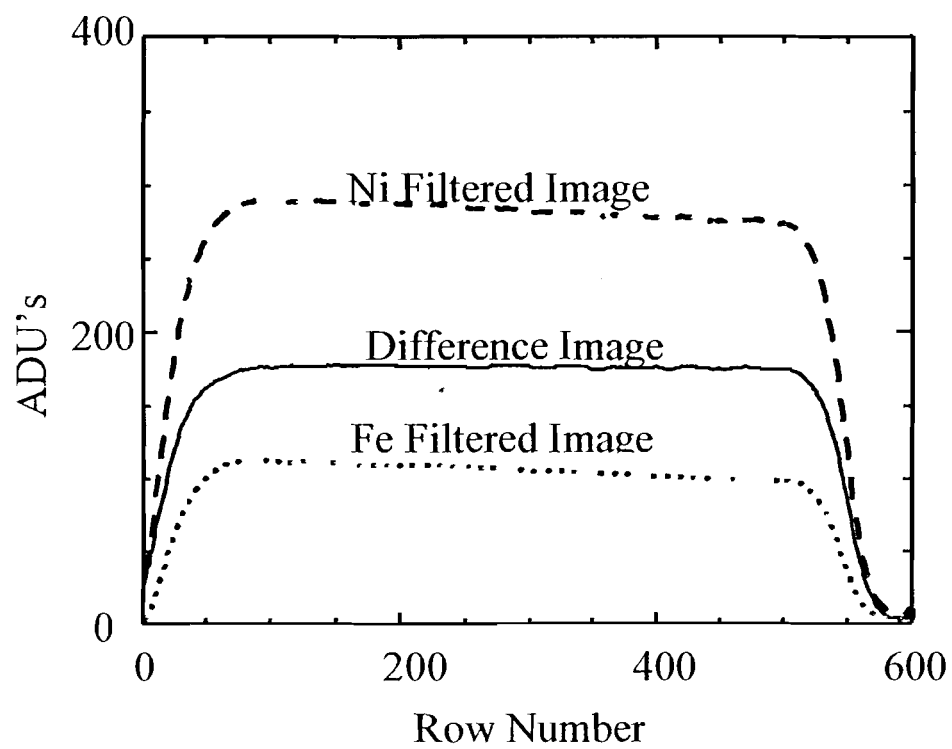


Figure 6

CID Difference Image

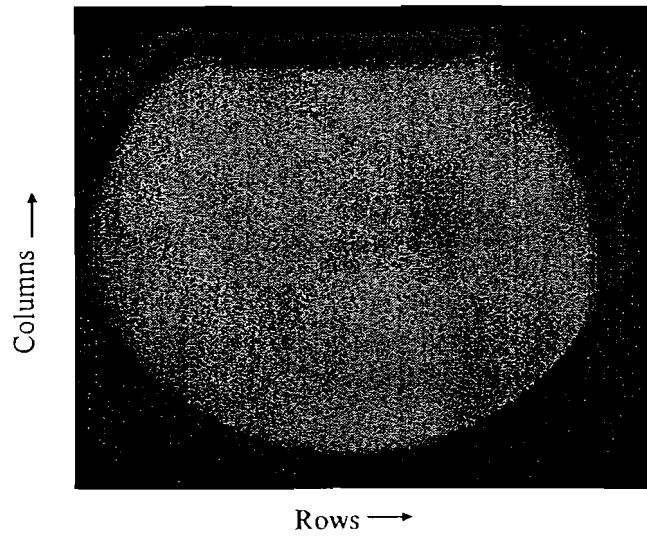


Figure 7

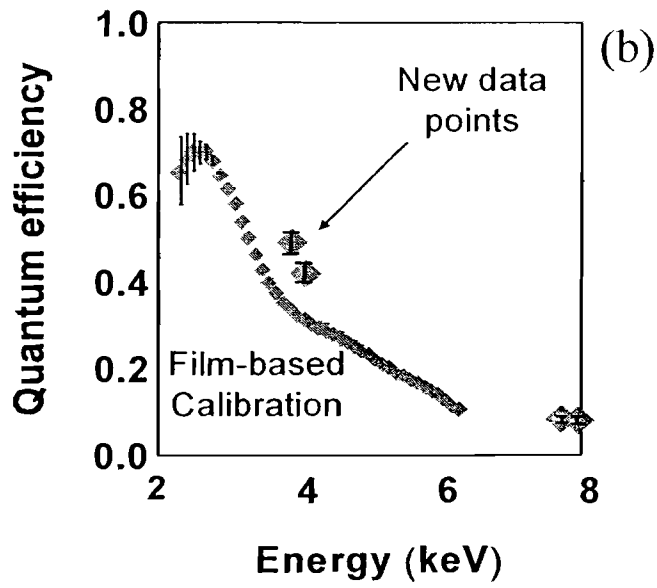
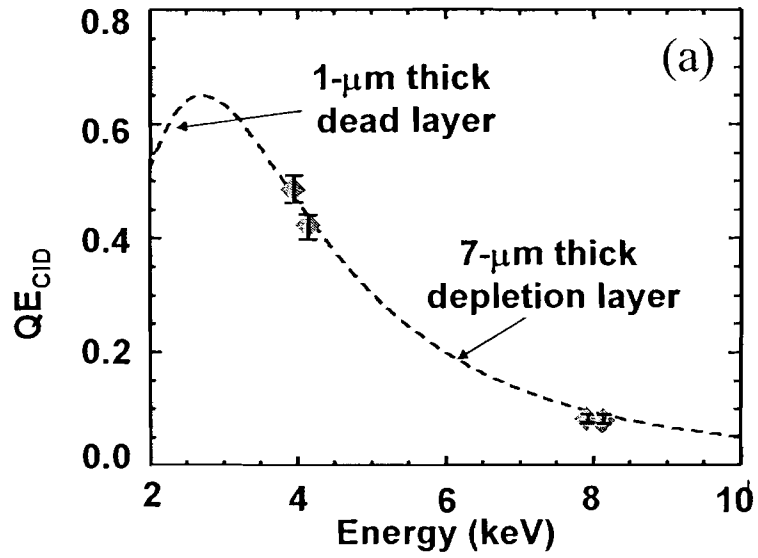


Figure 8

Simulation of Plasma Spectra and Images of Foil Targets Using the Prism SPECT3D Radiation-Transport Post-Processor

Binghai Ling

Advisor: Reuben Epstein

Laboratory for Laser Energetics
University of Rochester

Summer High School Research Program
2000

Abstract

Modeling spectra for certain experiments is helpful in determining what occurs inside an Inertial Confinement Fusion (ICF) experiment. At the high temperatures of ICF, many of an element's outer shell electrons are lost, and absorption spectra of the L-shell and K-shell series appear. Using modeling by the PRISM Spect3D¹ Radiation-Transport Post-Processor on DRACO² hydrodynamic simulations, spectra and the images irradiated targets can be modeled. The images of the target will show the relative optical depth of the whole material, and the spectra can show the temperature range of a doped region.

Introduction

Atomic spectroscopy of ICF is used to determine the conditions inside the target. Such information can tell physicists what needs to be done to improve the conditions of stability, confinement time, and temperature. Spect3D, a radiation-transport post-processor, uses multi-dimensional hydrodynamic output to simulate the absorption and emission of the plasma and models images and spectra of the experiment. Earlier, without Spect3D, only one-dimensional hydro output could be analyzed at LLE to produce simulated spectra.

From Spect3D output, the backlit images of the simulation show the relative optical depth of the material. From the amount of flux coming through the material and the dimensions of the target plasma, the opacity and the emissivity of the target can be

determined through calculations. In the course of this project, images were used to compare the completeness of different atomic models to a tabulated atomic model.

Space-integrated, time-resolved spectra can show the temperature range and the areal density³ of the materials used. Streak-camera absorption spectra are obtained from experiments done by the OMEGA laser,⁴ while space-integrated, time-resolved spectra are obtained from Spect3D. From the observed spectra, the temperature range of the target at a specific point in time can be determined from a temperature mosaic. Temperature mosaics were created with a single, thin, homogenous slab of the signature material at a specific temperature and density, then the spectra were graphed with respect to their temperatures. The temperature range inferred from the spectrum can be compared with the simulated temperature range of the plasma by viewing the DRACO output. If the physics in the simulation is complete, and if the simulated conditions reflect the experimental conditions, then the simulated spectra should resemble the experimental data.

Absorption Spectroscopy

Absorption and emission lines are caused by bound-bound transitions of electrons in an atom, while absorption edges are caused by bound-free transitions of electrons. For bound-bound transitions, a photon of an energy that is equal to the energy of the transition has a high probability, depending upon optical depth, of being absorbed. At this photon energy, there is an increase in opacity, and this will result in an absorption line on the backlit spectrum. The areal density of the material and the cross-section of the atom determine the depth of the absorption line.

For a bound-free transition, a photon of an energy that is equal to or greater than the minimum bound-free transition energy has a higher chance of being absorbed. This is just the photoelectric effect. If the photon energy is greater than the transition energy, this will give the freed electron some extra kinetic energy. The opacity increases abruptly at the transition energy and then drops with higher energies. As a result, the absorption spectrum of an edge drops at the transition energy and slowly increases back to the intensity of the backlighter. The depth of the drop depends the cross section, which is inversely proportional to the square of the shielded nuclear charge.⁵

Plasma Images

Plasma images were simulated for a target consisting of two strips of plastic, each 10 μm thick and 60 μm high and of indefinite length in the third dimension, placed against one another to make a target 20 μm thick. The laser irradiated one side of the target nonuniformly to cause hydrodynamic perturbations that seed the Rayleigh-Taylor instability.⁶ In Spect3D, the thickness in the third dimensional direction was changed to 0.27 cm to cause sufficient absorption to produce a significant contrast in the image. The images were taken at 1.6 ns after the beginning of the pulse. A figure of the setup of the experiment is shown in Figure 1a. All images were backlit with a Planckian blackbody radiating at a temperature of 2 keV.

The purpose of the images was to determine the completeness of the atomic models that were used for each simulation. A relatively complete model of the atom is necessary to represent all the important atomic processes that occur. Each image shows the relative opacity of each part of the material integrated over all frequencies,⁷ since the depth is a projection of the two-dimensional simulation. The images were taken from a sideways view of the plastic but were then rotated counterclockwise to make the laser irradiation at the top of the image. The nonuniformities in the laser causes the perturbations at the top of the target in the image. The part of the target furthest away from the laser is cool, and it shows the most differences between complete and incomplete atomic models.

Using the image of a non-DCA (nDCA) opacity table as a guide, shown in Figure 2a, comparisons between different atomic models can be made. The table results will be used as the standard because it was created with the most complete model. DCA stands for Detailed Configuration Accounting, with which Spect3D calculates opacities, emissivities and cross sections based on an atomic model, while with nDCA, Spect3D reads off a table of opacities and emissivities. Each model has a certain number of configurations, and the user selects the ones to be used. The model with the least number of configurations has the worst agreement with the opacity table, where the bottom of the image is very transparent. However, as more configurations are added, the image looks closer and closer to the image of the table, which is opaque at the bottom. As more and

more configurations are added to the atomic model, there will be an increase in the number of possible transitions between each of the configurations. As a result, if the average cross section increases, the opacity increases, and the bottom of the image becomes more opaque.

In Figure 2b, the image is derived from a 17-configuration DCA carbon atom, where most of the levels are allocated to the He-like isoelectronic species, which has two electrons. The hydrogen atom model always has three lowest principal energy levels selected in all the DCA models. The backside of the plastic away from the laser is very transparent, because it is too cold for the He-like species to exist and the heat front has not yet arrived. Therefore, in the second model, shown in Figure 2c, more configurations were added to the lower-temperature species. The lower-temperature species are those with only a few electrons removed, and they exist at cooler temperatures. The backside becomes more opaque, but there is still a discrepancy. Another set of levels was added in to make a 158-configuration model. This image, in Figure 2d, shows that it is almost exactly the same as the tabulated model, because the back edge is more opaque.

After obtaining an atomic model that is very complete, a new goal is to make a more efficient model. Another atomic model of 106 configurations was created, where only the configurations for the 1s-2p and 2s-2p transitions are included. 1s-2p and 2s-2p transitions were chosen because 1s-2p are the most prominent in absorption, and because 2s-2p fill up vacancies in the 2p shell. The 106-configuration image, Figure 2e, shows almost no difference between that and the 158-configuration model. There are fewer levels in the atom, which will result in a faster computational time when the simulation is run. This use of the images helped determine which atomic model for carbon is complete enough for an accurate representation of the opacity tables in the absorption images.

A calculation of efficiency was made, where each model was run to determine the amount of time it took for each simulation. This was done to determine if a DCA model is worth its cost in time. The results are summarized in Table 1. The incomplete models had times comparable to the table, but the complete models took much longer. The best model, the 106-configuration model, took about four times as long as the table did. Therefore, it is feasible to use the DCA models rather than the non-DCA tables. DCA models have better effective resolution for temperature, density, and frequency than non-

DCA tables, and they can be used to simulate full level kinetics, including photoionization and photoexcitation models, while the tables are either local thermodynamic equilibrium (LTE) tables or collisional-radiative equilibrium (CRE) tables.

Emission images are compared as well to support the accuracy of the absorption image. The emission image of the 106-configuration model is shown in Figure 3b, and that of the non-DCA table is shown in Figure 3a. The calculated emission image looks very much like the tabulated spectra. This shows that the 106-configuration model is probably complete for simulating plasma images.

Type	Configurations	Time (sec)
DCA	17	108
DCA	42	141
DCA	106	435
DCA	158	1002
nDCA	All included by PRISM	112

Table 1

Plasma Spectra at a Definite Time

The next step was to get spectra of the target, by doping some of the backside plastic with aluminum. Aluminum is usually used as a signature layer material during OMEGA experiments, so aluminum absorption will be simulated. Aluminum and silicon spectra were modeled with LTE. CRE could not be used because the temperature-dependence of the collision strengths were tabulated over too narrow a range of temperature in the atomic database. The setup for all spectroscopy experiments is shown in Figure 1b. From the spectral data, the amount of doping necessary for observable absorption was tested. For silicon, a 20% doped sample shows observable absorption, while aluminum that is doped only 5% shows observable absorption. Since aluminum and silicon differ by only one nuclear charge, it is surprising that they are not more closely interchangeable. The reason for this disparity is still under investigation. The absorption graphs of aluminum, shown in Figure 4a, show the spectra for different

percentages of doped aluminum, and the absorption graphs of silicon are shown in Figure 4b. Too much aluminum could saturate the lines and distinct lines could mesh together.

The aluminum model used in this simulation included the initial and final configurations with transitions that had a $gf > 0.05$ as described in Ref. 8. gf is the product of ground-state degeneracy and the oscillator strength. This model shows all of the prominent 1s-2p absorption lines. When a model was created with all the 1s-2p and 2s-2p absorption lines, the spectrum looked very similar to the one created by the model with $gf_{Al} > 0.05$. The model included 2s-2p transitions because that decreases the average number of vacancies in the 2p shell. As a result, this should lower the average absorption cross-section of the 1s-2p transition.⁹ If more configurations of the form $1s^2(2s2p)^{w-1}nl$ were added, where $3 \leq n \leq 10$ and $1 \leq l \leq 4$, it would increase the average number of vacancies in the 2p shell by allowing the excitation of those atoms. Therefore, an increase in the average cross-section occurs at temperatures greater than about 10 eV, and an increase in absorption will result.¹⁰ However, this was not done in the atomic model because of the time cost of increasing the number of configurations. The model with the $gf_{Al} > 0.05$ was the best model to use for accuracy and efficiency. Nonetheless, missing configurations were found in this model, such as the K-edges of M-shell species and of cold aluminum, but they were later added. The silicon model was the same as the best aluminum model with the same configurations.

Time-resolved absorption spectra

The next step is to make useful spectra from DRACO output. After obtaining the DRACO output files, Spect3D was used to make a space-integrated, time-resolved streak spectrum. In Figure 5a, the spectrum was created from a 1-D unperturbed simulation. The unperturbed simulation is a piece of 20 μm thick plastic, with a signature layer of 1 μm aluminum 9 μm deep, irradiated uniformly with a laser intensity of 200 TW/cm^2 for 2 ns.¹¹ The initial shock comes at about 200 ps, but the DRACO output time frequency is 100 ps so the Spect3D results resolution is only 100 ps; therefore, exactly when the shock comes is not clear. At around 1.4 ns, the heat front warms the aluminum very quickly, all the way up to its hydrogen-like state in about 150 ps. The laser is uniform; therefore, there is only a small range of temperature that the aluminum occupies. As a result, each

L-shell species disappears in about 300 ps. In the perturbed run, whose spectrum is shown in Figure 5b, the target foil is nonuniformly irradiated with the same laser. The shock appears at about 200 ps. However, the heat front does reach the aluminum about 100 ps earlier. Also, because of the perturbation and the Raleigh-Taylor instability, there is a wide range of temperatures. As a result, the F-like and O-like states persist, in contrast to the unperturbed DRACO run, for about 500 ps, until the end of the simulation. The range of temperatures determined by the F-like through H-like is about 600 eV. A plot of the maximum and minimum temperature of the aluminum signature layer for the perturbed and unperturbed DRACO simulations are shown in Figures 6a and 6b respectively.

The perturbed spectrum can then be compared to a streak camera output from an experiment done by OMEGA,⁴ in Figure 7b. However, only qualitative analysis can be done because the input parameters for the DRACO simulation were different from those of the OMEGA experiment. For the experiment, the laser intensity was 400 TW/cm^2 for a duration of 1 ns.⁴ In Figure 7a, the color scale has been adjusted so that the perturbed DRACO run looks like the experimental streak camera output. This is permissible because the streak camera output is uncalibrated. The shock of the DRACO simulation appeared at about 200 ps, while the shock of the experiment appears at around 100 ps. This is expected from the differing intensities of the lasers. There is less shock preheating in the simulation than the experiment. The K-edge shift in the experiment shows when the shock arrives. However, because there was no continuum-lowering model in Spect3D, the distinct K-edges of magnesium-like and sodium-like species appear with the shock. Because of differences in input parameters, there was a later heat front arrival in the simulation. The main heat front heats the aluminum quickly, bringing up higher ionized states. In the simulation, heating goes all the way up to hydrogen-like, and fully-ionized aluminum as well, but in the experiment, it only goes up through beryllium-like. The higher temperature of the heat front could be a result of the use of CH as the signature layer in the DRACO simulation (changed to Al in the Spect3D simulation), as opposed to Al, which can radiate away heat.

Temperature Determination

Hydrodynamically static LILAC¹² foils were simulated with Al foils 0.1 μm thick at different temperatures and densities as input for Spect3D. Spectra at the various temperatures are arranged along a temperature axis. Absorption bands indicate the relative abundance of each L-shell and K-shell species through their relative opacity. The results are shown as temperature mosaics in Figure 8a for a density of one times solid and in Figure 8b for a density four times solid. These temperature mosaics can help experimentalists determine what temperature ranges occur in the signature layers. For example, if the fluorine-like species is present and the oxygen like species is not present at one times solid density, the temperature is between 20 and 30eV.

A mosaic for different densities could be made, so that an experimentalist, given an estimate of the densities from a hydro run, can determine the temperature range of the foil as a function of time from a time-resolved spectrum. The spectrum is much more dependent on temperature than on density, so if the spectrum is known and if only a rough estimate of the density is available, temperature can be found.

Conclusions

Plasma images and spectra are outputs of the Spect3D radiation-transport post-processor. Backlit images can help determine the optical depth of the target. Spect3D can calculate opacities and emissivities based on an atomic model, and the plasma images help to determine which atomic model is the most complete and efficient. The completeness of the model is determined by how closely the image resembles the image of a table of opacities and emissivities obtained from a model known to be complete. The efficiency of the model can be determined by the run time of each model.

Plasma spectra can help determine the necessary amount of aluminum in a signature layer to obtain observable absorption. They also can create temperature mosaics for experimentalists to determine the temperature ranges of the signature layer from streak camera spectra. Most importantly, Spect3D can create space-integrated, time-resolved spectra to compare multi-dimensional hydrodynamic simulated spectra with streak camera spectra from experiments. Spect3D is a powerful tool that will be used in the future to solve the radiation transfer problem, to determine the properties of laser-driven plasmas, and thus help improve the effectiveness of laser fusion.

References

- [1] J. J. MacFarlane, et al., SPECT3D Imaging and Spectral Analysis Suite, PRISM Computational Sciences, Inc., (2000).
- [2] DRACO hydrodynamic code, Laboratory for Laser Energetics, University of Rochester, (2000).
- [3] B. Yaakobi, R. S. Craxton, R. Epstein, Q. Su, "Areal-Density Measurement of Laser Targets Using Absorption Lines," *J. Quant. Spectrosc. Radiat. Transfer* **58**, 75-83 (1997).
- [4] T.R. Boehly, private communication.
- [5] G. C. Pomraning, *The Equations of Radiation Hydrodynamics* (Pergamon, Oxford, 1973).
- [6] R. S. Craxton, et al., *Scientific American* **255**, 68-79 (1986).
- [7] J. J. MacFarlane, SPECT3D Getting Started Manual (Version 1.3), PRISM Computational Science, Inc., Report # PCS-R-011.
- [8] C. Chenais-Popovics, C. Fievet, J. P. Geindre, J.C. Gauthier, E. Luc-Koenig, J. F. Wyart, H. Pépin, M. Chaker, "K α absorption spectroscopy: Diagnostic of the radiative preheating of a laser-irradiated layered target", *Physical Review A* **40**, 3194-3208 (1989).
- [9] R. Epstein, "Satellite absorption lines and the temperature dependence of x-ray absorption features in high-temperature plasmas." *Physical Review A* **43**, 961-967 (1991).
- [10] J. Abdallah, Jr., R. E. H. Clark, J. M. Peek, "Excited-state $1s-2p$ absorption by aluminum ions with partially filled L shells." *Physical Review A* **44**, 4072-4075 (1991).
- [11] R. Town, private communication.
- [12] LILAC hydrodynamic code, Laboratory for Laser Energetics, University of Rochester.

Acknowledgements

I would like to thank first and foremost, my advisor Dr. Reuben Epstein for mentoring me throughout this whole project. I would also like to thank Richard Town for providing me with all the DRACO runs that were used as input in the Spect3D, and Tom Boehly for providing the experimental data. Additional thanks goes to the other theorists of the

Theory and Computation Group at LLE: Radha Bahukutumbi, and Jacques Delellez; the people at PRISM Computational Sciences: Joe J. MacFarlane, Andy Thomas-Cramer, and Pei Zeng; the computer managers at LLE: Tony Brancato, David Keller, and Alan Shechter. Finally I would like to thank Dr. R. Stephen Craxton for giving me the opportunity to work here at LLE for this summer.

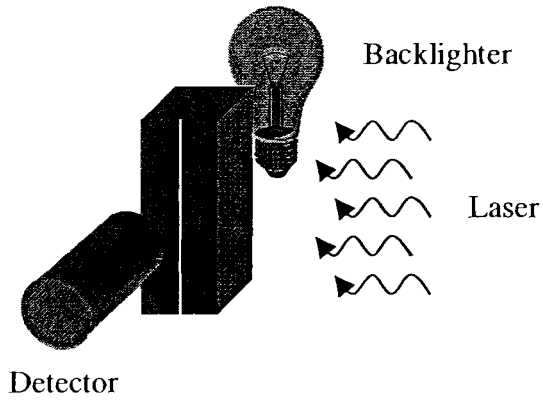


Figure 1a

This shows the setup of the simulation when modeling of the plasma images was done. The laser light is coming from the right, the backlighter is behind the target, and the detector is in front of the target. The backlighter is represented by a light bulb.

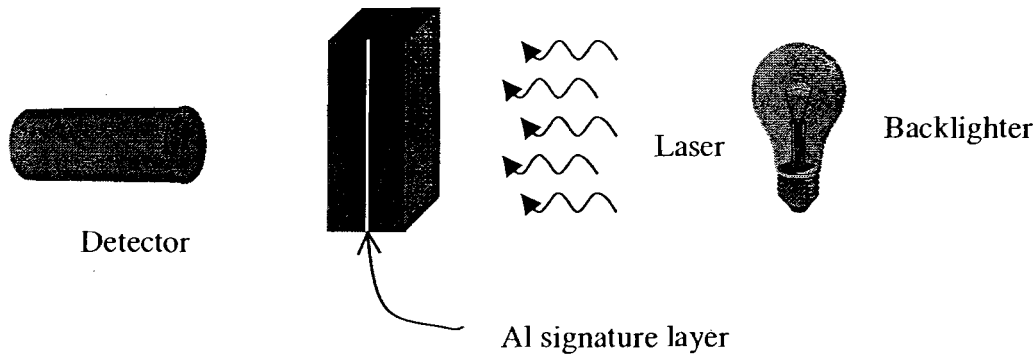


Figure 1b

This shows the setup of the simulation when the spectra of the targets were modeled. The laser light is still coming from the right, but the backlighter is also on the right, and the detector is placed on the left. In an actual experiment, the backlighter would be a piece of high-Z material. When a laser light shines upon it, it produces x-rays.

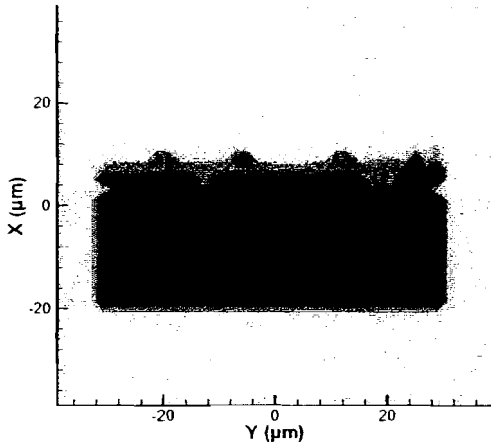


Figure 2a

This is the absorption image of a nDCA simulation. The bottom of the image is very opaque.

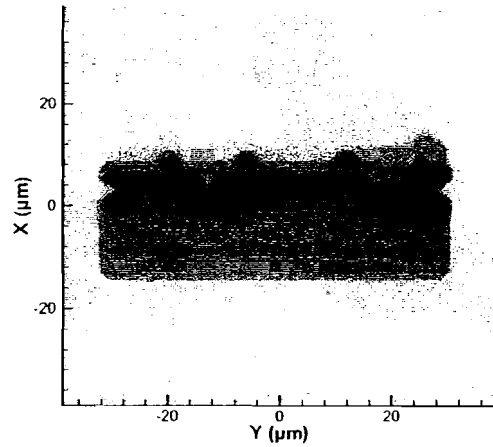


Figure 2b

This is the absorption image of the 17-configuration DCA model. The bottom of the image is very different from the nDCA model.

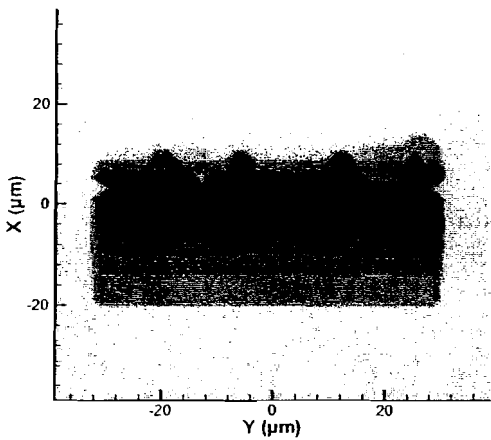


Figure 2c

The image of the 42-configuration model looks better than the 17-configuration model as compared to the nDCA model.

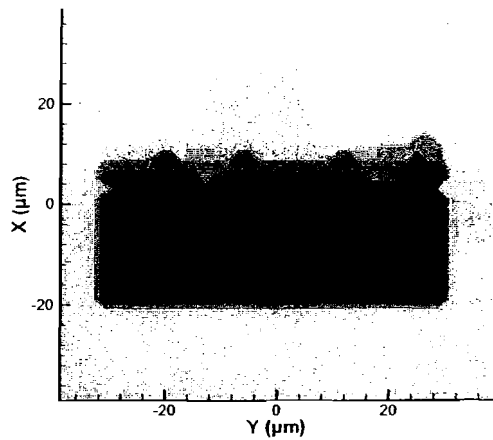
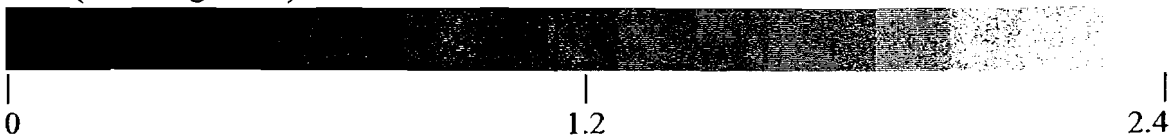


Figure 2d

This is the absorption image of the 158-configuration model, and it looks almost exactly like the nDCA model.

Absorption images:
Flux ($\times 10^{12}$ erg/cm²/s)



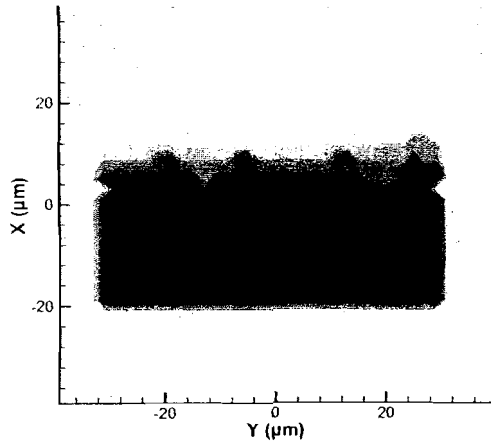


Figure 2e

This model, the 106-configuration one, is the best approximate of the nDCA model and is the most efficient.

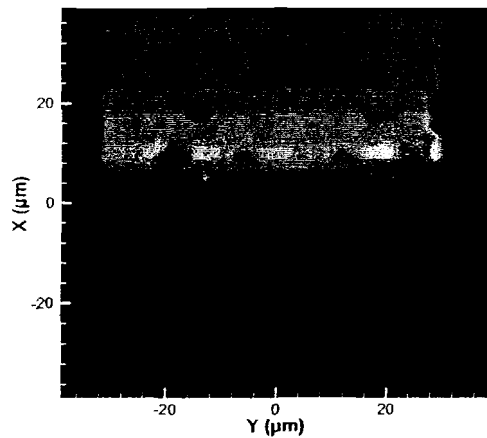


Figure 3a

This is the emission image of the nDCA simulation. The emission comes from the hotter part of the plasma where the H- and He-like species exist.

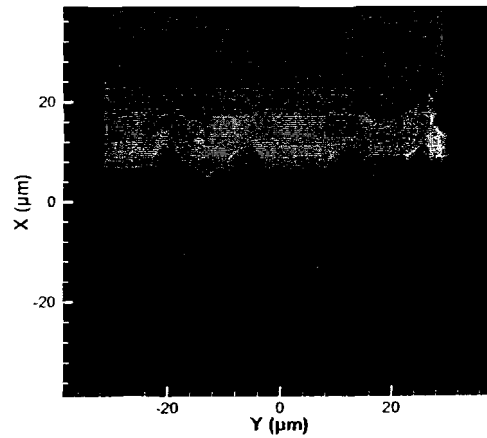


Figure 3b

This is the emission image of the 106-configuration model. It looks very similar to the nDCA simulation.

Emission images:
Flux ($\times 10^8$ erg/cm²/s)



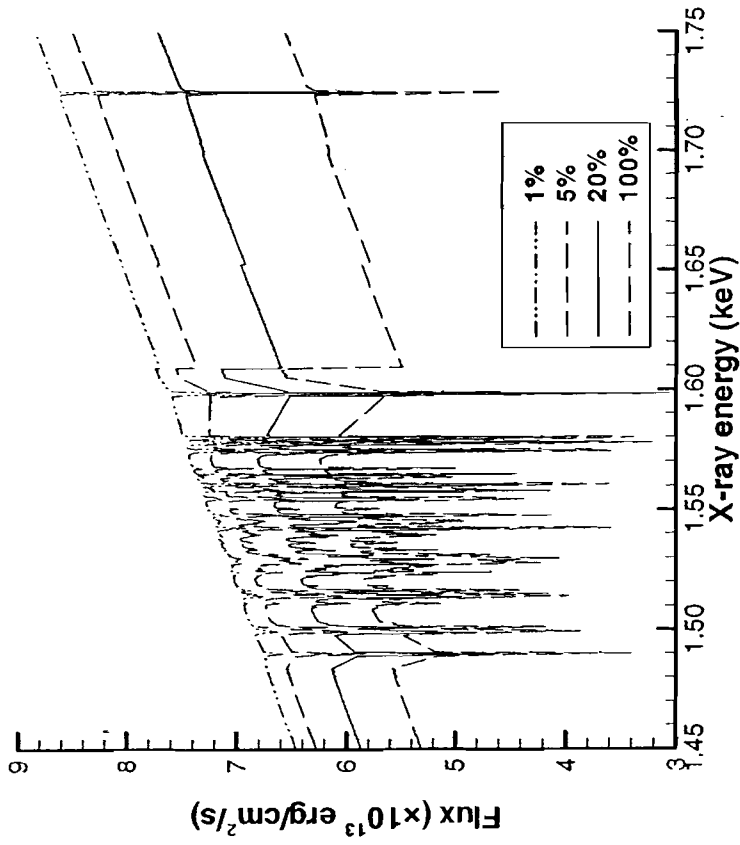


Figure 4a

This figure shows absorption spectra with different doped amounts of Al in a CH layer. When there is only a few percent of aluminum, the absorption spectrum is relatively small, but as the concentration of aluminum is increased, saturation begins to occur.

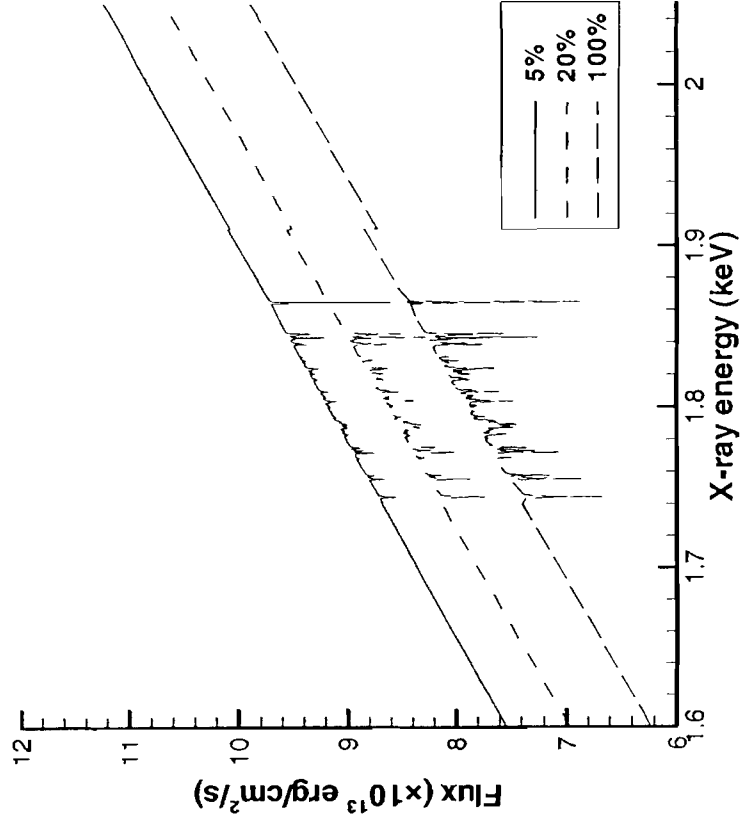


Figure 4b

This figure shows absorption spectra of different doped amounts of Si in a CH layer. The absorption of Si is much less than the absorption of Al, for reasons under investigation for the moment. However, an observable spectrum can be seen with a doped amount of 20% Si.

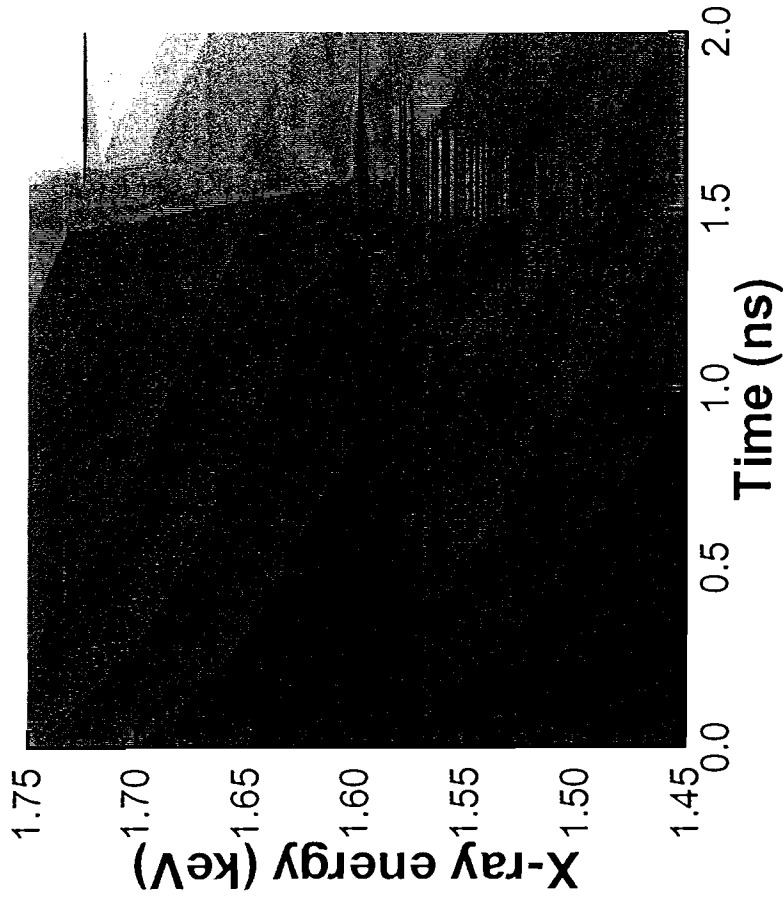


Figure 5a

A simulated space-integrated, time-resolved spectrum of a uniformly irradiated piece of plastic with an aluminum signature layer. Notice the lines of the different species disappear after a short time. They show that the temperature range of aluminum is relatively small.

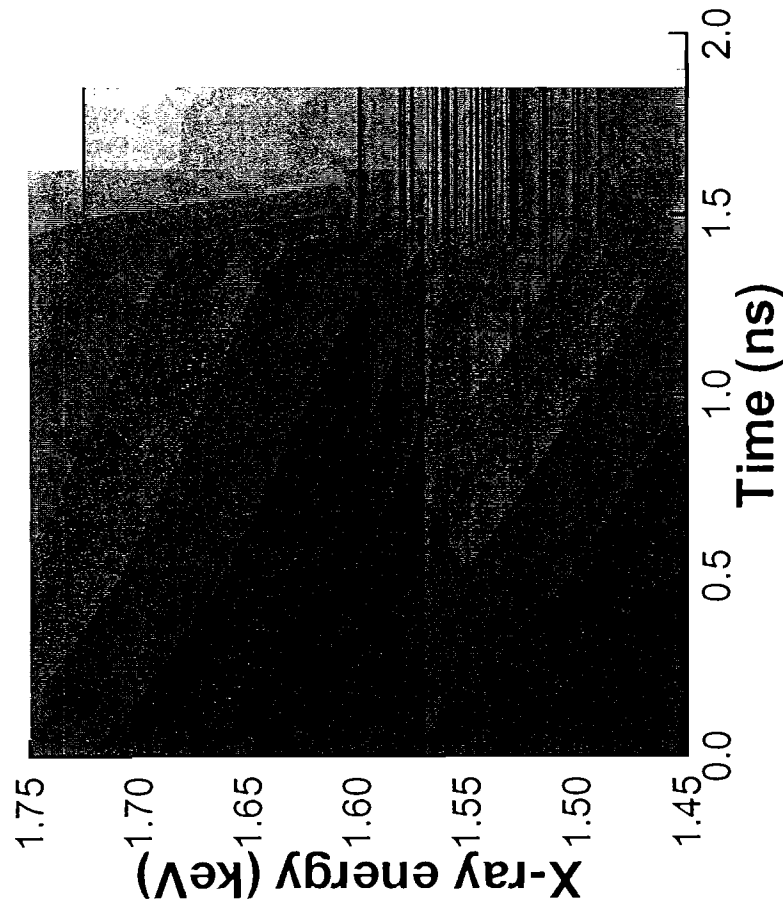
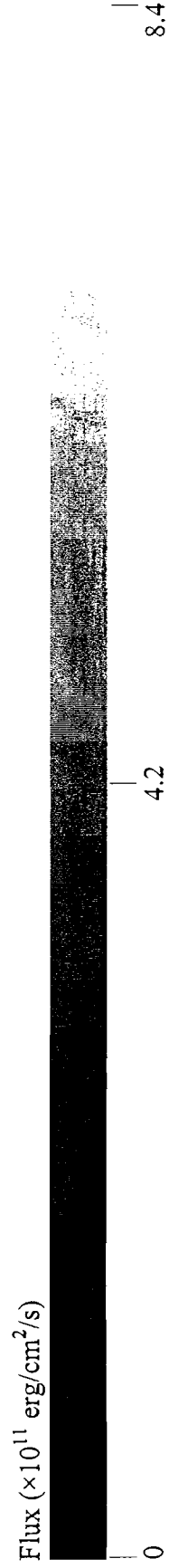


Figure 5b

A similar simulation is run with a non-uniformly irradiated target. Each of the ionization species persists until the end of the simulation to show the aluminum has a wide range of temperature. Also the heat wave arrives earlier due to the perturbation.



4.2

8.4

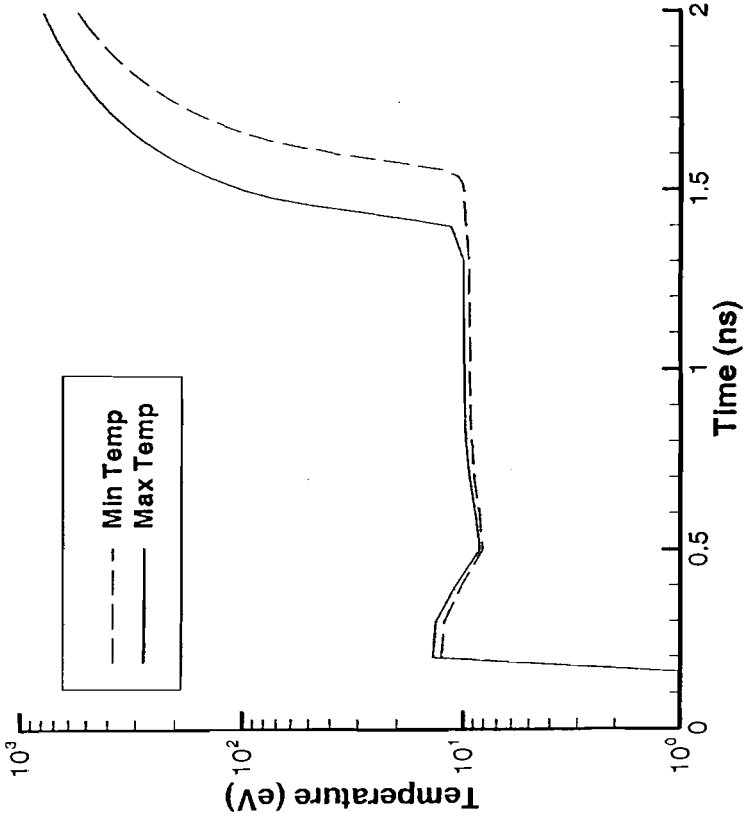


Figure 6a

A temperature profile of the aluminum signature layer. This is the unperturbed simulation, and it shows that the temperature range after the heat front arrival is small.

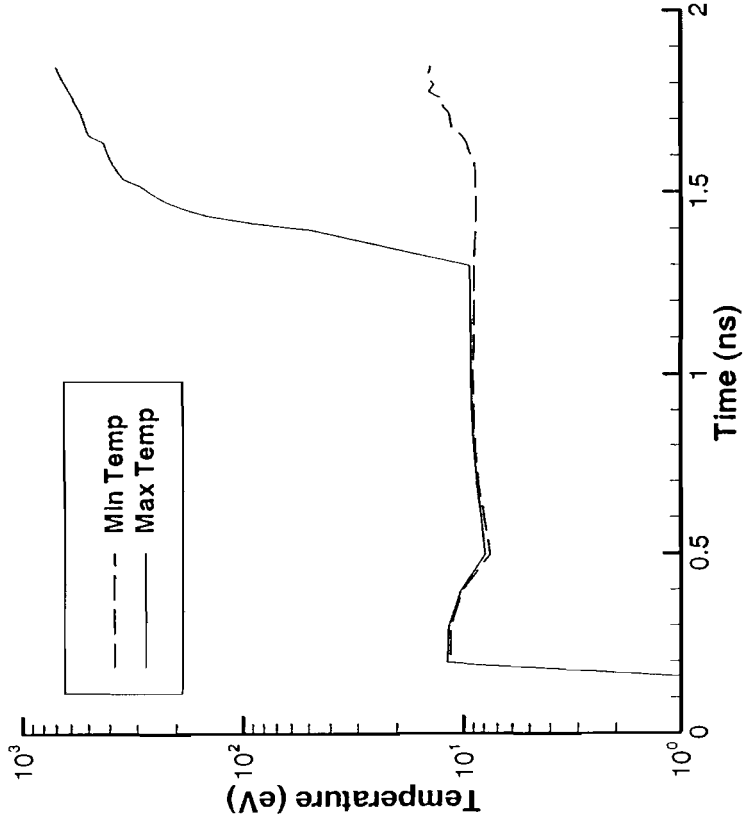


Figure 6b

A temperature profile of the perturbed simulation. Note that the minimum temperature stays relatively constant after the heat front arrives, while the maximum temperature increases.

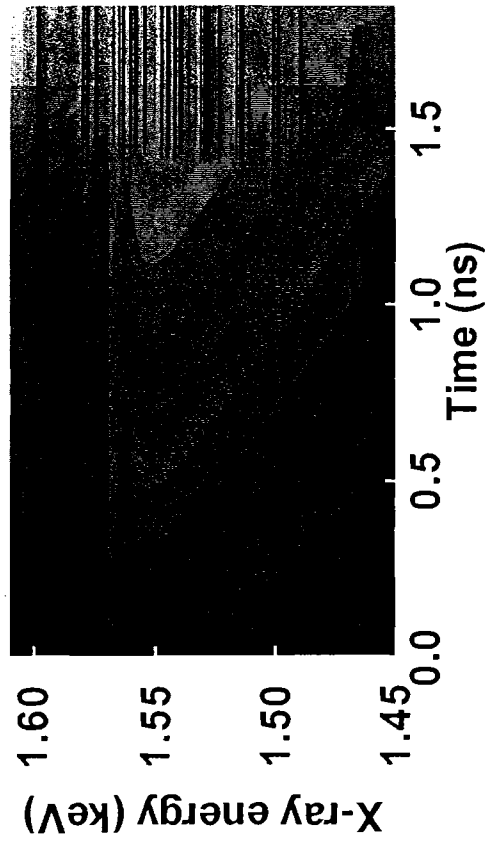


Figure 7a

This is the same as Figure 5b, but the colormap has been changed to match that of the experimental streak camera. The axes have also been changed to facilitate comparison between the images. The K-edges of M-shell species appear with the shock at ~ 200 ps, and the L-shell and K-shell species appear when the heat front arrives at ~ 1.3 ns.

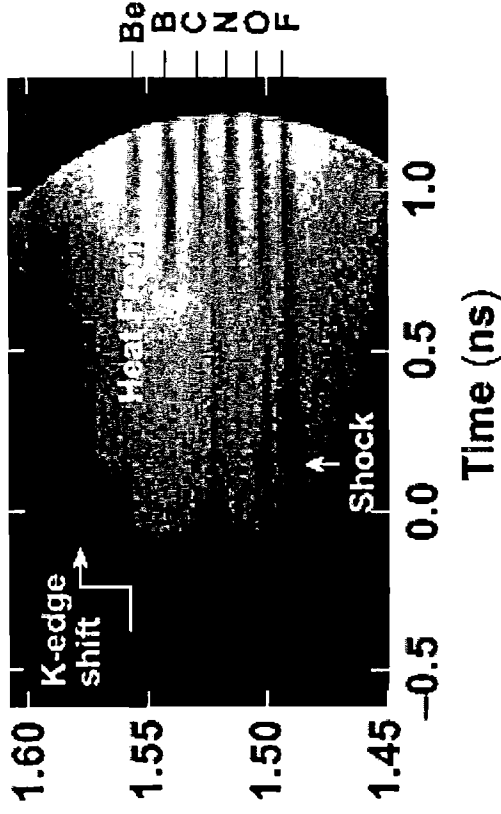
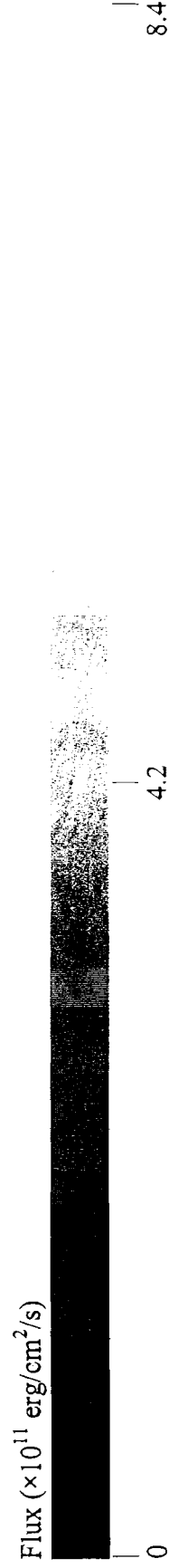


Figure 7b

This is an experimental spectrum of an OMEGA experiment. The shock arrives at ~ 100 ps heating the plasma to F- and O-like, and the heat front arrives at ~ 800 ps showing up to Be-like species.



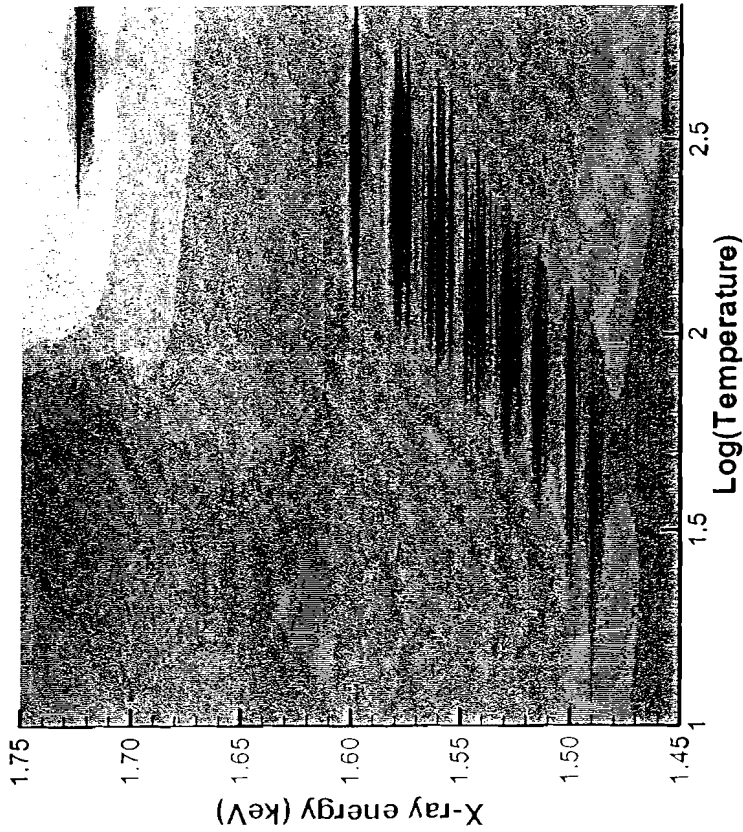


Figure 8a

A temperature mosaic of a simulated absorption spectrum for one times solid density aluminum. The temperature range is from 10 to 700 eV, and it shows the appearance and disappearance of most of the L-shell and K-shell species

Flux ($\times 10^{11}$ erg/cm²/s)

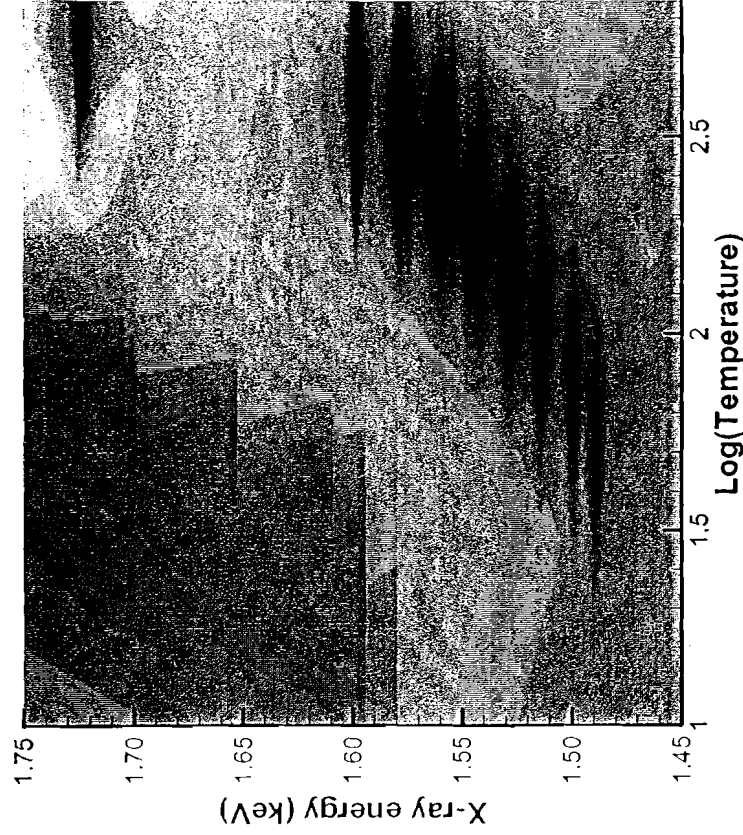


Figure 8b

A temperature mosaic of a simulated absorption spectrum for four times solid density aluminum. The temperature range is 10 to 700 eV. The absorption spectrum is highly saturated since the aluminum is denser.

Durable Phosphate Glasses with Low Glass Transition Temperatures

A. E. Marino
Summer Research Programs for Juniors
Laboratory for Laser Energetics
University of Rochester
250 E. River Rd, Rochester, NY, 14623

1.0 Abstract

Phosphate glasses have special applications, but traditionally never have had both durability and a low glass transition temperature (making them hard to work with). A composition study was used to find a more durable, easily fabricated phosphate glass with a low glass transition temperature. Batching, melting, casting, annealing and fabrication of test parts were performed. Glasses were characterized for hardness, glass transition temperature and chemical durability. An interesting composition with small amounts of borate, tin and alumina was found to have improved durability with a low glass transition temperature. Future work could include further composition improvement and doping with rare earth ions to study their electro-optical effects in the glass.

2.0 Background and Objectives

In the past, phosphate glasses have seldom incorporated durability with a low transition temperature. It would be beneficial to achieve the production of a glass with both of these characteristics because it would allow for molded phosphate optics and could possibly be a durable Nd^{+3} or Tb^{+3} host. Durability in water is the main issue because most optics are left in air where they are open to attack by water vapor. A Chinese group was able to produce a phosphate glass with both of these properties. They published a paper in the American Ceramic Society Bulletin with their findings.¹ The ingredients were given in the paper but the exact compositions were not. The initial goal of the experiment was to reproduce and possibly improve upon their compositions, but because accurate comparison was difficult other standards for comparison were chosen. A phosphate laser glass, LHG-8, was chosen as a standard because it has relatively good durability for a phosphate glass², but it has a high glass transition temperature, T_g . A phosphate glass, which we designate as "443"³, developed for use in an optical fabrication course at the University of Rochester was chosen as another standard. It exhibits relatively poor durability in water, but it has a low T_g . The objective of this experiment was to create a glass with a mixture of the favorable characteristics of LHG-8 and 443 which could later be doped with rare-earth ions to give the glass electro-optical properties.

3.0 Initial Work

An initial composition based on information the Chinese released about their most durable glass was devised in the USA. It assumed any unknown quantities in the composition to be equal. It was melted using the chemical precursors identified in reference 1. The use of three carbonates resulted in excessive bubbling and boiling over of the melt (which could potentially harm the melting furnace). Another trial was completed in which the calcium carbonate and zinc carbonate were replaced with calcium oxide and zinc oxide. Excess bubbling was still observed. However a glass was formed which was then ground, polished and tested for hardness. The fact that a glass (which could be polished and tested) was formed made further experimentation seem feasible.

4.0 Manufacturing

4.1 Melting and Annealing

All components were weighed on a balance that provided measurements accurate to $\pm 0.01\text{g}$. Components were mixed in 100 g batches with a mortar and pestle. Melting then was carried out in large ceramic crucibles.⁴ Glasses were melted at 1000°C for 90 minutes, with hand stirring 40 minutes into the processes. Problems with volatilization arose and an alternate melting schedule was devised. This involved ramping the temperature up to 1000°C over 150 minutes, followed by the 90-minute melting period at 1000°C . Glasses were poured into graphite molds,⁵ which had been pre-heated to 450°C . The annealing schedule in these molds consisted of 30 minutes at 450°C , followed by a 0.5°C per minute ramp down to 300°C , after which the annealing oven was turned off. After approximately 18 hours the blocks of glass were shaken out of the molds, and were ready for finishing.

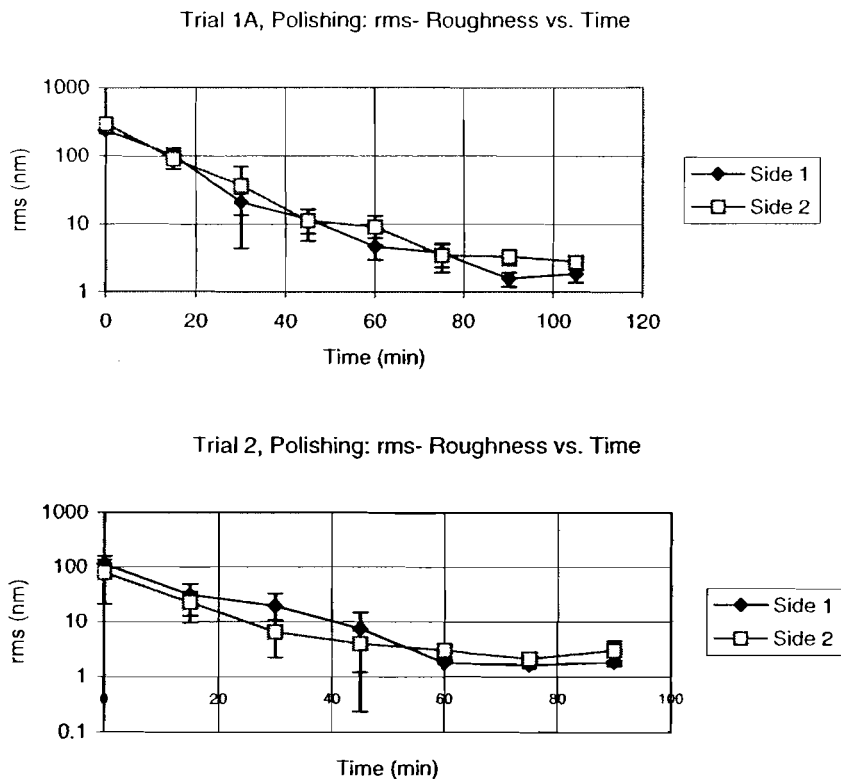
4.2 Finishing

The glass blocks taken from the molds were first ground to size (approximately 26mm x 26mm x 12mm). Grinding was done using 3M Trizact™ Film, color-coded, aluminum oxide pads.⁶ These pads were mounted on flat, cast iron tools and placed on a single spindle grinding machine, rotating counterclockwise. These pads were flooded with tap water using a hand held squirt bottle. Each part was placed on the pad and moved with moderate hand pressure clockwise by hand in an oval shaped path. Grinding was done in three steps based on the three, color-coded pads. The green pads were the coarsest and were used first. Each part was ground with the green pads until all shine and texture was removed, and they were within $\pm 2\text{mm}$ of the desired size. This involved removing between 1mm and 3mm from each side. Bevels were also added to all sides at this stage. The blue pads were used for a medium grind. Each part was ground on them for one to two minutes on each side, and about 30 seconds on each beveled edge. The orange pads were the finest and the last used. Each part was ground on them for two to three minutes

per side, and 30 seconds on each beveled edge. Fine grinding resulted in about a 200 nm rms surface roughness on all ground surfaces.

Following grinding, each part was polished on the two opposing 26mm x 26mm faces using the white 3M Trizact™ Film polishing pads which contained bound cerium oxide. Polishing was done on a single spindle-polishing machine, rotating counter-clockwise at approximately 150 rpm. The hand polishing procedure was the same as the grinding procedure with the exception that a pump was used to keep the pad wet with DI water, which was added at a rate of 50 ml/min. For Trials 1A and 2 (see section 6.0), surface roughness measurements were taken after every 15 minutes of polishing to get an idea of the polishability of these glasses. Measurements were made on a Zygo New View™ 5000® white light interferometer, with a 20x objective.⁷ Five spots were taken randomly distributed over the surface, and the average surface roughness with standard deviation was examined as a function of total elapsed polishing time (Figure 1). It was found that it was possible to polish all glasses to between a 1 and 2 nm rms finish.

Figure 1- Roughness Over Time During Phosphate Polishing



5.0 Characterization

5.1 Hardness

Hardness testing was done on a Tukon® Microhardness tester, with a 100 g load.⁸ Knoop hardness numbers⁹ were taken, but they had a large standard deviation. The indents were difficult to make in some glasses, and the results seemed unreliable compared to the Vickers measurements.¹⁰ Ten hardness measurements were taken with a Vickers indenter over the polished surface to obtain average hardness numbers for all glasses.

5.2 Glass Transition Temperature

Glass transition temperature and softening point were measured using a Perkin Elmer Differential Scanning Calorimeter.¹¹ The instrument was calibrated immediately before use. Samples were prepared by removing shards of glass from parts and crushing them with a small hammer. Between 15 and 20 mg of crushed glass were weighed on an analytical balance and then sealed in shallow aluminum sample pans.¹² The pans were placed in the instrument along with an empty reference pan, where they were heated from 300°C to 500°C (note: LHG-8 had to be heated to 550°C to obtain a complete thermal analysis curve) and scanned for heat flow. Each sample was heated twice. In the first heating, the onset of change in the thermal analysis curve provided the softening point. In the second heating, the onset of change in the thermal analysis curve provided the glass transition temperature.

5.3 Chemical Durability

Because water vapor in the air attacks the polished faces of phosphate glasses, a water durability test was chosen. Two samples of each melt were fine ground on all sides, using the orange bound abrasive pads, resulting in about 200 nm rms surface roughness. Sample size was measured using digital calipers and surface area was calculated. A typical sample was 26mm x 26mm x 12mm. Samples were cleaned using acetone and a drag-wipe method. They were then baked in a vacuum oven for 15 minutes at 50°C to drive off any moisture. Samples were then weighed on an analytical balance, and immediately immersed in 900 ml of 50°C DI water, agitated with a magnetic stir bar. After thirty minutes samples were removed, re-cleaned, re-baked and re-weighed. Most samples were then returned to their original beakers and suspended for an additional 30 minutes, and then re-cleaned, re-baked, and re-weighed. Gloves were used throughout this process to prevent oil/dirt from hands from being transferred to the samples.

Water durability was calculated as weight loss, per unit surface area, per unit time (or $\text{mg}/(\text{cm}^2 \cdot \text{h})$). LHG-8 and 443 were tested under the same conditions for comparison. Trials 1A, 2 and 3 did not undergo these testing procedures because Trial 1C (which was tested) was essentially the same composition (see section 6.0). Trial 7 exhibited serious levels of devitrification and was not tested.

6.0 Composition Study

Table 1 gives the compositions of melts. Trial 1A produced a strongly discolored glass that was very green (rather than clear). Two more trials (Trial 1B and Trial 1C) were batched using the same composition and precursors, with extra care taken to remove any possible source of contamination (e.g. dirty crucibles, stirring rod, mortar and pestle), other than the precursors themselves. Trial 1B was never melted, but Trial 1C was melted, and was also very discolored. The barium oxide precursor was determined to be the source of the discoloration.

Trial 2 kept the same composition (see Table 1), however the source for the barium oxide was changed to barium carbonate. Because the carbonate would result in volatilization, the batch was preheated at 200°C for 4 hours prior to melting. This method was suggested in reference 1. The preheating did not appear to have had much effect, because significant bubbling was observed when the melt was placed in the oven. Trial 2 was clear.

Table 1- Trial Compositions in Mole Percent

Trial	P ₂ O ₅	Na ₂ O	K ₂ O	Li ₂ O	BaO	CaO	ZnO	SnO	Al ₂ O ₃	B ₂ O ₃	Sb ₂ O ₃	Dopant
Precursor	P ₂ O ₅ , Na ₃ PO ₄ , K ₃ PO ₄ , Li ₃ PO ₄ , AlPO ₄	Na ₃ PO ₄	K ₃ PO ₄	Li ₃ PO ₄	BaO for Trial 1, BaCO ₃ for all others	CaCO ₃	ZnCO ₃	SnO	AlPO ₄	H ₃ BO ₃	Sb ₂ O ₃	
1 (a-c)	33.94	7.81	7.81	3.91	13.45	13.45	13.45	none	0.43	1.39	4.38	none
2	33.94	7.81	7.81	3.91	13.45	13.45	13.45	none	0.43	1.39	4.38	none
3	33.93	7.81	7.81	3.91	13.44	13.44	13.44	none	0.43	1.39	4.38	Co ₂ O ₃ 0.02
4	37	8	5	7	8	14	14.5	none	0.5	1.5	4.5	none
5	37	8	5	7	8	14	14	0.5	0.5	1.5	4.5	none
6	35	8	5	7	10	14	14	0.5	0.5	1.5	4.5	none
7	31.58	8.42	5.26	7.37	10.53	14.74	14.74	0.53	0.53	1.58	4.74	none
8	34	8	8	4	11	14	14	1	1	0.5	4.5	none
9	33	8	7	4	13	13	13	1	2	1.5	4.5	none

The next composition, Trial 3, was essentially done to see if ionic colorants (useful as optical filter glasses) would be compatible with this type of composition. The composition was essentially kept the same, with 0.02% Co₂O₃ added (see table 2). This produced a glass with a good, deep-blue color.

It was suggested by one of the authors of reference 1 that tin oxide be added to the composition to improve durability. Trials 4 and 5 were done to investigate that idea. Trials 4 and 5 were similar compositions varying only by the addition of 0.5% SnO in Trial 5 (see table 2). Trial 5 proved to be more durable than Trial 4, so it was decided to include SnO in future compositions. Spectral scans were done using an HP Spectroscopy System¹³ on parts with and without tin oxide, to verify that it was not having any effect on absorbance or transmission in the visible.

Trial 6 was done using a composition similar to Trial 5, except that the phosphorous pentoxide percentage had been lowered by two percent. Trial 7 had the phosphorus pentoxide content lowered an additional 1.5%. This trial did not form a glass, but instead crystallized.

Trials 8 and 9 were done with 34% and 33% phosphorus pentoxide, respectively (see Table 2). This was approximately the amount used in the initial trials. These compositions were melted to evaluate adjustments in the borate and alumina percentages. Both borate and alumina are known to strengthen the network in glasses, but it was not known what their effect would be on glass transition temperature.

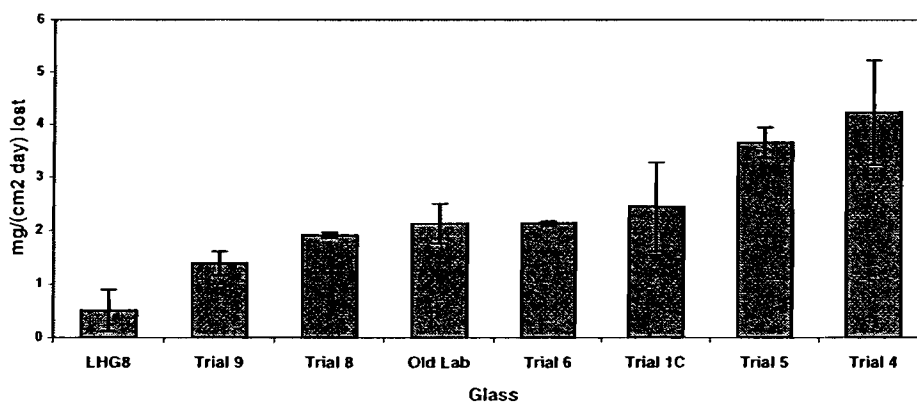
7.0 Summary of Results and Discussion

Results are summarized in Table 2 and Figure 2. The results are rank order in terms of decreasing durability.

Table 2 Summary of Characterization Results

Glass	Vickers Hardness Kgf/mm ²	Glass Transition °C \pm 1%	Durability: Weight Loss mg/(cm ² day)
LHG8	470 \pm 33	498	0.5 \pm 0.39
Trial 9	410 \pm 8	401	1.4 \pm 0.21
Trial 8	420 \pm 5	374	1.9 \pm 0.05
443	325 \pm 5	432	2.1 \pm 0.37
Trial 6	390 \pm 6	380	2.1 \pm 0.04
Trial 1C	375 \pm 4	393	2.4 \pm 0.83
Trial 5	395 \pm 14	371	3.7 \pm 0.29
Trial 4	395 \pm 12	370	4.2 \pm 1.00

Figure 2 Durability Defined By Weight Loss



Of all of the trials, Trial 9 was determined to be the best (see table 2). It had a chemical durability that while not near that of LHG-8, was much better than 443 (see figure 2). It

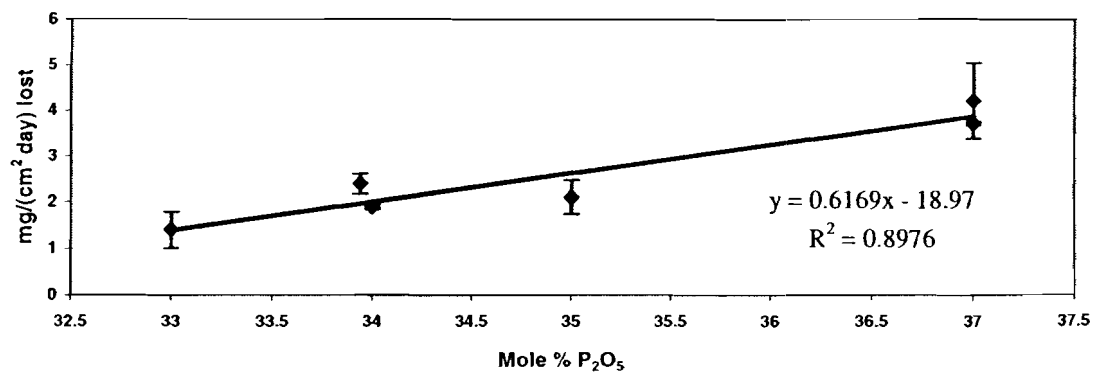
was reasonably hard, especially in comparison to 443. It also had a very desirable glass transition temperature, which was even lower than that of 443. This means that more composition adjustments could be made to increase the durability while keeping the glass transition temperature around 432°C (the T_g of 443). The key to reaching this composition involved increasing the amount of alumina in the composition, adding tin oxide, and decreasing the amount of P_2O_5 as far as possible, without causing devitrification.

Alumina is known to improve durability, but it is also known to raise the glass transition temperature. Because of this it was present in very low percentages in earlier trials. However these trials had glass transition temperatures well below 432°C , and had poor durability. The composition was adjusted and it was found that it could include up to two percent alumina, with the glass transition temperature remaining low. This increase resulted in increased durability.

The effect of tin oxide was determined through Trial 4 and Trial 5. These compositions differed only in the addition of tin oxide to Trial 5. As can be seen in Figure 2 SnO increased durability. It also did not appear to affect glass transition temperature (see Table 2). As a result it was included in all new trials. Because of its ability to increase durability without increasing glass transition temperature, SnO would be a good constituent for study in future work with this type of glass.

As can be seen in Figure 3, phosphorous pentoxide content shows a strong correlation to weight loss in water. This makes sense because phosphorous pentoxide decomposes in water. However because it is the glass former, it is required in large quantities in the glass. Finding the lowest possible concentration was key. Trial 9, which had 33 percent phosphorous pentoxide, formed a glass and was the most durable. Trial 7, which had approximately 31.5 percent phosphorous pentoxide, had an unknown durability. This is because it crystallized and therefore was not tested. Optimum phosphorous pentoxide percentage for this glass appears to be approximately 33 percent.

Figure 3 Phosphorous Pentoxide vs. Durability



8.0 Conclusion

It is possible to make a relatively durable phosphate glass that also has a low transition temperature. To do so the glass former (phosphorous pentoxide) percentage must remain as low as possible. Alumina must be added in amounts greater than one mole percent and the correct balance between alumina and borate must be achieved. Lithium should be included, but its concentration should remain low. Tin is a possible additive that increases chemical durability, while creating no observable change in glass transition temperature.

Other observations and conclusions include the fact that care must be taken during the melting procedure to deal with volatilization; one possible means of doing so is ramping up from room temperature. Preheating below the melting point did not seem effective. For small parts the short annealing schedule used is acceptable. The use of 3M bound-abrasive Trizact pads allows this glass to be easily polished to the 1 to 2 nm rms roughness level. With our durability test on ground parts in water, error bars can be large for any given glass; this is not necessarily the best test procedure. Future work could include improvement of testing procedures. It could also include more modification of composition for improved qualities. Work could be done to dope this glass with colorants and rare earth ions, to study their effects in this glass.

9.0 Acknowledgments

The author acknowledge the following University of Rochester colleagues for their contributions: Stephen Jacobs, advisor; Steven Arrasmith, compositions, formulation and melting; Leslie Gregg, hardness, durability, roughness; Jessica DeGroot, glass finishing and initial melting trials; Kenneth Marshall, DSC, spectroscopy; Alexander Maltsev, grinding; and Mikhail Kaplun, sample preparation.

Financial support was provided by the LLE Summer Research Program for High School Juniors and by the Center for Optics Manufacturing.

10.0 References

- 1) "Improved Properties for Precision Molding Phosphate Glasses," Guorong Chen, Wen Liang and Jijian Cheng, Am. Ceram. Soc. Bul., p. 44 (March 2000)
- 2) LHG-8 is a Nd^{+3} doped phosphate laser glass manufactured by Hoya Corporation, 3400 Edison Way, Fremont, CA 94538
- 3) Colored Glass Melting Laboratory by Prof. Kathleen Richardson, developed for Optics 443: Optical Fabrication and Testing, a graduate course taught in The Institute of Optics at the University of Rochester
- 4) Wide Form Crucible, 250 ml, CoorsTek, Inc., VWR, 3000 Hadley Rd., So. Plainfield, NJ 07080

- 5) Graphite molds, approximately 5cm x 5cm x 4.5cm, producing glass cubes approximately 3cm x 3cm x 3.5cm
- 6) 3M™ Trizact™ Film. 3M Abrasive Systems Division; St. Paul, MN 55144-1000
- 7) Zygo New View™ 5000 White Light Optical Profiler, areal over 0.26 mm x 0.35 mm with a 20x Mirau objective, Zygo Corp., Middlefield CT.
- 8) Tukon® Microhardness Tester, Wilson Instruments, Binghamton, NY 13905
- 9) Knoop indenter certified by Wilson® Standards Laboratory, Wilson Instruments, Binghamton, NY 13905
- 10) Vickers Indenter certified by Wilson® Standards Laboratory, Wilson Instruments, Binghamton, NY 13905
- 11) Perkin-Elmer Differential Scanning Calorimeter 7, Perkin-Elmer Analytical Instruments, 761 Main Ave., Norwalk, CT 06859.
- 12) Perkin-Elmer sample pan kit no. 0219-0041, VWR, 3000 Hadley Rd., So. Plainfield, NJ 07080
- 13) Hewlett Packard 8453E Spectroscopy System, Hewlett-Packard, 3000 Hanover Street, Palo Alto, CA 94304-1185

Adapting ASBO/VISAR for Foam Targets

Elizabeth McDonald

Advisor: Jon Zuegel

LABORATORY FOR LASER ENERGETICS

University of Rochester

Summer High School Research Program

2000

Abstract:

The scattering properties of foams were analyzed to investigate whether the Velocity Interferometer System for Any Reflector (VISAR) could be used with foam targets, or whether the scattering of the probe beam would reduce fringe contrast to an unusable level. A mock-up of the VISAR system was constructed using a HeNe laser as the light source. CH foam samples were tested, and it was determined that good fringe contrast can be achieved by adding a pinhole to the system to reduce the collection of scattered light. This pinhole, however, can lead to additional difficulties.

Drive uniformity is very important to Internal Confinement Fusion (ICF) experiments. Nonuniform irradiation of the target leads to hotspots and deformation of the target, therefore decreasing the efficiency of the target implosion. It has been proposed that a thin ($\sim 100 \mu\text{m}$) coating of foam over the target might increase the thermal uniformity on the target. The theory is that lower-density foams will turn into plasma faster than the traditional CH plastic shells and conduct the heat rapidly and evenly over the entire target.

Three foam types have been considered: CH foam, silica foam (aerogel), and carbonized silica foam (carbon resorcinol foam, CRF). These materials, however, have not yet been well characterized. Equation-of-state (EOS) measurements are crucial to better understand their properties. ASBO/VISAR (Active Shock Break Out / Velocity Interferometer System for Any Reflector) is an optical diagnostic used for EOS experiments, and there is interest in performing ASBO/VISAR experiments with foam targets. The largest potential problem with measuring the EOS of foam is that foams strongly scatter light and scattering reduces VISAR fringe contrast, which is essential for accurate velocity measurements. The goal of this project is to determine the feasibility of adapting ASBO/VISAR for use with foam EOS experiments.

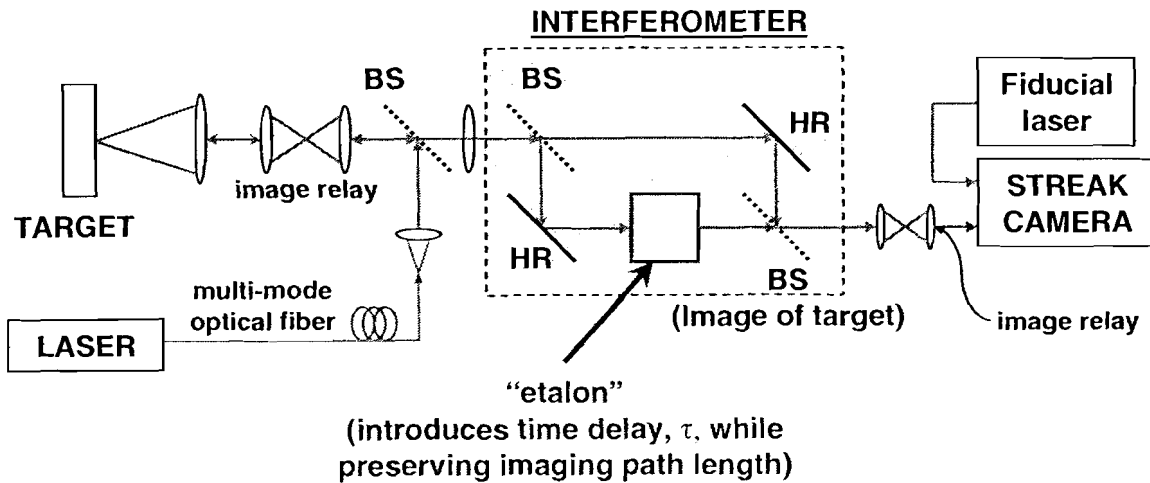


Fig. 1 - ASBO/VISAR with Mach-Zender interferometer as set up in OMEGA target bay. The beam splitters (BS) are coated with 50% reflectivity coatings on one side and antireflection coatings on the other. The etalon is antireflection coated on both sides.

ASBO/ is an Equation of State (EOS) diagnostic used in OMEGA to measure the velocity of a shock front propagating through a transparent target. (Fig. 1) VISAR employs a temporal shearing interferometer with a pulsed 532 nm laser beam. The beam illuminates the target and is reflected off of the propagating shock front, then enters a Mach-Zender interferometer with an etalon that introduces a time delay placed in one of its arms. The moving shock front induces a Doppler shift of the light based on the velocity of the shock front, so the interference pattern, which is collected by the streak camera, describes the change in velocity of the shock front through the material over time.

A typical planar target for measuring the EOS of a sample with VISAR is illustrated in Figure 2. The material to be tested is mounted on a stepped reflective “pusher,” which is usually made of aluminum. The back of the pusher is illuminated with several high-energy UV OMEGA beams. The force of these pulses generates a shock wave in the aluminum that is then launched into the target material under study. The shock front ionizes the target material, thus creating a reflective surface travelling through the target. The VISAR beam reflects off of this surface and undergoes a Doppler shift back towards the interferometer.

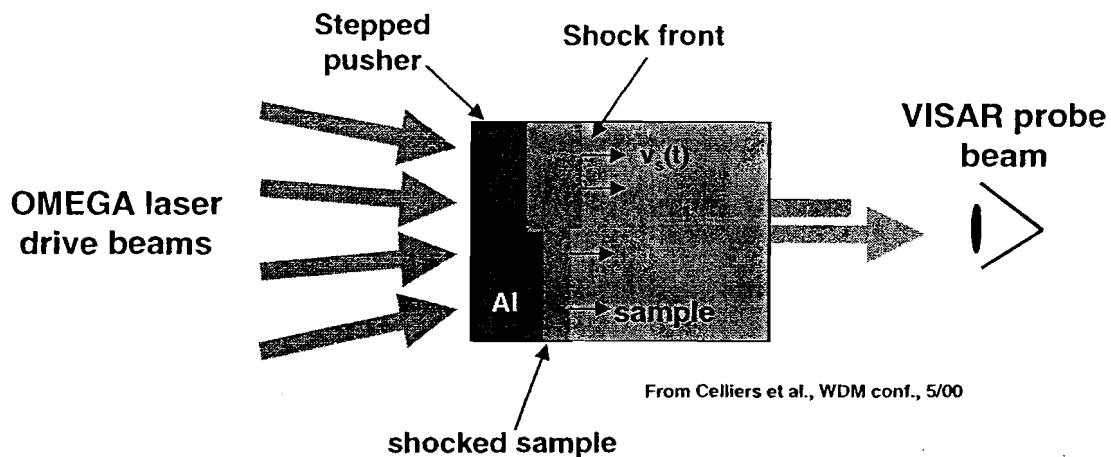


Fig. 2 - Planar VISAR target. OMEGA beams illuminate the aluminum, generating a shock wave. When the shock wave “breaks out” of the Al into the sample, the wave front ionizes and turns into plasma. This creates a moving reflective surface off of which the VISAR beam reflects, experiencing a Doppler shift.

A VISAR mockup was built to evaluate its performance with foam samples. The mockup differed from the VISAR installation in OMEGA in several ways. First, the mockup used a red helium-neon (HeNe) laser ($\lambda = 632.8 \text{ nm}$) instead of the green frequency-doubled Nd:YAG ($\lambda = 532 \text{ nm}$) used in the OMEGA system. Additionally, the HeNe laser in the mockup is spatially coherent, whereas the 531-nm beam is delivered by

a multi-mode optical fiber. Neither leg of the interferometer contained an etalon, as there was no change in wavefront characteristics over time. Lastly, a foam sample was placed in front of a 100 % reflectivity mirror, used to retro-reflect the VISAR probe beam.

Despite some potential difficulties, it was shown from the VISAR mockup that good fringe contrast can be achieved with the addition of a pinhole, as shown in Figure 3.

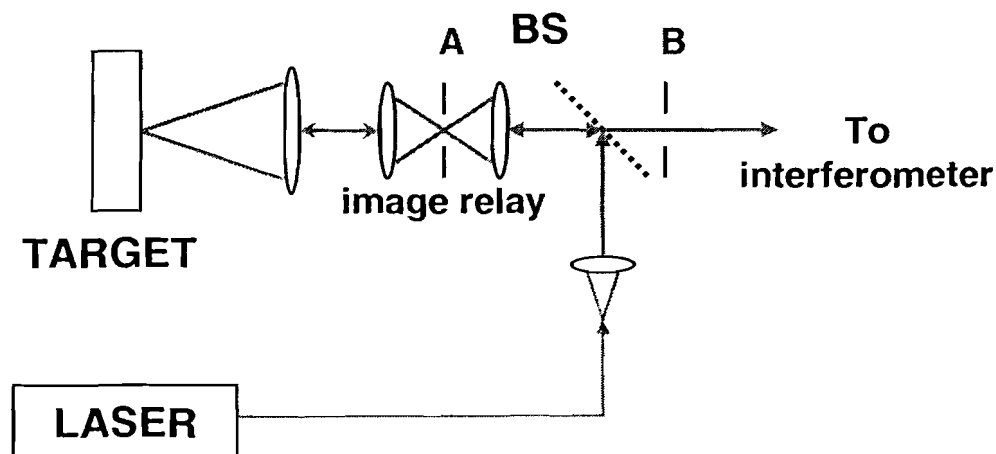


Fig. 3 - Pinhole placement: (A) represents the placement of the pinhole at the focal point of the image relay in the mock-up. (B) represents a possible pinhole location in on-line ASBO/VISAR. Placing the pinhole after the beam splitter means the beam only passes through the hole once, minimizing reduction of signal.

Figure 4 shows the fringes obtained from the VISAR mockup. The fringes in Figure 4(a) were collected with no foam sample interrupting the beam. The speckle pattern present in Figure 4(b) occurred when a nominally 50 mg/cc, 50 μm thick sample of CH foam was inserted directly before the mirror, where the beam is collimated, but with no pinhole. The speckle occurred due to the random nature of the light emerging

from the foam sample and entering the interferometer, which obliterated the fringe pattern. Figure 4(c) shows the fringes obtained with the same sample, but with a 0.405 mm pinhole added at the focal point of the beam relay (point A shown in figure 3). To obtain the same signal strength, the filters on the camera were adjusted to allow approximately 33 times more light through.

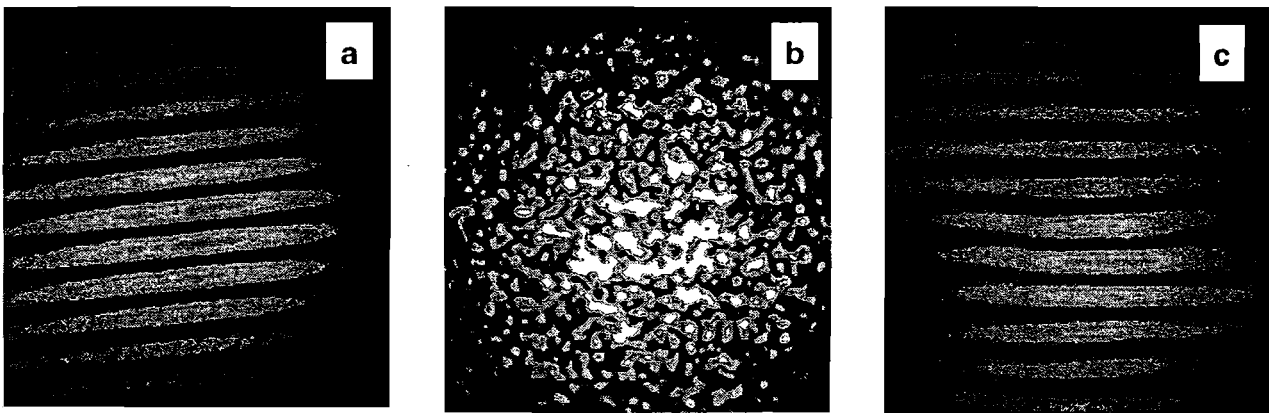


Fig. 4 - Fringes produced by interferometer in LDL mock-up. (a) No foam sample in beam. (b) 50 mg/cc, 50 μm thick (nominal) CH foam sample, no pinhole. (c) 50 mg/cc, 50 μm thick (nominal) CH foam sample, with 405 μm pinhole, 33x amount of light needed for same output intensity.

Introducing a pinhole reduces scattered light collected by the VISAR system and allows only directly reflected light to be collected, but this scheme introduces several other problems. The first of these is increased alignment sensitivity. The beam and target must be aligned much more precisely than without the pinhole so it does not miss the pinhole altogether which could be operationally impractical in OMEGA. Another problem is reduced signal. The scattering in the foam reduces the amount of light that actually enters the interferometer. Thus, if only unscattered light is collected, the signal is much weaker. It was found in these experiments that when a nominally 50 μm thick, 50

mg/cc CH foam sample was inserted in the beam, the filters on the camera needed to be adjusted to allow 33x more light into the camera. The signal in the OMEGA ASBO/VISAR installation may or may not be able to afford such a reduction.

A second problem caused by a pinhole is reduced spatial resolution. The size of the smallest resolvable target feature depends upon the wavelength of the light, the diameter of the pinhole, and the focal length of the beam relay by the equation

$$x_{obj} \geq \left(\frac{x_{freq}}{\lambda \cdot f} \right)^{-1} = \left(\frac{D_{pinhole}/2}{\lambda \cdot f} \right)^{-1} = 317 \mu m$$

Using the measurements from the mock-up ($\lambda = 0.633 \text{ nm}$, $f = 100 \text{ mm}$, and $D_{pinhole} = 400 \mu m$), the smallest resolvable feature is calculated to be about $317 \mu m$. For a target with a diameter of about 1 mm , only three resolution units of this size fit across the target. The stepped nature of the target causes a step in the shock front, as shown in Figure 5. With reduced spatial resolution, details such as this step would be lost and only an average velocity value can be obtained. Since edge effects will affect two of those, only one measurement will be useful. It may be noted that the shorter-wavelength green light used in the OMEGA ASBO/VISAR system will result in a slightly smaller resolution unit; the shorter wavelength, however, it will also suffer more scattering in the foam.

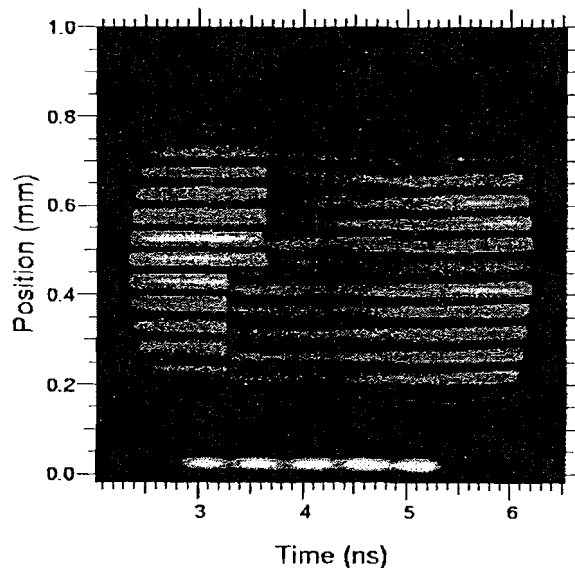


Fig. 5 - ASBO/VISAR streak camera image. Note the step. From Celliers et al, Warm Dense Matter conference (May 2000).

Spectrophotometer scans of an aerogel sample (a silica foam, also under consideration) were done to determine the relationship between the wavelength of light passing through the sample and the amount of scattering that occurred. Figure 6 shows the results of one scan, with wavelength plotted on the x-axis and absorbance on the y-axis. Since the aerogel is translucent, any loss of signal through the sample can be attributed to scattering, rather than actual absorbance. The results of these measurements showed that scattering of light increases exponentially with shortening of wavelength.

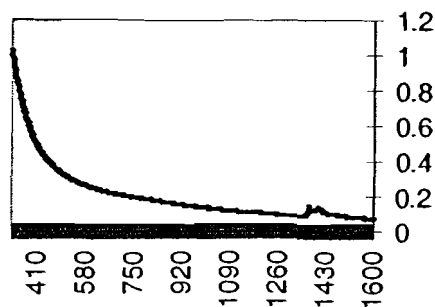


Fig 6 – Spectrophotometer scan of aerogel sample. X-axis shows wavelength, Y-axis shows the amount of scattering that occurred in the sample.

In conclusion, good fringe contrast can be achieved in foam ASBO/VISAR experiments, but trade-offs must be made. Further investigation is planned to continue to research the problem, including investigation of other types of foam and computer modeling.

Many thanks to Dr. Stephen Craxton for admitting me to the program and assigning me to this project. I would also like to thank Devon Battaglia for helping me out, particularly in the beginning. Thanks to Doug Smith for the loan of his fiber-optic spectrophotometer and to Matt Pandina for assisting me with my presentation. Finally, I would like to thank Jon Zuegel for being the best advisor I could have asked for. Thank you for a great experience and many memories.

References:

L. M. Barker and R.E. Hollenbach, "Laser interferometer for measuring high velocities of any reflecting surface," *Journal of Applied Physics*, Vol. 43, No. 11, 1972.

J. R. Asay and L. M. Barker, "Interferometric measurement of shock-induced internal particle velocity and spatial variations of particle velocity," *Journal of Applied Physics*, Vol. 45, No. 6, 1974.

L. M. Barker and K. W. Schuler, "Correction to the velocity-per-fringe relationship for the VISAR interferometer," *Journal of Applied Physics*, Vol. 45, No. 8, 1974.

William F. Hemsing, "Velocity sensing interferometer (VISAR) modification," *Review of Scientific Instruments*, Vol. 50, No. 1, 1979.

Scott Oppenheimer, "Ultraviolet Scattering Properties of Diffusing Material of OMEGA Target," *UR/LLE Student Research Reports*, 1996.

E. Moshe, E. Dekel, Z. Henis, and S. Eliezer, "Development of an optically recording velocity interferometer system for laser induced shock waves measurements," *Applied Physics Letters*, Vol. 69, No. 10, 1996.

P. M. Celliers, G. W. Collins, L. B. Da Silva, D. M. Gold, and R. Cauble, "Accurate measurement of laser-driven shock trajectories with velocity interferometry," *Applied Physics Letters*, Vol. 73, No. 10, 1998.

M. Koenig, A. Benuzzi, F. Philippe, D. Batani, T. Hall, N. Grandjouan, and W. Nazarov, "Equation of state data experiments for plastic foams using smoothed laser beams," *Physics of Plasmas*, Vol. 6, No. 8, 1999.

M. Koenig, A. Benuzzi-Mounaix, F. Philippe, B. Faral, D. Batani, T. Hall, N. Grandjouan, W. Nazarov, J. Cheize, and R. Teyssier, "Laser driven shock wave acceleration experiments using plastic foams," *Applied Physics Letters*, Vol. 75, No. 19, 1999.

Devon Battaglia, "Adapting ASBO/VISAR for Foam Targets," Summer Research Review 2000 (draft).

Frequency Conversion of Phase-Aberrated Laser Beams for the National Ignition Facility

Ronen Mukamel
Brighton High School
Rochester, NY

Advisor: R. S. Craxton
Senior Scientist
Laboratory for Laser Energetics
University of Rochester

Frequency Conversion of Phase-Aberrated Laser Beams for the National Ignition Facility

Summary

I simulated laser beams at the National Ignition Facility passing through frequency conversion crystals, which convert beams from the infrared to the ultraviolet, and phase plates, which distribute the laser's energy uniformly. I calculated the frequency conversion efficiency for designs where the phase plate precedes the crystals, previously thought to be impractical, and found these designs to be efficient and feasible. This is useful because these designs minimize damage to the optics.

Abstract

The effect of the placement of a direct drive phase plate on the frequency conversion efficiency of a National Ignition Facility (NIF) beam was studied. The frequency conversion efficiency was calculated for two possible positions for a direct drive phase plate, before and after the frequency conversion crystals. The phase aberrations arising from the phase plate resulted in only a small decrease in frequency conversion efficiency at a nominal operating point of 3 GW/cm^2 for three representative smoothing by spectral dispersion scenarios, implying that putting the phase plate before the frequency conversion crystals is a feasible option.

1 Introduction

Inertial confinement fusion (ICF) has the potential to solve the world's energy crisis. In fusion, the nuclei of two reactant atoms are joined forming a product nucleus that has less mass than the combined mass of the reactants. The lost mass is converted into energy which can be used to generate electricity. ICF is a scheme for achieving fusion by applying high temperatures and pressures to small, containable fuel pellets.

The National Ignition Facility (NIF) is currently under construction at Lawrence Livermore National Laboratories and upon completion will be the largest laser system in the world (the NIF will consist of 192 high-energy beams producing a total of 1.8 MJ). Studies of ICF will be conducted at the NIF by bombarding small plastic capsules, a few millimeters in diameter, which contain deuterium and tritium (two isotopes of hydrogen, one of the most abundant elements on Earth) with high-energy laser beams through a scheme called indirect

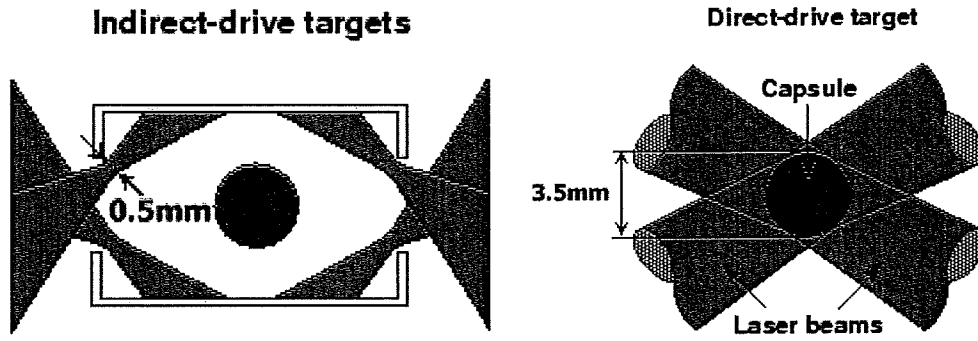


Figure 1: **Indirect and Direct Drive.** Left: Indirect drive involves passing the laser energy into a metallic vessel which absorbs the energy and re-emits it as X-rays which are absorbed by the target. Right: Direct drive is a scheme to achieve ICF by hitting targets with laser energy directly.

drive. Indirect drive involves passing the laser beams into a metallic vessel surrounding the capsule. The walls of the vessel absorb the laser energy and emit X-rays which are absorbed by the capsule.

The Omega laser system, at the University of Rochester's Laboratory for Laser Energetics (LLE), is currently the largest laser system in operation conducting ICF experiments (Omega is a 60-beam system which produces 30 kJ of energy). At Omega, fuels are bombarded through a scheme called direct drive. Each of Omega's laser beams is absorbed by the capsule directly. The two schemes for ICF are depicted in Figure 1. While the NIF is primarily designed for indirect drive experiments, it will be useful to conduct direct drive experiments on the larger system. In direct drive, the laser energy is focused onto the whole target (focal size is 3.5 mm, Figure 1 Right) whereas in indirect drive, the laser energy is focused to fit through a small hole in the metallic vessel (focal size is 0.5 mm, Figure 1 Left). The focus size in direct drive is therefore larger than that in indirect drive. At both systems, the energy absorbed by the capsule causes the outer layer of plastic to ionize, making it a

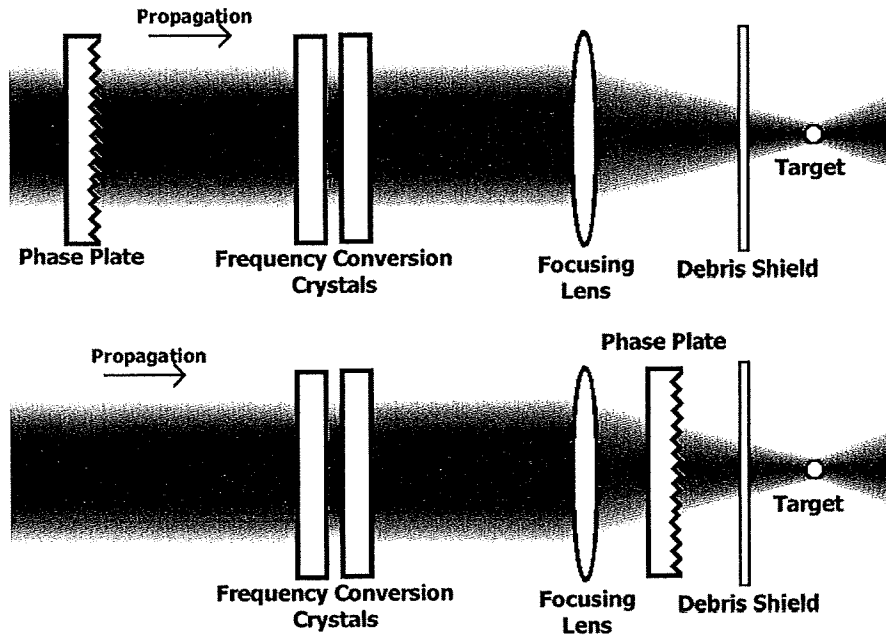


Figure 2: **NIF Final Optics.** Each of NIF’s 192 infrared beams is passed through a system of final optics consisting of frequency conversion crystals, a focusing lens, a phase plate and a debris shield. The figure shows two possible placements for the direct drive phase plate.

gas known as plasma. The layer of plasma expands explosively, compressing the rest of the capsule and the fuel, causing the deuterium and tritium to fuse.

At both the NIF and Omega, neodymium:glass beams (beams generated with neodymium-doped glass) with an infrared wavelength of $1.054 \mu\text{m}$ are frequency converted to ultraviolet beams because infrared beams are not absorbed well. Infrared beams cannot penetrate the layer of plasma surrounding the capsule. Consequently, energy of infrared beams is absorbed by the electrons of the plasma cloud rather than the capsule. These electrons oscillate with the electric field associated with the beams and gain enough kinetic energy to penetrate the plastic capsule and deposit energy in the fuel. The fuel is heated prematurely making it impossible to compress it sufficiently. Higher-frequency ultraviolet beams can penetrate farther into the atmosphere of plasma and are better absorbed [1].

The schematic in Figure 2 (Top) depicts the final optics through which each of the NIF's 192 beams is passed. The beam passes through two frequency conversion crystals which convert the beam's energy from infrared to ultraviolet. The focusing lens focuses the beam's energy on the target. The phase plate is like a piece of frosted glass; the thickness of the phase plate varies from point to point. The phase plate spreads the beam by diffraction, making it phase-aberrated. Beams that are not phase-aberrated are spatially coherent. For indirect drive experiments, this spreading decreases the intensity of the beam which at its focal point (Figure 1 Left) would otherwise overheat the gas in the vessel creating high-energy electrons. These electrons would prematurely heat the fuel in the same manner as the high-energy electrons in the plasma generated by infrared beams heat the fuel. For direct drive experiments, the phase plate serves a different purpose. By spreading energy from each portion of the lens over the whole target, the phase plate eliminates non-uniformities in target irradiation which would lead to uncontrollable implosions (Figure 1 Right). Notice that a phase plate for direct drive experiments would spread the beam with larger angles than a phase plate for indirect drive because the direct drive phase plate must focus the beam onto the whole target whereas the indirect drive phase plate focuses the beam to fit through a small hole in a metallic vessel. Finally, the debris shield prevents debris from the reaction from damaging the final optics.

The arrangement of the final optics for indirect drive experiments at the NIF has the phase plate preceding the frequency conversion crystals (Figure 2 Top). It has already been determined that the small angle deflections created by the indirect drive phase plate will not have a significant impact on frequency conversion efficiency. However, the larger

angle deflections created by the direct drive phase plate could have a significant impact on conversion efficiency if placed before the crystals and it has been believed to date that placing it after the frequency conversion crystals is preferable (Figure 2 Bottom). Placing the phase plate in the ultraviolet portion of the system, however, will limit the intensity allowed through the system because optics in the ultraviolet portion of the system cause self-focusing which can be harmful to the optics (this effect is less significant in the infrared portions of the system).

This investigation analyzes the effect of placing the direct drive phase plate in front of the frequency conversion crystals. Frequency conversion efficiency was calculated for a spatially coherent beam and a beam with phase aberrations due to a phase plate to determine the loss of frequency conversion efficiency in the second final optics design Figure 2 (Bottom). In Section 2, techniques for calculating frequency conversion are discussed. In Section 3, the way the calculation techniques were implemented is described. The results described in Section 4 show that the phase plate for direct drive can be placed before the frequency conversion crystals without suffering a large decrease in conversion efficiency.

2 Simulations of Frequency Conversion

Frequency conversion at the NIF is achieved by passing each of the laser beams through two potassium-dihydrogen phosphate (KDP) crystals (see Figure 3). The doubler crystal converts fundamental Nd:glass infrared beams polarized along the *o*-axis with wavelength $\lambda = 1.054 \mu\text{m}$ to second-harmonic green energy polarized along the *e*-axis. The tripler combines the green energy and residual infrared energy to form third-harmonic ultraviolet

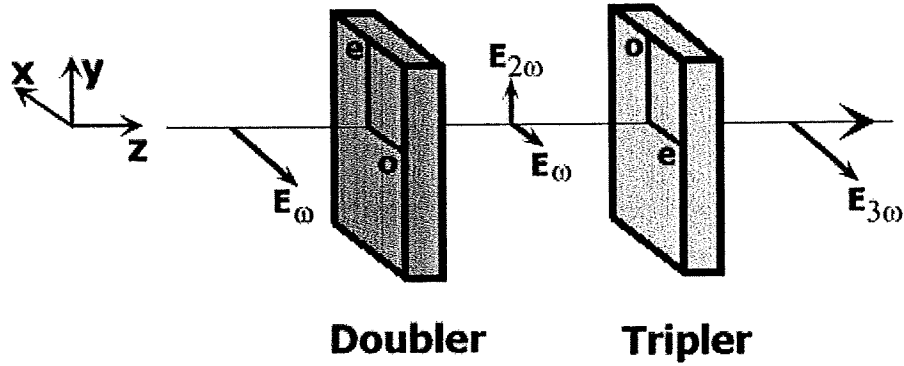


Figure 3: **KDP Crystals**. Each of the NIF's 192 beams is passed through two KDP crystals which convert infrared energy to ultraviolet energy.

energy polarized along the e -axis [2].

In general, an electric field \mathcal{E} associated with a beam of light propagating in the z direction can be represented by the real part of a complex function of time and space:

$$\mathcal{E}(x, y, z, t) = \text{Re}\{E(x, y, z, t)e^{i\omega t - ikz}\} \quad (1)$$

Here, E is a complex function of time and space which represents the slowly varying field envelope, ω is the field's frequency, x and y are coordinates perpendicular to the beam direction and the wave-number $k = \omega n/c$ where n is the refractive index and c is the speed of light in a vacuum. The intensity I is proportional to the square of the complex magnitude of E .

When light propagates through a crystal, it induces electronic motion: the associated electric field causes the electrons in the medium to oscillate thereby generating a field of their own which propagates similarly through the crystal. At low field intensities, an electron's oscillation amplitude is linearly proportional to the initial electric field and the electron's

field has the same frequency as the initial electric field. This is known as linear optics. However, two high-intensity fields with frequencies ω and ω' can give rise to oscillating electrons and associated electric fields oscillating at the sum of their frequencies $\omega + \omega'$. This phenomenon is known as sum-frequency generation [3] and is non-linear optics because the resulting field is non-linearly proportional to the initial field. In particular, sum-frequency generation can occur with one intense field whereby $\omega = \omega'$ and $\omega + \omega' = 2\omega$. This is known as second-harmonic generation.

Sum-frequency generation is significant when the generated field propagates at the same speed as the initial field and the electrons in both fields oscillate in phase throughout the sample. This is called phase matching. KDP crystalline structure causes light polarized along the ordinary o -axis to travel with an index of refraction that is independent of the direction of propagation. Light polarized along the extraordinary e -axis travels with an index of refraction that depends upon the direction of propagation. The frequency doubler in Figure 3 is cut at an angle where the speeds of the fundamental and second-harmonic fields are equal.

The growth of the second-harmonic field $E_{2\omega}$ from the initial first-harmonic electric field E_ω as it propagates along an axis z can be described by simultaneous differential equations:

$$\frac{\partial E_\omega}{\partial z} = -i\chi_1 E_{2\omega} E_\omega^* e^{-i\Delta K z} \quad (2a)$$

$$\frac{\partial E_{2\omega}}{\partial z} = -i\chi_2 E_\omega E_\omega e^{i\Delta K z} \quad (2b)$$

Here, E_ω and $E_{2\omega}$ are the slowly varying field envelopes which appear as E in Eq. 1, χ_i are constants (susceptibilities) which describe the tendency of electrons to oscillate with

frequencies ω and 2ω and are determined by properties of the crystal and the way they were cut, and ΔK is the phase matching coefficient which is a function of wavelength and direction of propagation. Eq. 2a describes the first-harmonic field's loss of energy and Eq. 2b describes the generation of the second-harmonic field in accordance with the law of conservation of energy.

Similarly, the tripler crystal in Figure 3 is cut at the angle such that the field emerging from the doubler is phase matched with the third-harmonic field with frequency 3ω polarized along the e -axis. As the field propagates through the tripler, a non-linear field with frequency 3ω is generated by the residual first-harmonic field and the generated second-harmonic field through sum-frequency generation. The generation of a third-harmonic field $E_{3\omega}$ can also be described by differential equations:

$$\frac{\partial E_{\omega}}{\partial z} = -i\chi_1 E_{3\omega} E_{2\omega}^* e^{-i\Delta K z} \quad (3a)$$

$$\frac{\partial E_{2\omega}}{\partial z} = -i\chi_2 E_{3\omega} E_{\omega}^* e^{-i\Delta K z} \quad (3b)$$

$$\frac{\partial E_{3\omega}}{\partial z} = -i\chi_3 E_{\omega} E_{2\omega} e^{i\Delta K z} \quad (3c)$$

Here, all the terms represent the same quantities as the terms in Eqs. 2.

For both the doubler and tripler crystals, the phase matching coefficient $\Delta K = 0$ in Eqs. 2 and 3 when the crystals are tuned for optimal second-harmonic generation and third-harmonic generation respectively. When ΔK is not 0, the added phase is destructive to frequency conversion. However, since ΔK varies with frequency and deflection angle, ΔK is only 0 when the crystal is tuned for a specific wavelength and angle of propagation. For

example, on a NIF tripler [4], in mks units:

$$\Delta K = \Delta\Theta \cdot (-4.581 \times 10^5) + \Delta\lambda \cdot (-62.7 \times 10^{10}) \quad (4)$$

Here $\Delta\Theta$ is the angle with which the beam is detuned and $\Delta\lambda$ is the frequency shift (from the reference $\lambda = 1.054 \mu\text{m}$). The dependence of ΔK on angle deflections is the source of frequency conversion efficiency losses due to the phase plate. Since the phase plate for direct drive produces larger angle deflections than the phase plate for indirect drive, the phase plate for direct drive would have a larger impact on frequency conversion efficiency.

When the doubler is tuned for optimal second-harmonic generation, almost all of the initial energy is converted to second-harmonic energy and little third-harmonic generation occurs because there are no residual first-harmonic photons to combine with the second-harmonic photons. The doubler is therefore detuned at an angle $\Delta\Theta_d = 350 \mu\text{rad}$ so that the field emerging from the doubler contains first-harmonic and second-harmonic photons in the ratio of 1:1 which is optimal for third-harmonic generation.

Wavelength shifts $\Delta\lambda$ affecting ΔK in Eq. 4 are mainly due to a system aimed at achieving better target irradiation uniformity called smoothing by spectral dispersion (SSD) [5, 6]. The phase plates for both direct and indirect drive cause the laser beam to interact with itself, creating an interference pattern at the target. A monochromatic beam passing through the phase plate would create a static interference pattern causing target irradiation non-uniformities. SSD is a system whereby the beam is given bandwidth; the beam's frequency oscillates as a function of space and time. An SSD modulated beam passing through the phase plate generates an interference pattern which averages out over time and uniformly

distributes energy across the target. Since ΔK depends on the wavelength shift, SSD wavelength shifts are destructive to the frequency conversion process. The SSD bandwidth at Omega and NIF is therefore limited. It was originally hypothesized by Eimerl that a larger SSD bandwidth could be frequency converted efficiently if a second tripler, tuned for a different frequency of light, were added [7]. His hypothesis was later verified for the Omega system by Oskoui who showed that three times the SSD bandwidth can be frequency converted with two frequency-tripler crystals tuned for slightly different wavelengths [8]. Eimerl's concept was first demonstrated experimentally by Babushkin, et al. [9]. Recently, a second tripler, tuned according to Oskoui's predictions, was installed on each of Omega's 60 beams.

To describe the SSD profile of the beam, the field envelope E from Eq. 1 is multiplied by an SSD phase term. The final expression for the initial field at $z = 0$ found in the frequency conversion Eqs. 2 and 3 is:

$$E(x, y, 0, t) = \bar{E}(x, y, 0, t) * \exp \{i(\delta_1 \sin(\omega_1 t + \alpha_x x + \Phi_x) + \delta_2 \sin(\omega_2 t + \alpha_y y + \Phi_y))\} \quad (5)$$

The instantaneous SSD wavelength shift ($\Delta\lambda$), which is used to calculate ΔK from Eq. 4, is given by the t -derivative of the phase exponent:

$$\Delta\lambda(t, x, y) = \Delta\lambda_1 \cos(\omega_1 t + \alpha_x x + \Phi_x) + \Delta\lambda_2 \cos(\omega_2 t + \alpha_y y + \Phi_y) \quad (6)$$

$$\text{where } \Delta\lambda_1 = -\frac{\lambda^2}{2\pi c} \omega_1 \delta_1 \quad \text{and} \quad \Delta\lambda_2 = -\frac{\lambda^2}{2\pi c} \omega_2 \delta_2$$

Here $\bar{E}(x, y, 0, t)$ is the real function which represents the spatial and temporal shapes of the laser beam, δ_1 and δ_2 are modulation depths for both dimensions of SSD, ω_1 and ω_2 are SSD

modulation frequencies for the two dimensions of SSD, α_x and α_y are modulation terms for SSD in space, Φ_x and Φ_y are relative phase terms for the two dimensions of SSD, c is the speed of light in a vacuum, and $\lambda = 1.054 \mu\text{m}$ is the reference wavelength of the incoming field. The SSD scenarios in calculations about the NIF were based on current SSD designs for Omega because no there is no alternative design for the NIF. For a 1-THz SSD beam, $\Delta\lambda_1 = 5.5 \text{ \AA}$, $\Delta\lambda_2 = 0.75 \text{ \AA}$, $\omega_1 = 2\pi \times 10.5 \times 10^9 \text{ Hz}$, $\omega_2 = 2\pi \times 3.3 \times 10^9 \text{ Hz}$, $\alpha_x = 42.9 \text{ m}^{-1}$, and $\alpha_y = 23.4 \text{ m}^{-1}$.

3 Modeling NIF Beams

A code (SPAN, Simulations of Phase-Aberrated NIF beams) was written in PV-WAVE [10], a command-line language, to integrate Eqs. 2 and Eqs. 3 with respect to z to calculate the field emerging from the frequency conversion crystals. The beam is represented by a three-dimensional grid in x , y , and t . Each of the $N_x \times N_y \times N_t$ points in the beam (where N_x , N_y and N_t are the number of pixels in x , y , and t respectively) has three associated quantities: a complex number which represents the electric field at that point (Eq. 1), a wavelength shift due to SSD ($\Delta\lambda$ from Eq. 6) and a deflection angle. Frequency conversion was calculated by integrating Eqs. 2 and 3 for every point in the beam with respect to z according to current specifications for the NIF final optics using the half-step whole-step method of integration. Frequency conversion efficiency Eff for a single point in the beam is the ratio of the final third-harmonic to the initial fundamental intensities:

$$\text{Eff} = \frac{I_{3\omega}}{I_\omega} = \frac{|E_{3\omega}|^2}{|E_\omega|^2} \quad (7)$$

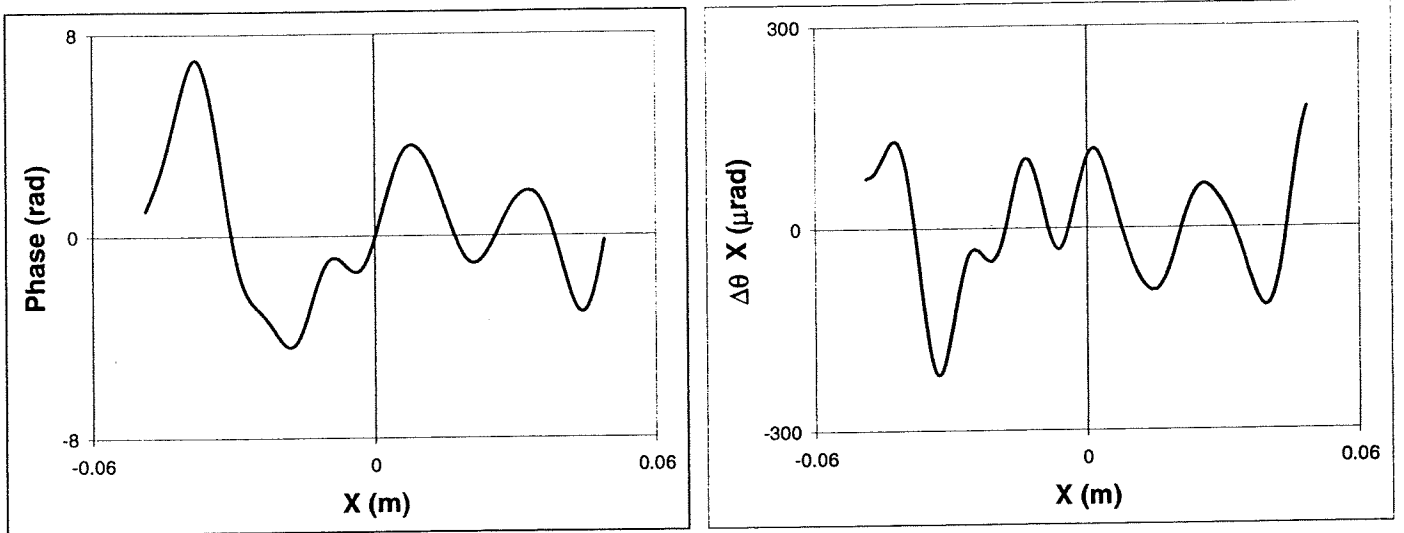


Figure 4: **Direct Drive Phase Plate.** Left: A cross-section of the phase-profile Φ is shown for a direct drive phase plate on the NIF. Right: The angle deflection along the x -axis is calculated from the phase-profile using Eqs. 8.

Here, I_ω and $I_{3\omega}$ are the intensities of the first and third harmonic fields respectively. Frequency conversion for the whole beam is the average efficiency for all points in the beam.

For phase-aberrated beams, each point in the beam is given an angle shift in x and y , which is calculated from an input phase profile of the phase-aberrated beam. The phase profile was scaled from a 27 cm beam diameter Omega direct drive phase plate designed by Lin et al. [11] to the 35 cm diameter of the NIF beam because no alternative design for the NIF has been proposed. The phase profile was also scaled so that the associated angle deflections produced a target irradiation profile that is consistent with current designs which are gaussian with the e^{-1} point 1112 μ m from the maximum [12]. In Figure 4, the phase profile Φ of the beam emerging from the direct drive phase plate scaled to the NIF is shown for a portion of the beam about 10 cm along the x -axis (Left). The angle deflections due to

the phase plate are calculated from the phase profile:

$$\Delta\Theta_x(x, y) = \arctan \frac{\partial\Phi(x, y)}{\partial x} / k \quad (8)$$

$$\Delta\Theta_y(x, y) = \arctan \frac{\partial\Phi(x, y)}{\partial y} / k$$

Here, $\Delta\Theta_x$ and $\Delta\Theta_y$ are the angle deflections along the x and y -axes respectively and are functions of x and y and k is the wave-number which appears in Eq. 1. In Figure 4 (Right), the angle deflection calculated by SPAN along the x -axis is shown for the same 10 cm portion of the beam.

SPAN was based on an earlier code written by Oskoui [8] and later modified by Grossman [13]. The previous code was written to calculate frequency conversion for a spatially coherent Omega laser beam and had limitations. Since only coherent beams were considered, the previous code considered the beam in the z and t dimensions only and could not calculate frequency conversion efficiency for a phase-aberrated beam. In addition, the SSD profile of the beam was simplified in the code because variations of the SSD profile in x and y (Eq. 5) could not be considered. Also, the previous code could only calculate frequency conversion according to the Omega final optics design which involves a different method of frequency doubling.

4 Results

To verify the accuracy of SPAN in calculating frequency conversion for the NIF final optics design, it was compared with a previous calculation made by Craxton of conversion efficiency

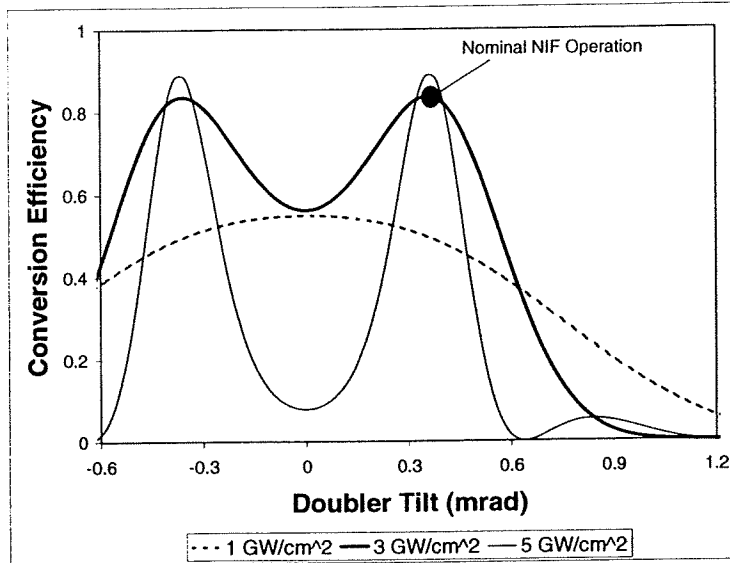


Figure 5: **Verifying NIF Conversion Calculation.** The extended code was used to reproduce the relationship between conversion efficiency and doubler tilt. The NIF nominally operates at 3 GW/cm^2 and $\Delta\Theta_d = 350 \mu\text{rad}$.

for a spatially coherent NIF beam as a function of doubler tilt $\Delta\Theta_d$ [14]. The previous results are reproduced in Figure 5.

The shape of the third harmonic conversion with respect to doubler tilt (for the 3 GW/cm^2 case, the thick solid line) illustrates an important property of the NIF final optics design. The curve has a minimum at $\Delta\Theta_d = 0 \mu\text{rad}$ which is where the doubler is phase matched and $\Delta K = 0$. Second harmonic conversion efficiency is high and there is little left-over first harmonic energy. When the beam passes through the frequency triplers, there are not enough residual first-harmonic photons to combine with the second-harmonic photons and there is little third harmonic conversion. The doubler is detuned to the nominal operating point of $350 \mu\text{rad}$ so that second harmonic conversion is exactly 67% and there is one infrared photon left for every green photon generated. This corresponds to a maximum in Figure 5.

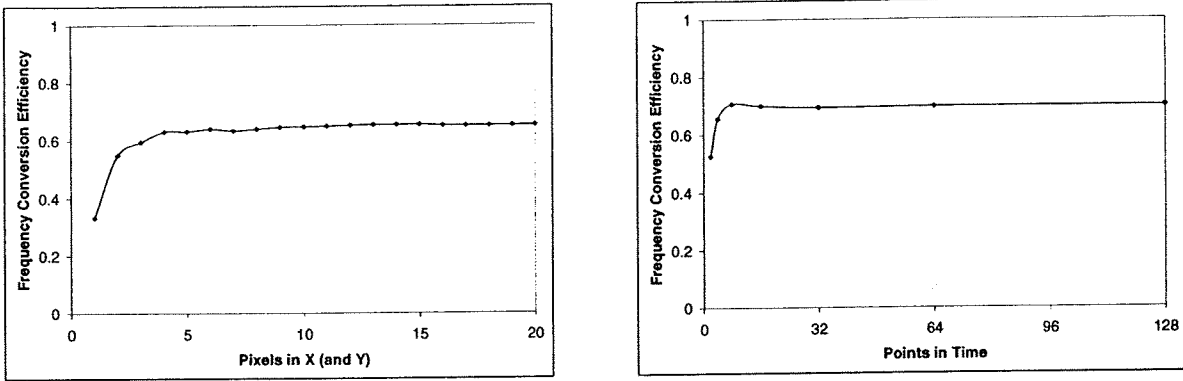


Figure 6: **Convergence of Conversion Efficiency** Left: The conversion efficiency for a 0.5 THz SSD field with $N_x \times N_x \times 50$ pixels is plotted with respect to N_x . Right: Frequency conversion efficiency for a 0.5 THz SSD field with $20 \times 20 \times N_t$ pixels is plotted with respect to N_t .

Three models for SSD were considered. For each SSD set up, conversion efficiency was calculated with the phase plate before and after the frequency conversion crystals. For the first two SSD models, a beam without SSD (0-THz) and a beam with SSD bandwidth of 0.5-THz, the NIF final optics design with one doubler crystal and one tripler crystal was used. If a third crystal were added, extra bandwidth could be passed through the system. The third scenario involved a full 1-THz SSD beam with three frequency conversion crystals.

The dimensions of the portion of the initial beam modeled (in x , y and t) were chosen to ensure convergence of the conversion efficiency. Figure 6 shows the relationship between the frequency conversion efficiency and the number of pixels. On the left, the efficiency is plotted with respect to the number of pixels N_x in the x and y dimensions for the 0.5 THz SSD model where $N_x = N_y$. On the right, the frequency conversion efficiency for the 0.5 THz SSD model is plotted with respect to the number of points in time N_t . The number of steps in z , N_z , was 200 points in each crystal for all scenarios. Grossman used the same

SSD Set-Up	Max SSD $\Delta\lambda$ (Both Dimensions 1 and 2)	Efficiency without Phase Plate	Efficiency with Phase Plate
0 THz Case	$\Delta\lambda_1 = 0.05\text{\AA}$, $\Delta\lambda_2 = 0.075\text{\AA}$	83.6%	77.5%
0.5 THz Case	$\Delta\lambda_1 = 2.5\text{\AA}$, $\Delta\lambda_2 = 0.75\text{\AA}$	69.9%	64.8%
1 THz Case	$\Delta\lambda_1 = 5.5\text{\AA}$, $\Delta\lambda_2 = 075\text{\AA}$	72.5%	67.7%

Table 1: Third-Harmonic Conversion Efficiencies for Various SSD-Setups at the NIF

N_z [13]. The number of points was sufficient to produce accuracy to within $\pm 2\%$ measured by calculating the difference between the beam size considered and a beam half the size considered. The beam dimensions were chosen in the same manner for the other SSD cases.

The actual field dimensions depended upon the SSD model and whether the phase plate was used. Without a phase plate, the beam varies only with time (spatial variations of the beam due to SSD are negligible when considering frequency conversion efficiency) so the dimensions in x and y are both 1. With a phase plate, the beam has an angle spread as a function of x and y . For the 0-THz case, only 1 point in time needs to be considered because the beam does not vary with time. An initial beam that was $80 \times 80 \times 1$ pixels (approximately $12.2\text{cm} \times 12.2\text{cm} \times 2\text{ns}$) in x , y , and t respectively was taken with the phase plate. Without the phase plate, the beam size was $1 \times 1 \times 1$ pixels. For the 0.5-THz and the 1-THz cases with the phase plate, a beam with dimensions $20 \times 20 \times 50$ in pixels (approximately $11.5\text{cm} \times 11.5\text{cm} \times 2\text{ns}$) in x , y , and t respectively was sufficient to reach a convergent efficiency. Without the phase plate, the beam size was $1 \times 1 \times 50$.

The results of the simulations of conversion efficiency are summarized in Table 1. The direct drive phase plate decreased the conversion efficiency of the NIF beam for the 0-THz, the 0.5-THz and the 1-THz case from 83.6% to 77.5%, from 69.9% to 64.8% and from 72.5%

to 67.7%, respectively. Only a small loss of $< 6\%$ on conversion efficiency arises from phase aberrations due to a direct drive phase plate.

5 Conclusions

Frequency conversion efficiency was calculated for both a spatially coherent NIF beam and a beam with phase aberrations due to a direct drive phase plate. The added phase aberrations resulted in only a small loss ($< 6\%$) in conversion efficiency. Placing the phase plate in front of the frequency conversion crystals could therefore be a viable alternative to the original concept of placing the phase plate after the crystals which would limit the intensity allowed through the system. Further studies should look at the tradeoff between conversion and ultraviolet damage limitations.

6 Acknowledgments

This study would not have been possible without Dr. R. S. Craxton, my advisor. I would also like to thank all of the scientists at the Laboratory for Laser Energetics at the University of Rochester who helped me complete my research. Specifically, I thank Dr. J. Morozas for information about the direct drive phase plate and his help in the calculations.

References

- [1] R. S. Craxton, et al. *Progress in Laser Fusion*, **Scientific American** Vol. 255, pg. 68 (1986)

- [2] R. S. Craxton. *High Efficiency Frequency Tripling Schemes for High-Power Nd:Glass Lasers*, **IEEE Journal of Quantum Electronics**. Vol. QE-17, pg. 1771 (1981)
- [3] N. Bloembergen. *Nonlinear Optics*. Benjamin, New York: 1965.
- [4] R. S. Craxton, et al. *Basic Properties of KDP Related to the Frequency Conversion of a 1 μm Laser Radiation*, **IEEE Journal of Quantum Electronics** Vol. QE-17, 1782 (1981)
- [5] S. Skupsky & R. S. Craxton. *Irradiation Uniformity for High-Compression Laser-Fusion Experiments*, **Physics of Plasmas** Vol. 6, pg. 2157 (1999)
- [6] S. Skupsky, et al. *Improved Laser-Beam Uniformity Using the Angular Dispersion of Frequency-Modulated Light*, **Journal of Applied Physics** Vol. 66, pg. 3456 (1989)
- [7] D. Eimerl, et al. *Multicrystal designs for efficient third-harmonic generation*, **Optics Letters** Vol. 22, pg. 1208 (1997)
- [8] S. Oskoui. *Broad-Bandwidth Frequency Conversion in Laser Fusion*, **Project report, 1996 Summer Research Program for High School Juniors at the University of Rochester's Laboratory for Laser Energetics** (1996)
- [9] A. Babushkin, et al. *Demonstration of dual-tripler, broadband third-harmonic generation and implications for OMEGA and the NIF*, **Reprinted from: Third International Conference on Solid State Lasers for Application to Inertial Confinement Fusion** pg. 406 (1998)
- [10] *Available from Precision Visuals: Houston, Texas*

- [11] Y. Lin, et al. *Design for continuous surface-relief phase plates by surface-based simulated annealing to achieve control of focal-plane irradiance.* **Optics Letters.** Vol. 21, pg. 1703 (1996)
- [12] *Data on NIF target specifications were obtained through private communication with R. Town*
- [13] P. Grossman. *Group Velocity Effects in Broadband Frequency Conversion on OMEGA,* **Project report, 1998 Summer Research Program for High School Juniors at the University of Rochester's Laboratory for Laser Energetics (1998)**
- [14] *Data from previous calculations of the effect of doubler tilt on frequency conversion efficiency was obtained through private communication with R. S. Craxton*

Improvements in the Strength of Visible Selective Reflection in Lyotropic Liquid Crystals Made from Cellulose Urethanes

Gloria Olivier

Advisor: Ken Marshall

Laboratory for Laser Energetics
University of Rochester

Summer High School Research Program
2000

Abstract:

Lyotropic liquid crystals based on mixtures of cellulose tricarbonylates (urethanes) generated stronger selective reflection in the visible range after an increase in concentration of approximately 9 wt.-% above the concentrations described by Müller, Zentel, and Keller in "Solid Opalescent Films Originating from Urethanes of Cellulose".[2] The cellulose urethanes used were of a lower molecular weight (less than $30,000 \text{ g mol}^{-1}$) than the material used in [2], which had a molecular weight of approximately $50,000 \text{ g mol}^{-1}$. In preparing the liquid crystal samples, the cellulose urethane was dissolved in a volatile solvent before mixing with the acrylate host. The solvent dramatically reduced sample preparation time and, as a result of its volatile nature, could be removed from the sample during film casting. Additionally, physically blending two urethane homopolymers, rather than using a copolymer, has the potential to allow for greater control over the concentrations and reproduction of lyotropic liquid crystal samples. The physical blend of homopolymers still incorporates multiple R-groups into a sample as with a copolymer. However, unlike a copolymer, new compounds do not need to be synthesized each time a new concentration of these R-groups is required to produce a different selective reflection color. This method of creating a homopolymer blend, rather than synthesizing numerous

copolymers, would simplify the procedure for reproducing such samples and would allow for the concentrations of the samples to be more easily adjusted.

Introduction:

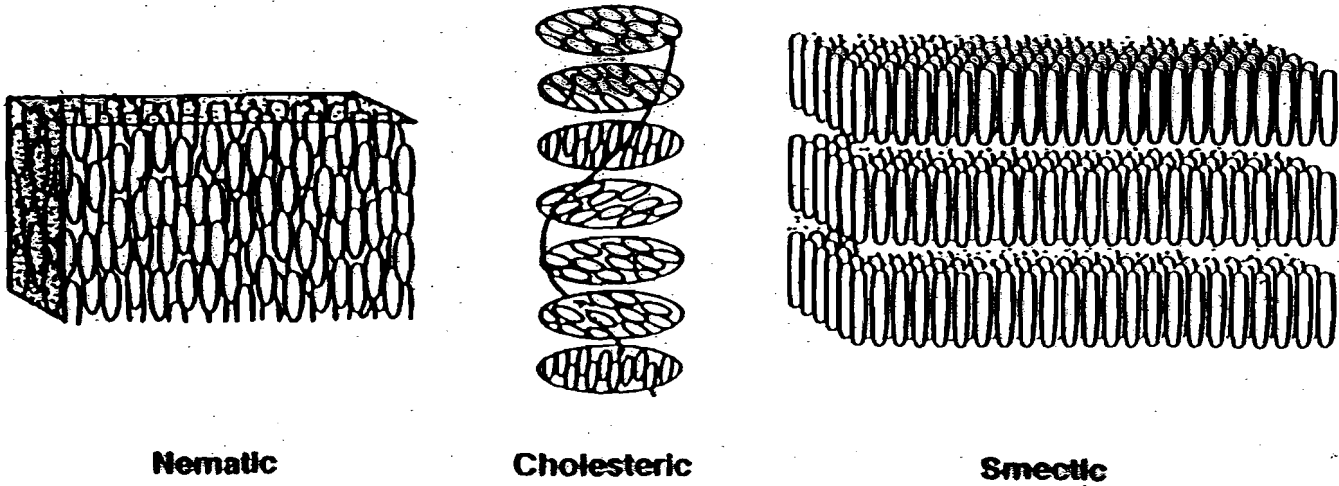
As their name might suggest, liquid crystals fall between the liquid and the crystalline phases of matter. Unable to be classified as strictly a liquid or a crystal, the liquid crystal mesophase exhibits properties of both its neighboring phases. Mechanically, liquid crystals behave like liquids, as exemplified by their viscosities. Optically, on the other hand, liquid crystals seem more similar to crystals. Some of their crystalline qualities include the optical properties of birefringence and selective reflection. Liquid crystals are also anisotropic, meaning their properties, such as selective reflection, vary depending on the angle of observation. In addition, liquid crystal material is uniquely sensitive to fluctuations in temperature, as in thermotropic liquid crystals, and some are even affected by changes in temperature and solute concentration, called lyotropic liquid crystals. [1]

Cholesteric liquid crystals respond to these minute alterations with a change in color, giving rise to their multitude of practical applications. Thermotropic liquid crystals can be used in special thermometers and other temperature-dependent devices. They are also often used as filters because their selective reflection properties allow them to block-out a certain band of light, while transmitting all other wavelengths. This ability becomes useful in products such as notch filters and safety glasses. Cholesteric liquid crystals are also essential to the OMEGA laser system as perfect circular polarizers.

The liquid crystal mesophase is divided into classes based on the arrangement of their cigar-shaped molecules (Fig. 1). The class having the most molecular order is the *smectic*.

Figure 1:

Structures of Liquid Crystal Phases

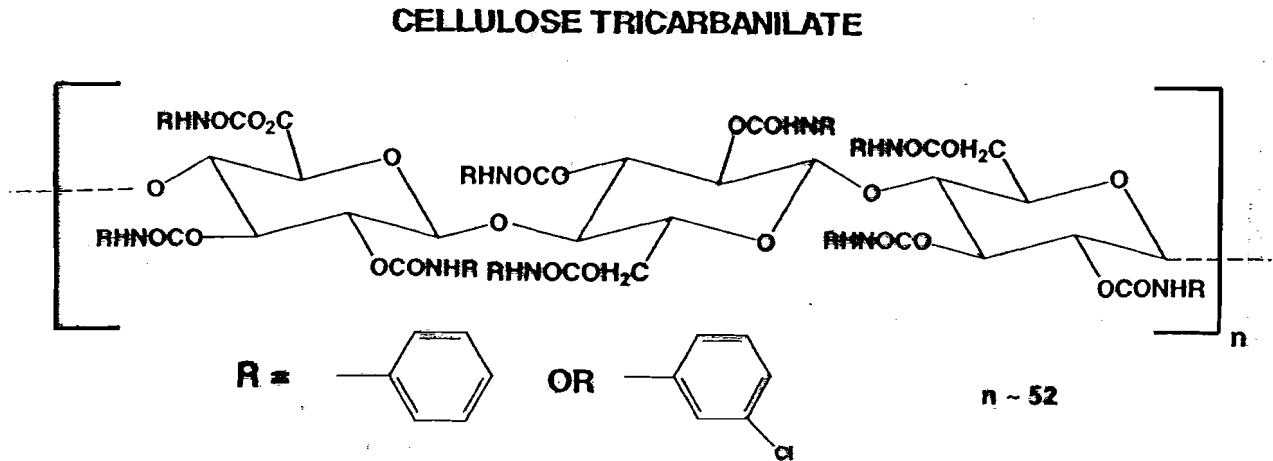


Goals:

The goal of this experiment was to strengthen the selective reflection produced by lyotropic liquid crystals based on cellulose tricarbaniates (urethanes) as presented in the work of [2] by Müller, Zentel, and Keller in Advanced Materials. The molecular structure of these urethanes is shown in Figure 2. Upon attempting to reproduce such experiments it became apparent that the method of preparation and analysis of the liquid crystal mixtures was in need of improvement. Specifically, reducing the sample preparation time and developing a means of casting smoother films of more uniform thickness became an additional goal of the project. Because of a lack of a supply of the 3-chlorophenyl isocyanate urethane used in [2] to create courethanes with the phenyl isocyanate urethane, the synthesis of the 3-chlorophenyl isocyanate cellulose urethane was also undertaken.

Members of this group show molecules arranged into ordered layers, each layer being one molecule thick. Within the layers, the molecules can be organized randomly or into rows with their long axes positioned parallel to each other. Van der Waals' forces keep the molecules within a layer from shifting out of position, but do not prevent the layers themselves from sliding over one another. The *nematic* class has the least molecular order. While its molecules are positioned parallel to each other, they are not separated into layers. The molecules are also free to slide past each other, similar to a box of toothpicks. *Cholesteric* liquid crystals comprise the third class of the mesophase. These liquid crystals are composed of very thin layers in which the molecules reside parallel to each other as well as to the plane of the layer. The direction of the long axes of the molecules rotates slightly among adjacent layers, eventually developing into a helical structure. This molecular arrangement is quite delicate, which explains why slight disturbances in the chemical environment can have a noticeable effect on the material's optical behavior. The cholesteric form also exhibits circular dichroism, or selective reflection. Thus, the findings presented in this paper, primarily the generation of strong selective reflection colors, are based strictly on experiments with cholesteric liquid crystals. [1]

Figure 2:

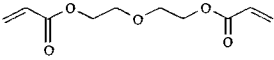
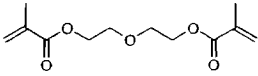
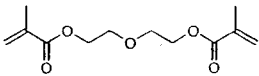


Experimental:

Cellulose tricarbanilate, (less than $30,000 \text{ g mol}^{-1}$), made with phenyl isocyanate, as prepared by Sarah Mitchell in [3], was mixed with an acrylate host before being cast into a film on a microscope slide and analyzed under the polarizing microscope. The cellulose urethane was measured out in a variety of concentration ratios with the acrylate host, differing by increments of 5 wt.-%. Three different hosts, 2-ethoxyethyl acrylate, di(ethylene glycol) diacrylate, and di(ethylene glycol) dimethacrylate, were used in the experiment. The solid cellulose urethane was dissolved in a volatile solvent, such as tetrahydrofuran, before being mixed with the acrylate host. After mixing with a magnetic stir bar in the dark for at least one hour, the solution was transferred and spread dropwise onto a microscope slide using a Pasteur pipette until a thin film covered the top surface on one end of the slide. A cover slip was used to shear the sample and generate proper cholesteric liquid crystal alignment. Any excess solvent that would dilute the concentration and prevent the liquid crystal phase from forming was removed from the sample using a hot stage. Each sample was observed under the polarizing microscope in search of strong selective reflection color, as well as liquid crystal texture and birefringence. All samples

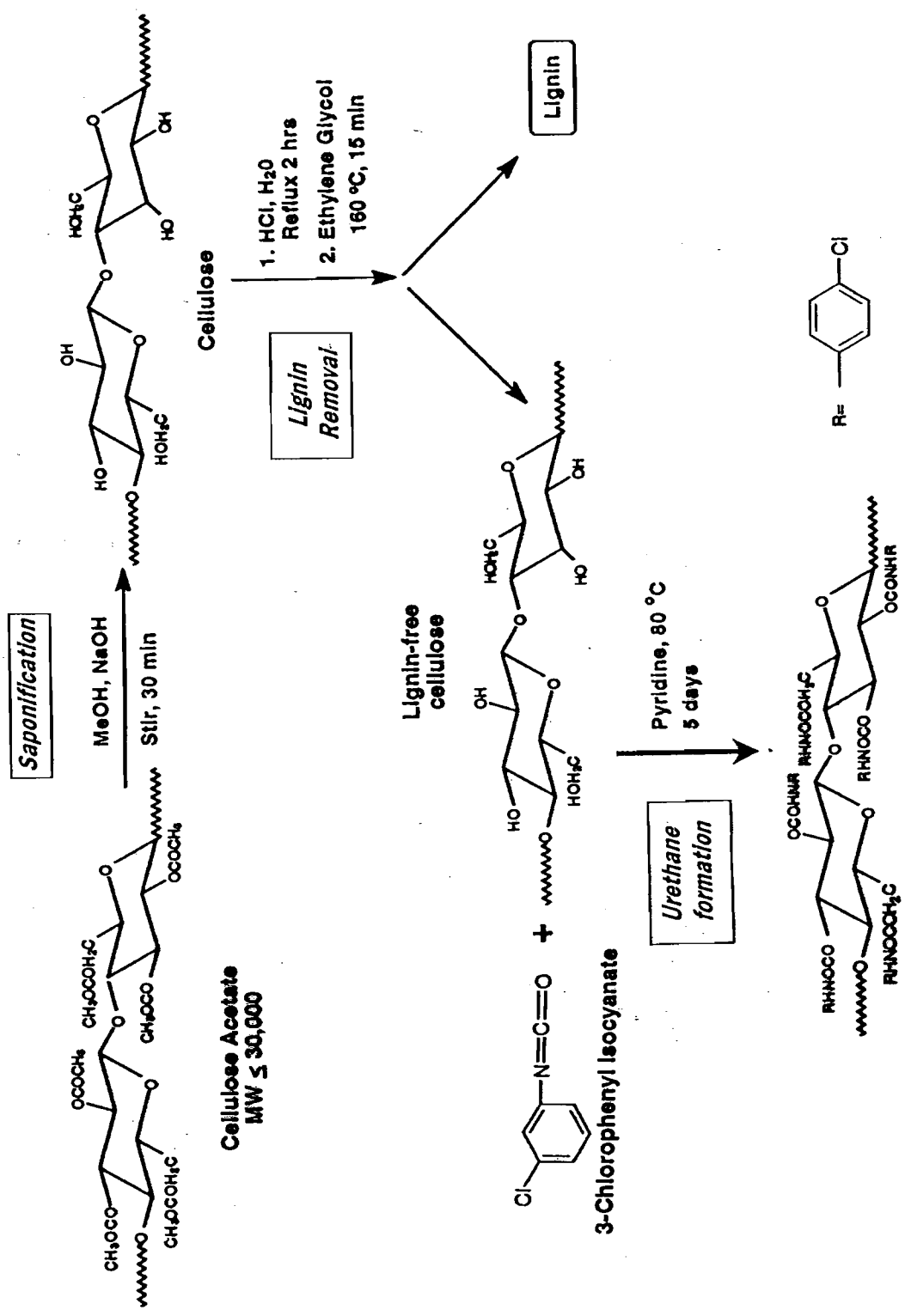
made from the phenyl isocyanate cellulose urethane were stored for days to weeks in a dark, closed drawer before any selective reflection color in the visible range appeared. These colors, and the concentration ratios that produced them, are listed in Table 1.

Table 1:

Wt.-% of Purified Phenyl Isocyanate Cellulose Urethane	Host Name	Visible Selective Reflection Color
70	 di(ethylene glycol) diacrylate	red
50	 di(ethylene glycol) dimethacrylate	green, red
55	 di(ethylene glycol) dimethacrylate	red

The synthesis of the 3-chlorophenyl isocyanate urethane for use in a blend of homopolymers with the phenyl isocyanate urethane was performed at half-scale using the procedure described in reference [3] and shown in Figure 3. The synthesis was not executed under a blanket of nitrogen and began at the urethane formation step by adding 5.0g of purified cellulose acetate to a reaction vessel, followed by the addition of 100ml of pyridine. After proceeding with the addition of 25ml of 3-chlorophenyl isocyanate, the solution exhibited a yellow color and an exothermic reaction occurred. The reaction was brought to 80°C using a heating mantle before being refluxed at this temperature for five days. Upon the conclusion of the reflux, the solution appeared dark brown in color and was allowed to cool for approximately

Figure 3:



The synthesis of 3-chlorophenyl isocyanate cellulose urethane is a multi-step procedure.

References:

- [1] Fergason, James L. "Liquid Crystals", *Scientific American*, Vol. 211--No. 2, pp. 72-82, 85 (1964).
- [2] Müller, Manfred and Zentel, Rudolf and Keller, Harold. "Solid Opalescent Films Originating from Urethanes of Cellulose", *Advanced Materials*, Vol. 9—No. 2, pp. 159-162 (1997).
- [3] Mitchell, Sarah. "Self-Organizing Lyotropic Liquid Crystals Based on Cellulose Derivatives", *1997 Summer Research Program for High School Juniors at the University of Rochester's Laboratory for Laser Energetics: Student Research Reports*, (1997).

Acknowledgements:

I thank the Laboratory for Laser Energetics and Dr. R. S. Craxton for providing me with the incredible opportunity to participate in the Summer Research Program for High School Juniors. I also thank Ken Marshall for his time and guidance throughout my research project. I also appreciate the contributions made by the staff of the materials lab and the additional assistance provided by Sarah Mitchell.

three hours. The solution was then transferred to a beaker and the product was precipitated with methanol. Because a large quantity of methanol was required to produce any crystals and these crystals were too fine to be collected by suction filtration, an improved method for isolation of the 3-chlorophenyl isocyanate product was desired. After attempting to dissolve and re-crystallize the material with a variety of solvent combinations, ethyl acetate and methanol were found to work most effectively in comparison to the other methods. Before purification with these solvents, the product was heated under vacuum using a rotovapor in order to remove the excess methanol and pyridine. The concentrated product was taken up in ethyl acetate, and the material went completely into solution after heating briefly. The solution was then placed in an ice bath while adding methanol in order to reach a cloud point. The solution was removed from the ice bath and suction filtered. The crystals were immediately collected off the filter paper to prevent the product from adhering to the paper. The product, although still not completely purified, was incorporated into a few samples containing a blend of homopolymers in varying concentrations with the 2-ethoxyethyl acrylate and the di(ethylene glycol) dimethacrylate hosts by following the same sample preparation and analysis procedures used with the phenyl isocyanate urethane samples. The blend of homopolymers contained 49 mol-% of the 3-chlorophenyl isocyanate urethane and was made by physically blending the 3-chlorophenyl isocyanate urethane with the phenyl isocyanate urethane.

Conclusions:

Dissolving the solid cellulose urethanes in a volatile solvent significantly shortened sample preparation time, which according to the procedure presented in [2], required three to five days of mixing in a closed vessel before films could be cast and cured. In addition, using

tetrahydrofuran in the mixtures made the solutions easier to cast by lowering the viscosity of the gel formed by the urethane-acrylate combination. The fact that the solvent could then be eliminated from the films using a hot stage was also a desirable result. However, it was found that tetrahydrofuran was too volatile for the purpose of casting smooth films because it caused ridges and bubbles in the film as it rapidly evaporated. Fortunately, ethyl acetate—a slightly higher boiling, yet volatile liquid—proved to be a more effective solvent for the work with liquid crystal castings. Ethyl acetate thoroughly dissolved the solid urethane material and also facilitated the smooth casting of films with uniform thickness. Another advantage of using this volatile solvent is that it has the ability to produce larger aperture films through knife or spin coating. Additionally, using a solvent allows the mixtures to be microfiltered, thus producing particle-free films that can be used for critical applications.

It should also be noted that samples made from the phenyl isocyanate cellulose urethane have proven to be capable of generating strong selective reflection in the visible range. These results came after adding approximately 9 wt.-% more of the urethane to each sample than was used in [2].

Results from physically blending the 3-chlorophenyl isocyanate urethane with the phenyl isocyanate urethane have yet to be determined. Further experimentation is needed to perfect the proportion of the two homopolymers, and the concentration of the homopolymer blend, being put into the samples.

Dynamic Focal Spot Size Using a Static Phase Plate

Colin James Parker, Brighton High School

1. ABSTRACT

A distributed phase plate (DPP) is designed for the University of Rochester Laboratory for Laser Energetics OMEGA laser system that can manipulate the focal spot size during a three-nanosecond pulse. These hybrid full aperture diffractive elements alter the focal spot size to match the diameter of an imploding target. When implemented in the OMEGA system, these DPPs will greatly increase on-target energy efficiency in direct drive experiments.

The OMEGA's current focal spot diameter is unchanging during the beam pulse. Because of this, much of the energy misses the target after it shrinks from implosion. The newly modified DPPs have the ability to dynamically control the focal spot diameter on target to account for an imploding target. Simulated illumination shows that the new DPPs increase the late pulse percent intensity on-target from 27.5% to 73.4%. They also produce an azimuthally symmetric and super-Gaussian intensity profile to maintain reasonable irradiation uniformity.

2. INTRODUCTION

The distributed phase plate (DPP) is a full aperture diffractive element that serves to add phase to the laser beam incident upon the lens. An unaberrated beam passing through a perfect lens creates an Airy pattern (see ref. 1 p. 64) in the target plane, thus creating a focal spot diameter of 2 microns as opposed to the desired 1 mm target size. Any phase aberration present in the near field tends to spread the energy out of the perfect Airy pattern. The DPP is employed to modify the beam phase front and spread the energy over the entire target area. As in fig. 1, the incident light bypassing the DPP is focused onto an Airy pattern in the far field while the light passing through the DPP is spread about that point. Each section of the DPP is a different predetermined thickness of glass; this adds a controllable phase aberration to the beam. This beam, or near field, is then focused by the lens onto the target plane, or far field. The target field is located at the two-dimensional Fourier transform plane of the lens (see Ref. 1 pp. 83-90, Ref. 2); thus, the far field is the two-dimensional Fourier transform of the near field.

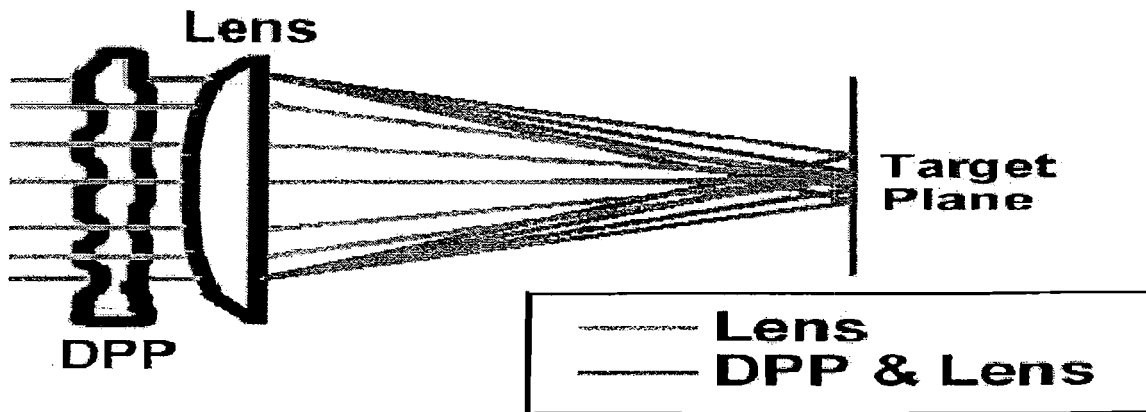


Fig. 1. Incident light bypassing the DPP is focused by the lens onto an Airy pattern of radius 2 microns in the target plane. Light passing through both the DPP and lens is diffracted about that point.

When the energy is spread out to many times the area of the Airy pattern, a speckle pattern forms as in fig. 2a. This speckle pattern is highly modulated due to the coherent interference in the far field. The process of smoothing by spectral dispersion (SSD) takes advantage of this high modulation. SSD spatially and temporally varies the beam phase such that the speckle pattern changes in time (see Ref. 3). As a result, the time-integrated far field has a smooth profile as in fig. 2b. These smoothed envelopes are those used in the DPP design process.

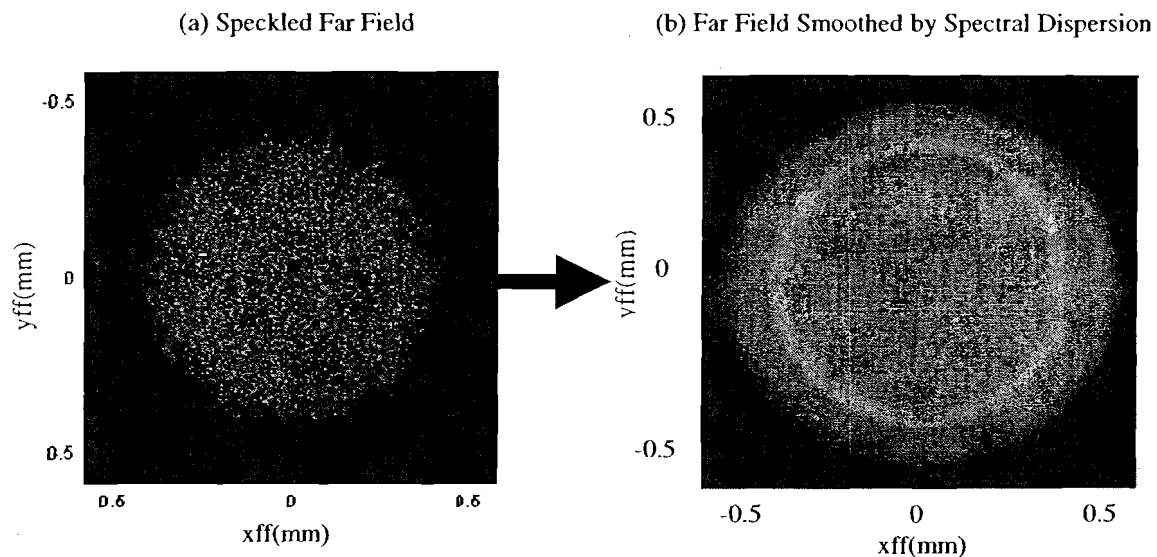


Fig. 2 Far field intensity images. The first is without Smoothing by Spectral Dispersion. The second is a time-integrated far field that has undergone smoothing by spectral dispersion.

The dynamic beam profile of the OMEGA laser system, in conjunction with the hybrid DPP, permits the far-field spot size to transform. Early in time, the intensity plot of the near field maintains a Gaussian profile as in Fig. 3a. As time progresses, the near field intensity plot transforms into an edge-peaked profile later in time as shown in Fig. 3b. In the Gaussian beam, a majority of the energy is concentrated in the center. In the

edge-peaked beam, the majority of energy is located at the outer edges. The DPP's ability to control the diffraction of the beam onto the far field is used to accomplish a dynamic spot size. Dividing the DPP into two corresponding regions permits control over two different regions in the far field. The inner disk region's radius is calculated by,

$$\pi r_d^2 = 0.5(\pi r_{DPP}^2),$$

$$r_d = \frac{1}{\sqrt{2}} r_{DPP},$$

where r_{DPP} is the radius of the DPP. The disk is used to control the far field early in time when it has a Gaussian profile. The annulus of the DPP, representing the remaining half, is used to control the far-field envelope later in time when the beam is edge-peaked. Thus, as the illumination of the DPP changes, so will the shape of the far-field envelope that it creates.

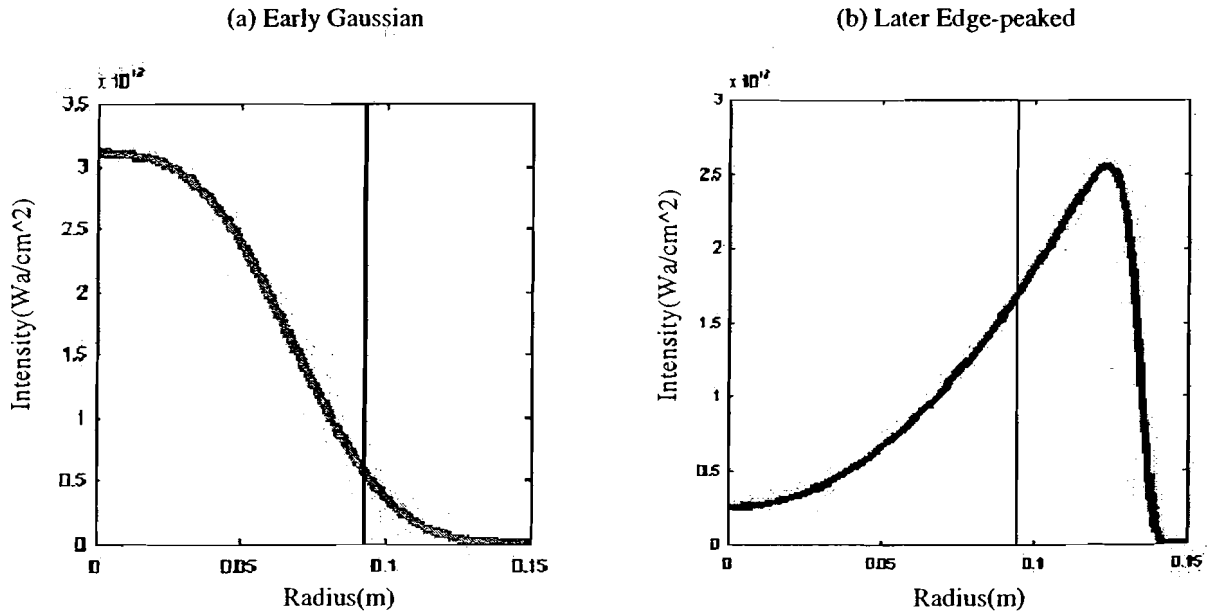


Fig. 3 Near-field beam profiles that plot Intensity versus radius. The first is at a time of 0.8 ns and is Gaussian shaped while the second is at 2.8 ns and maintains an edge-peaked profile.

3. DYNAMIC FOCAL SPOT SIZE CONCEPT

The process of amplification undertaken in the Neodymium (Nd) glass rods modifies the OMEGA beam profile. Because the Nd rods are pumped externally using flash lamps, the outer region has more gain; therefore, the outside of the beam experiences increased gain during the pulse. Because the inside receives less energy from the pump rods, more energy is put through it to even the mid pulse energy profile. This results in a Gaussian beam profile early in time as in Fig. 3a. Once the flash bulbs pump the gain medium, the edges of the Nd glass rod are more able to produce gain; this causes the beam to be edge-peaked later in time as shown in Fig. 3b.

These anomalies of the amplification process provide a temporally varying quality that the newer DPP can exploit. In order to obtain a decreasing focal spot size, the DPP is divided into two separate regions, a disk and annulus of equal area. For simulation purposes, shooting for flat target super-Gaussian envelopes of high order is beneficial; as the super-Gaussian order increases, the smoother the beam intensity plot and more visible the aberrations. Early in time, before the target implodes, a desirable far-field envelope as in fig. 4a is given by,

$$I'_{ff} = e^{-\ln(2)\left(\frac{r}{r'}\right)^8}, \quad (1)$$

where r is the radius and r' is the peak-intensity half max. For the 1-mm target, the early r' value is 0.6 mm. Since this far field is desirable early in time, the disk is modified to scatter energy as in equation 1. The desirable envelope for the imploded target is given by the equation,

$$I_{ff}'' = e^{-\ln(2)\left(\frac{r}{r''}\right)^8} \quad (2)$$

Since the target has dramatically decreased in size, the r'' value is 0.2 mm. Modifying the annulus of the DPP to diffract energy as in equation 2 produces this smaller far-field envelope later in time.

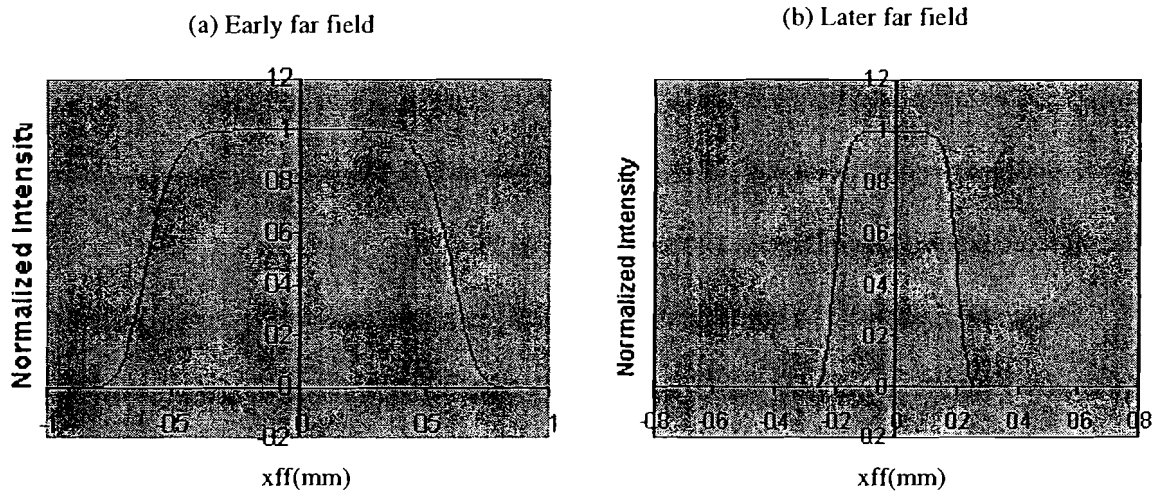


Fig. 4. Two desirable far field envelopes of super-Gaussian order 8. The first is the early in time far field created by the disk of the DPP. The second is the later in time far field created by the annulus of the DPP.

4. SIMULATION AND CREATION OF THE MODIFIED DPP

Mathematical functions are used to model the near-field and far-field profiles on the OMEGA laser system. These functions are then manipulated by written code to perform DPP simulations as well as to create the DPPs. The data represented in fig. 3b may be modeled using a super-Gaussian function added to a polynomial function. Certain radii of interest are computed,

$$\begin{aligned} r_0 &= r_p + 0.5d, \\ r_2 &= r_p + d, \end{aligned}$$

where r_p is the radius of the peak intensity value, r_0 is the radius of the location yielding 90% energy, r_2 is the radius yielding 10% energy and d is the radius differential from the intensity peak to the location yielding 10% of the intensity peak. Then, an initial guess at the polynomial coefficient is necessary. To determine the initial guess, assume that the super-Gaussian is near unity in the neighborhood of the peak value. Thus,

$$P = \frac{(I_p - y_i)}{r_p^2},$$

where P is the polynomial coefficient, I_p is the intensity value peak, and y_i is the y -intercept of the curve. Then, using the initial guess of the polynomial coefficient, an initial guess at the super-Gaussian order may be obtained,

$$m = \frac{\ln\left\{\frac{1}{\ln(2)}[\ln(y_i + Pr_2^2) - \ln(0.1I_p)]\right\}}{\ln\left(\frac{r_2}{r_0}\right)},$$

where m represents the guessed super-Gaussian order. The super-Gaussian order may now be computed by solving the transcendental equation,

$$m' = \ln\left(\frac{1}{\ln(2)}\right) \ln\left\{ y_i + \frac{\left[\frac{I_p}{e^{-\ln(2)\left(\frac{r_p}{r_0}\right)^m} - y_i} \right] r_2^2}{r_p^2} \right\} - \ln(0.1I_p) - m \ln\left(\frac{r_2}{r_0}\right)$$

where m' is the actual super-Gaussian order. The actual polynomial coefficient, P' , is calculated by,

$$P' = \frac{\left(\frac{I_p}{e^{-\ln(2)\left(\frac{r_p}{r_0}\right)^m} - y_i} \right)}{r_p^2}$$

The equation for the edge-peaked near field intensity profile of fig. 3b is then given by,

$$I_{nf}^E = \sqrt{(y_i + P'r^2) e^{-\ln(2)\left(\frac{r_p}{r_0}\right)^m}} \quad (3)$$

The equation for the Gaussian near field intensity profile of fig. 3a is modeled by,

$$I_{nf}^G = I_p e^{-\ln(2)\left(\frac{r}{r_0}\right)^2}, \quad (4)$$

where I_p is the peak intensity of the center of the Gaussian.

The phase of the DPP may be calculated from a given near field and a desired far field using an iterative process known as a Phase Retrieval Algorithm (see Ref. 4, 5, 6, 7). This algorithm uses two-dimensional spatial fast Fourier transforms to acquire the required near field for a given far field. Next, it determines the DPP phase necessary to convert the supplied near field into the necessary one. Because an exact DPP phase is not calculated on the first iteration, the loop is repeated with the new phase. The following iterations improve upon their predecessors until a reasonable accuracy is achieved. As a result, the Phase Retrieval Algorithm can be functionally expressed by,

$$\phi_{DPP}(x, y) = \Psi\{I_{nf}(x, y), I_{ff}(x_{ff}, y_{ff})\}, \quad (5)$$

where ϕ is the DPP phase, Ψ is the Phase Retrieval Algorithm, I_{nf} is the given near field and I_{ff} is the desired far field.

The Phase Retrieval Algorithm is used in each step of a three-step process to create the DPPs. The first step creates a randomly initialized DPP that functions as a template for the individual regions of the DPP. This run assumes an early Gaussian beam profile and produces a full aperture DPP by,

$$\phi_{DPP}(x_{nf}, y_{nf}) = \Psi\{I_{nf}^G(x_{nf}, y_{nf}), I_{ff}^G(x_{ff}, y_{ff})\}, \quad (6)$$

from equations 1 and 4 decomposed into x and y components and equation 5 describing the Phase Retrieval Algorithm. The second step solely modifies the annulus of the DPP. The program is provided with the desired far-field envelope described in equation 2. Then, the program, instead of undergoing full aperture illumination in the iteration process, only illuminates the annulus by truncating the energy in the center region of the

beam. Once finished, the newly calculated annulus is cut and pasted onto the template DPP from the original run. This process is represented by,

$$\phi_{DPP}(x'_{nf}, y'_{nf}) = \phi_{DPP}(x'', y'') + \Psi\{I_{nf}^E(x'_{nf}, y'_{nf}), I_{ff}''(x_{ff}, y_{ff})\}, \quad (7)$$

where x'_{nf} and y'_{nf} are the annulus's spatial components in the near field and x'' and y'' are the disk-only components of the DPP phase generated from equation 6. The third step only modifies the disk region of the DPP. As before, only this region of the DPP is illuminated and the resulting phase data is placed on the template. This process is represented by,

$$\phi_{DPP}(x''_{nf}, y''_{nf}) = \phi_{DPP}(x', y') + \Psi\{I_{nf}^G(x''_{nf}, y''_{nf}), I_{ff}'(x_{ff}, y_{ff})\}, \quad (8)$$

where x''_{nf} and y''_{nf} are the disk's spatial components in the near field and x' and y' are the annulus-only components of the DPP phase generated in the process described in equation 7. The output of this step is the newly modified DPP in fig. 5.

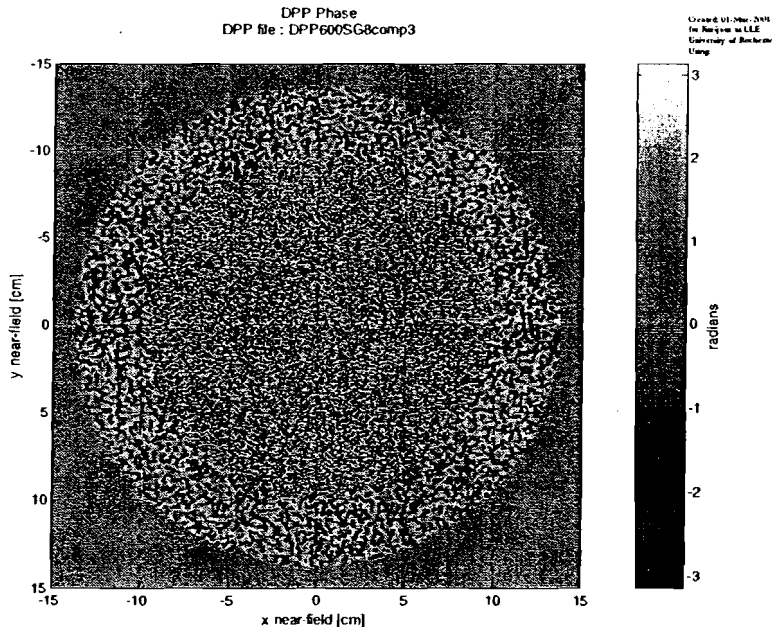


Fig. 5. DPP phase image and output of DPP creation program. Each gray shade represents a different thickness of the glass adding phase to the laser beam of pi to negative pi radians.

5. ACHIEVING HIGH IRRADIATION UNIFORMITY

The method of creating the DPPs solely involves illumination of each region individually. When the resultant DPP in fig. 5 is illuminated with a full aperture beam, energy found in the illumination overlap creates anomalies in the far field. Early in time, when a wide super-Gaussian envelope is desired, energy passing through the annulus creates a smaller super-Gaussian shaped bump in the far field as in fig. 6a. Later in time, a similar phenomenon occurs as energy passing through the disk creates a wide skirt in the far field as in fig. 6b. Although this causes an overall decrease in irradiation uniformity, the later example is inconsequential because it does not affect the irradiation uniformity on target. The early in time case, however, is a significant problem since it greatly distorts the desired far field envelope and will affect the stability of the imploding target.

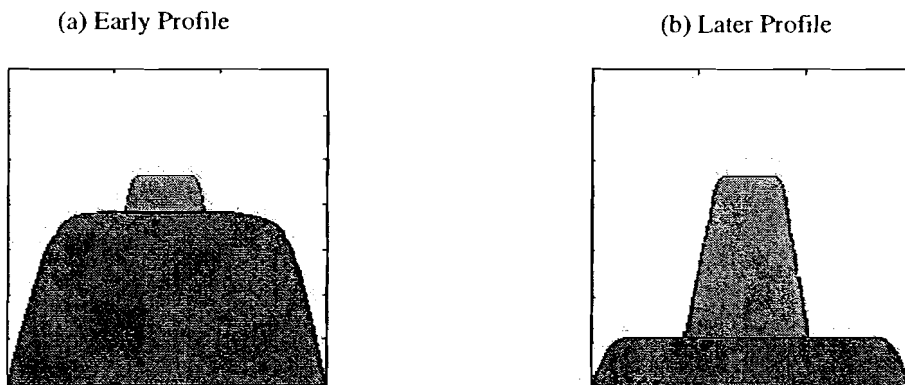


Fig. 6 These illustrations describe the effect of energy in the illumination overlap. The dark gray energy has passed through the disk while the light gray energy has passed through the annulus.

Restoration of a desirable far-field envelope involves a method of compensation for the undesired energy due to the illumination overlap in the annulus. The target far field may be modified such that upon addition of the excess energy, the desirable far field

is obtained. Determination of the energy in the illumination overlap involves the integration of the equation representing the beam profile and then rotating it around the origin. Thus, total excess energy (U'), is given by,

$$U' = 2\pi \int_{r_d}^{r_{DPP}} [I_p I_{nf}^G] r dr, \quad (9)$$

where r_d is the radius of the disk and r_{DPP} is the radius of the whole DPP. Because this energy passes through the annulus of the DPP, it has the super-Gaussian far field shape that is created in that region. The equation representing the far-field bump is thus obtained by multiplying a normalized equation 2 by the excess energy found using equation 9,

$$I_b = \frac{U' I_{ff}^*}{\int_0^{\infty} I_{ff}^* r dr}.$$

Compensating for this calculated energy simply involves subtracting this energy from the desired far-field envelope in equation 1,

$$I'_{ff} = I'_{ff} - I_b. \quad (10)$$

Then, as shown in fig. 7, illumination of the new DPP will allow the excess energy found in the illumination overlap to fill in the depression now present in the desired far field envelope of the disk. When the outcome of equation 10 is substituted for the far field from equation 1 in the DPP creation process, the result is the originally desired super-Gaussian far field and better irradiation uniformity.

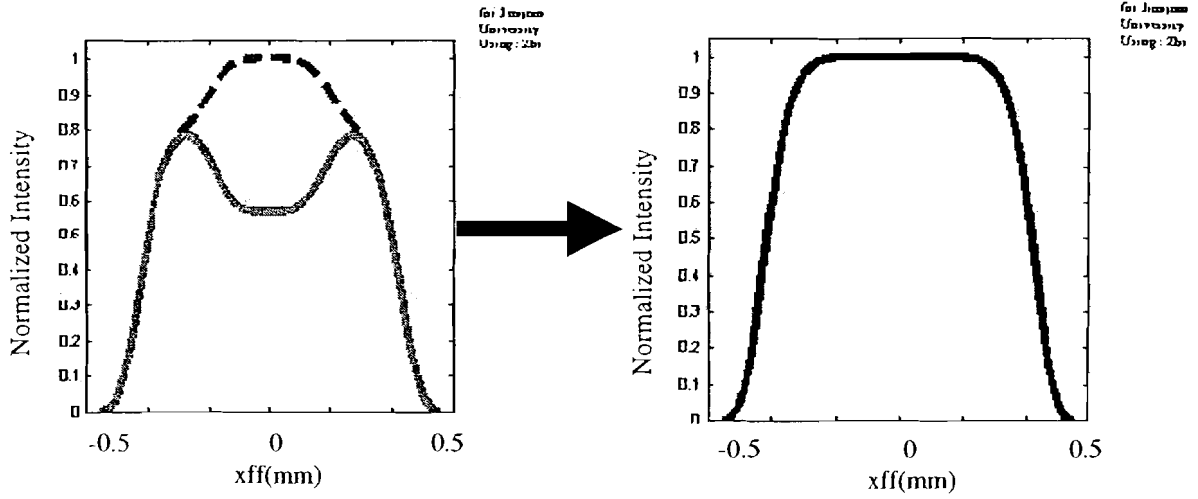


Fig. 7. The modified target far field produces a desirable far-field envelope by compensating for the illumination overlap in the annulus represented by the dotted line. The result is a desirable super-Gaussian far field.

6. TIME EVOLUTION OF THE FAR-FIELD ENVELOPE

In determination of the DPP phase data, two reference points were utilized, one describing the near-field profile at 0.8 nanoseconds and the other at 2.8 nanoseconds. In actuality, the jump between the two stages is not instantaneous, but gradual. And, as the near field changes in time, the far field temporally evolves. This section describes the procedure involved in determining the temporally evolving far-field envelope.

A model for the spatio-temporal evolution of the pulsed-beam on OMEGA is obtained by temporally blending the two reference near-field profiles. Using the blend function in fig. 8 and equations 1 and 2,

$$I_{nf}(x, y, t) = B_G(t)I_{nf}^G(x, y) + B_E(t)I_{nf}^E(x, y), \quad (11)$$

where B_G is the Gaussian component of the blend function and B_E is the edge-peaked component of the blend function. By illuminating the DPP with the full aperture, spatio-temporally evolving near field from equation 11, the evolving far-field envelope is obtained. This process is given by,

$$I_{ff}(x_{ff}, y_{ff}, t) = \left| \mathfrak{F} \left\{ \sqrt{I_{nf}(x_{nf}, y_{nf}, t)} \right\} \right|^2, \quad (12)$$

where $\mathfrak{F}\{\}$ represents the spatial 2D Fourier transform.

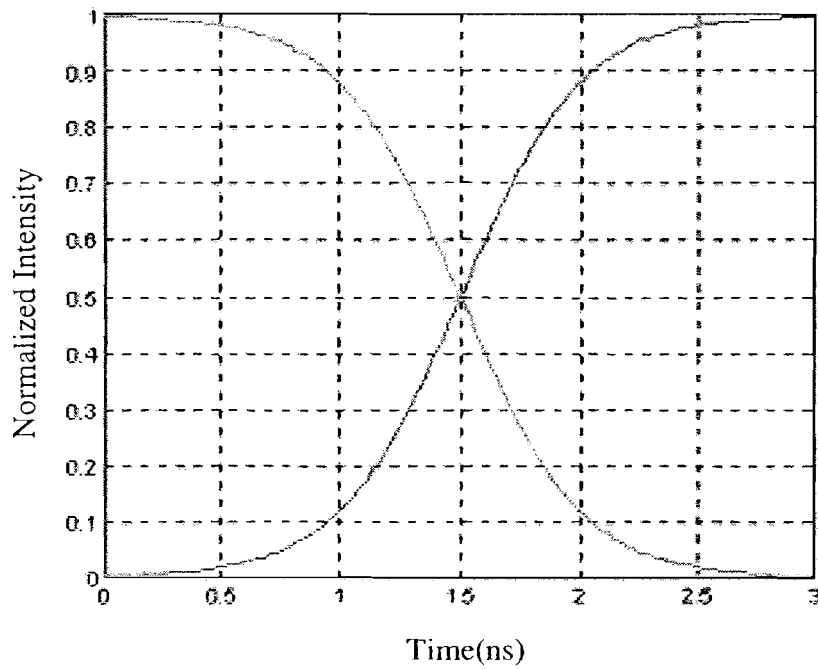


Fig. 8. The Blend function used to add a temporal element to the near field. The light gray line is the magnitude of the Gaussian profile's influence while the dark gray line is the edge-peaked profile's power.

7. RESULTS

Upon illumination and simulation, several positive results are obtained. As shown in fig. 9, the far-field spot size decreases in size throughout the shot.

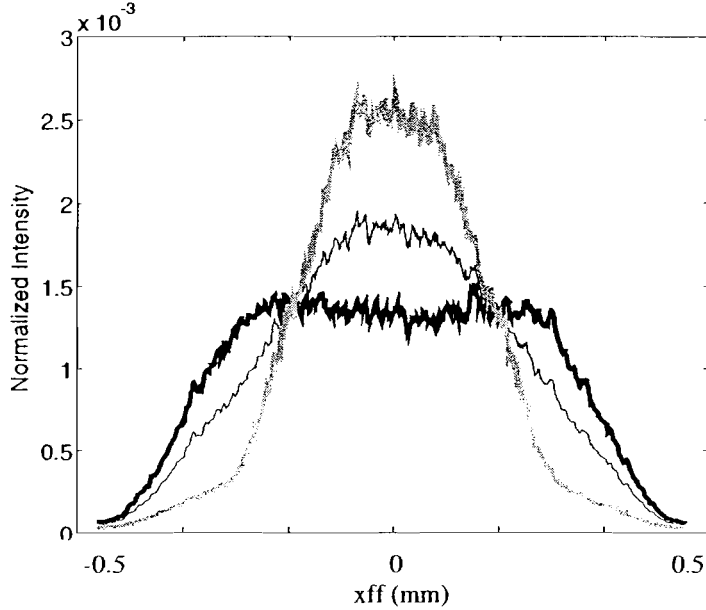


Fig. 9. Three Far-field lineouts. The thick, black line represents an early in time envelope, the thin black line is a mid-shot lineout and the gray line is extracted near the end of the 3ns shot.

In turn, the percent energy within the bounds of the imploded target also increases as shown in fig. 10. The energy ratio, $U_{\%}$, between energy on the small target and total energy is calculated at any time by,

$$U_{\%}(t) = \frac{\int_0^2 I_{ff}(t) r dr}{\int_0^{\infty} I_{ff}(t) r dr}.$$

The original DPP transfers 27.5% of the total energy onto the imploded target later in time. The modified DPP increases this to 73.4%, being over 2.6 times more efficient.

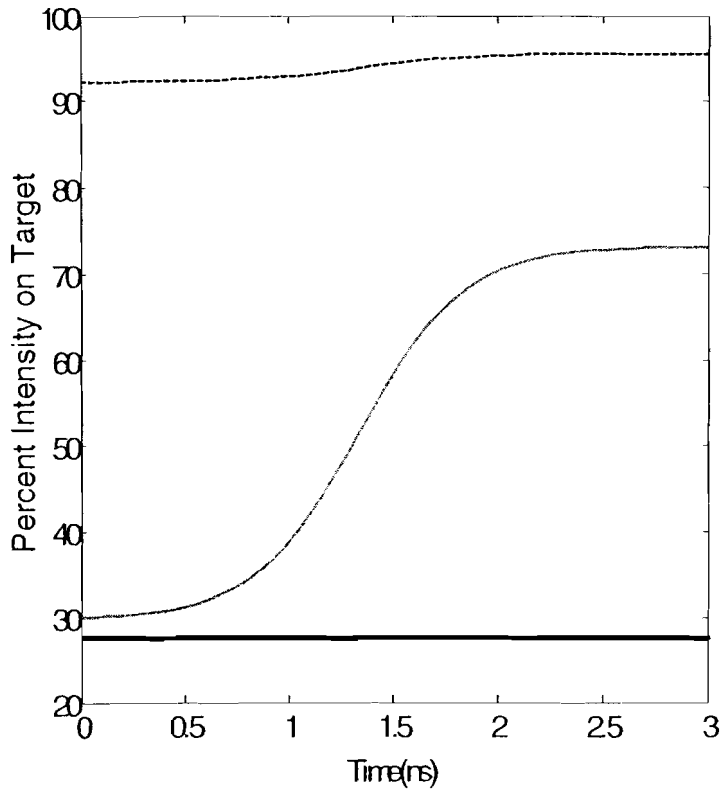


Fig. 10. This graph represents percent intensity on target over the 3ns shot. The dashed line depicts the percent energy in the modified DPP's far field that is transferred to the large, preimploded target. The thin gray line is the percent energy the modified DPP scatters onto the smaller, imploded target. The dark line is the percent energy that the original DPP transferred to the small target.

8. CONCLUSION

These new DPP's have demonstrated the ability to decrease the far-field spot size throughout the 3ns shot. They have also proven to maintain a high level of uniformity in the far-field envelope as well. The versatility of the DPP creation method provides added strength to the project. By altering variables, one can account for any size target, any given near field, and any desired far field. The hybrid DPPs already increase the OMEGA's late shot, on-target energy efficiency 2.6 times. If the current near-field profile could be better tailored using beam-shaping techniques, this could be increased as energy is eliminated from the illumination overlaps.

There is also interest in these modified DPPs being implemented in direct drive experiments to be performed on the National Ignition Facility in California. Instead of using cylindrical rods, the NIF employs slabs of gain medium that are more evenly pumped, thus eliminating many of the profile aberrations found in the OMEGA laser system. Further work could be done in attempt to determine if the current method could be altered to work on the NIF.

Fabrication of these modified DPPs requires additional manipulation of the DPP Phase data. The output of the DPP creation program is a matrix with varying phases at each point. Because a continuous relief is desired for the manufactured DPP, this data must be "unwrapped" such that instead of jumping from phase to phase, there is a continuous progression between neighboring phase values. Once "unwrapped", these DPPs can be fabricated and implemented in the OMEGA laser system, drastically increasing efficiency during direct drive experiments.

9. ACKNOWLEDGEMENTS

Special thanks are for my advisor, Dr. John Marozas, who always helped point me in the right direction, often providing literature and personal guidance throughout the summer and beyond. Also, thanks to the entire staff of researchers in the University of Rochester Laser Lab for Energetics Summer Research Program as well as the other students all of which were always happy and welcoming for discussion on any given topic.

10. REFERENCES

1. J. W. Goodman, *Introduction to Fourier Optics* (McGraw-Hill, New York, 1968).
2. R.N. Bracewell, *The Fourier Transform and Its Applications*, 2nd ed., rev., McGraw-Hill Series in Electrical Engineering. Circuits and Systems (McGraw-Hill, New York, 1986).
3. S. Skupsky, R. W. Short, T. Kessler, R. S. Craxton, S. Letzring, and J. M. Soures, J. Appl. Phys. 66, 3456 (1989).
4. J. R. Fienup, "Phase retrieval algorithms: a comparison," *Appl. Opt.* 21(15), 2758-2769 (1982).
5. "Distributed-phase-plate design using simulated annealing algorithms," Laboratory for Laser Energetics LLE Review 64, NTIS document No. DOE/SF/19460-99, 1995 (unpublished), pp.170-174.
6. Y. Lin, T. J. Kessler, and G. N. Lawrence, "Design of continuous surface-relief phase plates by surface-based simulated annealing to achieve control of focal-plane irradiance," *Opt. Lett.* 21(20), 1703-1705 (1996).
7. Y. Lin, T. J. Kessler, and G. N. Lawrence, "Distributed phase plates for super-Gaussian focal-plane irradiance profiles," *Opt. Lett.* 20(7), 764-766 (1995).

Improving Equation of State Tables

Priya Rajasethupathy

Advisor: Dr. Jacques Delettrez

University of Rochester

Laboratory for Laser Energetics

Summer High School Research Program 2000

Inertial Confinement Fusion is based on the idea of imploding a target (filled with deuterium and tritium gas) in an attempt to release energy in the form of neutrons. To understand and predict target behavior during the fusion process, it is necessary to produce accurate simulations of the implosion. The equation of state (EOS) forms an indispensable part of these simulations. In this project several available EOS, both tabular and analytic, were compared. Also, the concept of interpolation from tables as an alternative to using analytic expressions was considered and the accuracy of various interpolation methods was evaluated.

1. Introduction

Currently our Earth has three major sources of energy: fossil fuels, nuclear fission, and solar energy. However, all three sources have their share of disadvantages, whether it be in atmospheric pollution, inefficiency, or limited resources. Hence the question arises: "What source of energy is clean, safe, feasible, and inexhaustible?" As we step into the next millennium, the concept of Inertial Confinement Fusion (ICF) as a viable alternative to fossil fuels, is gaining interest and momentum. Looking at our sun

as a prime example of ICF, it becomes appealing for us to try and artificially create this naturally occurring phenomenon.

ICF is characterized by a series of fusion reactions between nuclei of light elements, releasing energy in the process. The Equation of State (EOS) performs a vital role in simulating this process as it is used to determine the pressure, heat capacity, and energy of a material under all conditions of temperature and density. Therefore, EOS is useful in not only understanding ICF, but also in predicting the end result.

As of now, there are four EOS tables that are available for computer simulations at LLE. They include SESAME tables³ (from Los Alamos National Laboratory, NM), LEOS tables² (from Lawrence Livermore National Laboratory, CA), tabular Thomas-Fermi tables⁴ (from Laboratory for Laser Energetics, NY), and Thomas-Fermi analytic tables¹ (from Rutherford Appleton Laboratory, UK). All four tables provide EOS for aluminum, plastic, and a 50/50 deuterium/tritium gas (all of which are present in most targets). One objective of this project was to compare the different tables, keeping in mind the fact that for cold and warm dense plasma (near solid densities and temperatures from 0.01 to 100 eV) equations of state are not well known. Another goal was to create a new equation of state table, from the analytic EOS, primarily to produce faster run-times on computers. This permitted us to study interpolation methods and their accuracy.

2. Comparison of EOS tables

Before discussing the similarities and differences between the EOS tables, it is helpful to introduce the units of measurement that are consistently used across all four tables mentioned in section 1. Temperature is measured in electron volts ($1\text{eV} = 11604\text{K}$),

density is measured in grams per centimeter cubed (g/cm^3), pressure is measured in megabars (Mb), energy is measured in ergs per atom (ergs/atom), and finally heat capacity is measured in ergs per atom per degree Kelvin (ergs/atom/ $^\circ\text{K}$). Temperatures of interest range from 2.5×10^{-2} eV (room temperature) to 32 keV, while the densities range from $1.e-3$ to 1000 g/cm^3 .

First, we compare the pressure of deuterium gas between SESAME and LEOS (Fig. 1). The relative agreement between two independent tables increases our confidence in the accuracy of these tables. Next, we compare the analytic and tabular Thomas-Fermi EOS for pressure, energy, and heat capacity, each as a function of temperature and density. Thomas-Fermi EOS needs a quantum mechanical correction to describe conditions for a warm dense plasma. A correction is applied only to the electron pressure in the tabular Thomas-Fermi and to all quantities in the analytic Thomas-Fermi EOS. As a result, while both tables agree fairly well in computing pressure (Fig. 2), they disagree to a large extent when calculating energy (Fig. 3) and heat capacity (Fig. 4). As expected all three variables show good agreement in the ideal gas region ($T > 1 \text{ keV}$).

Since the analytic and tabular Thomas-Fermi EOS differ, we turn to SESAME and LEOS to resolve the disagreement, or at least distinguish the correct table from the incorrect. Comparing the analytic Thomas-Fermi EOS with SESAME confirms that the analytic code is more accurate than tabular Thomas-Fermi for pressure (Fig. 5) and energy (Fig. 6), but not for heat capacity (Fig. 7). Similar comparisons with respect to aluminum confirm the above conclusions as seen in Figs. 8, 9, and 10.

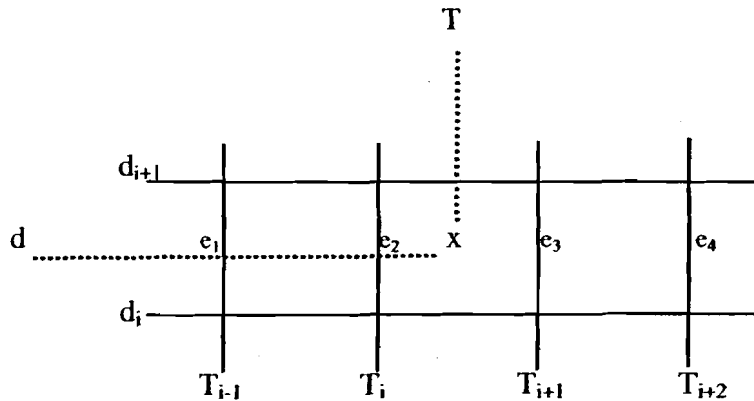
Thus, the conclusion obtained from comparing the EOS tables is that the analytic Thomas-Fermi EOS is more reliable than the tabular Thomas-Fermi EOS (except for heat

capacity). In addition to being more accurate, the analytic EOS is advantageous because it finds pressure or heat capacity for any specific values of temperature and density, whereas the tabular EOS needs to be interpolated.

3. Interpolation methods

The analytic EOS gives us the opportunity to test interpolation methods and to check whether interpolation from tables is faster than calculating analytic expressions. To that end, a table was created from the analytic EOS, which we call "tabulated analytic EOS".

When comparing interpolation methods with analytic computation, the two major factors involved are speed and accuracy. To find the values for pressure and energy, we decided to interpolate from the tabulated analytic EOS. However, to find the specific heat, we need to calculate the derivative of the interpolated energy value. The following methods were used to find interpolated values for the energy (e) and the specific heat (C_v) at point x with values T and d for temperature and density:



The energy was interpolated using two methods:

1. The first method calculates the derivative at $e(t_i, d_i)$, to approximate the behavior of the curve at point x .

$$e(T, d) = e(T_i, d_i) + \left(\frac{de}{dd_i} \right)_{d_i} (d - d_i) + \left(\frac{de}{dT_i} \right)_{d_i} (T - T_i)$$

$$e(T, d) = e(T_i, d_i) + \frac{e(T_i, d_{i+1}) - e(T_i, d_i)}{d_{i+1} - d_i} (d - d_i) + \frac{e(T_{i+1}, d_i) - e(T_i, d_i)}{T_{i+1} - T_i} (T - T_i)$$

(1)

2. The second method interpolates bi-linearly (in two directions). Thus, first we interpolate along the temperature axis over the densities, and then along the density axis over the temperatures, to approximate the value of the curve at point x .

$$e_2 = e(T_i, d_i) + (d - d_i) \frac{e(T_i, d_{i+1}) - e(T_i, d_i)}{d_{i+1} - d_i}$$

$$e_3 = e(T_{i+1}, d_i) + (d - d_i) \frac{e(T_{i+1}, d_{i+1}) - e(T_{i+1}, d_i)}{d_{i+1} - d_i}$$

$$e(T, d) = e_2 + (T - T_i) \frac{e_3 - e_2}{T_{i+1} - T_i} \quad (2)$$

The specific heat, which is the first derivative of energy with respect to temperature at constant volume, was interpolated using one method.

1. This method first calculates the 'centered' derivatives at the temperature grid points from the interpolated values e_1 , e_2 , e_3 , and e_4 as defined when deriving Eq. 2.

$$e'_2 = \frac{e_3 - e_1}{T_{i+1} - T_{i-1}} \quad e'_3 = \frac{e_4 - e_2}{T_{i+2} - T_i}$$

Now the value at x can be found by linearly interpolating over the temperature.

$$C_v = \frac{d\{e(T, d)\}}{dT} = e'_2 + \left(\frac{e'_3 - e'_2}{T_{i+1} - T_i} \right) (T - T_i). \quad (3)$$

We considered evaluating spline interpolation for speed and accuracy, but it still remains to be done.

3.2 Accuracy and speed of interpolation methods versus analytic computation

When comparing the interpolation methods for energy with the analytic EOS code, the second method was more accurate (Fig. 11), showing less than 0.3 percent error. When comparing the interpolation methods for specific heat with the analytic EOS code (Fig. 12) results showed less than 1 percent error. Thus, the interpolation methods show good accuracy.

When computing the run-time, both interpolation methods ran at about the same speed, and were both more than 200 times faster than the analytic EOS code. When both codes were looped 1 million times, the interpolation code was completed in 0.12s while the analytic code took 28.47s. Even with this enormous time difference, it is actually possible to widen this gap even further by traversing the table more efficiently (performing a binary search rather than a sequential search). Our conclusion is that the

speed of the interpolated EOS outweighs any slight inaccuracies in the methods and is a very efficient method of calculating EOS quantities.

3.2 Scaling of tabulated values before interpolation

The density and temperature grid points in the SESAME and LEOS tables are obtained by dividing \log_{10} decades into equal spacing. The resulting grid points are then not equally spaced. We call these tables "logarithmically scaled" tables. The analytic EOS table was created with the same grid pattern. In an attempt to improve the accuracy of the interpolation, we created a "linearly scaled" analytic EOS table consisting of the \log_{10} of all values. The resulting temperature and density grid points are then equally spaced. Certainly, it seems that a logarithmic curve would be harder to bi-linearly interpolate than a linear curve. However, when the two were compared, it was found that logarithmically (Fig. 12) interpolating was actually more accurate than linearly interpolating (Fig. 13):

$$\text{Logarithmic interpolation: } \frac{de}{dt} \text{ (same as Eq. 3)}$$

$$\text{Linear interpolation: } \frac{de}{dT} = \frac{d \ln e}{d \ln T} \left(\frac{e}{T} \right)$$

Linear interpolation is inaccurate because it involves not only calculating the derivative, but also multiplying by the energy value. This is the problem because the energy values can be several magnitudes apart between two temperature grid points. This becomes clearer when looking at figure 12, in which the specific heat (C_v) takes a big jump at a temperature of 1eV because the energy graph shows a very steep gradient at that

temperature. Thus we conclude that, for general interpolation linear scaling is appropriate, but when taking the derivative it is better to use logarithmic scaling.

4. Conclusion

This project produces three conclusions. Firstly, it was found that the Thomas-Fermi analytic EOS matched SESAME and LEOS tables more closely than tabular Thomas-Fermi EOS, which makes the analytic EOS more accurate and reliable. Secondly, we found that interpolating from tables is more than 200 times faster than analytic calculation. This led to the creation of another EOS table - the interpolated or tabulated analytic EOS. Finally, in general, linear scaling enables the tabulation of more accurate interpolated values. However, when interpolation requires computing derivatives, logarithmic interpolation is more accurate.

Acknowledgements

First and foremost, I would like to sincerely thank my advisor Dr. Jacques Deleltrez for not only his time and advice, but also for his continued patience and support. My experience at LLE would not have been the same without him. I would like to give a special thanks to the many scientists in the lab, especially those in the theory division Drs. Radha, Epstein, and Town, who were both approachable and helpful. Finally, I would like to thank the other students of the program for truly making this experience a memorable one.

References

1. A.R.Bell, "*New Equations of State for Medusa*", Report FL-80-091, Rutherford Appleton laboratories (1980).
2. D.A.Young, (private communication, 2000)
3. J. Abdallah Jr. et al, HYDSES, "*A subroutine package for using SESAME in Hydrodynamic codes*", LANL report LA-8209 (1980)
4. S. Skupsky, (private communication, 1975)

Total pressure of DT as given by SESAME and LEOS tables

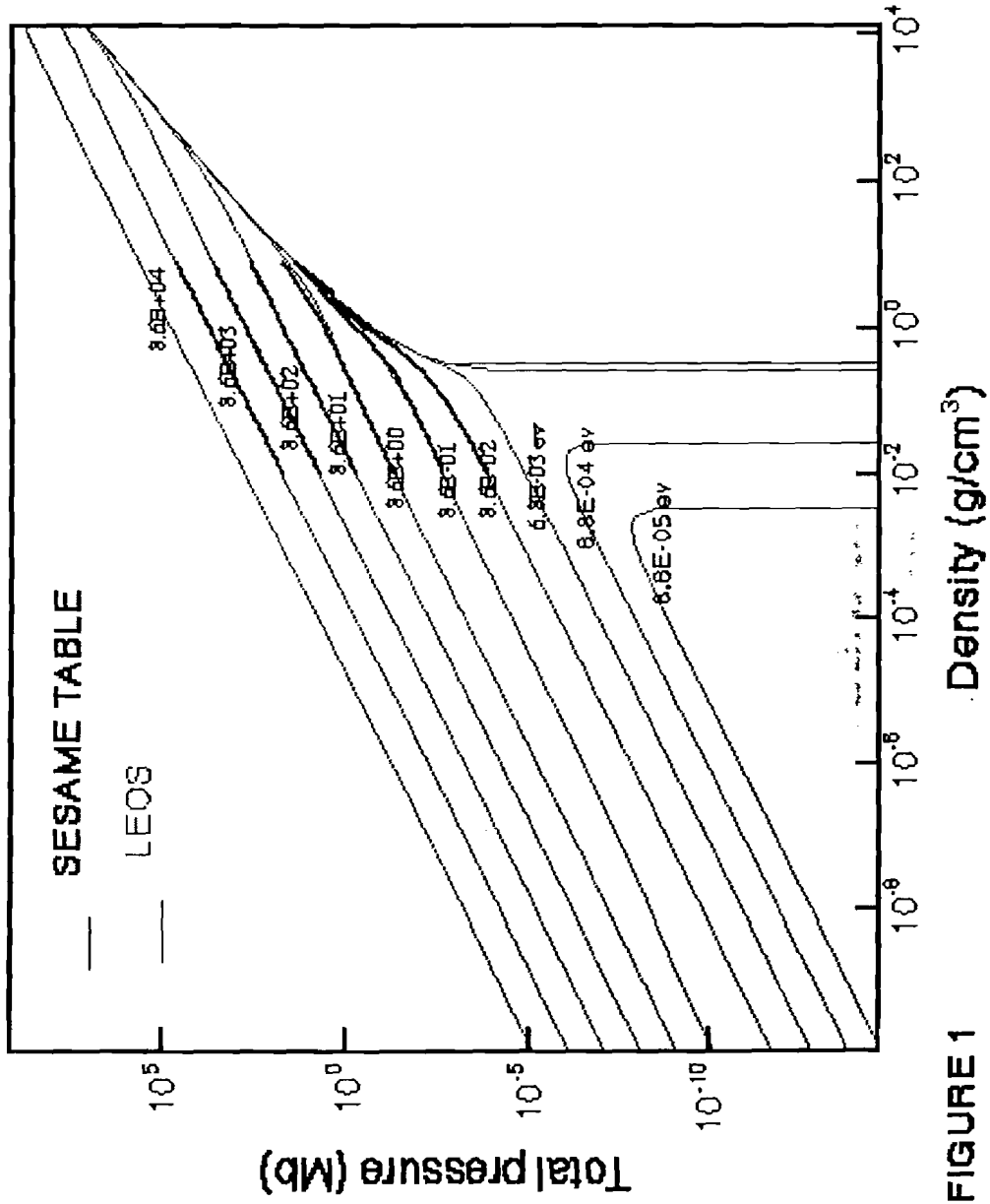


FIGURE 1

Comparing the pressure of DT between
TF analytic and tabular TF

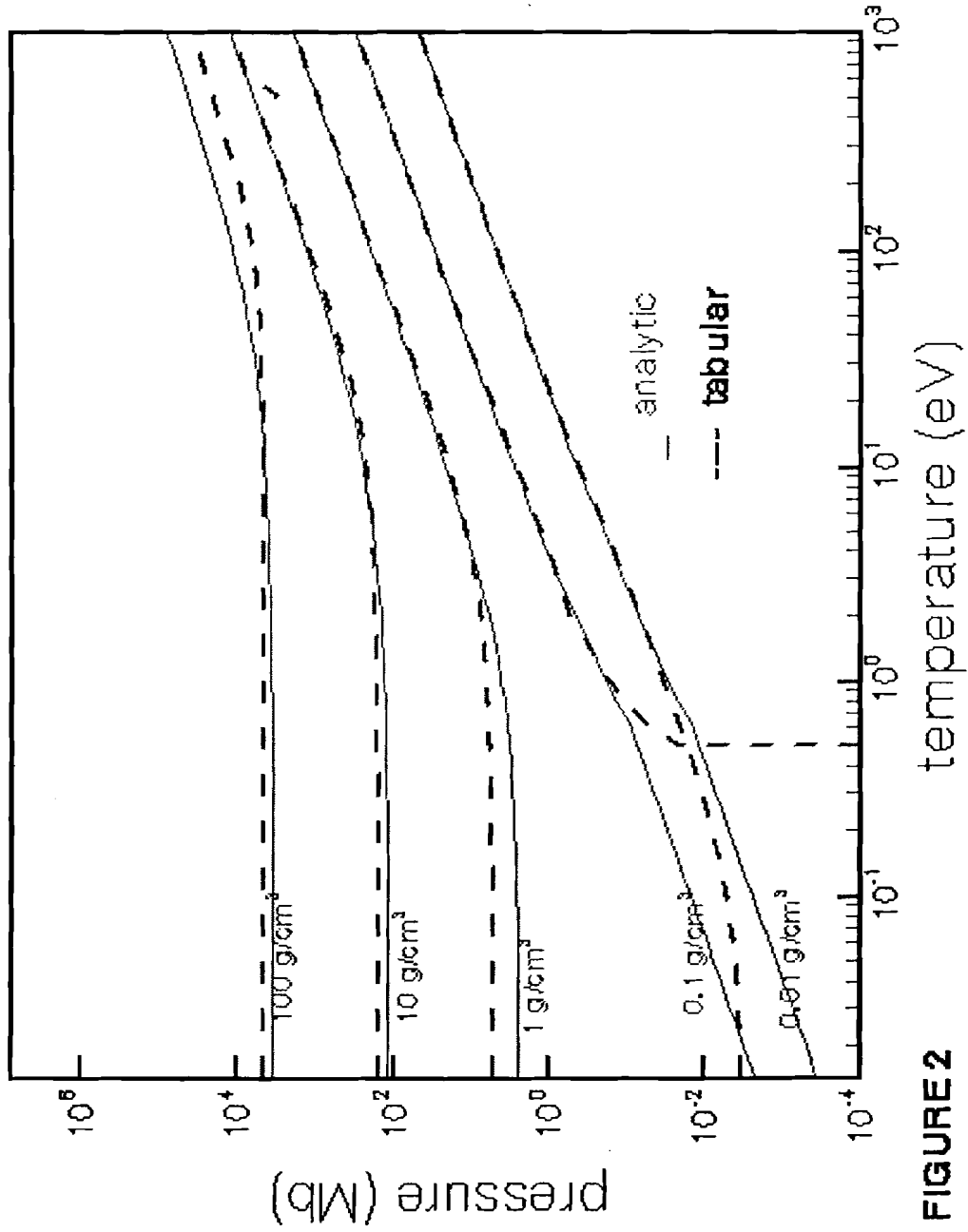


FIGURE 2

Comparing the electron internal energy of DT
between TF analytic and tabular TF

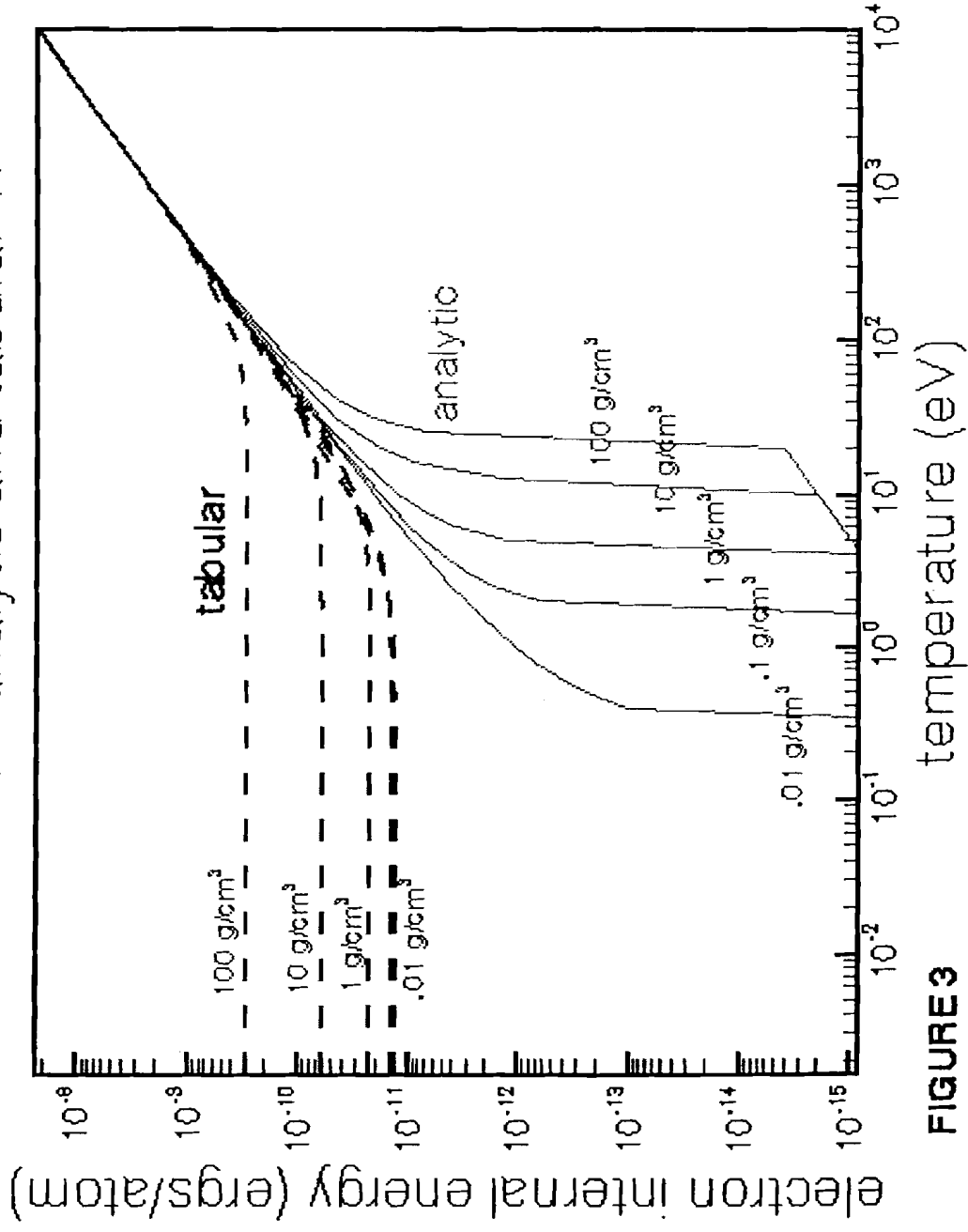


FIGURE 3 temperature (eV)

Comparing the electron specific heat of DT
between TF analytic and tabular TF

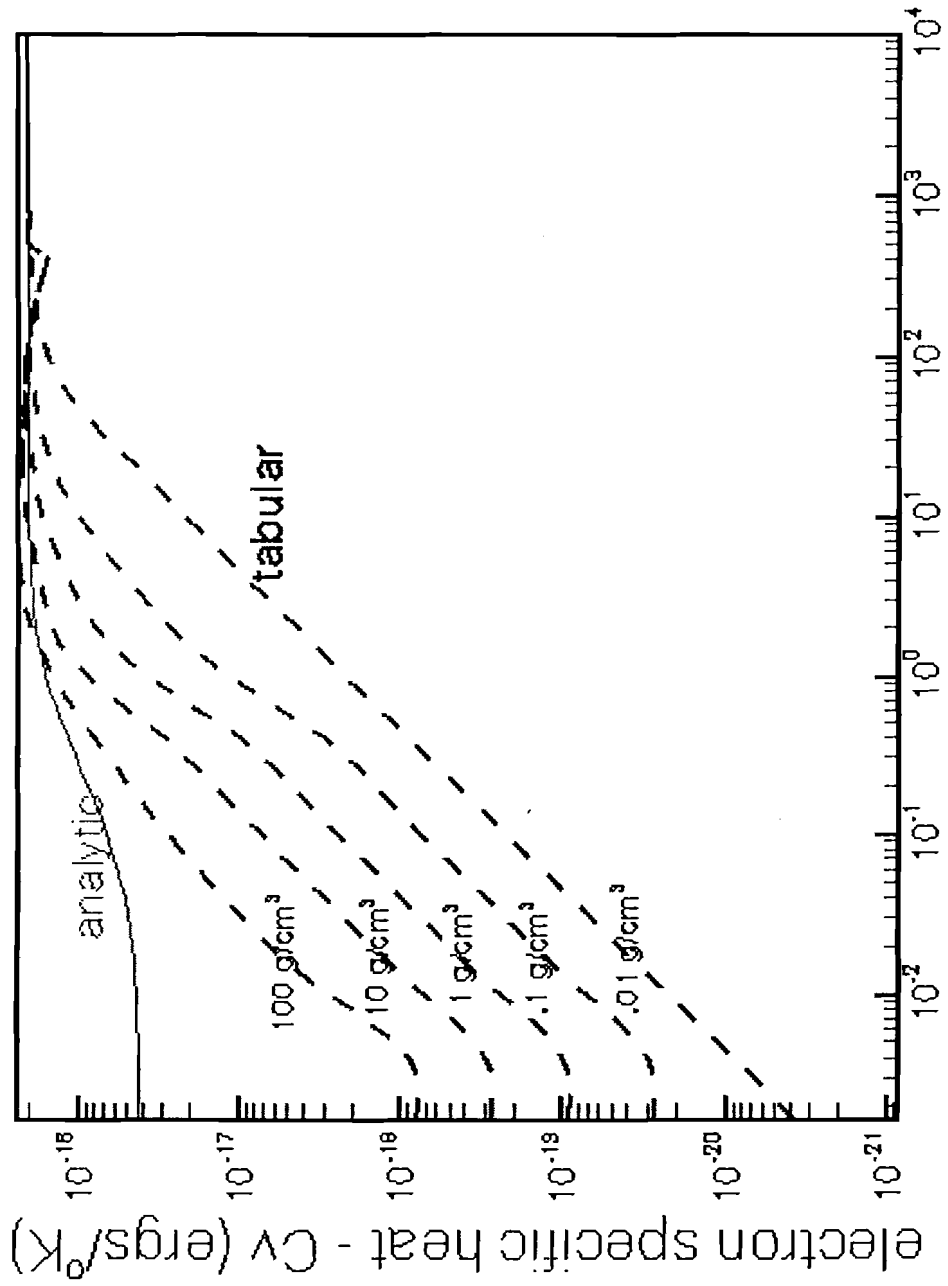


FIGURE 4 temperature (eV)

A comparison of DT pressure
between Sesame and TF analytic

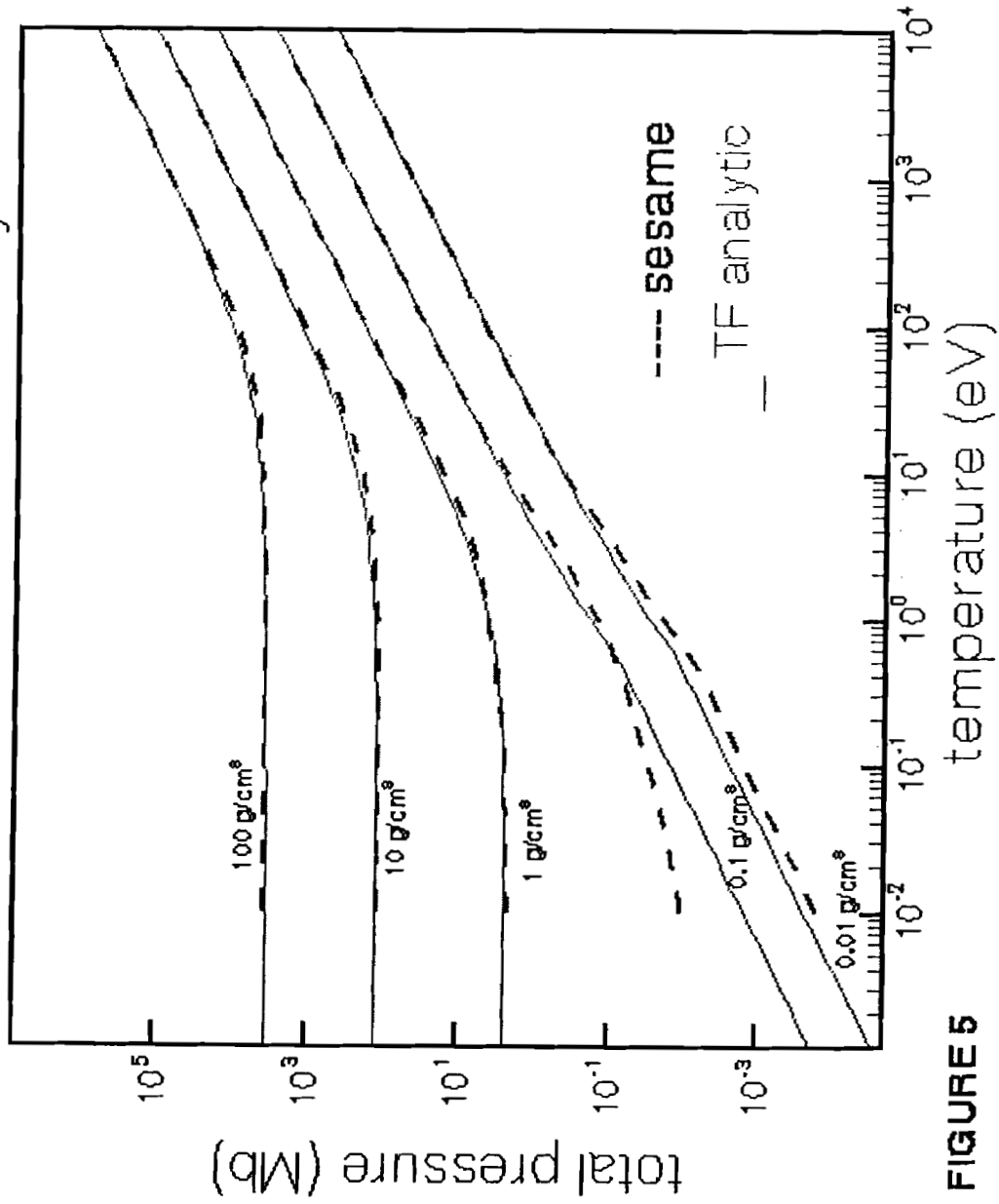


FIGURE 5

Comparing sesame and TF analytic tables for electron internal energy

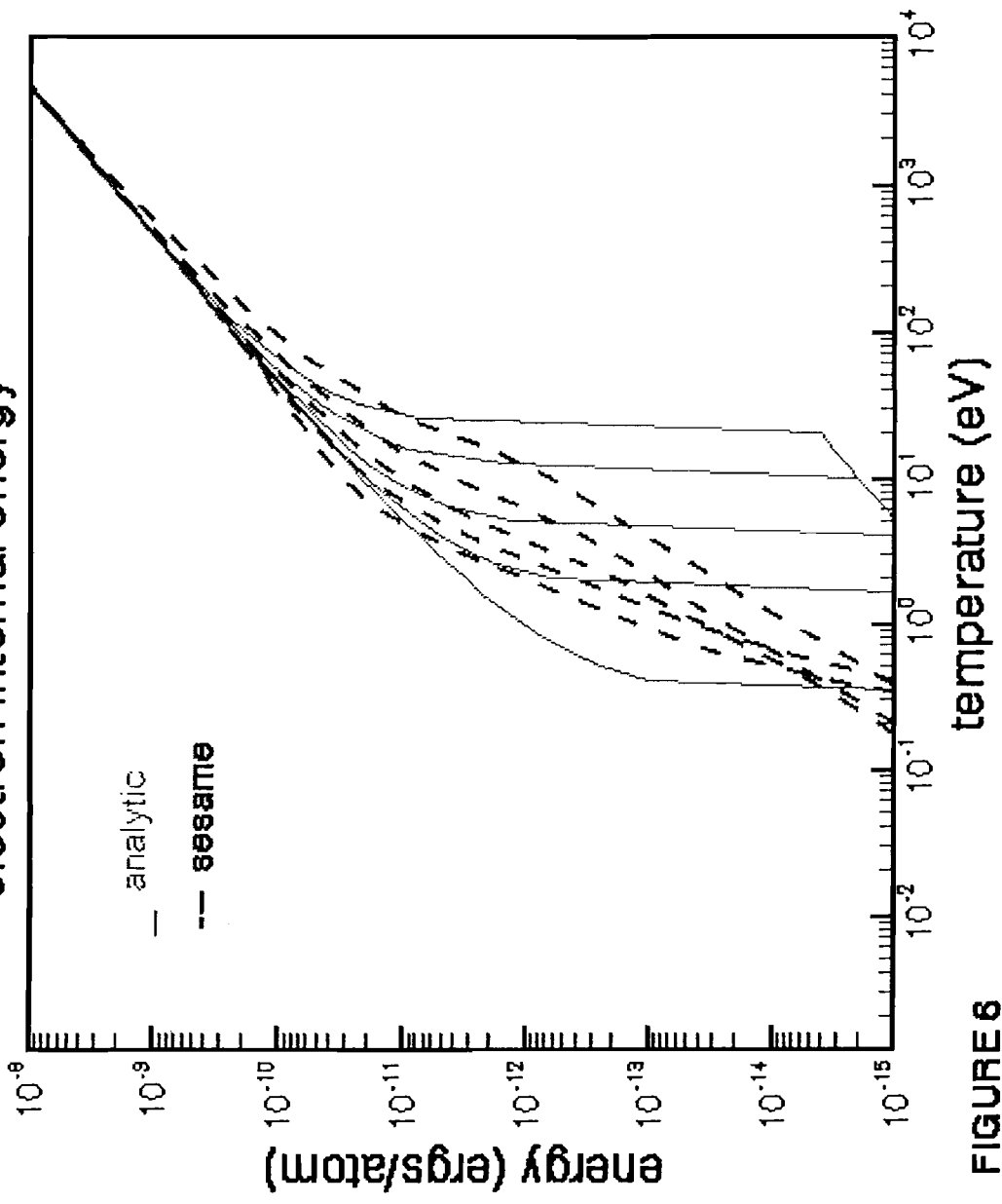


FIGURE 6

Comparing sesame and TF analytic tables for specific heat

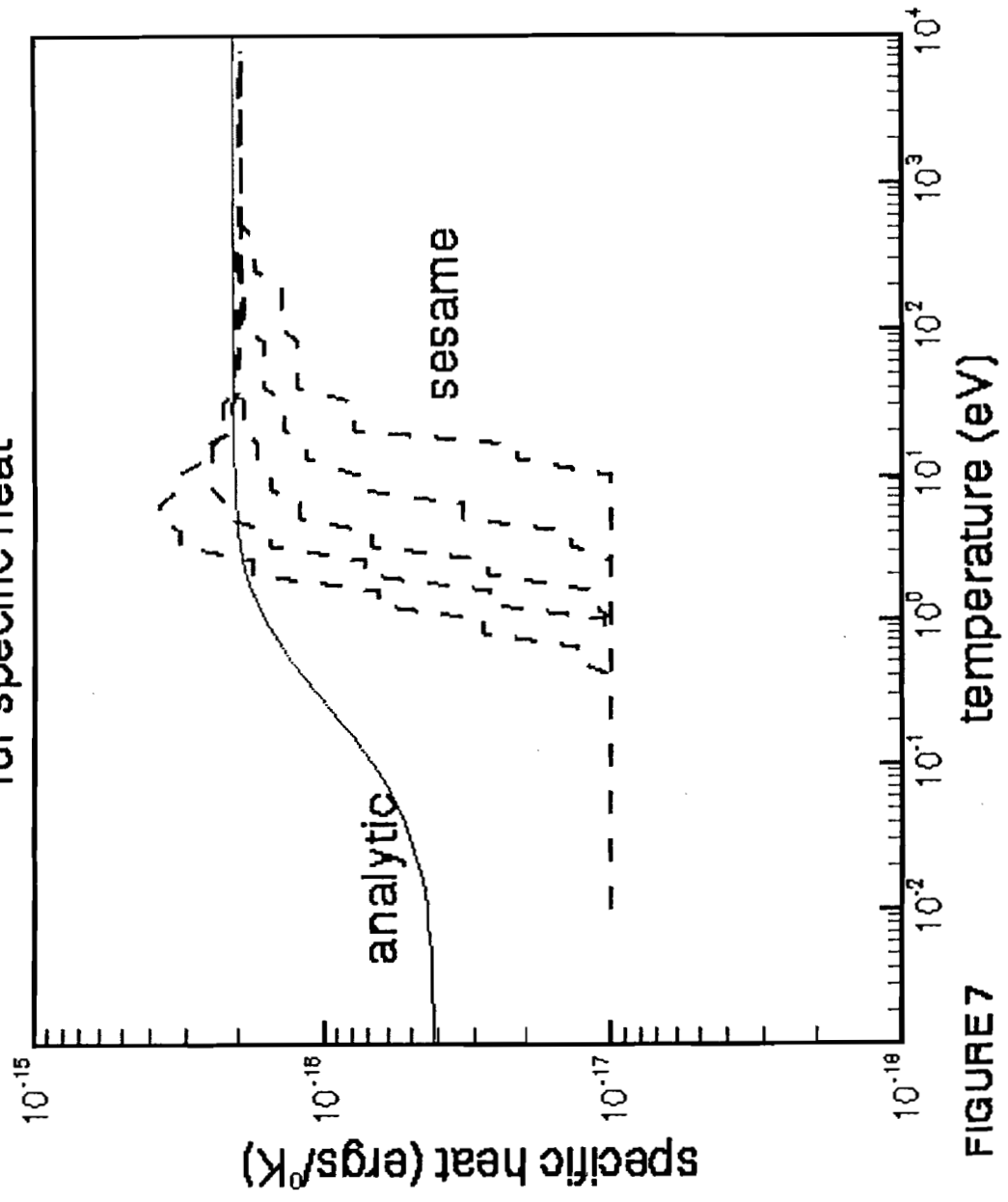


FIGURE 7

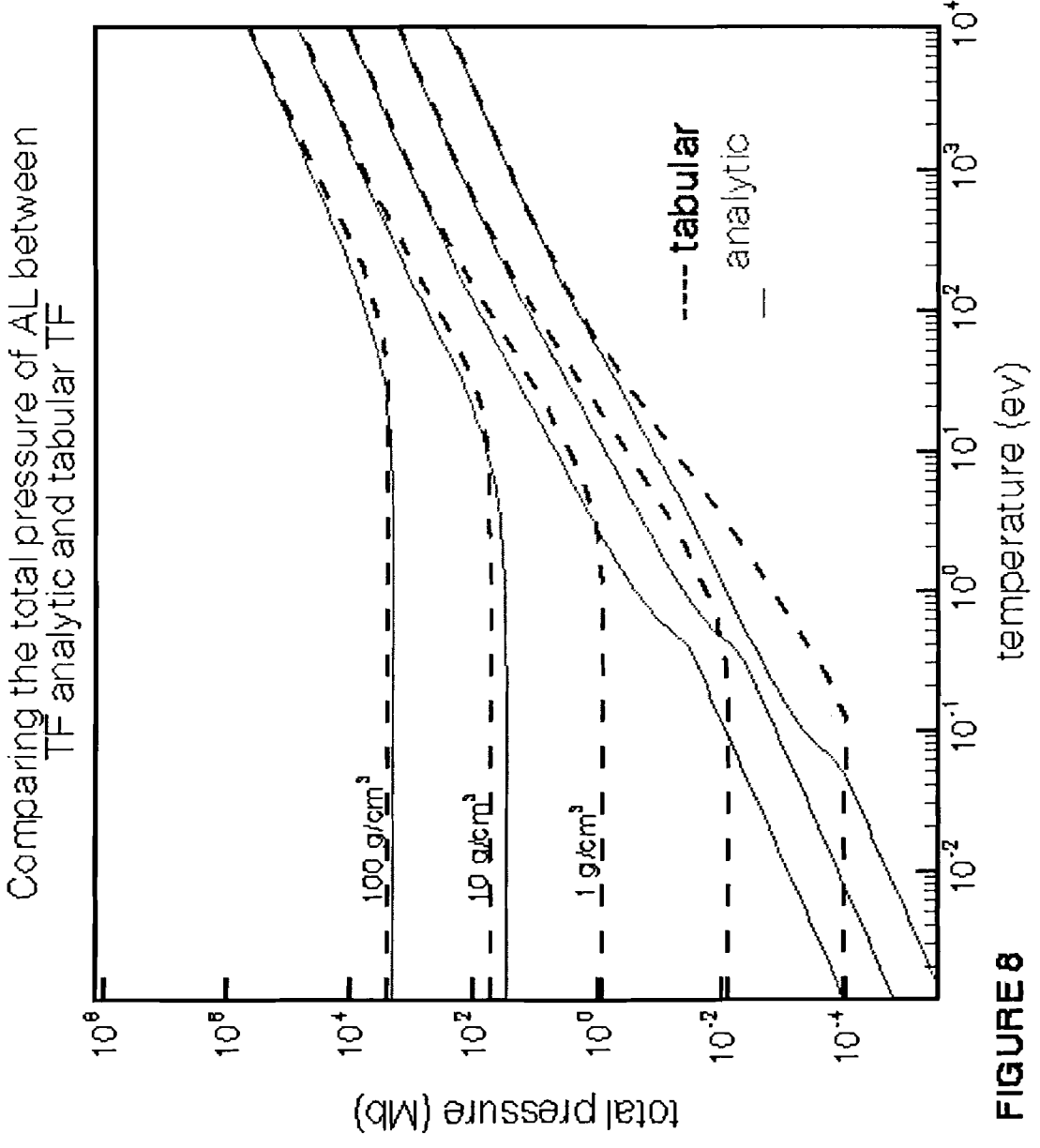


FIGURE 8

Comparing the electron internal energy of AL
between TF analytic and tabular TF

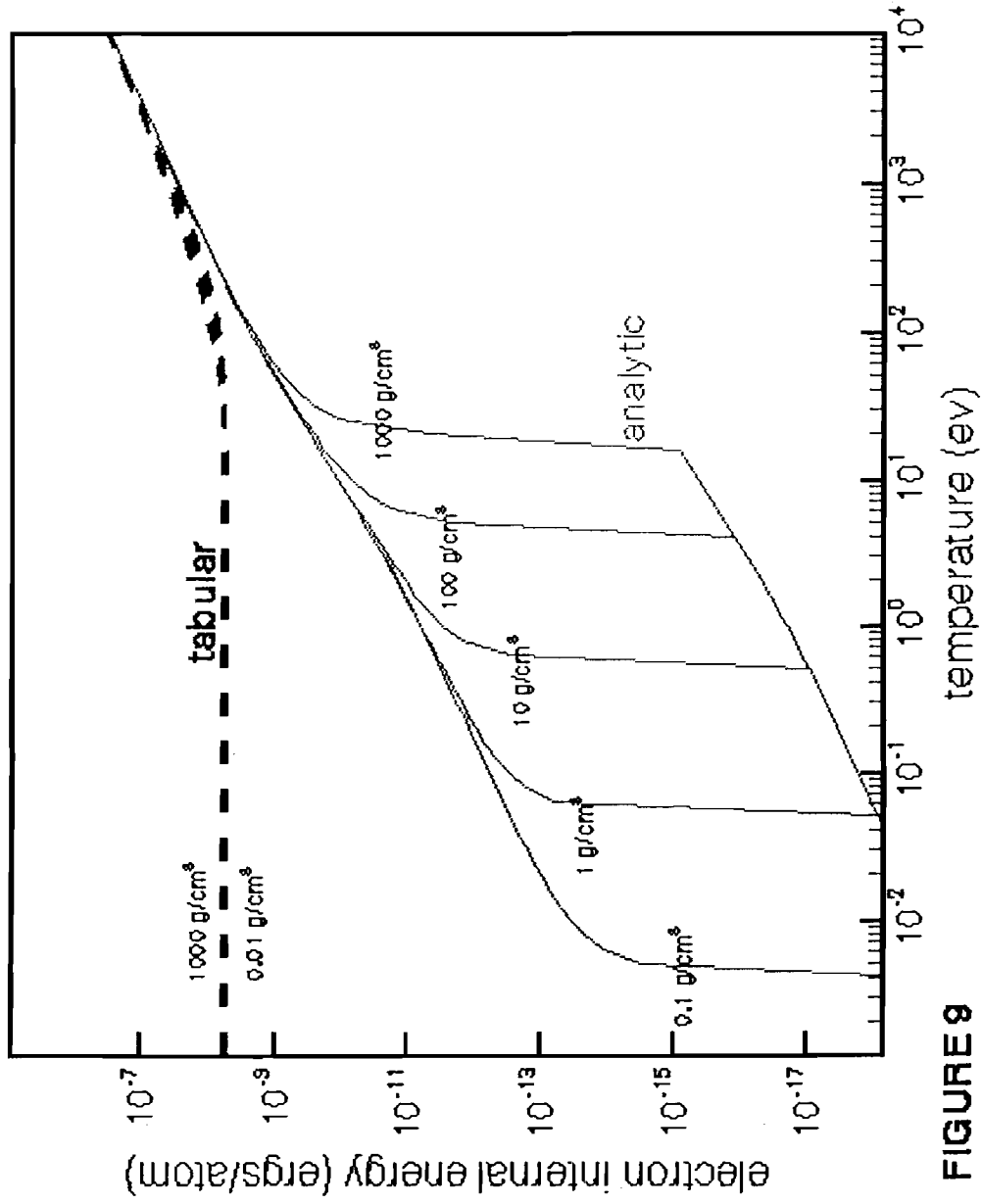


FIGURE 9

Comparing the specific heat of AL between
TF analytic and Tabular TF

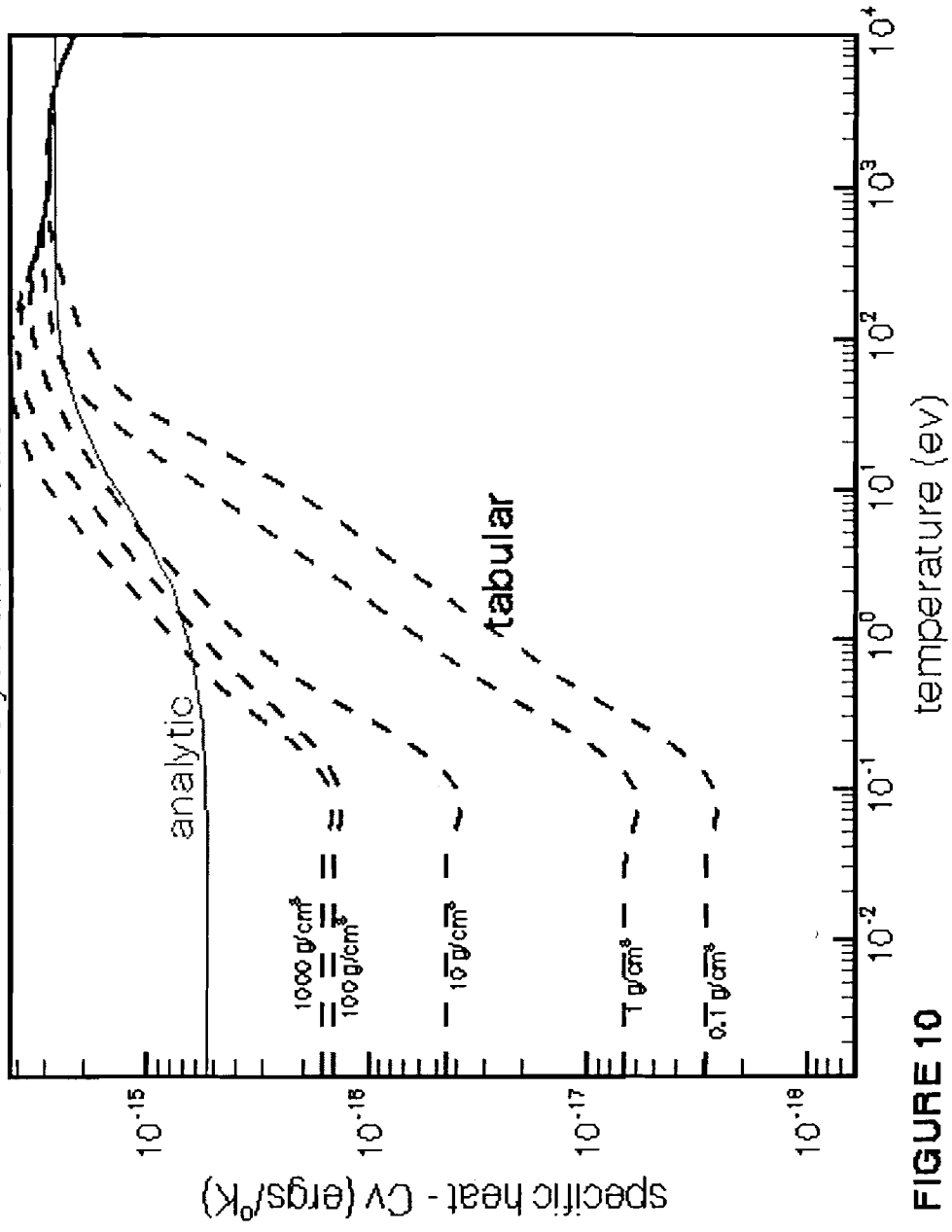


FIGURE 10

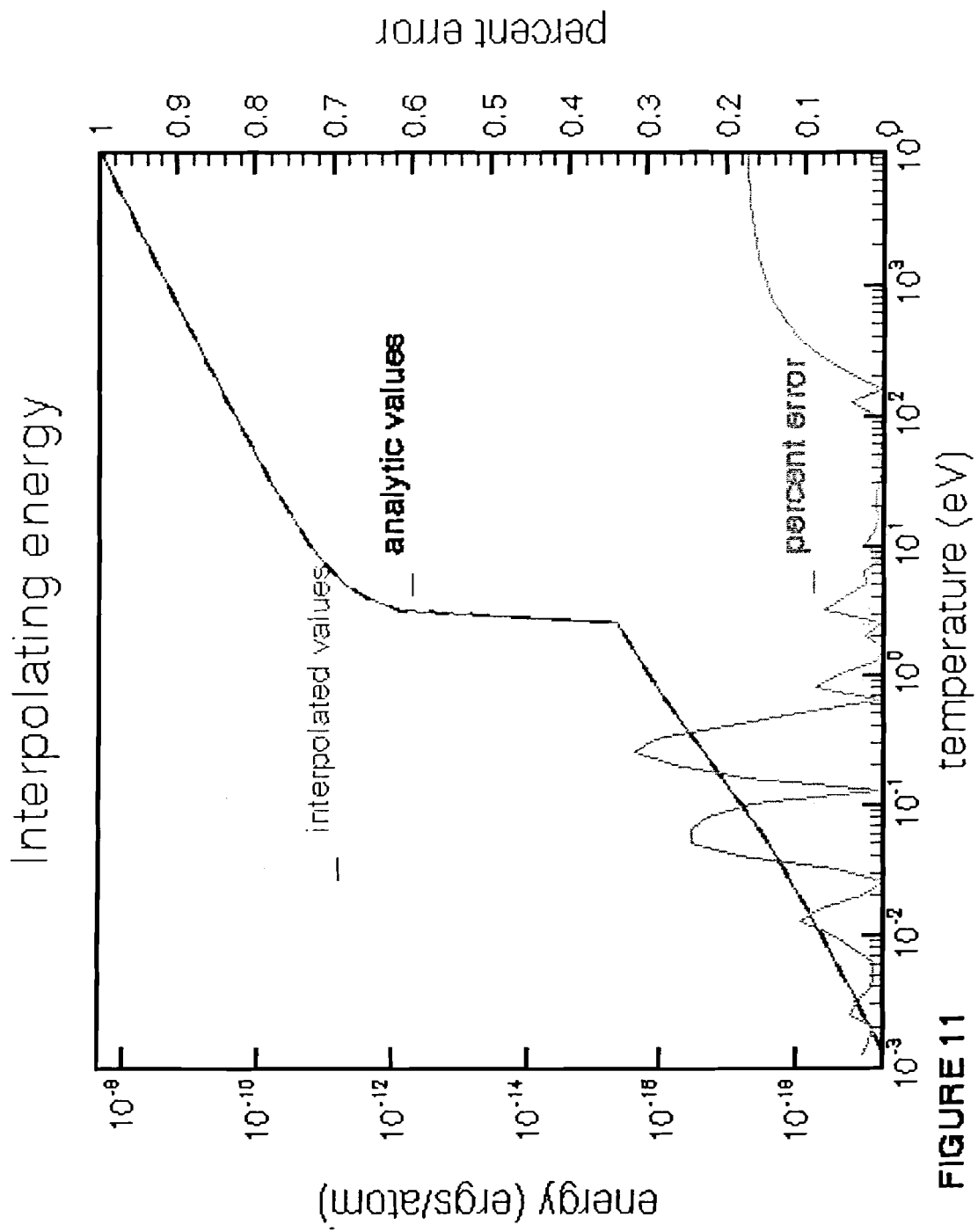


FIGURE 11

Logarithmically Interpolating specific heat

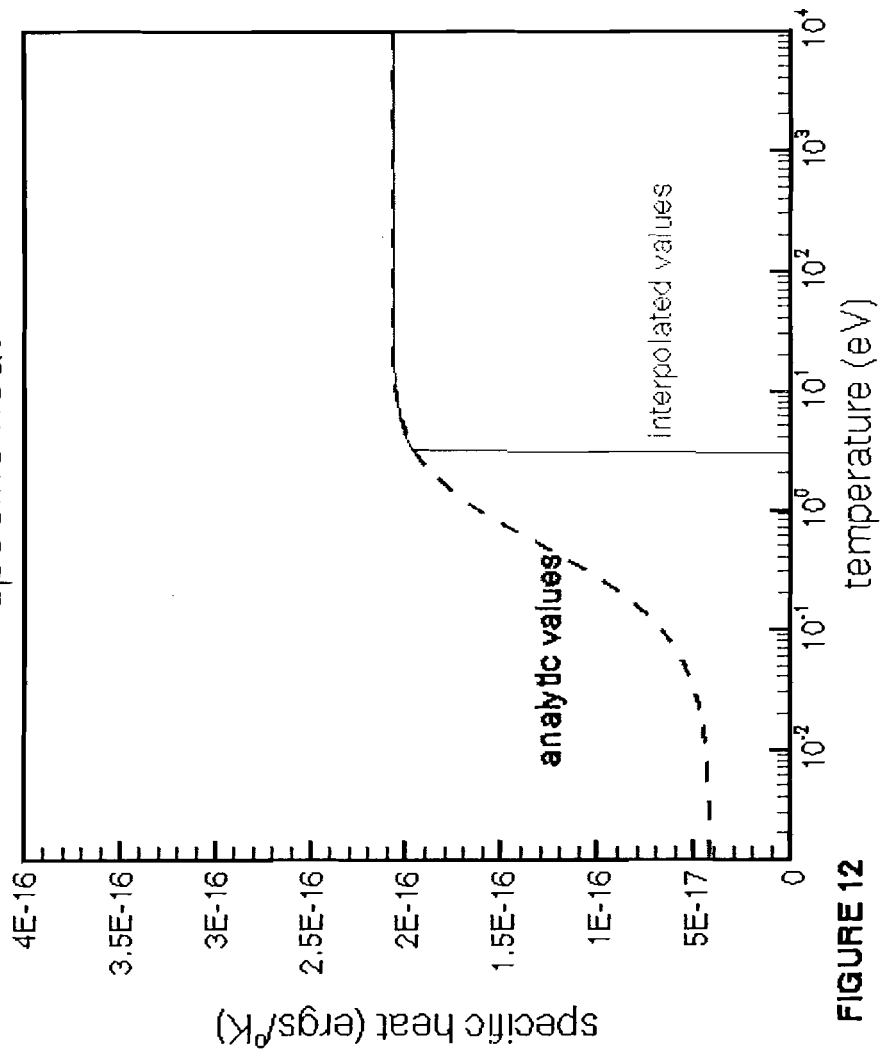


FIGURE 12

Linearly interpolating specific heat

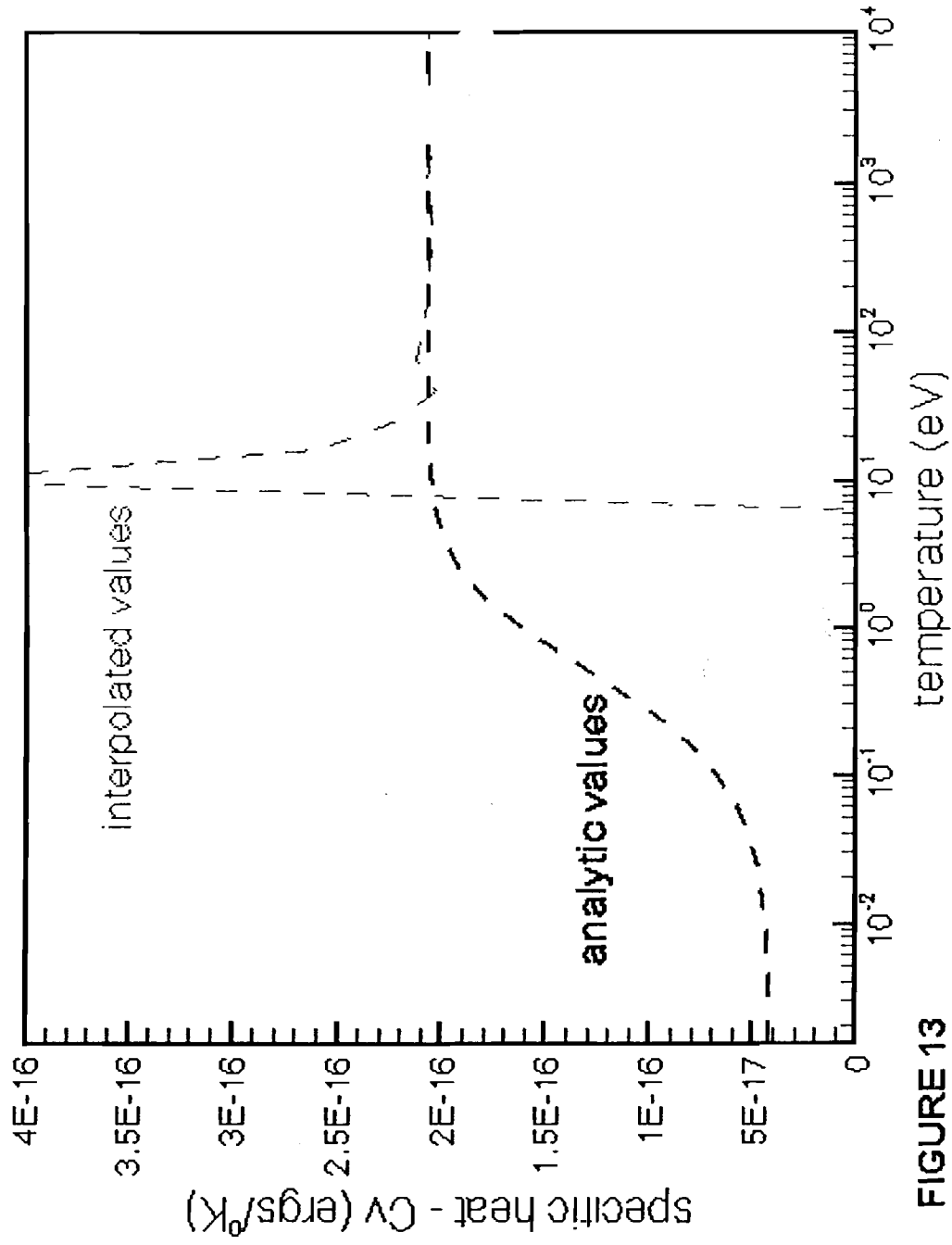


FIGURE 13

Characterization of Ultrafast Superconducting Optoelectronic Devices

John Savidis
University of Rochester's
Laboratory for Laser Energetics
Advisor: Professor Roman Sobolewski
Summer 2000

Abstract:

Superconductors are materials that exhibit zero resistivity and ideal diamagnetism below a certain critical temperature, current and magnetic field. Zero resistivity is achieved by the formation of Cooper pairs (CP), which are paired electrons with opposite wave vectors and spins that are bonded together through electron-phonon interactions. In 1962, Brian D. Josephson theorized that CP's were capable of tunneling through an insulating barrier of a superconductor-insulator-superconductor (SIS) junction [2]. The phase coherence of these CP's produces unique electronic attributes of superconductive materials. Research in the field of low temperature superconductivity has focused on using Josephson junctions (JJ) for applications in digital electronics [5]. The JJ response that is produced when the junction switches into a resistive state is the single-flux quantum (SFQ). This is a voltage response that is equivalent to a logic "1" and could be used in superconducting digital circuitry.

Since the discovery of high temperature superconductors (HTS) in 1986 [1], much research and development has been carried out on these materials. Using Josephson junctions based on $\text{YBa}_2\text{Cu}_3\text{O}_{7-x}$ (YBCO) thin films, junction devices can generate ~ 1 picosecond wide pulses, corresponding to ~ 3 Terahertz operating speeds.

Many problems arise due to the physical limitations of terahertz operation of JJ's. Using JSPICE simulations and experiments, we characterized JJ properties for further understanding of the junction physics itself, as well as JJ applications in superconducting digital circuitry [7]. Experimentally, our ultrafast electronic circuits were measured using electro-optic sampling, which is sufficiently fast and sensitive to test the SFQ circuit performance.

With the possibility of using JJ's in digital circuitry, many parameters of the circuit require evaluation for further understanding. One motivation for simulation is testing the switching dynamics of grain-boundary JJ's that produce picosecond-wide single-flux quantum responses, which are applicable in digital circuitry. Simulations also investigate parameters of very fast optoelectronic circuitry to understand what input pulse requirements are necessary for the JJ operation.

As mentioned in the abstract, superconductors are materials that exhibit zero resistivity and ideal diamagnetism. Superconductive properties, however, are only maintained below a certain critical temperature, DC-current density and magnetic field, specific for various materials. Exceeding any of the critical parameters results in the loss of superconducting properties.

Both zero resistivity and ideal diamagnetism are a direct result of an attractive electron-electron interaction, mediated by phonons for conventional superconductors [1]. These interactions lead to the formation of pairs of electrons with opposite wave vectors and spins. These Cooper pairs are capable of tunneling across the potential barrier of a S-I-S junction. Figure 1 is a diagram of a simple JJ junction with the grain boundary cutting across the two superconducting plates [2]. The production of the grain boundary is quite simple. The S-I-S junction is made using a layer of YBCO material. It is configured by applying two substrate bases with different crystal lattice alignments and layering them with YBCO. Since there is a difference in alignment, the YBCO forms a border that has insulative properties, known as the grain boundary. Josephson predicted that below a certain critical current (I_c), there is no voltage drop across the junction, and the current is a harmonic function of the wave-function phase difference. Above the critical current, however, a voltage drop develops across the barrier, and there is a current oscillation with a frequency directly proportional to the voltage. Figure 2 is a representation of the voltage response that is generated when the critical current is exceeded.

Grain Boundary JJ

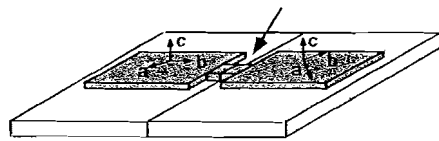


Figure 1: The single-flux quantum response is generated along the boundary as the current crosses the grain.

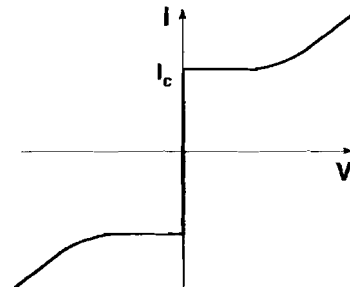


Figure 2: The occurrence of zero resistance is shown by the vertical line on the y-axis. The semi-curved line displays a current response when the junction "jumps" into a resistive state.

Currently, a relatively new and very unique approach of superconducting electronics is being pursued. It is based on overdamped JJ's [4]. Junctions with small capacitance are overdamped junctions that exhibit nonhysteretic I-V curves (see Fig. 2). These overdamped

junctions use binary representation; however, logical states are represented not by two distinct voltage states, but by JJ-generated SFQ pulses with quantized area [1]:

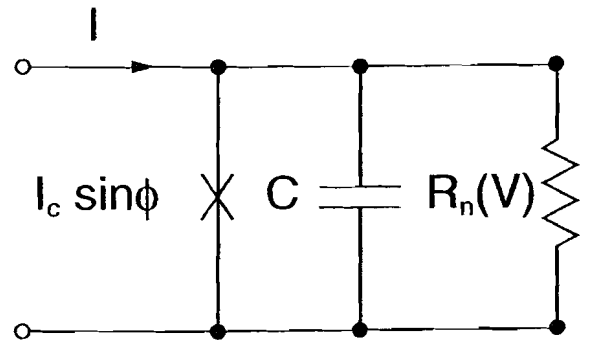
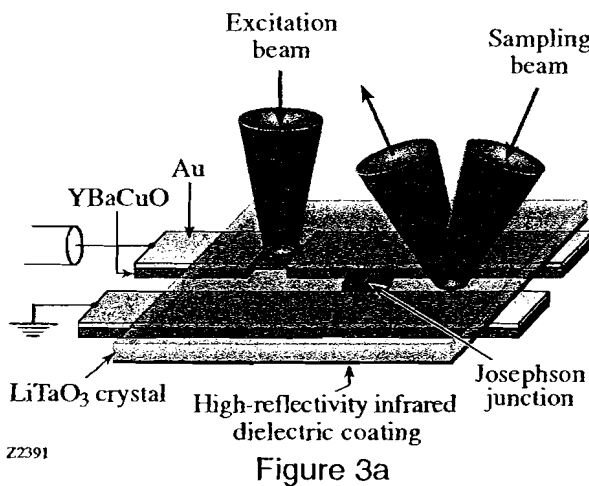
$$V_{\text{output}} \approx 2I_c R_n$$

$$\int V \cdot dt = \Phi_0 \quad (\Phi_0 \text{ is single-flux-quantum})$$

In SFQ circuits, junctions are biased just below their critical currents and a short control pulse (usually another SFQ pulse) drives the junction into a voltage state. In the voltage state, the junction produces an SFQ pulse with amplitude $\sim 2I_c R_n$ (where I_c is the critical current and R_n is the normal resistance of the junction) and pulse width $\sim \Phi_0 / 2I_c R_n$, and returns to the zero-voltage state. Since the junction remains in the voltage state for a very short period of time (single picosecond range), the power dissipated per pulse is extremely low and is in the order of $\Delta E \approx 10^{-18}$ J for junctions with $I_c = 0.5$ mA [1].

An important parameter for SFQ circuit performance is the amount of time that it takes for the junction to respond to the applied bias transient, this is the turn-on delay time (T_D) of the JJ [7]. The T_D of a junction depends on various characteristics of the input pulse well as the junction damping and capacitance. Turn-on delay seems to be a larger factor when the junction damping and capacitance are high, and also when the transient amplitude is small.

The experimental setup and equivalent circuit used in JSPICE simulations are shown below in Figures 3a and 3b [1].



In the experimental setup on the previous page, an excitation beam strikes the YBCO thin film where the gold layer was extracted. This excitation beam produces an electromagnetic pulse that propagates along the transmission line (the gap between the two plates) towards the Josephson junction. When this pulse reaches the junction, the excess current causes the junction to switch into a resistive state. This resistive state produces a voltage response, the SFQ pulse, which could be used in digital circuitry [8]. The equivalent circuit (Figure 3b) is used for the numerical simulations of the circuit response. In the simulated circuit, the input pulse propagates from the left side of the diagram to the right. The Josephson junction is represented by an X. The junction capacitance and normal resistance is added to the simulation to duplicate as many of the experimental parameters as possible. Through these simulations various properties of the input pulse as well as the junction were examined.

The critical overdrive of the Josephson junction is an important attribute that if totally understood, benefits substantially to the ongoing research of the junction. The overdrive of a junction is the amount of current required to produce a resistive state in the junction. It is the minimum current that will produce a voltage response. Figure 4 shows the mechanics behind the overdrive of a junction. In Figure 4 the junction bias is represented by the red dot in the vertical range of the I-V curve [4]. The excitation beam (current pulse) must be larger than the point where the junction loses its superconductive properties. The loss of superconductive properties implies that a voltage output is produced by the junction. The amount of current above the point where the junction is in a normal state is considered the overdrive.

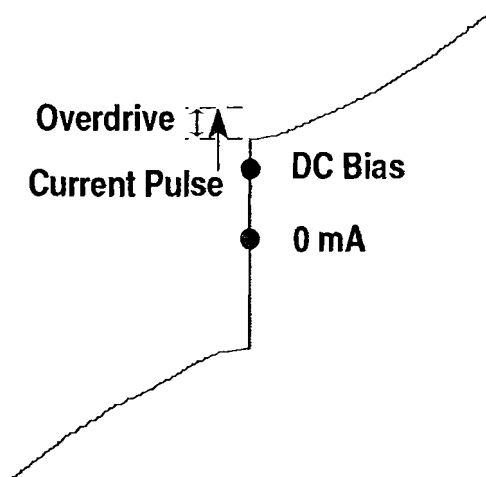


Figure 4

Variations in overdrive occur due to changes in critical current. Also, the bias current plays a significant role in junction overdrive. Using JSPICE, some unexpected results were produced that actually seem contrary to junction operation, but were substantiated by further testing with various critical currents.

As mentioned on the previous page, the unanticipated results occurred with changes in the required critical current of the junction. It was evident that a decrease in critical current

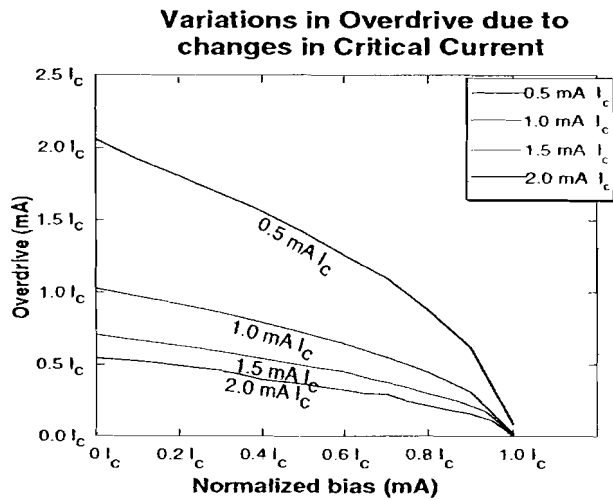


Figure 5

Pendulum Model

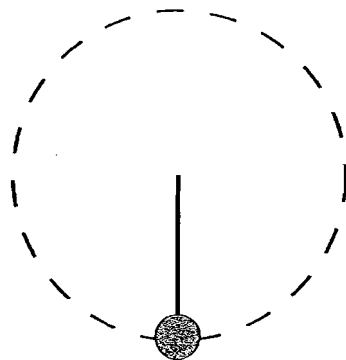


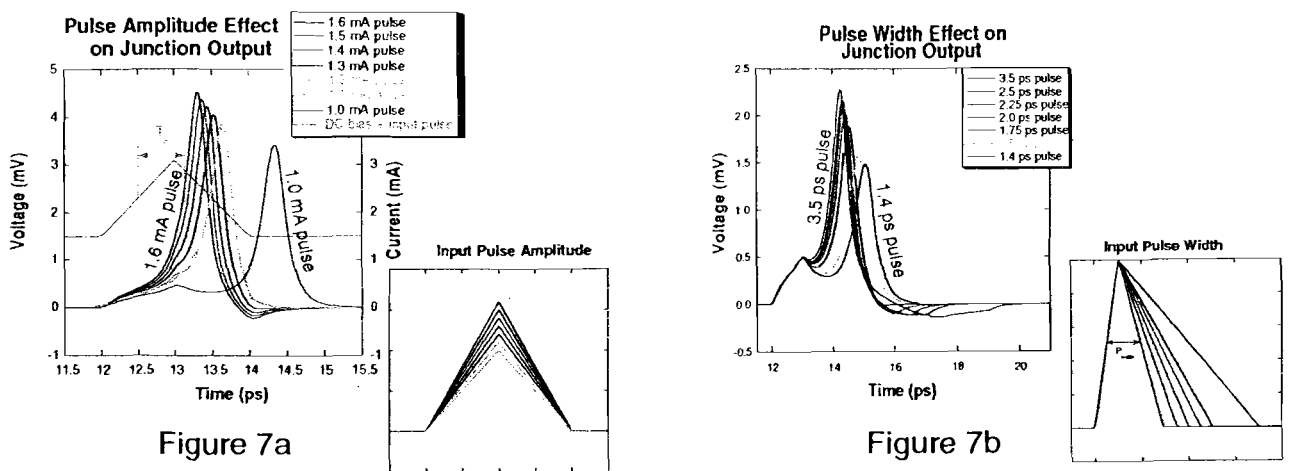
Figure 6

required a larger overdrive when intuition would believe otherwise. According to simulations, a critical current of 0.5 mA required about four times as much current (compared to itself, meaning an overdrive of about 2 mA) compared to the 0.5 mA overdrive that the 2 mA critical current needed to produce a resistive state. Figure 5 is a graph that displays an increase in overdrive as a function of decreasing the critical current. In addition, according to the graph, an increase in the DC bias at every critical current requires a smaller quantity of pulse current or overdrive to produce a response. Looking at just one curve on the graph, a junction is expected to respond with any input pulse greater than the curve. All points below the curve produce no SFQ output. This is a major contribution to superconductive studies since minimum overdrive requirements were calculated for various critical currents.

A simple model is used to describe the concept behind the overdrive of a JJ. The pendulum model (Figure 6) fully describes a response of JJ taking into consideration the overdrive parameter [9]. A complete revolution of the pendulum is equivalent to a voltage output produced by the junction. The DC bias is represented by starting the junction at a position other than the resting position.

A high DC bias is conceived by locating the pendulum closer to the top of the circle. The overdrive is the amount of power that is required to cause the pendulum to complete the full revolution. Hitting the pendulum really hard will push it over the peak and produce the SFQ output. The harder the hit, the faster and more certain a response will be produced. For example, if the pendulum is not hit hard enough, then it will not complete a full revolution, thus not producing the anticipated voltage response. It is also important to note that the pendulum will never fall below the point it is biased at.

Another important characteristic of the Josephson junction deals with the amount of time that it takes for the junction to respond to a transient pulse. Briefly mentioned before, this time delay between the pulse and the junction response is known as the turn-on delay of the JJ. There are two major factors of turn-on delay based on parameters of the input pulse. The pulse width and pulse amplitude cause similar results on junction output. Figures 7a and 7b display the similarity between outputs originating from varying pulse amplitudes and widths respectively, and also what is implied by varying pulse amplitude and pulse width.



In Figure 7a, the gray line that forms a pyramid represents a transient pulse. The other line with the arrowheads and the label T_D symbolizes the points at which turn-on delays are calculated. Turn-on delays are measured from the point at which 50 percent of the input pulse strikes the junction to approximately 65% of the junction response. It is measured in picoseconds. Usually the turn-on delay does not surpass 4 to 5 picoseconds.

Both graphs show similar trends. When either the pulse amplitude or pulse width are increased, the turn-on delay decreases. This means that the junction is responding at a faster rate than the previous simulation. Another observation was that the amplitude of the output decreased with an increase in turn-on delay. This decrease in pulse amplitude is justifiable. From the given equation on page three, the single-flux quantum voltage response is the integral of the voltage as a function of time. This SFQ response must remain constant by the equation of $V_{\text{output}} \approx 2I_c R_n$. From these two equations, it is deduced that as the turn-on delay increases from variations in pulse amplitude or pulse width, the area below the voltage curve is kept constant by a decrease of the SFQ amplitude. Smaller pulse amplitudes or widths cause junction interference, which is the area of the voltage curve before the actual response is produced. These pulses do not have the required overdrive immediately, but eventually do cause the junction to respond, thus producing longer turn-on delays. Once the basic parameters of pulse width and amplitude were tested, experimentation was necessary to produce a critical input pulse width and amplitude.

A critical input pulse width is a required width that causes the junction to respond with an SFQ output with any width exceeding the measured quantity. The input pulse width is measured at fifty percent of the pulse amplitude. Two different critical currents were examined each with variations in the overdrive. In retrospect, the overdrive is the amount of current above the critical current that are necessary to cause a junction response. Figures 8a and 8b display results on the critical input pulse width for 1 mA and 2 mA critical currents.

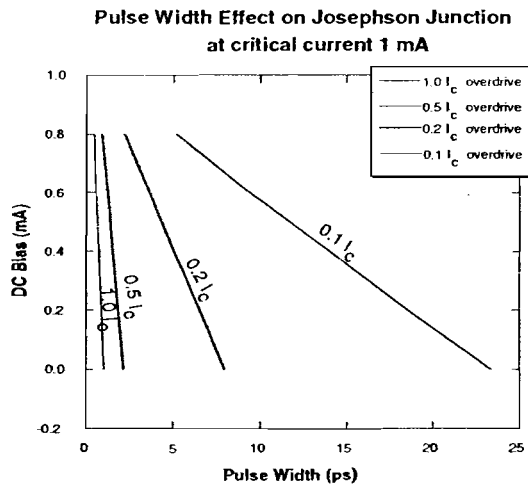


Figure 8a

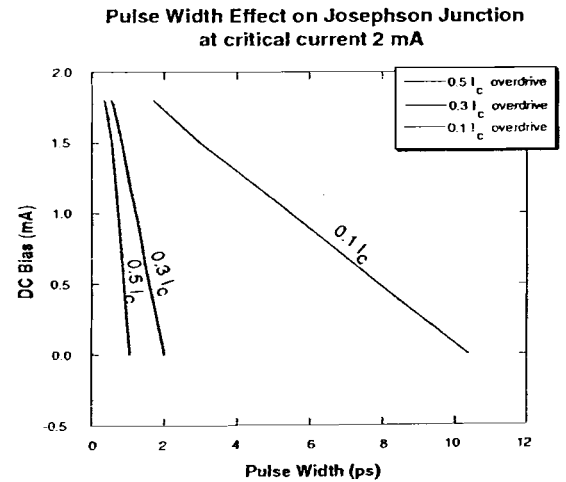


Figure 8b

From the results on the previous page, many deductions can be made. It is obvious that an increasing overdrive produces faster outputs from the junction. This is proven by the steeper sloped curves on both graphs. More importantly, an increasing overdrive requires a smaller pulse width, measured in picoseconds, to produce the SFQ pulse. Using this piece of information in the lab, high overdrives require smaller pulse widths, and therefore are capable of faster junction responses. Observations on DC bias reveal that a narrow pulse width is needed with increases in the bias. This too improves the frequency of outputs that are produced by the JJ. On both the 1 mA and 2 mA graphs, any pulse width that is greater than the lines labeled as various overdrives will cause the junction to respond. For example, looking at the $0.1 I_C$ overdrive on the 1 mA critical current, a 14 picosecond pulse will induce an SFQ at a DC bias of 0.4 mA. At the same DC bias, the JJ will respond with a 17 picosecond pulse width, but not a 10 picosecond width.

Understanding this data is crucial in formulating relevant experiments in the laboratory. For instance, knowing the pulse width that will produce SFQ's at various DC biases simplifies experimentation. It is then possible to calculate a range of optimal input pulse widths, where neither output or input pulse frequencies are hindered. If for instance, a 20 picosecond input pulse width is required for junction response, there is a 20 picosecond delay time before another pulse is processed by the JJ for usage in digital circuitry. Reducing that width to about a fourth would quadruple JJ response to excitation pulses. It is also important to note again that higher overdrives reduce pulse widths necessary for wanted results. With these factors in mind, experimentation in the lab is benefited by outcomes produced in JSPICE simulations.

Comprehending input pulse width is just the beginning. On page six it was noted that there was a similar effect on junction output with variations in input pulse width and amplitude. Therefore, there must be a dependency between input pulse amplitude and width. Using JSPICE simulations, the parameters of requirements on the input pulse were fully examined. The data collected also has much relevance to the laboratory. In general, an increase in input pulse amplitude causes a reduction in the input pulse width required to produce an SFQ response by the junction and vice-versa. Using this data and the data from the critical pulse width, an overall picture is drawn on some specified requirements to produce optimal JJ output. A range of amplitudes and widths capable of producing favorable outcomes has to be considered in experimentation. If either the input pulse amplitude or width are too large, multiple SFQ outputs are produced. Looking back on the pendulum mode on page five, hitting the pendulum too hard could cause it to revolve numerous times, which is equivalent to more than one output. This is an unfavorable outcome and therefore must be eliminated. Reducing the pulse width at a critical point requires a larger pulse amplitude for the JJ to respond.

In this fashion, reducing pulse width, which reduces delay-time for the junction to respond to following inputs, increases the required amount of input amplitude, and controlling output. Figure 9 shows the dependency of input pulse amplitude and width in greater detail. The graph compares pulse amplitude and pulse width for various DC biases for a 1 mA critical current. It is evident from the chart that an increase in pulse width reduces the necessary pulse amplitude required to produce an SFQ. With this data, experimentation adjusts for variations in either the amplitude or the width of the incoming input pulse. Closely related to pulse width, the rise time of the input pulse causes an impact on junction response.

The rise time of an input pulse is the amount of time, in picoseconds, measured from about twenty percent of full amplitude to eighty percent of full amplitude. Variations in rise time usually display changes in delay-time and reduce the required input pulse amplitude or width. In JSPICE simulations, a 1 mA critical current was tested with variations in DC bias at three different overdrives: a $0.1 I_C$, $0.2 I_C$, and a $0.5 I_C$ overdrive. Figures 10a, 10b, and 10c display outcomes with these variations in the input pulse risetime.

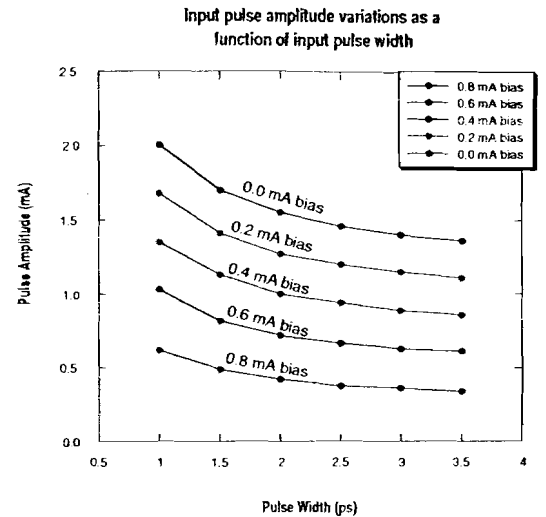


Figure 9

For a 1 mA critical current ($0.1 I_C$ overdrive)

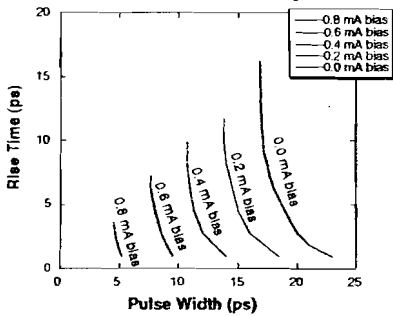


Figure 10a

For a 1 mA critical current ($0.2 I_C$ overdrive)

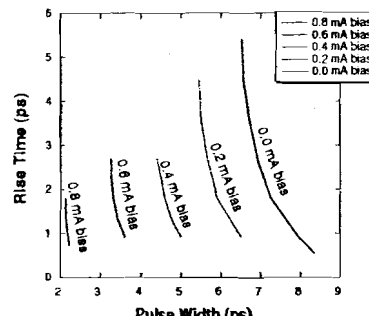


Figure 10b

For a 1 mA critical current ($0.5 I_C$ overdrive)

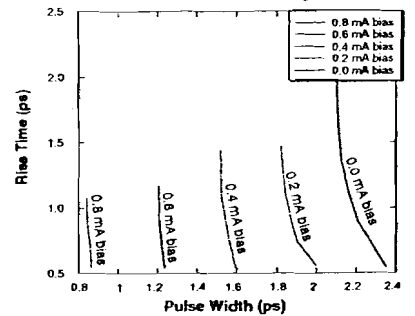


Figure 10c

From the data, it is evident that a general decrease occurs in pulse width as the rise time of the input pulse increases. This too is beneficial, especially when observing wider

input pulses. With large input pulses, increasing the rise time of the input pulse will actually reduce the pulse width, thus making the junction more efficient in processing proceeding input pulses. In addition, looking at individual graphs, a higher DC bias reduces either the pulse width or rise time requirements. Therefore, changes in the bias are crucial for optimal junction response, as mentioned before. It is also important to note that at each DC bias, a response occurs to the right of the curve, while no SFQ is produced on the left side.

In conclusion, all characteristics of the input pulse are crucial for the Josephson junction to respond as predicted. A change in one variable produces variations in the expected results. Through JSPIICE simulations, variations in input pulse parameters were experimented with, and it was evident that their correlation is very intertwined. This means that changing one parameter produces a change in other parameters, and if used correctly could be very beneficial to experiments performed in the lab. Further understanding of these properties is extremely beneficial to further comprehending the junction physics and to possibly develop superconducting digital circuitry using JJ as a means of producing voltage responses equivalent to logic 1 in contemporary circuitry.

Acknowledgements

I would like to begin by thanking Dr. Craxton for accepting me into this years Summer 2000 research program at the University of Rochester's Laboratory for Laser Energetics. His time and effort organizing the program is greatly appreciated. I'm also grateful to Dr. Roman Sobolewski and his wonderful team of graduate students whom I was fortunate to work with. All members of the team were extremely helpful in my endeavors this past summer. I would also like to show my undying gratitude to my mentor Roman Adam, who spent much of his time guiding me through the summer. He not only worked diligently on completing his graduate thesis, but also found time during the day to answer any questions I might have had. I wish him and the rest of the graduate team the best of luck in the future, and once again thank them for all their support.

References

- [1] Adam, Roman, "Ultrafast Phenomena in Superconducting Optoelectronic Circuits," University of Rochester thesis proposal, January 2000.
- [2] J. Bardeen, L.N. Cooper, and J.R. Schieffer, "Theory of superconductivity," *Phys. Rev.*, vol. 108, pp.1175-1204, July 1957.
- [3] B. D. Josephson, "Possible new effects in superconductive tunneling," *Phys. Lett.*, vol.1, pp. 251-253, July 1962.
- [4] Williams, Carlo, "Ultrafast Photodetectors Based on the Hot-electron Effect in Superconductors," University of Rochester thesis proposal, May 2000.
- [5] R. Adam, R. Sobolewski, W. Markowitsch, C. Stockinger, and W. Lang, "Optically-Induced Effects in Y-Ba-Cu-O Josephson Junctions," *Appl. Supercon.*, vol. 6, pp. 759-766, 1998.
- [6] C.C. Wang, M. Currie, C.A. Williams, T.Y. Hsiang, P.M. Fauchet, R. Sobolewski, S.H. Moffat, R.A. Hughes, J.S. Preston, and F.A. Hegmann, "Intrinsic picosecond response times of Y-Ba-Cu-O superconducting photodetectors," *Appl. Phys. Lett.* vol. 74, pp. 853-855, February 1999.
- [7] R. Adam, C. Williams, R. Sobolewski, O. Harnack, and M. Darula, "Experiments and simulations of picosecond pulse switching and turn-on delay time in Y-Ba-Cu-O Josephson junctions," *Supercon. Sci. Technol.*, vol.12, pp. 912-914, 1999.
- [8] R. Adam, M. Currie, R. Sobolewski, O. Harnack, and M. Darula, "Picosecond response of optically driven Y-Ba-Cu-O microbridge and Josephson-junction integrated structures," *IEEE Trans. Appl. Supercond.*, vol. 9, pp.4091-4094, June 1999.
- [9] R. Adam, M. Currie, C. Williams, R. Sobolewski, O. Harnack, and M. Darula, "Direct observation of subpicosecond single-flux-quantum generation in pulse-driven Y-Ba-Cu-O Josephson junctions," *Appl. Phys. Lett.*, accepted for publication in January, 2000 issue.

Coatings for Ultraviolet Lithography

Stephanie Wolfe
Advisors, Jim Oliver and Doug Smith

The University of Rochester, Laboratory for Laser Energetics
Optical Manufacturing

Abstract

Research into an optical thin film coating that enhances the current design of lithographic excimer laser gratings operating at 193 and 157 nm has been performed. The goal of such research is to improve durability and reflective efficiency. Possible coating materials include the fluorides, magnesium fluoride, barium fluoride, lanthanum fluoride and calcium fluoride. Each fluoride material was deposited on calcium fluoride and silicon substrates and tested for a variety of physical, optical and coating properties. The results from percent transmission tests and ellipsometric analysis were then used to characterize the materials and determine the index of refraction and extinction coefficients for the coating materials. Finally, a system calibration was developed in order to coat a final mirror with an enhanced aluminum reflector.

Background

The driving forces behind optical lithography improvements lie in shorter wavelengths of the light source and increasing numerical apertures of the projection lens. When such improvements are made, microprocessor features can be reduced in size by great orders of magnitude. Moore's Law, which predicts that semiconductor linewidth will halve every two to three years is currently in danger of becoming obsolete. Unless

new technologies are developed which allow lasers to operate under extreme ultraviolet wavelengths, an alternative to optical lithography may soon become necessary.

Currently, lasers operating under 193 nm are emerging from research labs and are beginning to operate within industry. 157 nm lasers are currently in development and pose an even greater challenge because of the millions of pulses of ultraviolet energy that each grating must endure (3). Such a high volume of pulses can cause failures in laser parts such as the gratings used in narrowing the spectrum to 193 or 157 nm. Gratings used in excimer lasers for lithographic purposes are exposed to millions of pulses in relatively short periods of time. The challenge is to build a grating that can withstand continuous pulses of high energy with a minimum of absorption.

Introduction

The challenge in creating an effective optical thin film coating lies in the fact that relatively few coating materials exist which can withstand the continuous bombardment of ultraviolet light that is required in lithographic applications. A layer of aluminum, protected by a layer of magnesium fluoride, currently coats the grating in excimer lasers. While the current grating is substantially effective as an ultraviolet reflector, a greater level of durability and reflectivity is desired. In order to increase grating durability and reflective efficiency, optical thin film coatings will be applied to the grating in alternating layers of materials of high and low refractive indices. Fluorides have been selected as possible materials to test because of their low absorption at 193 and 157 nm. An additional desirable quality lies in their low ultraviolet cut-off, which is at or below 140 nm (1). Fluorides also possess relative durability when exposed to continuous high-energy

pulses. Disadvantages to using fluorides lie in their poor deposition properties. It is often advantageous to use heat or ion assistance to pack down the coating, thereby reducing porosity and increasing physical durability. Unfortunately, this process creates difficulties in coating gratings for industrial applications. As a result of this, the methods described above were not utilized. It should be noted that oxides were considered as a possible coating material because of their desirable refractive indices and better deposition properties, however, because of their high absorption at ultraviolet wavelengths, they were disregarded. After the final coatings are characterized, they will be deposited on a substrate in alternating quarterwave layers of high and low indices of refraction. A quarterwave is defined as the index of refraction, n of a coating, multiplied by its physical thickness, d , or

$$nd = \lambda/4$$

In order to determine n somewhat accurately, measurements of percent transmission are taken, and n and k are altered in order to assign a best-fit curve to the percent transmission data. Once n is determined, d , or the physical thickness can be determined according to the equation above. Characterization software calculates the physical thickness of the coating deposited. A simple proportion consisting of the thickness recorded by a crystal, or monitor in the coater, and the thickness calculated by the computer, can be used to calibrate the coater so that the desired thickness' are accurately deposited in the final coatings.

Coating Deposition

The BALZERS 19" coater was used to deposit coating materials onto substrates, utilizing the electron beam gun deposition method without the use of heat or ion assistance. During electron beam gun deposition, a hot filament emits electrons, which are formed into a beam by a magnetic field and directed onto the material to be evaporated. The coating material is held in a crucible that is water cooled, and the substrate is rotated above the crucible to ensure relatively even coating. The coater is vacuum pumped into the 10^{-5} to 10^{-6} Torr range using a diffusion pump before deposition begins. A crystal, which is located in the upper right hand corner of the coater, monitors the physical thickness of the coating. It is necessary in the final stages of design to make a calibration to adjust for the discrepancies between the position of the crystal and the position of the substrate in order to deposit accurate physical thicknesses.

Each coating material is initially deposited on a Crystalline Fused Quartz (CFQ) substrate, and coating properties such as deposition rate, electron beam emission current and sweep latitude/longitude frequency are noted. After physical tests are performed on the CFQ optics, 5000 angstroms of each coating is deposited on each of the following substrates: a 1" diameter single crystal Calcium Fluoride substrate, and a 2" diameter silicon wafer that is p-doped with boron, has an orientation of 1-0-0 and a resistivity of 1-10 ohms. The calcium fluoride coating material was deposited on 1" squares of UV grade fused silica. In an attempt to avoid crazing, 1000 angstroms of lanthanum fluoride were deposited instead of 5000. This will be taken into account during characterization but should have little effect on the final product because all layers of interest at 193 or 157 nm will be significantly thinner than 5000 angstroms.

The same scan is repeated and the results are compared to the baseline, creating a 100% reflectance line. In figure 1, the computer sets the value of R equal to 1. In figure 2, a coated optic takes the place of r_2 , and r_2 is moved in front of the coated optic. The beam is reflected across r_1 , r_s , r_2 , r_s , and r_3 respectively, giving the equation

$$R' = R_0 r_1 r_s r_2 r_s r_3$$

Since R is given to equal one, it can be substituted into the above equation giving

$$R' = r_s^2$$

The square root of r_s^2 is calculated by the computer, which represents the absolute percent reflection of the coated optic across the spectrum tested.

IV. Roughness

Roughness of a coated optic is measured in order to determine the surface structure of the coating. It is defined as any closely spaced irregularity in a surface such as cutting tool marks or irregular coating texture. Rayleigh's Law states that the intensity of scattered light (I_s) increases as wavelength decreases according to the equation

$$I_s = k \lambda^{-4}$$

where k is a constant and λ is equal to wavelength. Because of this property, it is necessary to minimize the roughness of a coating's surface structure in order to minimize the scattering of light. The roughness of the coated calcium fluoride substrates are measured using a WYKO surface profiler which scans the optic and calculates the root mean squared roughness over the entire measured array according to the equation

$$R_q = \sqrt{\frac{1}{n} \int_{i=1}^n (z_i - \bar{z})^2}$$

where n equals the number of peaks across the measured array, and z equals the height of the peak.

Coating Properties and Test Results

Below is a summary of the results of the tests described above.

Coating	MgF ₂	BaF ₂	LaF ₃	CaF ₂
Substrate	CaF ₂	CaF ₂	CaF ₂	fused silica
Tape Test (Pass/Fail)	P	F	F	F
Rub Test (Pass/Fail)	P	F	F	F
Root Mean Squared Roughness (nm)	42.95	65.55	71.85	71.48
% T Referenced to Substrate @193 nm	98.13%	97.08%	96.14%	95.27%
Absolute % Reflectance @193 nm	3.84%	5.16%	7.37%	4.25%
Emission Current (A)	0.02	0.02	0.02	0.02
Deposition Rate (Angstroms/sec)	3.0-5.0	0.5-1.0	1.0-2.0	8.0-10.0

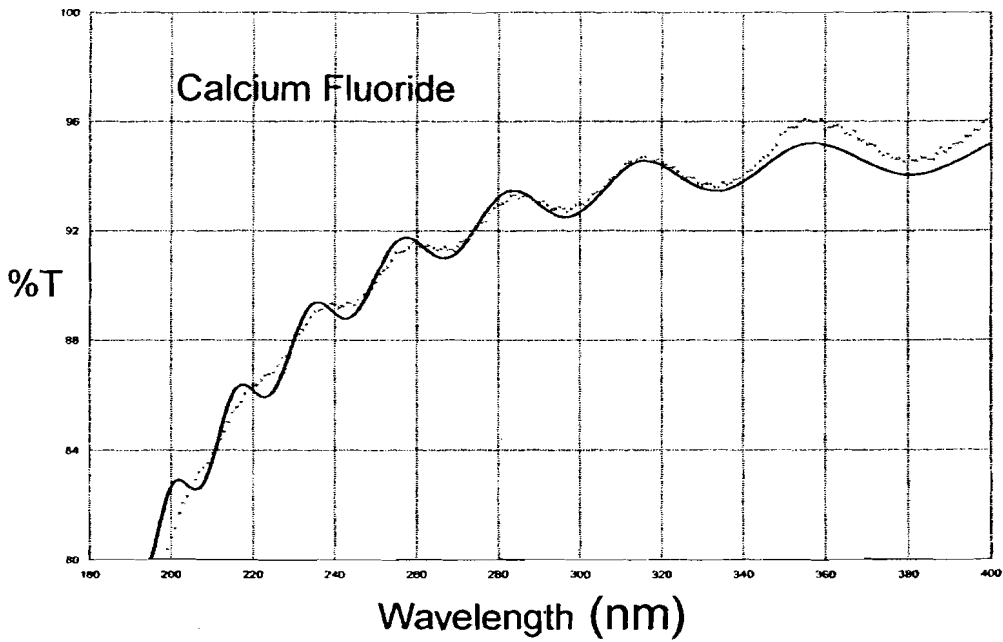
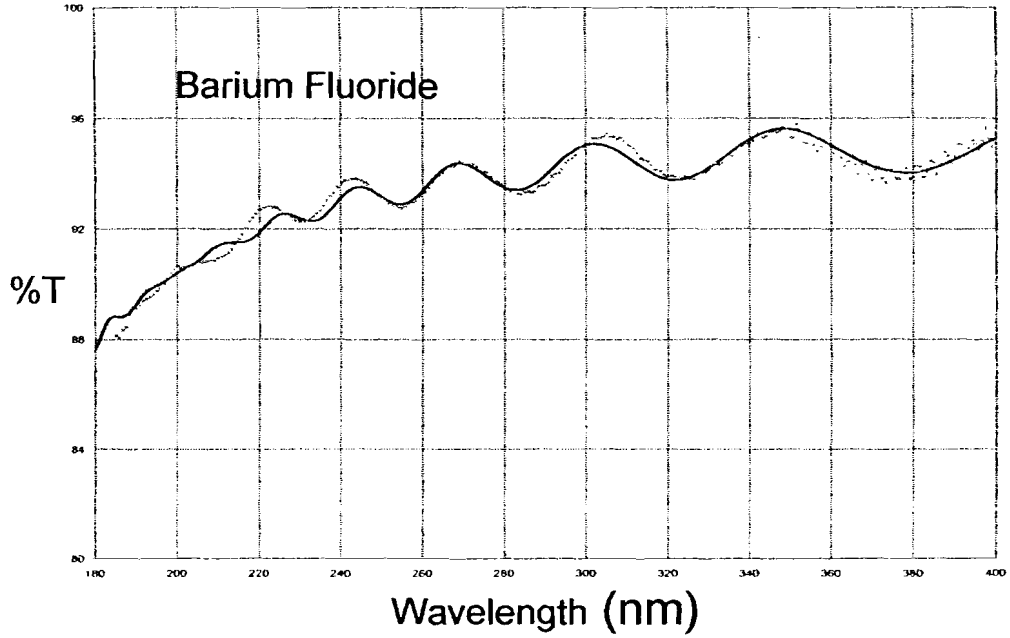
Characterization

I. Characterization and Design at LLE

The CARY percent transmission data is characterized using OptiChar for Windows Version 2.22 software. Characterization involves the altering of index of refraction values ' n ' and extinction coefficients ' k ', as a function of wavelength, in addition to the film thickness d and the inhomogeneity of n , to assign a best fit curve to the percent transmission data. Due to the crazing noted, lanthanum fluoride was disregarded as a possible high index material in the initial stages of characterization. Magnesium fluoride characterization yielded an index value that was too high when compared to reported values. Due to these factors, calcium fluoride was selected as the

low index material, and barium fluoride was selected as the high index material.

Attempts to assign a best-fit curve are pictured below.



While these materials were chosen and used to coat a mirror, their selection is the result of the process of elimination. Characterization of barium fluoride yielded an n value of 1.6 compared to a reported value of 1.7⁽⁴⁾. Its k value was equal to zero compared to a reported value of 0.018⁽⁴⁾. Similarly, calcium fluoride yielded an n value of 1.13 compared to 1.39⁽⁴⁾. Its k value was calculated to be 0.0015 compared to 0.011⁽⁴⁾. Despite these discrepancies, a table of n and k values was produced as a function of wavelength. These values were used to calculate the physical thickness of the coating deposited on the samples. The physical thickness of barium fluoride deposited was calculated to be 7,170 angstroms while the physical thickness of calcium fluoride was calculated to be 11,937 angstroms. Keeping in mind that the crystal monitor in the coater was programmed to deposit 5000 angstroms, we can set up a simple proportion for each coating material in order to deposit an accurate quarterwave layer. These proportions are listed below.

Barium Fluoride: $0.69735 = \text{physical thickness recorded by monitor} / \text{actual physical thickness measured on substrate}$

Calcium Fluoride: $0.41887 = \text{physical thickness recorded by monitor} / \text{actual physical thickness measured on substrate}$

OptiLayer software designed a coating by calculating the thickness of 1 quarterwave. Knowing the above proportions, the crystal monitor was programmed to coat a mirror with the following characteristics:

Barium Fluoride: Physical Thickness = 362.544 Angstroms

Calcium Fluoride: Physical Thickness = 532.683 Angstroms

Multiplying the optical thickness of each coating by its respective monitor to physical thickness ratio yields the physical thickness that must be deposited according to the coater monitor.

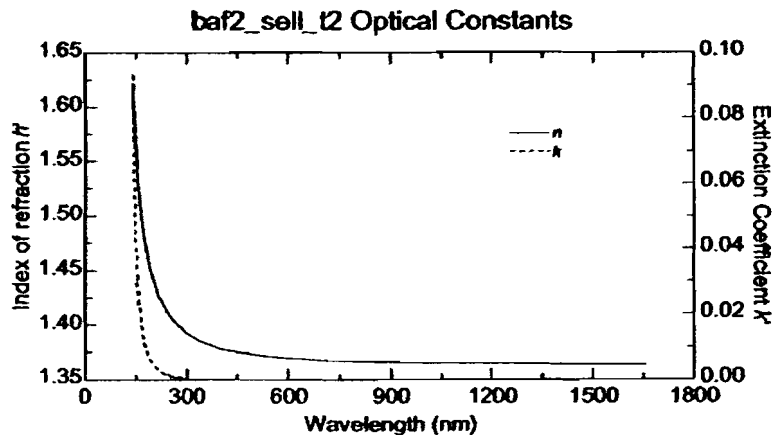
Barium Fluoride: Physical thickness deposited according to monitor = 253 Angstroms

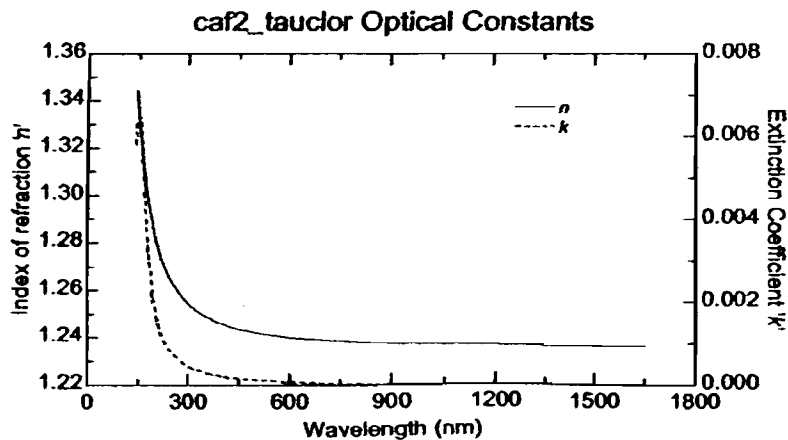
Calcium Fluoride: Physical thickness deposited according to monitor = 223 Angstroms

The final mirror was coated with alternating layers of barium fluoride and calcium fluoride, respectively. The results showed a significant increase in absolute percent reflectance, however, the peak of the coated aluminum curve occurs in the visible spectrum, not in the ultraviolet. In order to shift the peak, it is necessary to adjust the thickness' of the system by the multiplying by the percent desired peak divided by the current peak.

II. Characterization at J.A. Woolam Co., Inc.

In addition to being scanned on the CARY, the coated silicon wafer optics were sent to J. A. Woolam Company for Variable Angle Spectroscopic Ellipsometry (VASE) analysis in order to characterize film thickness and optical properties. Data was acquired over the spectral range of 146 nm to 1800 nm. Results from ellipsometric analysis are expected to yield more reliable results concerning film thickness and optical properties. n and k data is shown below (2).





Conclusion

Research into optical coatings for ultraviolet excimer laser gratings has been performed. Unfortunately, due to time constraints, this project was unable to be completed within the time allotted. My advisor will complete it by using the n and k data from ellipsometric analysis performed by J. A. Woolam Company. Although the first mirror design yielded inaccurate results, one must keep in mind the difficulties encountered in both the deposition methods and spectrophotometer used. Due to the industrial implications of such a coating, it was recommended that each sample be made without heat or ion assistance, as it would be difficult to utilize such methods in the coating of an actual grating. As a result of this, the porosity of the sample coatings along with the CARY's inability to measure accurately in the deep ultraviolet spectrum contributed significantly to the final inaccurate results. On a more positive note, data regarding physical, optical and deposition properties for the fluorides was collected and will be utilized by the lab in the completion of this project and future endeavors.

I would especially like to thank my advisors Jim Oliver and Doug Smith for taking the time out of their busy days to familiarize me with both the labs and the theory behind my project. Thank you also to Mary Risely for collecting optical constant data and teaching me how to use the CARY. Especial thanks to Nelson LeBarron and everyone in OMAN for teaching me how to use the coater and always being there when it broke down. Finally, I would like to thank Dr. Craxton for selecting me to work at LLE and giving me the chance to experience scientific research.

References

1. R. Conwell. "Investigation of Fluoride Thin Films for Reflective Coatings at 157 nm". SPIE vol. 3268 p.352-356
2. Hilfiker, James N. "VUV-VASE Measurement of Fluoride Thin Films". J.A. Woolam Co., Inc. August 22, 2000
3. Lawes, R. A. "Future Trends in High Resolution Lithography". Central Microstructure Facility, Rutherford Appleton Laboratory, Chilton, Didcot, Oxfordshire UK. Online: www.elsevier.nl/locate/apsusc. Elsevier Science B.V., 2000
4. M. Zukic, D. Torr, J. Spann, M. Torr, "Vacuum Ultraviolet Thin Films 1: Optical Constants of BaF₂, CaF₂, MgF₂, Al₂O₃, HfO₂, and SiO₂ Thin Films". Applied Optics vol. 29 No. 28 p. 4284-92, 1990.